UNIVERSIDADE DE LISBOA

INSTITUTO SUPERIOR TÉCNICO

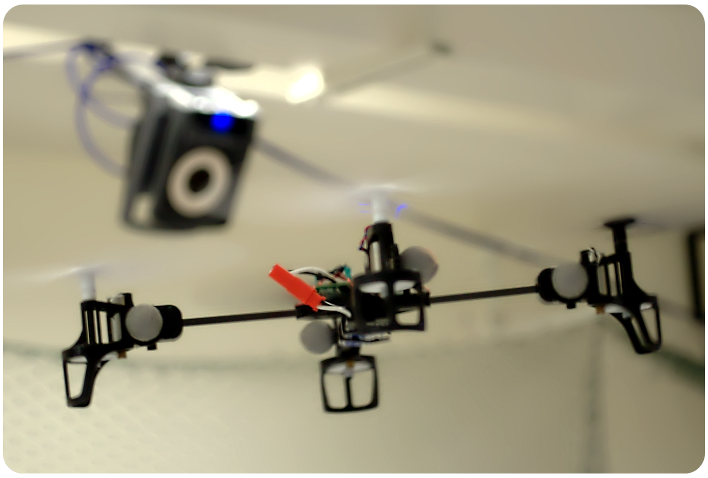

Nonlinear control of autonomous air vehicles

David Alexandre Cabecinhas

Supervisor: Doctor Carlos Jorge Ferreira Silvestre
Co-Supervisor: Doctor Rita Maria Mendes de Almeida Correia da Cunha

Thesis approved in public session to obtain the PhD Degree in Electrical and Computer Engineering

Jury final classification: Pass with Distinction

Jury

Chairperson: Chairman of the IST Scientific Board
Members of the committee:
Doctor Tarek Hamel
Doctor Urbano José Carreira Nunes
Doctor Maria Isabel Lobato de Faria Ribeiro
Doctor Paulo Jorge Coelho Ramalho Oliveira
Doctor Rita Maria Mendes de Almeida Correia da Cunha

2014

UNIVERSIDADE DE LISBOA

INSTITUTO SUPERIOR TÉCNICO

Nonlinear control of autonomous air vehicles

David Alexandre Cabecinhas

Supervisor: Doctor Carlos Jorge Ferreira Silvestre
Co-Supervisor: Doctor Rita Maria Mendes de Almeida Correia da Cunha

Thesis approved in public session to obtain the PhD Degree in Electrical and Computer Engineering

Jury final classification: Pass with Distinction

Jury

Chairperson: Chairman of the IST Scientific Board

Members of the committee:

Doctor Tarek Hamel
Full Professor, Université Nice Sophia Antipolis, France
Doctor Urbano José Carreira Nunes
Full Professor, Faculdade de Ciências e Tecnologia, Universidade de Coimbra
Doctor Maria Isabel Lobato de Faria Ribeiro
Full Professor, Instituto Superior Técnico, Universidade de Lisboa
Doctor Paulo Jorge Coelho Ramalho Oliveira
Associate Professor, Instituto Superior Técnico, Universidade de Lisboa
Doctor Rita Maria Mendes de Almeida Correia da Cunha
Assistant Researcher, Instituto Superior Técnico, Universidade de Lisboa

Funding Institution:

Fundação para a Ciência e a Tecnologia

2014

Abstract

This thesis focuses on the challenge of achieving autonomous control of aerial vehicles, motivated by the requirements of current, and yet to be envisaged, applications of unmanned aerial vehicles (UAVs). Particular emphasis is given to the design and experimental evaluation of control algorithms that are simultaneously rooted in solid principles from nonlinear systems theory and specifically targeted at applications of interest for vertical takeoff-and-landing rotorcraft, in particular quadrotor vehicles. The motion control problems addressed include stabilization, trajectory tracking, and path following, all defined in free-flight mode, and robust take-off and landing taking into account interaction with the environment. The first key contribution of this thesis is a landmark-based controller for force and torque actuation that almost globally stabilizes a fully-actuated rigid body. The controller is based on the position coordinates of a collection of landmarks fixed in the environment and velocity measurements as observed from the vehicle. The next contributions focus on designing tracking controllers for more realistic vehicle models. A trajectory tracking controller is proposed for steering a quadrotor vehicle along a time-dependent trajectory considering constant force disturbances and ensuring actuation bounds. In an effort to achieve global stabilization, the trajectory tracking problem is relaxed and a controller to steer a quadrotor vehicle along a predefined path is presented, with a secondary control objective related to the velocity. The proposed solution guarantees global convergence of the closed-loop path following error to zero in the presence of constant disturbances and ensures that the actuation does not grow unbounded as a function of the position error. The remaining main contributions go a step further in the effort to improve the autonomy of the vehicle, and include the design of a hybrid robust take-off and landing maneuver and an output-feedback controller for free-flight. The robust take-off and landing of a quadrotor UAV is targeted at critical scenarios, where sloped terrains and surrounding obstacles are present. A cascaded output-feedback architecture comprising a nonlinear attitude observer and a nonlinear controller is proposed for position and attitude stabilization of a quadrotor based on measurements provided by a pan and tilt camera and rate gyros.

Keywords: trajectory tracking; path following; backstepping; adaptive control; output-feedback; vision-based control; stability of nonlinear systems; hybrid systems; autonomous unmanned aerial vehicles; quadrotor vehicles.

Resumo

Esta tese tem como foco o desafio de conseguir controlo autónomo de veículos aéreos, motivado pelos requerimentos das aplicações actuais e futuras de veículos aéreos não tripulados. É prestada particular ênfase ao desenho e avaliação experimental de algoritmos de controlo que sejam simultaneamente baseados em princípios sólidos de teoria de sistemas não lineares e especificamente direccionados a aplicações de interesse para veículos a rotor capazes de descolagem vertical. Os problemas de controlo de movimento endereçados incluem estabilização, seguimento de trajectórias e seguimentos de caminhos, definidos em voo livre, e descolagem e aterragem robustos tendo em conta interações com o ambiente. A primeira contribuição-chave desta tese é um controlador baseado em marcas para actuação em força e momento que estabiliza quase-globalmente um corpo rígido completamente actuado. O controlador é baseado nas coordenadas de posição de uma colecção de marcas fixa no ambiente e medidas de velocidade observadas do veículo. As contribuições seguintes focam-se no desenho de controladores para modelos de veículos mais realistas. Um controlador de seguimento de trajectória é proposto para guiar um veículo quadrirotor segundo uma trajectória na presença de perturbações constantes em força e assegurando que a actuação é limitada. Num esforço para conseguir estabilidade global, o problema de seguimento de trajectória é relaxado para um problema de seguimento de caminho para um veículo quadrirotor, com um objectivo secundário relacionado com a velocidade. A solução proposta garante, em malha fechada, convergência global do erro de seguimento de caminho para zero, na presença de perturbações constantes em força e assegura que que a actuação é limitada como função do erro de posição. As restantes contribuições-chave são esforços para melhorar a autonomia do veículo e incluem o desenho de um controlador híbrido robusto para manobras de descolagem e aterragem e de um controlador para voo livre baseado em retroação da saída. A manobra de descolagem e aterragem robusta para um quadrirotor é direccionada a cenários críticos, em terrenos inclinados e com obstáculos circundantes. Uma arquitectura em cascada que inclui um observador de atitude não-linear e um controlador não-linear é proposta para estabilização em posição e atitude de um veículo quadrirotor baseada em medidas obtidas por uma câmara capaz de movimento horizontal e inclinação e por giroscópios.

Palavras-chave: Seguimento de trajectórias; seguimento de caminhos; backstepping; controlo adaptativo; retroacção da saída; controlo baseado em visão; sistemas híbridos; estabilidade de sistemas não lineares; veículos aéreos não-tripulados; veículos quadrirotores.

Acknowledgments

First and foremost, I acknowledge the support and friendship of my two supervisors. I am grateful to Carlos Silvestre for encouraging me to embark on this project and supporting me all the way. It has been an enormous pleasure to work with such dedicated researcher as Rita Cunha. I am very grateful for her thorough work in our articles, his critical attitude towards the results, his encouragement, and several precious pieces of advice.

A subset of the work presented in Chapter 5 was done in collaboration with Professor Lorenzo Marconi and his then PhD student Roberto Naldi. I gratefully acknowledge their scientific help and thank them for accompanying me during my stay at the University of Bologna. A subset of the work presented in Chapter 6 was done in collaboration with Sérgio Brás, my colleague at ISR.

I am very grateful for the financial and logistic support provided by Fundação para a Ciência e Tecnologia through the Ph.D. grant SFRH/BD/31439/2006, the Institute for Systems and Robotics and the University of Macau. I would also like to thank Professors João Sentieiro and Paulo Oliveira for having accepted to be part of the steering committee. I am extremely grateful for the sound advice, insightful suggestions and comments, which helped me to improve this document.

This thesis would not have been possible without the help of many friends and colleagues that I have encountered throughout my journey. This section is too small to fit all of their names but special thanks are due all of them at the DSOR group, ISR, DEIS - University of Bologna and University of Macau.

Finally, my thoughts go to my family. I am ever so grateful to my parents for their exceedingly support and encouragement throughout all of my life. My last thank you goes to Agnieszka for all her help.

Contents

List of Figures

Notation

$\mathbb{R}$

set of real numbers.

$\mathbb{R}^n$

set of n-dimensional vectors with real entries.

$\mathbb{R}^{n \times m}$

set of $n \times m$ matrices with real entries.

a, A, α, Γ

scalar variable or constant.

$\mathbf{a}, \boldsymbol{\alpha}$

vector variable or constant.

a_i

element i of a vector $\mathbf{a} \in \mathbb{R}^n$.

$A, \boldsymbol{\gamma}$

matrix variable or constant.

a_{ij}

element of a matrix $A \in \mathbb{R}^{n \times m}$, located at row i and column j.

$\mathbf{0}$

vector of zeros of the appropriate length, $\mathbf{0} = [0\ 0 \ldots 0]^T$.

$\mathbf{1}$

vector of ones of the appropriate length, $\mathbf{1} = [1\ 1 \ldots 1]^T$.

$\mathbf{e}_i$

the i^{th} unitary vector. The vectors $\mathbf{e}_1$, $\mathbf{e}_2$, and $\mathbf{e}_3$ denote the unit vectors co-directional with the x, y, and z axes, respectively.

I_n

$n \times n$ identity matrix.

$(.)^T$

transpose operator of a vector or matrix.

$(.)^{-1}$

matrix inverse operator.

sign(.)

signum function of the elements of its argument, possibly a vector or matrix.

$|.|$

absolute value operator, for scalar arguments.

$||.||$

norm operator, for vector arguments.

$\det A$

matrix determinant operator, $A \in \mathbb{R}^{n \times n}$.

tr(.)

trace of a matrix operator.

$\mathrm{diag}(\mathrm{A_1}, \ldots, \mathrm{A_n})$

block diagonal matrix composed by the matrix elements A_1 to A_n.

$f'(x)$

partial derivative a function with respect to the parameter, $f'(x) = \frac{\partial f}{\partial x}(x)$.

$\dot{f}(x)$

total time derivative of a function, $\dot{f}(x(t)) = f'(x(t))\dot{x}(t)$.

$SO(n)$

group of $n \times n$ proper rotation matrices, $SO(n) = \{R \in \mathbb{R}^{n \times n} : R\ R^T = I_n, \det R = 1\}$.

$SE(n)$

special euclidean group of rigid body transformations in n-dimensional space, where each element $(R, \mathbf{p})$ is composed of a proper rotation matrix and a translation vector, such that $SE(n) = \{R, \mathbf{p} : R \in SO(n), \mathbf{p} \in \mathbb{R}^n\}$.

$\mathfrak{so}(n)$

Lie algebra associated with the Lie group $SO(n)$.

$\mathfrak{se}(n)$

Lie algebra associated with the Lie group $SE(n)$.

$\{\mathcal{I}\}$

local inertial reference frame.

$\{\mathcal{B}\}$

body-fixed reference frame, rigidly attached to the vehicle.

${}^{B}_{A}R$

rotation matrix in SO(3) from reference frame $\{\mathcal{B}\}$ to reference frame $\{\mathcal{A}\}$.

$R_x(.)$

rotation matrix in SO(3) about the x-axis of the argument angle.

$R_y(.)$

rotation matrix in SO(3) about the y-axis of the argument angle.

$R_z(.)$

rotation matrix in SO(3) about the z-axis of the argument angle.

$\tilde{x}$

the error in estimating the unknown quantity x, defined as $\tilde{x} = x - \hat{x}$.

$\hat{x}$

the estimate of the unknown quantity x.

$\sigma(s)$

A function $\sigma(s) : \mathbb{R} \to \mathbb{R}$ is a *saturation function* if it is differentiable and verifies, for positive M and σ_{max},

$$\begin{aligned} 0 < \sigma'(s) < M, &\text{ for all } s, \\ \sigma(-s) = -\sigma(s), &\text{ for all } s, \\ s\sigma(s) > 0, &\text{ for all } s \neq 0, \sigma(0) = 0, \\ \lim_{s \to \pm\infty} \sigma(s) = \pm\sigma_{\text{max}}. \end{aligned}$$

.

$\mathbf{a} \times \mathbf{b}$

external product of vector $\mathbf{a}$ and $\mathbf{b}$.

$S(\mathbf{x})$

the skew-symmetric operator map is an isomorphism between $\mathbb{R}^3$ and the Lie algebra $\mathfrak{so}(3)$, denoted as $S(\mathbf{x}) : \mathbb{R}^3 \to \mathfrak{so}(3)$, and verifies $S(\mathbf{x})\mathbf{y} = \mathbf{x} \times \mathbf{y} =$, where $\mathbf{x}, \mathbf{y} \in \mathbb{R}^3$.

$S(\mathbf{x})^{-1}$

the inverse map for the skew operator, $S^{-1}(.) : \mathfrak{so}(3) \to \mathbb{R}^3$, is defined such that $S^{-1}(S(\mathbf{x})) = \mathbf{x}$.

Acronyms

AGAS

almost globally asymptotically stable. 14, 15, 24–26, 29, 138

CCD

charge-coupled device. 19

DGPS

differential global positioning system. 3

DSSS

direct sequence spread spectrum. 45

FOG

fiber optic gyro. 3

GAS

globally asymptotically stable. 14, 37

GNSS

global navigation satellite system. 3, 4

GPS

global positioning system. 3, 4, 19, 36

IMU

inertial measurement unit. 3, 36

LiPo

lithium polymer. 2

LRG

laser ring gyro. 3

MEMS

micro electro mechanical systems. 3

NOAA

National Oceanic and Atmospheric Administration. 2

OMCS

optical motion capture system. 44, 45, 59, 100

PD

proportional-derivative. 139

PID

proportional-integral-derivative. 31, 82

RC

radio control. 47

RF

radio frequency. 45, 46

RMS

root mean square. 48, 51

RTK

real time kinematic. 3

SLAM

simultaneous localization and mapping. 4, 5

UAV

unmanned aerial vehicle. 1–5, 8, 9, 11, 32, 79, 81, 83, 85, 89, 106, 137–139

VTOL

vertical take-off and landing. 32, 81

1 Introduction

1.1 Motivation

Over the past decades small-scale unmanned aerial vehicles (UAVs) have evolved from a hobby to an industry where the vehicles are mass produced on a wide range of sizes and serve as robust commercial and research platforms. Fueling this interest is the fact that aerial vehicles are no longer restricted to being remote controlled airships but are progressively being imbued with autonomous capabilities, so that a larger number of complex missions can be carried out by non-skilled operators or even without any human intervention.

Autonomous and remotely operated UAVs perform a plethora of civilian operations with most of them falling under the umbrella term of remote sensing. Unmanned aerial vehicles provide stable platforms that are not restricted to a given location in space and can be equipped with different purpose sensors and survey a wide region in a short time span. The UAV platforms also provide access to areas which are hazardous to human life or inaccessible by conventional means, as its operation in risk theaters does not endanger human lives. Prominent examples include search and rescue operations at sea or inhospitable locations and post-disaster assessment at a nuclear site (see the recent Fukushima Daiichi nuclear disaster [Gui12], on the wake of a major earthquake and tsunami). Another important civilian application of UAVs in dangerous environments is forest fire detection and monitoring [Emb]. The autonomy of the vehicles enables sustained flight, in both day and night conditions, and provides the fire crews with helpful real-time data, like thermal imaging, wind speed and temperature profiles, so they can optimize the fire suppression efforts.

Commercially, UAVs can be used to save time and money by efficiently performing tasks which previously required professional pilots, a crew, and a full scale helicopter. Examples include the inspection of structures such as oil and gas pipelines, power lines, bridges, and industrial buildings such as power plants and mills. Moreover, it is common for oil and gas pipelines to cross vast regions in dangerous and unsafe areas. These stretches of pipeline can be continuously patrolled by UAVs equipped with night vision cameras, in order to keep thieves, pirates, and other attackers at bay, improving the security of both workers and equipment [Aer].

The unique ability of unmanned aircraft to penetrate areas which may be too dangerous to risk manned flights has also been exploited for scientific research. The National Oceanic and Atmospheric Administration (NOAA) began utilizing an unmanned aircraft system in 2006 as a hurricane hunter. Beyond the data typically obtained with manned hurricane hunters, the UAV system provides measurements far closer to the water surface than previously captured and can be used to obtain data in severe weather conditions, without putting human lives at stake. . Another use of UAVs for scientific research in extreme conditions is being carried out by the British Antarctic Survey in Antarctica [Bri]. Unmanned aerial platforms are also starting to have a predominant role in agriculture where they can be used for spraying, seeding, remote sensing, precision agriculture, frost mitigation and variable rate dispersal. The large-scale Yamaha RMAX helicopters have been used for monitoring of crops and rice fields spraying in Japan [rma]. Additional applications include environmental surveys and helping animal conservation efforts.

The popularity that UAVs enjoy nowadays, both as a mass market hobby and as commercial and research platforms, was only made possible by recent technological progress in several key areas. We now detail some of these improvements in the areas of aerial platforms, sensors, and actuators, before going into their applications and automation challenges.

Power sources play a preponderous role in defining the characteristics of the aircraft they power. Internal combustion engines are the most common power source for large outdoor aircraft due to the unsurpassed endurance and range that they provide. Nonetheless, electrical motors and related components have experienced a tremendous evolution, allowing electrical vehicles to be competitive with respect to their gas powered counterparts, in all but the most endurance demanding applications. Electrical motors are cleaner than traditional combustion engines and allow for the use of aerial vehicles in closed spaces and in situations where combustion engines are a potential hazard. The development of strong rare-earth magnets led to powerful and efficient motors. These are produced in an array of sizes, ranging from large motors that can power heavy aircraft to the miniature scale, where highly agile aerial rotorcraft vehicles spanning only a few centimeters can be produced. Battery technology also evolved considerably over the past years. Common lithium polymer (LiPo) batteries now pack enough energy density to allow even the smallest rotorcraft to fly from 10 to 20 minutes. Besides high energy densities, LiPo batteries are capable of high discharge rates, which are required for aggressive maneuvers and aerobatic flight. Along with the motors, the servo actuators for the moving control surfaces and blades also evolved to a point that enables the production of miniature linear and angular actuators, which are fast enough to enable aggressive controlled flight.

Sensors are a fundamental component of an autonomous aerial vehicle. The UAV depends on them to assess its current state and perceive the environment, so that it can react in the most appropriate way to the internal and external conditions it is experiencing. Sensor outputs are used to estimate the UAV state and to generate the appropriate control action, in order to progress towards the mission goal, while avoiding potential hazards. Typically UAVs are equipped with additional sensors that, while not required for a successful autonomous flight, are needed to achieve the objectives of the envisaged application. These additional sensors might include video cameras, thermographic cameras, air quality sensors, thermometers, radar and doppler radar, laser rangefinders, among other alternatives, depending on the mission objectives. The miniaturization effort and the emergence of micro electro mechanical systems (MEMS) technology influenced the sensors that can be carried on an autonomous aerial vehicle. Researchers and UAV developers now have at their disposal small, lightweight, and sufficiently accurate sensors that enable an autonomous vehicle to estimate its state and help its self-stabilization.

The state of a rigid body, such as an UAV, is composed by its position, attitude, velocity and angular velocity. The angular states are the ones for which the most accurate onboard sensors exist. Modern inertial measurement units (IMUs), comprising gyroscopes, accelerometers and magnetometers, are available that output the estimated vehicle attitude and angular velocity. They exist in a wide range of prices starting from the cheapest, but also less accurate, used in toys and hobby vehicles to the intermediate, used essentially for research platforms, both based on MEMS technology. On the more accurate range we find IMUs based on fiber optic gyros (FOGs) and laser ring gyros (LRGs) technology, which are expensive, export-restricted, and used mostly for large civilian and military aircraft, submarines, as well as missiles and satellites.

For positioning, aerial vehicles that operate outdoors are able to use global navigation satellite systems (GNSSs) such as the american global positioning system (GPS), the russian GLONASS, and, in the future, the european Galileo. The GPS system, although initially a military effort, has been open to civilians in its non-degraded accuracy mode since the year 2000. There are several problems with the GPS approach to UAV positioning, primarily concerning the location accuracy, as the positions obtained from GPS receivers have, in the best circumstances, standard deviations in the order of meters. Differential global positioning system (DGPS) and real time kinematic (RTK) are improvements over plain GPS that can increase the accuracy of the position estimated to the order of centimeters.

However, they require additional ground-based reference stations that also acquire GPS signals so the onboard and the fixed ground-based station data can be compared and improved upon, using the fact that the ground station is at a known fixed position and that the atmospheric perturbations suffered by the GPS signals received at the vehicle and the ground station are the same. Another drawback of current GPS technology is that the position information is obtained at a low sampling rate, typically 1 Hz. As a consequence, neither the positions nor the velocity estimates obtained by filtering GPS signals are very accurate and an UAV cannot rely solely upon GPS positioning signals for high precision flight. As previously mentioned, satellite navigation is only feasible for vehicles operating outdoor in unobstructed environments. In indoor environments, or outdoors among high buildings, the satellite signals are weak and satellite-only navigation is impossible. A solution to fly an autonomous UAV under these circumstances is the use of additional short range sensors, such as onboard cameras, laser range finders or sonars, to determine the relative distance to the ground and obstacles around the vehicle. These sensors measure distances at much higher sampling rates than GPS (typically in the order of 50 Hz), and the velocity estimates obtained by discrete differentiation and filtering of the position signals are usable for control purposes.

As an alternative to GNSSs, other external sensor approaches can also be employed to the yield absolute measurements for the positioning problem. Absolute position measurements are typically obtained from an array of cameras that observes the vehicle and determines its position by computer vision methods. In this scenario, the position is determined by an offboard computer, and is relayed to the vehicle as soon as it is available. Through triangulation of matching image points across high resolution and high speed video cameras it is possible to obtain all of the vehicle state information (position, velocity, attitude and angular velocity) with sub-milimeter and sub-degree accurately at high sampling rates, typically in the order of hundreds of Hz. This approach provides the best results for estimating position and velocity but requires a room equipped with a fixed camera setup and *a priori* calibration of the cameras. Its usefulness is limited to the room where the camera setup is installed as it is not practical to transport the camera setup and recalibrate it for an outdoor UAV mission. In order to overcome this practical limitation, the use of lasers and 3D time-of-flight cameras has been proposed for vehicle simultaneous localization and mapping (SLAM). In this mode, the vehicle builds a map of the terrain while simultaneously locating itself, using for that purpose the information provided by the sensors along the way. SLAM is still an active research topic in the UAV and mobile robotics community and has had moderate success in exploring structured and, to a lesser degree, unstructured environments.

The development of novel communication technologies and the ongoing effort of computer miniaturization that is still taking place also contributed to the surge in UAVs and their applications. Better communication channels brought out by spread spectrum techniques enable the operation of multiple vehicles simultaneously without radio interference. Additionally, modern WiFi hardware and protocols enable the real-time transmission of the large quantities of data generated by onboard sensors, including live video streams and laser rangefinder scans, from the vehicles to ground stations for further offboard analysis. This renders the data analysis faster, as we are not constrained by the computational power available onboard nor by the time it takes for the vehicle to return from its mission and the data to be finally transferred to a more powerful computing platform for analysis. The ongoing microcomputer revolution brought innovations that contribute for a more complete autonomy of aerial vehicles. The miniaturization efforts taken by microchip companies, which have supported Moore's Law for more than half a century, have made possible for a device as small as a cellphone to carry the same computational power that some years ago was only available on desktop computers. The ever increasing performance of microcomputers has enabled even small UAVs not only to execute advanced control algorithms for self stabilization but also to employ computationally heavy techniques such as image processing to propel more sophisticated navigation and control algorithms. Nowadays, even medium sized UAVs can easily carry onboard the computational power available to the best laptop computers, thereby enabling the use of state of the art image and video processing techniques, allied to computationally heavy SLAM algorithms, to achieve the best navigation estimates possible.

The aforementioned technological advances have given rise to a variety of aircraft platforms, each with different characteristics regarding payload, autonomy, and flying qualities. We now describe some of these platforms, restricting ourselves to rotorcraft similar in concept and maneuverability to the helicopter, in order to keep the discussion focused on the subject matter of the thesis.

Toy helicopters are small electric helicopters, usually with a coaxial rotor configuration and mechanically stabilized with a stabilizer bar. The possible control actions span from 2 control inputs (thrust and yaw) all the way to 4 control inputs (thrust, yaw, pitch and roll). The coaxial configuration and the stabilizer bar mechanically provide stability augmentation, resulting in vehicles that are easy to control and making them popular with children. The downside of the additional stabilization is that the resulting vehicles are slow, limited in the attitude angles they can attain, and do not fulfill their potential as flying machines. Moreover, the extra stabilization induces undesirable couplings and side effects, like the pendulum effect that one can see when trying to abruptly start moving or make one of these vehicles come to a full halt. This also causes these rotorcraft to be poor flyers in even the lightest wind conditions as they cannot tilt enough to counteract the

Figure 1.1: Picooz micro helicopter.

Figure 1.2: CX2 coaxial helicopter.

Figure 1.3: mCPx micro helicopter.

Figure 1.4: Yamaha RMAX helicopter.

wind breeze and are dragged by it. Despite their high stability, most of the platforms have very little payload capability, making them a weak choice for robotic platforms. Examples of the use of these platforms for research include the two channel micro helicopter [PW09] shown in Figure 1.1 and the larger four channel helicopter [RSTE+10, HSDM09] depicted in Figure 1.2.

Remote controlled helicopters exist in several sizes, ranging from the 20 cm rotor span of a mCPx micro helicopter to the 3.63 meters of a Yamaha RMAX. These rotorcraft are highly maneuverable and the blades can have fixed or variable pitch. The variable pitch makes inverted flight possible and allows the vehicle to perform very aggressive maneuvers. These platforms are also more robust to wind disturbances as they can easily reject them, unlike toy helicopters, that get projected away even with a calm or mild breeze. The most common helicopter designs employ a bell-hiller stabilizing bar (also known as flybar) to help stabilize the platform, without which the rotation of the blades would make the helicopter vibrate uncontrollably. However, this mechanical solution for stable helicopter flight has negative effects on performance. Recent advances in microelectronics and miniaturization of sensors and actuators have led to the development of flybarless helicopters that have all the advantages of flybar helicopters but imposes fewer restrictions on flight envelope, as they do not have the additional mechanical stabilizing dynamics. An electronic feedback inner-loop replaces the stabilizer bar and allows for unprecedented performance and the tracking of more aggressive maneuvers.

The mechanics and moving parts of the helicopter, in particular the rotor head, are intricate and complex, with a large amount of moving parts which are susceptible to wear and tear. Quadrotors and other multirotor aerial vehicles are a recent trend in the hobby and research community and have been gaining popularity due to their simpler mechanics and easier maintenance, compared to helicopters. The multirotor configuration results in smaller rotor span to achieve the same thrust force, leading to less pronounced unmodeled higher order effects such as blade flapping. The major drawback of this configuration is that the vehicles are not able to perform inverted flight, although in practice this is not a relevant feature. There is some research on variable pitch quadrotors but it sort of defeats the purpose of having a robust machine with simple mechanics [MRU+11].

The quadrotor's simple mechanics, high versatility, and payload capability, allied to its high maneuverability and challenging controllability, make it an ideal platform for the development, implementation, and testing of advanced control algorithms for autonomous rotorcraft. As with helicopters, quadrotor platforms are available in a wide range of sizes, from which we highlight only some representative examples. The Blade mQX, a commercially available micro quadrotor, is used in Chapters 3, 4, and 5, to experimentally validate the proposed rotorcraft control solutions for trajectory tracking, path following ,and landing, respectively. Small and medium sized quadrotors like the

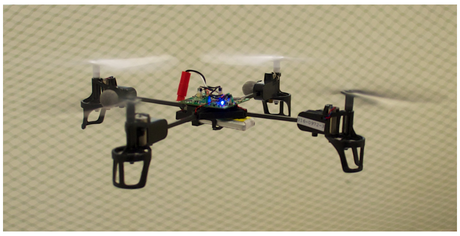

Figure 1.5: mQX quadrotor.

Asctec Hummingbird and Pelican, the latter of which is used in Chapter 6 to validate an approach to quadrotor stabilization with a pan and tilt camera, are tried and tested turnkey quadrotor platforms extensively used by the research community. Contrasting

Figure 1.6: Hummingbird quadrotor.

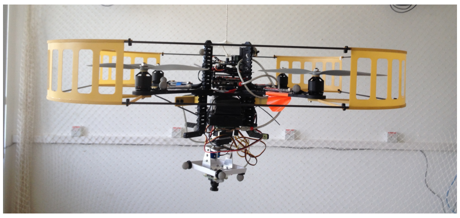

Figure 1.7: Pelican quadrotor.

with the wide availability of under 2 kg quadrotors, large quadrotors weighing over 3 kg are a rarity. A detailed explanation of the design challenges and engineering trade-offs of developing a large quadrotor platform (over 4 kg) with high payload capabilities (over 1 kg) is detailed in [PMC10]. This research culminated with the first successful outdoor flight of a quadrotor UAV weighing over 4 kg, the X4 quadrotor depicted in Figure 1.8. The Serafim quadrotor, depicted in Figure 1.9 and developed at ISR, is another example of a large and high payload quadrotor that can fly autonomously indoors and outdoors, carrying a collection of sensors that include optical flow sensors and a camera with the respective image processing computer unit.

Figure 1.8: X4 quadrotor.

Figure 1.9: Serafim quadrotor.

A rotorcraft similar in spirit to the helicopter and quadrotor is the ducted fan aerial vehicle. This configuration provides extra protection from the rotating blades, allowing the vehicle to be used in cluttered environments, where the probability of contact with people or buildings is greater. The vehicle is composed by a fixed pitch main rotor that provides the thrust force, a set of control surfaces located on the downwash of the main rotor, and a shroud that involves the main rotor and separates the dangerous rotating blades from the environment. This configuration allows the vehicle to come into contact and interact safely with the environment, albeit at the expense of mechanical simplicity, since it involves more moving parts such as the control surfaces. A vehicle using this configuration is being developed and tested at the University of Bologna [NGMS10].

The rotorcraft described in the preceding paragraphs are very versatile aerial vehicles and are able to perform maneuvers unattainable by conventional fixed-wing aircraft, such as vertical flight, hovering and vertical takeoff and landing. The ability to vertically take-off and land makes these helicopter-like rotorcraft great scientific platforms since they can perform their missions without the use of a large runway. The ability to hover is also desirable as it enables the vehicle to move slowly and with great precision. This feature also allows continuous data acquisition at the same location and helps the operation of some of the sensors, e.g. video or photo cameras, air quality sensors and chemical analysis tools.

1.2 Summary of Contributions

This thesis focuses on the challenges and difficulties of the autonomous control of aerial vehicles, motivated by the requirements of current, and yet to be envisaged, applications of UAVs. Particular emphasis is given to the design and experimental evaluation of control algorithms that are simultaneously rooted in solid principles from nonlinear systems theory and specifically targeted at applications of interest for vertical takeoff-and-landing rotorcraft, in particular quadrotor vehicles. This thesis key contributions are

- A landmark-based controller for force and torque actuation that guarantees almost global asymptotic stability of the desired equilibrium point for a fully-actuated rigid body. The controller is based on the position coordinates of a collection of landmarks fixed in the environment and velocity measurements. As an additional feature, the control law is designed so as to verify prescribed bounds on the actuation and is formulated considering the natural configuration space for rigid bodies, the Special Euclidean group SE(3).

- A trajectory tracking controller for steering a quadrotor vehicle along a time-dependent trajectory that asymptotically stabilizes the closed-loop system, even in the presence of constant force disturbances, and ensures that the actuation does not grow unbounded as a function of the position error.

- A controller to steer a quadrotor vehicle along a predefined path, with a secondary control objective of enforcing velocity tracking. The proposed solution guarantees global convergence of the closed-loop path following error to zero in the presence of constant wind disturbances and ensures that the actuation does not grow unbounded as a function of the position error.

- A robust solution to the problem of taking-off a quadrotor UAV in critical scenarios, such as in the presence of sloped terrains and surrounding obstacles. The original take-off problem is addressed as the problem of tracking suitable reference signals in order to achieve the desired transitions between different hybrid states of the automaton. Reference trajectories and feedback control laws are derived to explicitly account for uncertainties in both the environment and the vehicle dynamics.

- A cascaded architecture comprising a nonlinear attitude observer and a nonlinear controller for position and attitude stabilization of a quadrotor. The attitude estimates are obtained from rate gyros measurements, corrupted by bias, and image coordinates from a set of landmarks on the terrain, obtained by a controllable pan and tilt camera. Stabilization of the vehicle is achieved with a nested saturation control law by feedback of the image measurements, estimated body attitude, and corrected rate gyros measurements.

The detailed contributions are addressed in the introduction of each chapter, whereas the specific publications resulting from each chapter are provided in the next section.

1.3 Dissertation Outline

In this dissertation, the notation and most acronyms are introduced the first time they are used. Nonetheless, a list of acronyms and the notation summary can be found before this introductory chapter for quick reference. To distinguish between the author's published work and the remaining literature, the dissertation features two bibliography styles, using only numbers for the former and alphanumeric codes for the latter, combining the initials of the coauthors and the year of publication.

Following this introductory chapter, Chapters 2 to 6 present the core of this dissertation. Chapter 2 addresses the problem of stabilizing a fully-actuated rigid body. The problem is formulated considering the natural configuration space for rigid bodies, the Special Euclidean group SE(3). The proposed solution consists of a landmark-based controller for force and torque actuation that guarantees almost global asymptotic stability of the desired equilibrium point. As such the equilibrium point is asymptotically stable and only a nowhere dense set of measure zero lies outside its region of attraction. The controller uses velocity measurements and the position coordinates of a collection of landmarks fixed in the environment. As an additional feature, the control law is designed so as to verify prescribed bounds on the actuation. This body of work resulted in the presentation of a conference paper [1] and subsequent publication of a journal paper [2].

Chapter 3 addresses the problem of designing and experimentally validating a controller for steering a quadrotor vehicle along a time-dependent trajectory, while rejecting wind disturbances. The proposed solution consists of a nonlinear adaptive state feedback controller for thrust and torque actuation that asymptotically stabilizes the closed-loop system in the presence of constant force disturbances, used to model the wind action, and ensures that the actuation does not grow unbounded as a function of the position errors. A prototyping and testing architecture, developed to streamline the implementation and the tuning of the controller, is also described. Experimental results are presented to demonstrate the performance and robustness of the proposed controller. The work presented in this chapter culminated in the presentation of the conference papers [4, 11, 12] and in the publication of the journal paper [17].

Chapter 4 addresses the design and experimental evaluation of a controller to steer a quadrotor vehicle along a predefined path. The problem is formulated so as to enforce bounds on the actuation while guaranteeing robustness against constant wind disturbances. The proposed solution consists of a nonlinear adaptive state feedback controller for thrust and torque actuation that *i)* guarantees global convergence of the closed-loop path following error to zero in the presence of constant wind disturbances and *ii)* ensures that the actuation does not grow unbounded as a function of the position error. A prototyping and testing architecture, developed to streamline the implementation and tuning of the controller, is also described. Simulation results and experimental results, which include a hovering flight in the slipstream of a mechanical fan, are presented to assess the performance and robustness of the proposed controller. The work developed in this chapter gave rise to the conference papers [3, 8, 10] and to a journal article [13].

Chapter 5 addresses the problem of robust take-off of a quadrotor UAV in critical scenarios, such as in presence of sloped terrains and surrounding obstacles. Throughout the maneuver the vehicle is modeled as a hybrid automaton whose states reflect the different dynamic behavior exhibited by the UAV. The original take-off problem is then addressed as the problem of tracking suitable reference signals in order to achieve the desired transitions between different hybrid states of the automaton. Reference trajectories and feedback control laws are derived to explicitly account for uncertainties in both the environment and the vehicle dynamics. Simulation results demonstrate the effectiveness of the proposed solution and highlight the advantages with respect to more standard open-loop strategies, especially for the cases in which the slope of the terrain renders the take-off maneuver more critical to be achieved. Preliminary versions of these results were presented in [5, 14], a posterior journal version concerning the takeoff maneuver has been published [9] and another focusing on landing has been submitted for possible publication [15].

Chapter 6 proposes a cascaded architecture comprising a nonlinear attitude observer and a nonlinear controller for position and attitude stabilization of a quadrotor. The attitude estimates are obtained from rate gyros measurements, corrupted by bias, and image coordinates from a set of landmarks on the terrain, obtained by a controllable pan and tilt camera. Lateral-longitudinal stabilization is achieved with a nested saturation control law by feedback of the image measurements, estimated body attitude, and corrected rate gyros measurements. The vehicle is stabilized vertically using an additional vertical position sensor. Due to the input-to-state stability property of controller, the quadrotor position and attitude are shown to converge to the desired equilibrium point and the convergence is robust to the estimation errors. Additionally, the pan and tilt camera is actively actuated to keep the landmarks visible in the image sensor for most operating conditions. The performance of the proposed ensemble is illustrated with some simulation results. The work developed in this chapter gave rise to the conference papers [6, 7] and a full paper version has been submitted to a renowned journal in the field of control and robotics [16].

Finally, Chapter 7 provides the conclusions and outlines research directions for future work.

1.4 Basic notation and nomenclature

Throughout this work we use the prime $f'(x)$ to denote the partial derivative of the function f with respect to x, $f'(x) = \frac{\partial f}{\partial x}(x)$, and the upper dot $\dot{f}(x(t)) = f'(x(t))\dot{x}(t)$ to denote the total time derivative of the function. We use boldface to denote vectors and $\mathbf{e}_i$ to denote the i^{th} unitary vector. Vectors are represented by bold characters and $\mathbf{e}_1$, $\mathbf{e}_2$, and $\mathbf{e}_3$ denote the unit vectors co-directional with the x, y, and z axes, respectively. When designing an estimator for the unknown quantity x, we use $\hat{x}$ to denote the estimate and $\tilde{x} = x - \hat{x}$ to denote estimation error. The rotation group is denoted by $\mathrm{SO}(3) = \left\{R \in \mathbb{R}^{3\times 3} : R^T R = I_3, \det(R) = 1\right\}$, where I_3 denotes the 3×3 identity matrix, and the associated Lie algebra is denoted by $\mathfrak{so}(3)$ and is composed by the 3×3 skew-symmetric matrices $\mathfrak{so}(3) = \left\{K \in \mathbb{R}^{3\times 3} : K^T = -K\right\}$. The skew-symmetric operator is denoted as $S(\mathbf{x}) : \mathbb{R}^3 \to \mathfrak{so}(3)$ such that $S(\mathbf{x})\mathbf{y} = \mathbf{x} \times \mathbf{y} =$, where $\mathbf{x}, \mathbf{y} \in \mathbb{R}^3$, whereas the inverse map $S^{-1}(.) : \mathfrak{so}(3) \to \mathbb{R}^3$ is defined such that $S^{-1}(S(\mathbf{x})) = \mathbf{x}$. The Special Euclidean group $\mathrm{SE}(3) = \mathrm{SO}(3) \times \mathbb{R}^3$ is used to express rigid body motions. The notation $\mathrm{diag}(\mathbf{a})$ describes a diagonal matrix formed by placing the elements of $\mathbf{a} \in \mathbb{R}^n$ in the main diagonal. The Frobenius norm of matrices is denoted by $\|M\|_F$. A function $\sigma(s) : \mathbb{R} \to \mathbb{R}$ is a *saturation function* if it is differentiable and verifies, for positive M and $\sigma_{\max}$,

$$
\begin{aligned}
0 < \sigma'(s) < M, &\text{ for all } s,\\
\sigma(-s) = -\sigma(s), &\text{ for all } s,\\
s\sigma(s) > 0, &\text{ for all } s \neq 0, \sigma(0) = 0,\\
\lim_{s\to\pm\infty} \sigma(s) = \pm\sigma_{\max}&.
\end{aligned}
$$

Examples of smooth saturation functions are $\sigma_1(s) = s/\sqrt{1+s^2}$ and $\sigma_2(s) = \arctan(s)$. Further notation will be introduced when necessary.

2

Almost global stabilization of fully-actuated rigid bodies

This chapter addresses the problem of stabilizing a fully-actuated rigid body. The problem is formulated considering the natural configuration space for rigid bodies, the Special Euclidean group SE(3). The proposed solution consists of a landmark-based controller for force and torque actuation that guarantees almost global asymptotic stability of the desired equilibrium point. As such the equilibrium point is asymptotically stable and only a nowhere dense set of measure zero lies outside its region of attraction. The controller uses velocity measurements and the position coordinates of a collection of landmarks fixed in the environment. As an additional feature, the control law is designed so as to verify prescribed bounds on the actuation.

2.1 Introduction

Rigid body stabilization is a difficult control problem that plays a central role in many mechanical systems applications and has therefore received considerable attention over the years. The classical approach to the stabilization of rigid bodies in position and orientation relies on a local parametrization of the rotation matrix, such as the Euler angles. This kind of parametrization transforms the state space into an Euclidean vector space [Sas99], where the problem admits a trivial solution. However, stability results can only be of local nature and there is no guarantee that the system trajectories will not evolve to one of the singularities of the parametrization.

Unit quaternions and the axis-angle representation are other widely used alternative parametrizations for rotation matrices. For example, Isidori et al. [IMS03] present a nonlinear controller based on quaternions that solves an attitude regulation problem for low-Earth orbit rigid satellites. This and other parameterizations are also applied in different settings, such as in [MC02], where Malis and Chaumette use the angle-axis representation to tackle a visual-servoing problem.

These representations are globally nonsingular and thus allow for global results to be attained, making them more interesting than the Euler angles. However, they cover the Special Orthogonal group SO(3) multiple times, introducing ambiguities. As noted by Bhat and Bernstein [BB00], these approaches lead to control laws that are generally not well-defined in the Special Euclidean group SE(3), yielding closed-loop systems that exhibit unwinding. Under such control laws, a system can start at rest and arbitrarily close to the desired configuration and still have to rotate through large angles before coming to rest at the desired configuration. Other authors like Koditschek [Kod89], Bullo and Murray [BM99], Chaturvedi, McClamroch, and Bernstein [CMB07, CM07] consider rotation matrices in their natural space, as elements of SO(3). In this work, we adopt the latter approach so as to avoid problems related to singularities or multiple coverings.

As pointed out by several authors [BB00, Ang01, MKS06, CMB07, Kod89], even if the control law is well-defined it is impossible to achieve global asymptotic stability of a rigid body with a continuous feedback controller. For systems evolving continuously on manifolds not diffeomorphic to the Euclidean space, as is the case of SE(3), there are topological obstacles that preclude the existence of globally asymptotically stable (GAS) equilibrium points. The objective of GAS must then be relaxed to almost globally asymptotically stable (AGAS). In loose terms, this corresponds to saying that the equilibrium point is stable and all solutions but those starting in a nowhere dense of measure zero converge asymptotically to that point. A nowhere dense set of measure zero is considered *thin* and negligible in both a measure-theoretical and a topological sense. In practical terms, and from an asymptotic point of view, this relaxation is fairly innocuous since disturbances or sensor noise will prevent system trajectories from remaining on this *thin* set [Ang04, CBM06]. However, it should be noted that close to this set the system trajectories are strongly affected and convergence to the desired equilibrium can be arbitrarily slow [CMB07, CM07].

In this chapter, we consider a fully-actuated rigid body modeled as a simple mechanical control system and address the stabilization problem guaranteeing that prescribed bounds on the actuation are satisfied. Building on previous results for a kinematic model [CSH08], also explored and developed in [VCSO07] for attitude and position estimation, we specifically take into account the dynamics and propose an output-feedback solution defined on a setup of practical significance. It is assumed that there is a collection of landmarks fixed in the environment and that the output available for feedback are the position coordinates of the landmarks and the velocities expressed in the body frame. The approach followed in this chapter is in line with the methods presented in [Kod89, BM99, CBM06], which address the stabilization problem using full-state feedback control and prove stability based on total energy-like Lyapunov functions. Actuator saturation is also considered in [CBM06, CM07]. In this chapter we consider the combined position and attitude stabilization problem and, equally important, provide a controller that is based on landmark measurements. In order to obtain this controller, a landmark-based error function is introduced for potential energy shaping and is combined with a dissipative force map, yielding a dissipative closed-loop system with an AGAS equilibrium point at the minimum of the error function.

The chapter is structured as follows. Section 2.2 introduces some background on differential geometry used in the remainder of the chapter. Section 2.3 describes the dynamics of the rigid body and defines the setup and the output vector considered. In Section 2.4 we present the landmark-based error function that is used for stabilization. The stabilization control law is derived and expressed as landmark-based feedback law in Section 2.5. A study of the resulting closed-loop system's stability properties follows in Section 2.6. Simulation results that illustrate the performance of the control law are presented in Section 2.7 and finally Section 2.8 summarizes the contents of the chapter and presents the concluding remarks.

2.2 Mathematical background

In this section we briefly introduce the mathematical formalism of differential geometry needed for the rest of the chapter. The notation on differential geometry is standard and the reader is referred to [Lee97, Lee03] for additional material. The concept of a forced simple mechanical control system and respective notation is borrowed from [BL04]. We start by presenting the general setup for a simple control system evolving on a generic Riemannian manifold and then particularize and simplify it for the case where the control system evolves on a Lie group. Last, we discuss the definition of force norms on the cotangent bundle $\mathsf{TSE(3)}^*$, which is needed to characterize actuation boundedness.

Definition 1. *A forced simple mechanical control system is a 6-tuple* $(\mathsf{Q},\mathbb{G},F_{\mathrm{ext}},V,\mathcal{F},U)$, *where*

1. Q *is a configuration manifold;*
2. $\mathbb{G}$ *is a Riemannian metric on* Q, *corresponding to the kinetic energy of the mechanical system;*
3. F_{ext} *is an uncontrolled external force on* Q;
4. V *is a potential function on* Q;
5. $\mathcal{F} = \{F^1,\dots,F^m\}$ *is a collection of covector fields on* Q, *representing the control forces;*
6. $U \subset \mathbb{R}^m$ *is the control set.*

The pair $(\mathsf{Q}, \mathbb{G})$ is a Riemannian manifold and consequently there exists a unique Levi-Civita connection $\overset{\mathbb{G}}{\nabla}$. Let $q(t) \in \mathsf{Q}$ denote the configuration of the mechanical system at time t and the tangent space element $\dot{q}(t) \in \mathsf{T}_{q(t)}\mathsf{Q}$ denote the velocity. Then, the governing dynamic equations for the forced simple mechanical control system are

$$\overset{\mathbb{G}}{\nabla}_{\dot{q}(t)}\, \dot{q}(t) = \mathbb{G}^{\sharp}(F_{\text{ext}}(\dot{q}) - dV(q)) + \sum_{a=1}^{m} u^a(t)(\mathbb{G}^{\sharp}(F^a(q))) \tag{2.1}$$

where $u : I \mapsto U$ are smooth control inputs and $dV(q)$ denotes the differential of the potential function $V(q)$. The map $\mathbb{G}^{\sharp} : \mathsf{T}^*_q\mathsf{Q} \mapsto \mathsf{T}_q\mathsf{Q}$ is the associated isomorphism corresponding to the Riemannian metric $\mathbb{G}$ defined as $\langle\langle \mathbb{G}^{\sharp}(\alpha_q), v_q \rangle\rangle = \langle \alpha_q, v_q \rangle$ where $\alpha_q \in \mathsf{T}^*_q\mathsf{Q}$, $v_q \in \mathsf{T}_q\mathsf{Q}$, $\langle\langle \cdot, \cdot \rangle\rangle$ denotes the inner product and $\langle \cdot, \cdot \rangle$ is the natural application between tangent vectors and covectors.

We now consider the more specific case where the configuration manifold Q is a Lie group. We assume the Lie group is endowed with a Riemannian metric $\mathbb{G} = \mathbb{G}_{\mathbb{I}}$ determined via left translation of $\mathbb{I}$, an inner product on the Lie algebra $\mathfrak{g}$. In this particular setup, the dynamics (2.1) can be simplified to Euler-Poincaré equations. Consider a simple mechanical control system evolving on a Lie group Q, subject to a potential force derived from the potential function $V(q)$ and actuated by body-fixed forces u. The Euler-Poincaré dynamic equations for such a system are

$$\mathbb{I}\dot{\xi} = \mathrm{ad}^*_{\xi}\, \mathbb{I}\xi + (T_eL_q)^*(F_{\text{ext}}(\dot{q}) - dV(q)) + u. \tag{2.2}$$

In equation (2.2), ξ denotes the body velocity, ad^* the dual adjoint operator, and T_eL_q denotes the tangent map at the group identity of the left translation by $q \in \mathsf{Q}$. It is important to note that the pullback $(T_eL_q)^*(df(q))$ can be computed without introducing coordinates by noting that

$$\mathcal{L}_{\xi_L} f(q) = \frac{d}{dt} f(q(t))|_{t=0} = \langle (T_eL_q)^*(df(q)), \xi \rangle$$

where $\mathcal{L}$ denotes the Lie derivative and ξ_L is the left-invariant vector field with $\xi_L(e) = \xi$ at the identity.

In the geometrical control framework, forces and torques are modeled as covectors, existing in the cotangent bundle $\mathsf{TSE}(3)^*$ for a rigid body. To measure the magnitude of forces and torques we need a metric on the cotangent bundle. In the case of rigid bodies, the forces and torques are body-fixed. These are modeled as left-invariant covector fields and are completely defined by their value at the identity.

The cotangent bundle $\mathsf{TSE}(3)^*$ can be trivialized as $\mathsf{TSE}(3)^* \simeq \mathsf{SE}(3) \times \mathfrak{se}(3)^*$. The Lie coalgebra $\mathfrak{se}(3)^*$ is isomorphic to, and can be identified with $\mathbb{R}^3 \times \mathbb{R}^3$. Furthermore, we identify left-invariant covector fields with their value at the identity $u \in \mathfrak{se}(3)^*$.

We proceed to define two norms on $\mathfrak{se}(3)^*$. One that measures the total torque and one that measures the total force exerted on the rigid body, viewed on the body frame. We denote these as the torque norm $\|\cdot\|_\tau$ and the force norm $\|\cdot\|_f$, respectively. Their expressions are $\|u\|_\tau = \|\boldsymbol{\pi}_\tau(u)\|$ and $\|u\|_f = \|\boldsymbol{\pi}_f(u)\|$, where the norm $\|\cdot\|$ denotes the standard euclidean norm on $\mathbb{R}^3$ and we do the standard identifications $\mathfrak{so}(3)^* \simeq \mathbb{R}^3$ and $(\mathbb{R}^3)^* \simeq \mathbb{R}^3$. The maps $\boldsymbol{\pi}_\tau : \mathfrak{se}(3)^* \mapsto \mathfrak{so}(3)^*$ and $\boldsymbol{\pi}_f : \mathfrak{se}(3)^* \mapsto (\mathbb{R}^3)^*$ are the canonical projections from the Lie coalgebra $\mathfrak{se}(3)^*$ to $\mathfrak{so}(3)^*$ and $(\mathbb{R}^3)^*$, respectively. Using these definitions we can now measure forces and torques on the cotangent bundle in a physically meaningful way.

2.3 Problem formulation

In this section we particularize the mathematical notation of Section 2.2 for a rigid body evolving on SE(3) to obtain the equations of motion. Additionally, we introduce the measurements available for feedback and state the problem of stabilization on SE(3).

2.3.1 Equations of motion

Consider a fixed inertial frame $\{\mathcal{I}\}$ and a frame $\{\mathcal{B}\}$ attached to the rigid body's center of mass. The configuration of the body frame $\{\mathcal{B}\}$ with respect to $\{\mathcal{I}\}$ can be viewed as an element of the special euclidean group, $q = (R, \mathbf{p}) = ({}^I_B R, {}^I\mathbf{p}_B) \in \mathrm{SE}(3)$. The kinematic equations of motion for the rigid body expressed in an inertial frame $\{\mathcal{I}\}$ are

$$\begin{aligned} \dot{R} &= RS(\boldsymbol{\omega}) \\ \dot{\mathbf{p}} &= R\mathbf{v} \end{aligned}$$

where $\boldsymbol{\omega}$ and $\mathbf{v}$ are, respectively, the angular and linear velocities of the rigid body with respect to $\{\mathcal{I}\}$ expressed in $\{\mathcal{B}\}$. The vectors $\boldsymbol{\omega}$ and $\mathbf{v}$ are called the angular and linear body velocities. The map $S(\cdot) : \mathbb{R}^3 \mapsto \mathfrak{so}(3)$ is an isomorphism between $\mathbb{R}^3$ and the Lie algebra $\mathfrak{so}(3)$ and verifies $S(\mathbf{a})\mathbf{b} = \mathbf{a} \times \mathbf{b}$.

The Euler-Poincaré equations (2.2) for the specific case of a rigid body evolving on SE(3), subject to potential forces derived from the potential function $V(q)$ and to external forces $F_{\text{ext}}(\dot{q})$, can be decomposed in angular and linear motions as

$$\mathbb{J}\dot{\boldsymbol{\omega}} = S(\mathbb{J}\boldsymbol{\omega})\boldsymbol{\omega} + S(\mathbb{M}\mathbf{v})\mathbf{v} + \boldsymbol{\pi}_\tau\Big(\bar{F}_{ext}(\mathbf{v},\boldsymbol{\omega}) + \bar{F}_p(\mathbf{p},R)\Big) + \mathbf{u}_\tau \tag{2.3}$$

$$\mathbb{M}\dot{\mathbf{v}} = S(\mathbb{M}\mathbf{v})\boldsymbol{\omega} + \boldsymbol{\pi}_f\Big(\bar{F}_{ext}(\mathbf{v},\boldsymbol{\omega}) + \bar{F}_p(\mathbf{p},R)\Big) + \mathbf{u}_f \tag{2.4}$$

where $\bar{F}_{ext}(\mathbf{v},\boldsymbol{\omega}) = (T_e L_q)^*(F_{\text{ext}}(\dot{q}))$, $\bar{F}_p(\mathbf{p},R) = (T_e L_q)^*(-dV(q))$, $\mathbb{J}$ is the total inertia matrix, and $\mathbb{M}$ the total mass matrix. Both $\mathbb{J}$ and $\mathbb{M}$ include added terms, though added cross terms are neglected.

In the Euler-Poincaré equation on SE(3), the body velocity is represented by the angular and linear velocities. We have $\xi = (\boldsymbol{\omega}, \mathbf{v}) \in \mathfrak{se}(3) \simeq \mathfrak{so}(3) \times \mathbb{R}^3$. The vectors $\mathbf{u}_\tau$ and $\mathbf{u}_f$ in (2.3)-(2.4) correspond to the canonical projections of $u \in \mathfrak{se}(3)^*$ to $\mathfrak{so}(3)^*$ and $(\mathbb{R}^3)^*$, respectively, each one identified with $\mathbb{R}^3$. In the current setup, the rigid body is assumed to be fully actuated. This means there are no restrictions on the allowable directions for the torque and force vectors, i.e. $\mathbf{u}_\tau, \mathbf{u}_f \in \mathbb{R}^3$. The external force F_{ext} accounts for viscous effects experienced by the rigid body when moving through a fluid.

2.3.2 Potential function

The setup in consideration can model several realistic situations and it is applicable to both aerial and underwater vehicles. For aerial vehicles there is a potential force one cannot ignore: gravity. Its potential function, when close to the Earth's surface, is given by

$$V(q) = -mg\mathbf{e}_3^T\mathbf{p} \tag{2.5}$$

where m is the total mass of the body, g the gravitational acceleration, and $\mathbf{e}_3 = \begin{bmatrix}0 & 0 & 1\end{bmatrix}^T$. In the definition of the potential function it is implied that the z axis of the inertial frame points towards the center of the Earth.

When considering underwater vehicles one has to take into account not just gravity but also buoyancy, yielding a potential function that is position and attitude dependent [SCPP09]. Other examples where attitude dependent potentials are present include the 3D pendulum [CMB07, CM07] and spacecraft under gravity fields [LML06]. Although we particularize the potential function to be position dependent only, the proposed methodology can also be applied in the general case.

2.3.3 Problem statement

Consider a target configuration $q^* = (R^*, \mathbf{p}^*) = ({}^I_D R, {}^I\mathbf{p}_D) \in \text{SE}(3)$ defined as the configuration of the desired frame $\{\mathcal{D}\}$ with respect to the inertial frame $\{\mathcal{I}\}$. The frame $\{\mathcal{D}\}$ is assumed to be fixed in the workspace.

Figure 2.1 illustrates the setup at hand, where the coordinates of n points acquired at the current and desired configurations q and q^*, respectively, are available to the system for feedback control along with the body velocities $\boldsymbol{\omega}$ and $\mathbf{v}$. In loose terms, the control objective amounts to designing a control law for the actuation $\mathbf{u}_\tau$ and $\mathbf{u}_f$ that verifies some prescribed bounds and ensures the convergence of q to q^* (or, equivalently, of $\{\mathcal{B}\}$ to $\{\mathcal{D}\}$), with the largest possible basin of attraction.

The control law uses measurements that come in the form of the coordinates of n fixed points expressed in the body frame. The coordinates of these points, which we call landmarks, are available both in the current body frame and in the desired body frame,

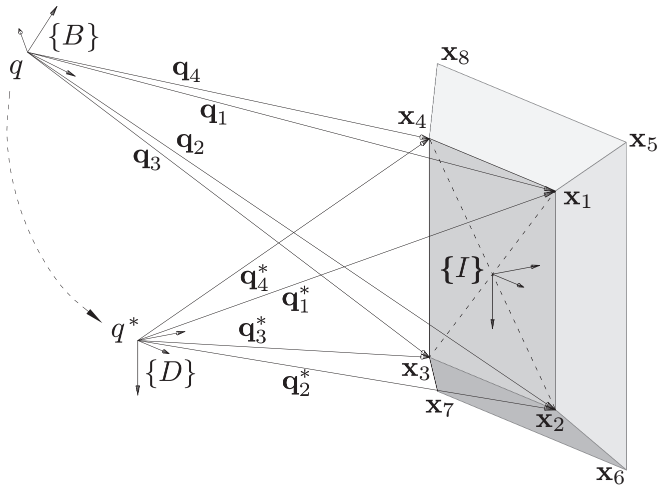

Figure 2.1: Problem Setup.

as shown in Figure 2.1. We also consider the body velocities ω and $\mathbf{v}$ to be available for feedback.

The landmark measurements are typically obtained from onboard sensors that are able to locate landmarks fixed in the environment. Because the sensors are onboard, they produce the coordinates of the landmarks positions in the body frame. Examples of such sensors include charge-coupled device (CCD) cameras, laser scanners, pseudo-GPS, etc. The body velocities readings are typically obtained by combining dedicated sensor measurements (e.g. pitot tubes) with positioning information and sensor readings from inertial measurement units, which comprise triads of rate-gyros, accelerometers, and magnetometers.

According to Figure 2.1, we define the matrix of inertial landmark coordinates $X = [\mathbf{x}_1 \dots \mathbf{x}_n] \in \mathbb{R}^{3\times n}$, where $\mathbf{x}_j \in \mathbb{R}^3$ denotes the coordinates of the jth point expressed in $\{\mathcal{I}\}$, and the matrix of body landmark coordinates $Q = [\mathbf{q}_1 \dots \mathbf{q}_n] \in \mathbb{R}^{3\times n}$ where $\mathbf{q}_j = R^T(\mathbf{x}_j - \mathbf{p})$, $j \in \{1, 2, \dots, n\}$ denotes the coordinates of the jth point expressed in $\{\mathcal{B}\}$. Similarly, we introduce the target matrix $Q^* = [\mathbf{q}_1^* \cdots \mathbf{q}_n^*] \in \mathbb{R}^{3\times n}$, where $\mathbf{q}_j^* = R^{*T}(\mathbf{x}_j - \mathbf{p}^*)$. Defining the vector $\mathbf{1} = [1 \cdots 1]^T \in \mathbb{R}^n$, the Q and Q^* matrices of coordinates can be rewritten as $Q = R^T(X - \mathbf{p}\mathbf{1}^T)$, $Q^* = R^{*T}(X - \mathbf{p}^*\mathbf{1}^T)$.

The landmarks are required to satisfy the following condition.

Assumption 1. *The n landmarks are not coplanar.*

Assumption 2. *The target configuration is such that the singular values of the matrix of desired landmark coordinates Q^* are all distinct.*

We can now state Proposition 3, which will prove useful in the sequel.

Proposition 3. *If Assumption 1 is verified there exists*

1. *a vector* $\mathbf{a} = [a_1 \dots a_n]^T \in \mathbb{R}^n$ *such that* $\mathbf{1}^T\mathbf{a} = 1$ *and* $Q^*\mathbf{a} = 0$ *and*

2. *a vector* $\mathbf{b} = [b_1 \dots b_n]^T \in \mathbb{R}^n$ *such that* $\mathbf{1}^T\mathbf{b} = 1$ *and* $Q^*\mathbf{b} = R^{*T}\mathbf{e}_3$.

To conclude the problem statement, we introduce the error configuration $q_e = (R_e, \mathbf{p_e}) \in$ SE(3), with

$$R_e = R^T R^* \in \mathrm{SO}(3),$$
$$\mathbf{p_e} = R^T(\mathbf{p} - \mathbf{p}^*) \in \mathbb{R}^3,$$

and the state-space model for the error system, which can be written as

$$\dot{R}_e = -S(\boldsymbol{\omega})R_e,$$
$$\dot{\mathbf{p}}_\mathbf{e} = \mathbf{v} - S(\omega)\mathbf{p_e}.$$

Using the configuration error, the output matrix Q can be expressed as $Q = R_e Q^* - \mathbf{p_e}\mathbf{1}^T$. Notice that, if Assumption 1 holds, the configuration error $(R_e, \mathbf{p_e})$ is uniquely determined and can be fully recovered from the landmark measurements Q.

2.4 Landmark-based error function

We wish to drive the error between the measured outputs $\mathbf{q}_j$ and the desired outputs $\mathbf{q}_j^*$ to zero. Since the system under study evolves on SE(3), we express the error as a function on SE(3) given by

$$e(q_e) = \frac{n}{2}\Phi(\mathbf{p_e}^T\mathbf{p_e}) + \mathrm{tr}((I_3 - R_e)Q^*Q^{*T}) \tag{2.6}$$

where the function Φ is defined as

$$\Phi(x) = \frac{x}{1+\sqrt{x}}.$$

It is convenient to note that the previous error function can be expressed as a function of the landmark measurements. Using Proposition 3, the error function (2.6) can be expressed in terms of the landmark measurements Q as

$$e(Q) = \frac{n}{2}\Phi\Big(\mathbf{a}^T Q^T Q\mathbf{a}\Big) + \mathrm{tr}\Big((I_3 - \mathbf{a}\mathbf{1}^T)^T(Q-Q^*)^T(Q-Q^*)(I_3 - \mathbf{a}\mathbf{1}^T)\Big)$$

Considering that Assumption 2 holds, the error function (2.6) is a Morse function, i.e. its critical points are non-degenerate and are consequently isolated. From the properties of the *modified trace* function, which can take the form $tr((I_3 - Re)Q^*Q^{*T})$, the error function (2.6) is positive definite and has a global minimum at $(R_e, \mathbf{p_e}) = (I_3, \mathbf{0})$. It has exactly four critical points: one minimum, one maximum and two saddle points. For further details on Morse functions and the modified trace, the reader is referred to the discussion in [Kod89] and references therein. As shown latter in the chapter, these are important properties that will allow for the definition of an almost globally stabilizing law.

Computing the time derivative of the error function, we obtain

$$\dot{e}(q_e) = n\frac{2+\|\mathbf{p_e}\|}{2(1+\|\mathbf{p_e}\|)^2}\mathbf{p_e}^T\mathbf{v} - S^{-1}(R_e Q^* Q^{*T} - Q^* Q^{*T} R_e^T)^T \boldsymbol{\omega}$$

As such, the differential of the error function $e(q_e)$ expressed in the body frame, identifying $\mathfrak{se}(3)$ with $\mathbb{R}^3 \times \mathbb{R}^3$, is

$$(T_e L_q)^* de(q_e) = \begin{bmatrix} -S^{-1}(R_e Q^* Q^{*T} - Q^* Q^{*T} R_e^T) \\ n\frac{2+\|\mathbf{p_e}\|}{2(1+\|\mathbf{p_e}\|)^2}\mathbf{p_e} \end{bmatrix}. \tag{2.7}$$

Notice that due to the use of function Φ in the definition of the error function (2.6), the norm of the differential is a bounded function of the configuration error q_e.

Proposition 4. *The differential of the error function* (2.6) *is bounded. Its torque and force norms observe the following bounds*

$$\begin{aligned} &\|(T_e L_q)^* de(q_e)\|_\tau \leq \lambda_1(Q^* Q^{*T}) + \lambda_2(Q^* Q^{*T}) \\ &\|(T_e L_q)^* de(q_e)\|_f \leq n \end{aligned}$$

where $\lambda_1(Q^* Q^{*T})$ *and* $\lambda_2(Q^* Q^{*T})$ *denote respectively the largest and second largest eigenvalues of the matrix* $Q^* Q^{*T}$.

2.5 Control law design

In this section we present the strategy devised for designing the control law and describe the stability properties of the resulting closed-loop system. To stabilize the error system we use a proportional-derivative control law that takes the form

$$u = -K_p (T_e L_q)^*(de(q_e)) + (T_e L_q)^*(dV(q_e)) - \Psi(\xi) \tag{2.8}$$

where K_p is defined as a positive definite block diagonal matrix given by $K_p = \mathrm{diag}(K_{p_\tau}, K_{p_f})$, $K_{p_\tau}, K_{p_f} \in \mathbb{R}^{3\times 3}$. In (2.8), the position error and the potential functions act as potential energy shaping terms, whereas the map $\Psi(\xi)$ acts as a dissipative term.

2.5.1 Potential force

Expressing the potential (2.5) as a function of the configuration error we obtain $V(q_e) = -mg\mathbf{e}_3^T(R^* R_e^T \mathbf{p_e} + \mathbf{p}^*)$. The differential of the gravitational potential $V(q_e)$ written in the body frame is given by

$$(T_e L_q)^*(dV(q_e)) = \begin{bmatrix} \mathbf{0} \\ -mgR_e R^{*T}\mathbf{e}_3 \end{bmatrix}. \tag{2.9}$$

2.5.2 Damping force

We now introduce the dissipative force map $\Psi(\xi)$ used in the control law (2.8). Let $\Psi_\tau : \mathfrak{so}(3) \mapsto \mathfrak{so}(3)^*$ be the C^1 map given by

$$\Psi_\tau(\omega) = \frac{K_{d_\tau}\boldsymbol{\omega}}{1 + \|K_{d_\tau}\boldsymbol{\omega}\|}$$

with the usual identification $\mathfrak{so}(3)^* \simeq \mathbb{R}^3$ and where K_{d_τ} is a positive definite matrix. It is easy to verify that the natural application $\langle \Psi_\tau(\omega), \omega \rangle$ is a positive definite function of ω. We proceed analogously to define $\Psi_f : \mathbb{R}^3 \mapsto (\mathbb{R}^3)^*$ and obtain the force map $\Psi(\xi) : \mathfrak{se}(3) \mapsto \mathfrak{se}(3)^*$

$$\Psi(\xi) = \Big(\Psi_\tau(\omega), \Psi_f(\mathbf{v})\Big). \tag{2.10}$$

Proposition 5. *The force map as defined in* (2.10) *is bounded, and its torque and force norms verify* $\|\Psi(\xi)\|_\tau \leq 1$ *and* $\|\Psi(\xi)\|_f \leq 1$.

Using (2.7), (2.9), and (2.10), the control law (2.8) can be written explicitly as

$$\begin{bmatrix} \mathbf{u}_\tau \\ \mathbf{u}_f \end{bmatrix} = \begin{bmatrix} K_{p_\tau} S^{-1}(R_e Q^* Q^{*T} - Q^* Q^{*T} R_e^T) \\ -K_{p_f} n \frac{2+\|\mathbf{p_e}\|}{2(1+\|\mathbf{p_e}\|)^2} \mathbf{p_e} \end{bmatrix} + \begin{bmatrix} \mathbf{0} \\ -mg\mathbf{e}_3^T R^* R_e^T \end{bmatrix} - \begin{bmatrix} \Psi_\tau(\omega) \\ \Psi_f(\mathbf{v}) \end{bmatrix}$$

2.5.3 Bounded actuation

The torque and force actuations generated by the control law (2.8) are bounded. However, their bounds may not be compatible with the prescribed saturation of actuators. In the sequel we will show how to derive a control law that observes some prescribed bounds in the actuation.

We start by defining the constants M_τ and M_f as the maximum magnitudes of the total torque and force available at the actuators and consider the control constraint

$$\{u \in \mathfrak{se}(3)^* : \|u\|_\tau \leq M_\tau \text{ and } \|u\|_f \leq M_f\}$$

Necessary conditions for the stabilization of the configuration error considering an arbitrary desired configuration are

$$M_\tau > \sup_{q_e \in Q} \|(T_e L_q)^*(dV(q_e))\|_\tau = 0 \tag{2.11}$$

$$M_f > \sup_{q_e \in Q} \|(T_e L_q)^*(dV(q_e))\|_f = mg \tag{2.12}$$

since to maintain the system stabilized at a given point in space it is at least necessary to counteract the potential force.

Given a maximum torque M_τ and force M_f satisfying (2.11)-(2.12), we define the constants δ_τ and δ_f as

$$\delta_\tau = M_\tau - \sup_{q_e \in \mathrm{Q}} \|(T_e L_q)^*(dV(q_e))\|_\tau = M_\tau$$
$$\delta_f = M_f - \sup_{q_e \in \mathrm{Q}} \|(T_e L_q)^*(dV(q_e))\|_f = M_f - mg$$

The previous constants express the total amount of force and torque available for the potential shaping and dissipative control. To specify the control law we need to define the bounds m_τ and m_f

$$m_\tau \geq \sup_{q_e \in \mathrm{Q}} \|(T_e L_q)^* de(q_e)\|_\tau$$
$$m_f \geq \sup_{q_e \in \mathrm{Q}} \|(T_e L_q)^* de(q_e)\|_f$$

We then redefine the error function as

$$e_m(q_e) = \frac{n k_f \delta_f}{2 m_f} \Phi(\mathbf{p_e}^T \mathbf{p_e}) + \frac{k_\tau \delta_\tau}{m_\tau} \operatorname{tr}((I_3 - R_e) Q^* Q^{*T}) \tag{2.13}$$

and the dissipative force map as

$$\Psi(\xi) = \Big((1-k_\tau)\delta_\tau \Psi_\tau(\omega), (1-k_f)\delta_f \Psi_f(\omega)\Big) \tag{2.14}$$

where $k_\tau, k_f \in (0,1)$ are tuning parameters that control the damping of the closed-loop system. Small values for k_τ, k_f lead to highly damped closed-loop dynamics. Using the error function (2.13) and the force map (2.14) in (2.8), we obtain a new control law

$$\begin{bmatrix} \mathbf{u}_\tau \\ \mathbf{u}_f \end{bmatrix} = \begin{bmatrix} \frac{k_\tau \delta_\tau}{m_\tau} S^{-1}(R_e Q^* Q^{*T} - Q^* Q^{*T} R_e^T) \\ -\frac{n k_f \delta_f}{m_f} \frac{2 + \|\mathbf{p_e}\|}{2(1+\|\mathbf{p_e}\|)^2} \mathbf{p_e} \end{bmatrix} + \begin{bmatrix} \mathbf{0} \\ -mg \mathbf{e}_3^T R^* R_e^T \end{bmatrix} - \begin{bmatrix} (1-k_\tau)\delta_\tau \Psi_\tau(\omega) \\ (1-k_f)\delta_f \Psi_f(\mathbf{v}) \end{bmatrix} \tag{2.15}$$

that verifies the following proposition.

Proposition 6. *If the control law* (2.15) *is applied, the actuation bounds* $\|u\|_\tau < M_\tau$ *and* $\|u\|_f < M_f$ *are guaranteed hold.*

2.5.4 Landmark-based control law

We now express (2.15) in an output-feedback form. Recall that the measured outputs are given by the matrix of landmark coordinates Q, and the body velocities ω, $\mathbf{v}$. The constants k_τ, δ_τ, m_τ, k_f, δ_f, and m_f are determined *a priori* based on the desired closed-loop characteristics and input saturation limits. Assuming that ω and $\mathbf{v}$ are directly measured by the onboard sensors, we need only express $\mathbf{p_e}$, $S^{-1}(R_e Q^* Q^{*T} - Q^* Q^{*T} R_e^T)$, and

$-\, mgR_eR^{*T}\mathbf{e}_3$ as functions of the outputs. These can be written as follows

$$\mathbf{p_e} = -Q\mathbf{a}, \tag{2.16}$$

$$S^{-1}(R_eQ^*Q^{*T} - Q^*Q^{*T}R_e^T) = S^{-1}(QQ^{*T} - Q^*Q^T) - S(Q^*\mathbf{1})Q\mathbf{a}, \tag{2.17}$$

$$-mgR_eR^{*T}\mathbf{e}_3 = -mgQ(I - \mathbf{a}\mathbf{1}^T)\mathbf{b}, \tag{2.18}$$

where $\mathbf{a}$ and $\mathbf{b}$ are the vectors defined in Proposition 3. Using the previous identities, we can express the full control law (2.15) given the current and desired output measurements Q and Q^* and the velocities $\boldsymbol{\omega}$ and $\mathbf{v}$.

2.6 Stability analysis

In this section, we analyze the stability of the closed-loop system, from now on denoted by Σ, that results from the feedback interconnection of (2.1) and the control law obtained by left translation of (2.15). We show that the desired equilibrium point is AGAS, in the sense that the set outside its region of attraction is nowhere dense and has measure zero.

Theorem 7. *The point* $(q_e, \xi) = (q_0, 0) \in \mathsf{TSE}(3)$*, where* $q_0 = (I_3, 0)$*, is an AGAS equilibrium point of the closed-loop system* Σ*. Moreover, there exists a neighborhood of* $(q_0, 0)$*, such that all solutions starting inside it converge exponentially fast to* $(q_0, 0)$*.*

To prove Theorem 7, we follow a constructive approach yielding a succession of intermediate results. First, we show that the closed-loop trajectories converge to one of four well-defined equilibrium points of the system. We then proceed to linearize the system about each of these equilibria. Based on the stability analysis of these linearized systems, we can conclude that the initial conditions for which the system diverges from $(q_0, 0)$ form a closed set whose dimension is lower than that of the state-space $\mathsf{TSE}(3)$, meaning that it has measure zero and is nowhere dense.

Consider the total energy function $W : \mathsf{TSE}(3) \mapsto \mathbb{R}_0^+$ of the closed-loop system Σ defined as

$$W(t) = e_m(q_e(t)) + \frac{1}{2}\langle\langle \dot{q}_e(t), \dot{q}_e(t)\rangle\rangle \tag{2.19}$$

where $\dot{q}_e = T_eL_{q_e}(\xi)$. Using (2.19), we can apply LaSalle's invariance principle to obtain the following result.

Lemma 8. *Under Assumptions 1 and 2, the solutions of* Σ *converge to one of the four equilibria in the set* $M = \{(q_c, \xi_c) \in \mathsf{TSE}(3) : de_m(q_c) = 0,\ \xi_c = 0\}$*.*

Proof. Under Assumption (1), the energy function W is positive definite. Its time derivative is given by

$$\begin{aligned}\dot{W}(t) &= \frac{d}{dt}\left(e_m(q_e(t)) + \frac{1}{2}\langle\langle \dot{q}_e(t), \dot{q}_e(t)\rangle\rangle\right)\\ &= \nabla_{\dot{q}_e} e_m(q_e(t)) + \langle\langle \nabla_{\dot{q}_e}\dot{q}_e, \dot{q}_e\rangle\rangle\\ &= \langle d e_m(q_e), \dot{q}_e\rangle + \langle -d e_m(q_e) - \widetilde{\Psi}(\dot{q}_e) + F_{\text{ext}}(\dot{q}_e), \dot{q}_e\rangle\\ &= -\langle \widetilde{\Psi}(\dot{q}_e), \dot{q}_e\rangle + \langle F_{\text{ext}}(\dot{q}_e), \dot{q}_e\rangle\end{aligned}$$

where $\widetilde{\Psi} = (T_e L_{q^{-1}})^*(\Psi)$. From the definition of $\Psi(\xi)$ given in (2.10) and the strictly dissipative nature of the external drag force F_{ext}, it follows immediately that $\dot{W}$ is negative semi-definite. Applying LaSalle's invariance principle, we conclude that the closed-loop trajectories converge to the largest invariant set such that $\dot{W}(q_e, \xi) = 0 \Leftrightarrow \xi = 0$. This largest invariant set is then the set of points $(q_c, \xi_c) \in \mathsf{T}\mathrm{SE}(3)$ such that q_c is a critical point of e_m and $\xi_c = 0$ which is exactly the set M. As shown for example in [Kod89], if Assumption 2 holds the set M has exactly four elements. □

Remark 9. *The external force F_{ext} models the drag on the rigid body and thus is a strictly dissipative force. Therefore, the natural application verifies $\langle F_{\text{ext}}(\dot{q}_e), \dot{q}_e\rangle \leq 0$ for all $\dot{q}_e$ and $\langle F_{\text{ext}}(\dot{q}_e), \dot{q}_e\rangle = 0$ if and only if the body velocity is zero.*

Remark 10. *The actual expressions for the critical points of e_m can be readily obtained from the zeros of (2.7). These take the form $q_c = (R_c, \mathbf{0})$, with $R_c = I_3$ for the minimum and $R_c = I_3 + 2S(v_i)^2$ for the remaining critical points, where v_i is a unitary eigenvector of the symmetrical matrix $Q^* Q^{*T}$.*

Until now, we have shown that, for all initial conditions, the solutions of the system converge to one of four points and that this set includes the desired equilibrium point $(q_0, 0)$. To prove that the closed-loop system is AGAS, we show that except for $(q_0, 0)$ all equilibrium points $(q_c, 0) \in M$ have an unstable manifold. To reach this result, we consider the linearizations of the closed-loop system Σ about each of the four points of interest.

Let $(q_c, 0) \in M$ and consider the system (2.1) in closed-loop with the control law obtained by the left translation of (2.8). As shown in [BL04], rewriting the dynamics in first-order form and linearizing about the equilibrium points $(q_c, 0)$, using the decomposition $\mathsf{T}_{(q_c,0)}\mathsf{T}\mathrm{SE}(3) = \mathsf{T}_{q_c}\mathrm{SE}(3) \oplus \mathsf{T}_{q_c}\mathrm{SE}(3)$, yields the linear system

$$A_\Sigma(q_c) = \begin{bmatrix} 0 & -\left((\mathbb{G}(q_c)^\sharp \circ \operatorname{Hess} e_m(q_c)\right)^T \\ \mathrm{id}_{\mathsf{T}_{q_c}\mathrm{SE}(3)} & \left(\mathbb{G}(q_c)^\sharp \circ d_{\dot{q}_e}(F_{\text{ext}} - \widetilde{\Psi})|_{(q_c,0)}\right)^T \end{bmatrix}^T \tag{2.20}$$

From the positive definiteness of the natural application $\langle \Psi(\xi), \xi\rangle$ and the dissipative nature of the external force, the tensor $d_{\dot{q}_e}(F_{\text{ext}} - \widetilde{\Psi})\big|_{(q_c,0)}$ is symmetric and negative definite.

Consequently, the linear system (2.20) is stable (respectively unstable) if and only if the linear system

$$\dot{x} = -\mathrm{Hess}(e_m(q_c))x$$

is stable (respectively unstable) [Kod89]. We can therefore conclude that the stability of (2.20) is completely determined by the Hessian matrix $\mathrm{Hess}(e_m(q_c))$.

Lemma 11. *If Assumptions 1 and 2 hold, the set of initial conditions for which the solutions of Σ converge to $(q_c, 0) \in M \setminus \{(q_0, 0)\}$ is a closed set of Lebesgue measure zero, whose complement is open and dense.*

Proof. As stated in the proof of Lemma 8, if Assumption 2 is satisfied, it can be shown that e_m is a Morse function with four critical points: one minimum, one maximum, and two saddle points. At the global minimum, the Hessian is positive definite, i.e. $\mathrm{Hess}(e_m(q_0)) > 0$, and at the other critical points, it is nonsingular and exhibits at least one positive eigenvalue. Consequently the dimension of the stable manifold for each of the equilibrium points $(q_c, 0) \in M \setminus \{(q_0, 0)\}$ is smaller than that of the tangent bundle $\mathsf{TSE}(3)$. □

We have now gathered the ingredients needed to prove Theorem 7.

Proof: Theorem 7. Let $\mathcal{M} = \bigcup_{i=1}^{3} \mathcal{M}_i$, where the sets $\mathcal{M}_i$ correspond to the unstable manifolds of the equilibria $(q_c, 0) \in M \setminus \{(q_0, 0)\}$, which according to Lemma 11 have measure zero and are nowhere dense. As the finite union of these sets, $\mathcal{M}$ is also a measure zero nowhere dense set. Since the solutions of Σ converge to $(q_0, 0)$ for all initial conditions in $\mathsf{TSE}(3)\backslash\mathcal{M}$, it follows that $(q_0, 0)$ is AGAS. Given that $d_{\dot{q}_e}(F_{\text{ext}} - \widetilde{\Psi})\big|_{(q_c,0)}$ is negative definite, the dampening of the linear system (2.20) is positive definite, which implies the system is locally exponentially stable. Hence, we can also conclude that in a neighborhood of $(q_0, 0)$, the solutions of Σ converge to $(q_0, 0)$ exponentially fast.

□

2.7 Simulation results

In this section we present simulation results for the stabilizing control law derived in the Section 2.5. The simulation objective is to stabilize the configuration of a rigid body that starts at rest. We consider the landmark placement corresponding to

$$X = \begin{bmatrix} 5 & 0 & 0 & -5 & 0 & 0 \\ 0 & 2 & 0 & 0 & -2 & 0 \\ 0 & 0 & 3 & 0 & 0 & -3 \end{bmatrix}$$

and a vehicle with inertia matrices $\mathbb{J} = \mathrm{diag}([1\ 2\ 3])$, $\mathbb{M} = mI_3$, and a mass $m = 2$ Kg. To model the drag we consider as external force the left-invariant covector field with

$F_{\mathrm{drag}} = (-0.01\boldsymbol{\omega}\|\boldsymbol{\omega}\|, -0.01\mathbf{v}\|\mathbf{v}\|)$ at the identity. The actuation is limited to 25 N for force and 5 Nm for torque, meaning that, after compensating the gravity, a force of 5 N and a torque of 5 Nm are available for stabilization. The control parameters were tuned so as to achieve a balanced closed-loop response.

The time evolution of the position error and attitude error are presented in Figures 2.2 and 2.3. For the attitude error, we consider the angle of rotation from the angle-axis representation for the error rotation matrix R_e. As expected, both errors converge asymptotically to zero.

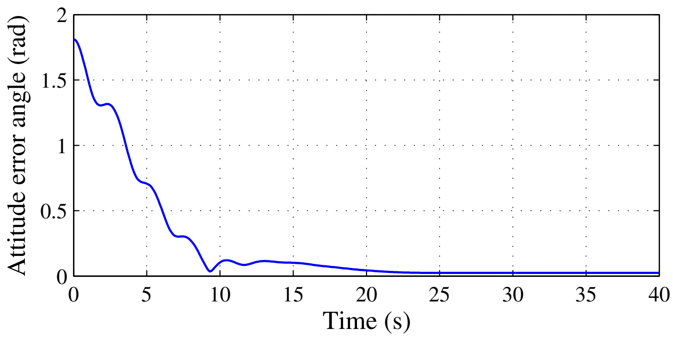

Figure 2.2: Attitude error.

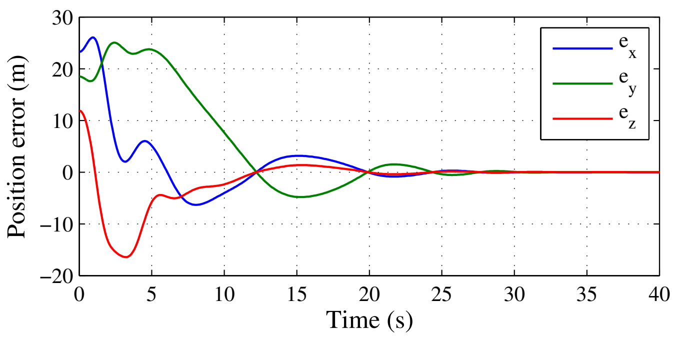

Figure 2.3: Position error.

Figures 2.4 and 2.5 display the torque and force actuations, respectively. Since there is no potential torque acting on the vehicle, the steady state torque is zero. As for the actuation force, its steady state value is the force required to counteract gravity, given the final configuration of the vehicle. It can be observed that the torque and force actuations verify the imposed constraints.

To assess the robustness of the proposed solution to measurement noise we also present results of a simulation considering additive noise on the measurements $\mathbf{q}_i$ with zero mean and standard deviation 0.3 m. The attitude and position errors evolution shown in Figures 2.6 and 2.7 are very similar to those of the noiseless situation, meaning that in this case the system is not driven to instability by the measurement noise. As expected,

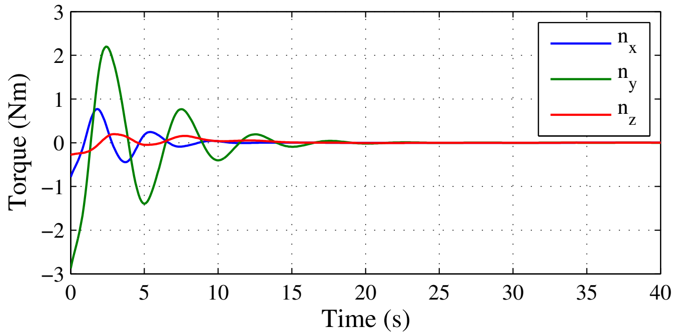

Figure 2.4: Torque actuation.

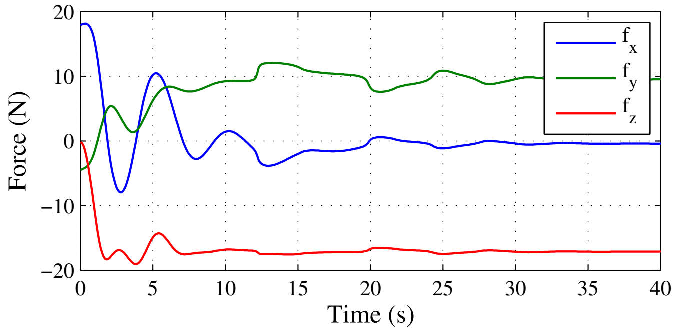

Figure 2.5: Force actuation.

after reaching the steady state regime, the position and attitude errors are bounded by the measurement errors. Comparing Figures 2.8 and 2.9 one sees that measurement noise has a more significant impact on the actuations than on the vehicle's position and attitude. This can be explained due to the direct influence of the measurement matrix Q on the feedback expressions (2.16), (2.17), and (2.18).

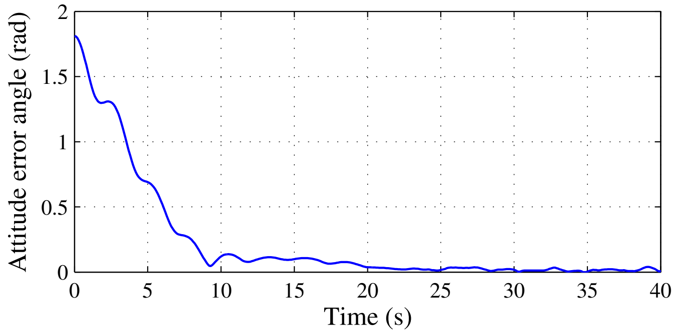

Figure 2.6: Attitude error in the presence of sensor noise.

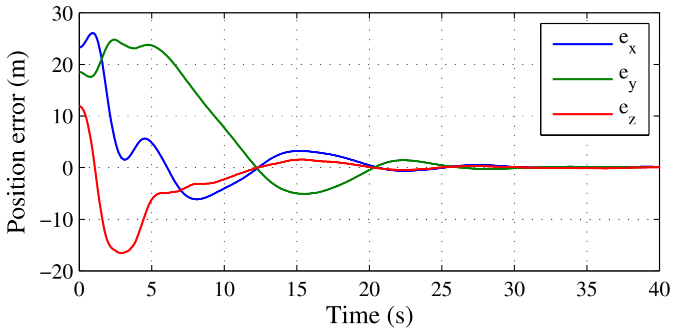

Figure 2.7: Position error in the presence of sensor noise.

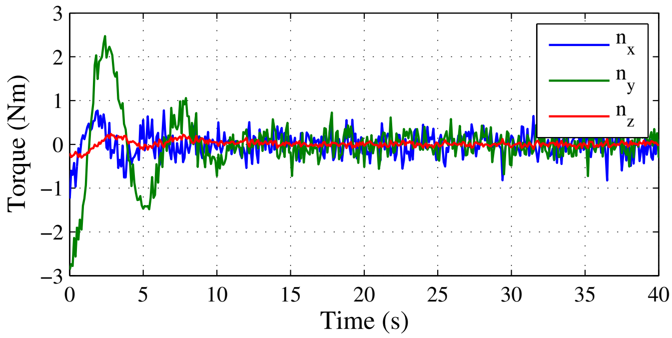

Figure 2.8: Torque actuation in the presence of sensor noise.

2.8 Concluding remarks

A landmark-based solution to the problem of stabilizing a fully-actuated rigid body while keeping the force and torque actuation within predefined bounds was presented in this chapter. A landmark-based error function was introduced for potential energy shaping and combined with a dissipative force map to obtain a dissipative closed-loop system that has an AGAS equilibrium point at the minimum of the error function. The prescribed bounds on the actuation were enforced by appropriately scaling a modified version of the error function and defining a bounded dissipative force map. Simulation results attested

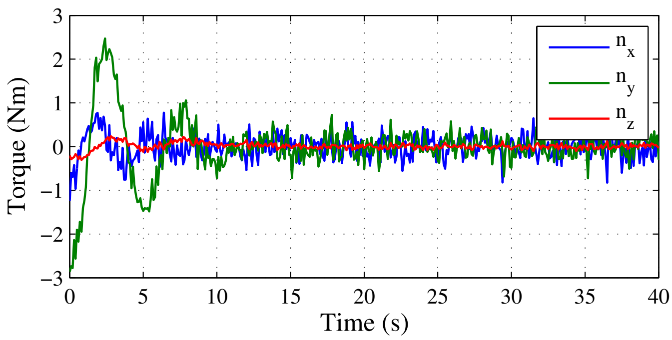

Figure 2.9: Force actuation in the presence of sensor noise.

to the performance and robustness of the proposed stabilization controller.

3

Nonlinear trajectory tracking control of a quadrotor vehicle

This chapter addresses the problem of designing and experimentally validating a controller for steering a quadrotor vehicle along a time-dependent trajectory, while rejecting wind disturbances. The proposed solution consists of a nonlinear adaptive state feedback controller for thrust and torque actuation that asymptotically stabilizes the closed-loop system in the presence of constant force disturbances, used to model the wind action, and ensures that the actuation does not grow unbounded as a function of the position errors. A prototyping and testing architecture, developed to streamline the implementation and the tuning of the controller, is also described. Experimental results are presented to demonstrate the performance and robustness of the proposed controller.

3.1 Introduction

In recent years, several approaches to the problem of helicopter and quadrotor motion control have been proposed, ranging from proportional-integral-derivative (PID) control [GMHT08, PMC10] to nonlinear methods such as feedback linearization [KS98, CDL04], dynamic inversion [DSL09], high gain and nested saturation control [MN07], and backstepping [FDF00, MH04, HHMS09]. While PID control has demonstrated good flying qualities for hovering and tracking of straight line trajectories in the low speed regime, it has the drawback of relying on linearization of the quadrotor system. The control laws obtained in this way cannot provide explicit guarantees regarding the size of the basins of attraction for the stable equilibrium points and do not fully explore the vehicle's flight envelope. Nested saturation control and backstepping are examples of nonlinear control techniques able to provide larger regions of attraction.

Backstepping is a well known technique extensively used for control of nonlinear systems. For example, it has been applied to helicopter trajectory tracking [FDF00] and [MH04], to control of a two tilt rotor aircraft [KFL06] and also to quadrotor trajectory tracking [GHM08] and tracking of parallel linear visual features [MH05]. In general, the backstepping technique is not applicable to underactuated systems. However, as shown in [KS98], a simplified model commonly adopted for both quadrotors and helicopters is feedback linearizable by dynamic augmentation of the thrust actuation, and hence stabilizable by means of backstepping. Several methodologies can be combined with backstepping to attain desirable characteristics of a control law, such as robustness to external disturbances and actuation boundedness. The use of integral action to achieve zero steady state error or equivalently rejection of constant disturbances in a closed-loop regulation system is standard in the control literature and can be combined with the backstepping technique as discussed in [SF04]. The control methodology known as adaptive backstepping [KKK95] relies on an estimator to achieve the disturbance rejection effect of integral control. One problem with a straightforward application of adaptive backstepping is that the parameter estimate can grow, without an *a priori* bound, depending on the initial conditions of the system. The typical approach to this problem is to use a projection operator to constrain the parameter estimate to a given set [KKK95]. The discontinuity of the projection operation is a twofold problem. First, it leads to practical problems when applied to continuous time systems. Second, the recursive application of the backstepping procedure is no longer possible, as Lipschitz continuity is violated and the usual theorems on the existence and uniqueness of differentiable equations can no longer be applied. To overcome both these problems, we employ the arbitrarily smooth projection operator proposed in [CdQD06], which generates parameter estimates with sufficient smoothness to complete the backstepping procedure.

Several works for the stabilization of thrust propelled rotorcraft based on dynamic extension of the thrust input have also been proposed, namely the ones presented in [FDF00, MH04] and more recently [GL13, LMA12, Kob13]. Despite employing different control laws, a common characteristic unifies these controllers: the existence of a singularity in the control law for zero thrust. The typical scenario is for either the singular condition to be ignored or for the control laws to be *ad hoc* modified when near the singularity. This course of action can lead to a loss of the stability properties and can endanger a vehicle unnecessarily. Nonetheless, for a set of initial error conditions, it can be proven that the thrust never reaches zero and the control law is well defined for all time, as detailed in [MH04].

The work in [RT11] employs similar adaptive techniques to achieve control of a vertical take-off and landing (VTOL) UAV for a set of constant external disturbances. The quadrotor control is constructed by designing a bounded thrust virtual control, which is then tracked using the thrust and torque available controls. The zero thrust singularity is avoided by constraining the virtual control law but that leads to a rather conservative control action. Two controllers are then presented, one which achieves almost global stabilization and other which presents some restrictions on the initial conditions. The estimation and cancelation of the external disturbance is performed using the smooth projection from [CdQD06] to ensure that the estimates are differentiable. As opposed to our method, which treats the rotational degree-of-freedom inherent to these vehicles independently from the position tracking objective, the solution in [RT11] completely prescribes the desired rotation matrix through the attitude extraction method proposed. Simulation results are presented for the proposed controllers, although they are not evaluated in an experimental setup.

Typically, small-scale quadrotors are either controlled in thrust and angular velocity or thrust and torque. With today's technology, there are commonly available sensors for angular velocity with an extremely small footprint that can be carried by even the smallest quadrotor vehicles. This fact makes it easy for aircraft manufacturers to measure the angular velocity and design inner-loop controllers to track angular velocity commands. Torque commands for quadrotor vehicles are also trivial to implement since most electric motors employed in remote controlled aircraft are internally controlled in speed. The motor's angular speed is directly related with the thrust force they generate and by acting on the motors the manufacturer can impose a different force on each motor, so as to track a torque reference.

In this chapter we address the problem of trajectory tracking for quadrotors, using a backstepping procedure that builds on the dynamic augmentation principle presented in [KS98]. The desired trajectory is specified by a sufficiently smooth time-parameterized position vector. The desired attitude of the vehicle is not prescribed since attitude convergence (up to a rotation about the body z axis) is naturally accomplished by solving the position tracking problem. Robustness to external constant disturbances is accomplished through adaptive backstepping. These disturbances can be used to represent both exogenous inputs such as constant wind and model uncertainties such as quadrotor mismatches. The proposed control laws allows us to determine a Lyapunov function for the closed-loop system whose time derivative is negative definite with regard to the tracking errors, rendering it inherently robust to small errors and noise. Experimental results are presented to attest the robustness and performance of the proposed control laws.

This chapter is structured as follows. Section 3.2 introduces the quadrotor model. The problem and control objectives are stated in Section 3.3. Controller design is described in Section 3.4, including the necessary steps to ensure disturbance rejection. Experimental results illustrating the performance of the proposed control law are presented in Section 3.6 and Section 3.7 summarizes the contents of the chapter.

3.2 Quadrotor model

The quadrotor vehicle is modeled as a rigid body, that can generate a thrust force along the body z axis. We consider two distinct forms of angular actuation: *i)* torque, which is equivalent to controlling the force exerted by electric motors; and *ii)* angular velocity. Both are common in quadrotors, whether they are commercial off-the-shelf vehicles or custom built ones.

Consider a fixed inertial frame $\{\mathcal{I}\}$ and a frame $\{\mathcal{B}\}$ attached to the vehicle's center of mass. The configuration of the body frame $\{\mathcal{B}\}$ with respect to $\{\mathcal{I}\}$ can be viewed as an element of the Special Euclidean group, $(R, \mathbf{p}) = ({}^{I}_{B}R, {}^{I}\mathbf{p}_{B}) \in \mathrm{SE}(3)$, where $\mathbf{p} \in \mathbb{R}^3$ is the position and $R \in \mathrm{SO}(3)$ the rotation matrix. The kinematic and dynamic equations of motion for the rigid body can be written as

$$\dot{\mathbf{p}} = R\mathbf{v}, \tag{3.1}$$

$$\dot{\mathbf{v}} = -S(\omega)\mathbf{v} + \frac{1}{m}\mathbf{f}, \tag{3.2}$$

$$\dot{R} = RS(\omega), \tag{3.3}$$

$$\dot{\omega} = -\mathbb{J}^{-1}S(\omega)\mathbb{J}\omega + \mathbb{J}^{-1}\mathbf{n}, \tag{3.4}$$

where the linear velocity $\mathbf{v} \in \mathbb{R}^3$, the force $\mathbf{f} \in \mathbb{R}^3$, the angular velocity $\omega \in \mathbb{R}^3$, and the torque $\mathbf{n} \in \mathbb{R}^3$ are expressed in the body frame $\{\mathcal{B}\}$. For quadrotors actuated in angular velocity, only equations (3.1)-(3.3) are necessary for a complete model of the vehicle, whereas for actuation in torque the additional angular dynamics (3.4) is required. The scalar m and the matrix $\mathbb{J} \in \mathbb{R}^{3\times 3}$ represent the quadrotor's mass and moment of inertia, respectively. For both quadrotor models, the aerodynamic drag forces due to the fuselage are neglected given the low speeds at which the quadrotors operate.

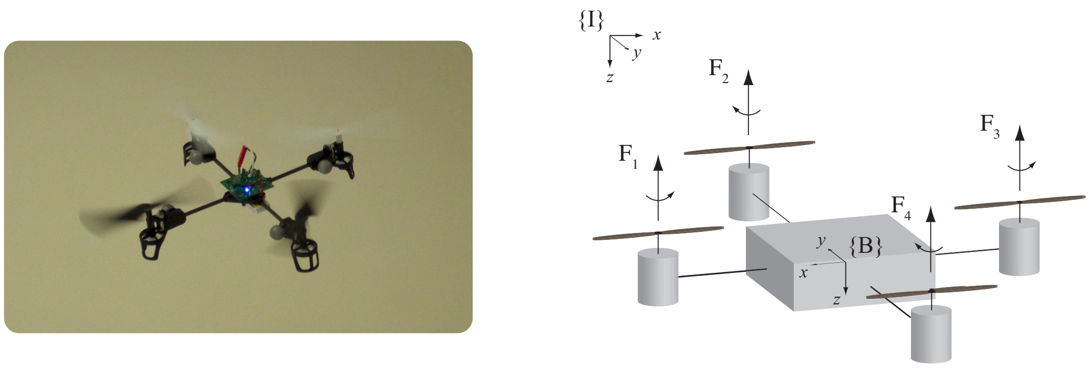

(a) Quadrotor platform (b) Quadrotor setup

Figure 3.1: Quadrotor experimental platform and diagram.

Bearing in mind the geometry of the quadrotor and assuming that the forces and moments generated by each of the four rotors are approximately given by the thrust and torque components perpendicular to the rotor disk plane, we can consider a quadrotor model such that torques (or angular velocities) can be generated in any direction and the generated thrust force is always aligned with the body z axis. Figure 3.1(a) shows a small-scale quadrotor platform and a sketch of the quadrotor setup is presented in Figure 3.1(b), together with illustrations of reference frames, the force F_i generated by each motor and the direction of rotation for each propeller. There is a bijective correspondence between the motor forces F_i and the total thrust T and torque $\mathbf{n}$ applied to the quadrotor. We consider that the torque is either an input for the quadrotor or that an inner-loop controller exists that adjusts the torque in order to track angular velocity references. We call this latter design a quadrotor *controlled in angular velocity*.

The total force acting on the quadrotor, in body coordinates, is given by

$$\mathbf{f} = -T\mathbf{e}_3 + mgR^T\mathbf{e}_3 + mR^T\mathbf{b} \tag{3.5}$$

where T is the thrust generated by the motors, $\mathbf{e}_3 = [0\ 0\ 1]^T$, g is the gravitational acceleration, and $\mathbf{b} \in \mathbb{R}^3$ is an unknown external force disturbance expressed in $\{\mathcal{I}\}$. The force disturbance $m\mathbf{b}$ can model exogenous inputs, such as constant wind, and also model uncertainties, such as imperfect knowledge of the mass of the vehicle. With the full torque control available, the angular dynamics (3.4) can be reduced to the integrator form $\dot{\boldsymbol{\omega}} = \boldsymbol{\tau}$, using the input transformation

$$\mathbf{n} = \mathbb{J}\boldsymbol{\tau} + S(\boldsymbol{\omega})\mathbb{J}\boldsymbol{\omega}. \tag{3.6}$$

The quadrotor is thus an underactuated vehicle, as evidenced by (3.2) and (3.5), making the control problem much more difficult to address than what it would be for a fully-actuated vehicle, such as the one discussed in the previous chapter. In this particular case we only have one degree of freedom for the force actuation in the body frame and we are required to control the three-dimensional linear position of the vehicle $\mathbf{p} \in \mathbb{R}^3$. As shall be demonstrated in the sequel, it is indeed possible to control the vehicle's position, as its attitude can be used to drive the thrust force to some desired direction.

3.3 Problem statement

Let the desired trajectory $\mathbf{p}_d(t) \in \mathbb{R}^3$ be a curve of class at least C^4. The control objective consists of designing a control law for the quadrotor actuations $T(t)$ and $\boldsymbol{\omega}(t)$, or $T(t)$ and $\tau(t)$, that ensures convergence of the vehicle's position $\mathbf{p}(t)$ to the trajectory $\mathbf{p}_d(t)$ with the largest possible basin of attraction. Throughout the remainder of the chapter, the time dependence of variables is often omitted to lighten notation.

Due to the underactuated nature of the vehicle, the desired attitude cannot be arbitrarily selected. From (3.2) and (3.5), it is easy to observe that the equilibrium for trajectory tracking satisfies

$$T_d R_d \mathbf{e}_3 = mg\mathbf{e}_3 - m\ddot{\mathbf{p}}_d + m\mathbf{b}. \tag{3.7}$$

Consequently, the desired rotation matrix R_d is automatically prescribed up to a rotation about the body z axis ($T_d R_d R_z(\psi)\mathbf{e}_3 = mg\mathbf{e}_3 - m\ddot{\mathbf{p}}_d + m\mathbf{b}$, with $\psi \in \mathbb{R}$). The symmetry exhibited by the quadrotor vehicle dictates that there is an additional degree of freedom. Rotations about the body z axis bear no influence on the control action as it is possible to generate any angular velocity and thrust, within the vehicle's limits of operation, regardless of its heading angle. Throughout the design of the trajectory tracking controller, the attitude is handled in its natural space, the Special Orthogonal group SO(3), as a rotation matrix. This avoids the introduction of artefacts related only to the parameterization used for the attitude, as is the case of singularities with Euler angles and multiple coverings with the quaternion representation [BB00].

We consider the full state of the vehicle to be available for feedback. In an experimental setup, the orientation and angular velocity readings are typically produced by IMUs, equipped with advanced algorithms which combine triads of rate-gyros, accelerometers, magnetometers [MHP08, BSO10, VCSO10]. The position and linear velocity are commonly obtained from GPS signals [BSO09], if they are available. Whenever the quadrotor is being operated indoors, and thus GPS is not available, the position and velocity can be estimated resorting to additional onboard sensors such as laser scanner units [CMcTN07] or cameras [PPTN08]. In our setup we employ a high speed motion tracking system, based on a set of external cameras tracking reflective markers on the vehicle, as described in section 3.6.

Although this is hardly ever the case in practice, the external disturbance $\mathbf{b}$ is assumed to be constant for controller design purposes. An upper bound is assumed to be known on the external disturbance, so that the quadrotor can perform a trajectory tracking maneuver with bounded thrust input.

Assumption 12. *The external disturbance* $\mathbf{b}$ *in* (3.5) *is constant and is bounded as* $\|\mathbf{b}\| \leq B$ *with* $B > 0$.

In practice, this assumption is an idealization that approximates reality and thus perfect tracking is never achieved. Nonetheless, the robustness added to the controller by considering constant disturbances is beneficial and results in smaller closed-loop errors.

Even though the disturbance is bounded, straightforward or naïve implementations of estimators can lead to wind-up phenomena and result in unbounded growth of the estimate. To avoid a wind-up effect on the disturbance estimator, and keep the estimate bounded, we employ a sufficiently smooth projection operator when designing the estimators. This procedure is detailed in the next section, together with the design of the controller based on the backstepping technique. The smooth projection method requires overparameterization of the disturbance due to the higher order of the quadrotor system. The multiple estimates of the external disturbance, denoted by $\hat{\mathbf{b}}_1$ and $\hat{\mathbf{b}}_2$, are obtained by adaptive backstepping and used for feedback control. Stability of the estimation errors is guaranteed by Lyapunov-like methods, from which we can also assert the convergence of the first estimate $\hat{\mathbf{b}}_1$ to the real value of the disturbance, as detailed in the sequel.

3.4 Controller design

We start the design process by considering a virtual controller for the translational subsystem, which is backstepped through the angular subsystem to obtain the final implementable controllers, one for angular velocity and another for torque actuation. The proposed controller for the translational subsystem is based on the procedure detailed in [MI04], which is presented in the following Proposition for a one-dimensional double integrator.

Proposition 13. *Consider the double integrator system*

$$\dot{x}_1 = x_2,$$
$$\dot{x}_2 = u,$$

driven by input $u \in \mathbb{R}$ and let σ and ρ be saturation functions of class C^2 and Ω a function of class C^3 such that $\Omega(s) = s$, for $|s| < 2\sigma_{max}$ and $\Omega'(s) \geq 1$ for all s. The control law

$$u(x_1, x_2) = -\frac{(x_2 + \sigma(x_1))(\rho(x_2 + \sigma(x_1)) + \sigma(x_1))}{\Omega'(x_2)\Big(\Omega(x_2) + \Omega(\sigma(x_1))\Big)} + \frac{\sigma'(x_1)x_2}{\Omega'(x_2)} \tag{3.8}$$

renders the origin of the double integrator GAS and the input verifies

$$|u(x_1, x_2)| \leq \frac{1}{\Omega'(x_2)}\Big(\rho_{max} + \sigma_{max} + \sigma'_{max}|x_2|\Big).$$

Notice that if Ω is, at least, asymptoticly quadratic, then an upper bound on $|u(x_1, x_2)|$ can be established *a priori* and for all $(x_1, x_2) \in \mathbb{R}^2$. The Lyapunov function for the double integrator

$$V(x_1, x_2) = \phi(x_1) + \tfrac{1}{2}(\Omega(x_2) + \Omega(\sigma(x_1)))^2,$$

with $\phi(s) = \int_0^s \sigma(t)\mathrm{d}t$, has closed-loop negative-definite time derivative

$$\dot{V}(x_1, x_2) \leq -\sigma(x_1)^2 - (x_2 + \sigma(x_1))\rho(x_2 + \sigma(x_1)).$$

In order to define the virtual controller for the translational subsystem, consider the following error states

$$\mathbf{z}_1 = \mathbf{p} - \mathbf{p}_d, \tag{3.9a}$$
$$\mathbf{z}_2 = \dot{\mathbf{z}}_1 + \sigma(\mathbf{z}_1), \tag{3.9b}$$

for the double integrator driven by

$$\ddot{\mathbf{z}}_1 = \mathbf{u} = -\frac{T}{m}R\mathbf{e}_3 + g\mathbf{e}_3 + \mathbf{b} - \ddot{\mathbf{p}}_d. \tag{3.10}$$

A tentative Lyapunov function is devised as

$$V_{DI} = \phi(\mathbf{z}_1)^T\mathbf{1} + \frac{1}{2}\Big(\Omega(\mathbf{z}_2 - \sigma(\mathbf{z}_1)) + \Omega(\sigma(\mathbf{z}_1))\Big)^T\Big(\Omega(\mathbf{z}_2 - \sigma(\mathbf{z}_1)) + \Omega(\sigma(\mathbf{z}_1))\Big),$$

where, with a slight abuse of notation, ϕ, σ, and Ω are applied element-wise. For a fully-actuated vehicle, the control law

$$\mathbf{u}^\star = \begin{bmatrix} u(z_{11}, z_{21} - \sigma(z_{11})) \\ u(z_{12}, z_{22} - \sigma(z_{12})) \\ u(z_{13}, z_{23} - \sigma(z_{13})) \end{bmatrix}, \tag{3.11}$$

with the controller u defined as in (3.8), globally asymptotically stabilises the system and renders the Lyapunov function derivative negative definite

$$\dot{V}_{DI} \le -\sigma(\mathbf{z}_1)^T\sigma(\mathbf{z}_1) - k_2\mathbf{z}_2^T\rho(\mathbf{z}_2) = -W_2(\mathbf{z}_1, \mathbf{z}_2).$$

In the next step, we consider the real vehicle and the errors introduced by the underactuation. Furthermore, a term is added to the Lyapunov function to enable disturbance rejection. The new tentative Lyapunov function is

$$V_2 = V_{DI} + \frac{1}{2k_{b1}}\tilde{\mathbf{b}}_1^T\tilde{\mathbf{b}}_1, \tag{3.12}$$

with positive gain k_{b1}, and has the following time derivative

$$\begin{aligned}\dot{V}_2 &\le -W_2(\mathbf{z}_1, \mathbf{z}_2) + \frac{\partial V_2}{\partial \mathbf{z}_2}(\mathbf{u} - \mathbf{u}^\star) - \frac{1}{k_{b1}}\tilde{\mathbf{b}}_1^T\dot{\hat{\mathbf{b}}}_1 \\ &\le -W_2(\mathbf{z}_1, \mathbf{z}_2) + \frac{\partial V_2}{\partial \mathbf{z}_2}(\hat{\mathbf{u}} - \mathbf{u}^\star) + \tilde{\mathbf{b}}_1^T\Big(\frac{\partial V_2}{\partial \mathbf{z}_2}^T - \frac{1}{k_{b1}}\dot{\hat{\mathbf{b}}}_1\Big),\end{aligned}$$

where the real control input, computed using the estimated disturbance, is

$$\hat{\mathbf{u}} = -\frac{T}{m}R\mathbf{e}_3 + g\mathbf{e}_3 + \hat{\mathbf{b}}_1 - \ddot{\mathbf{p}}_d. \tag{3.13}$$

and the partial derivative of (3.12) with respect to $\mathbf{z}_2$ is written as

$$\frac{\partial V_2}{\partial \mathbf{z}_2}^T = (\Omega(\mathbf{z}_2 - \sigma(\mathbf{z}_1)) + \Omega(\sigma(\mathbf{z}_1))) \otimes \Omega'(\mathbf{z}_2 - \sigma(\mathbf{z}_1))$$

where $\otimes$ denotes element-wise vector multiplication.

The term $\hat{\mathbf{u}} - \mathbf{u}^\star$ can be regarded as an actuation error due to the fact that the quadrotor is an underactuated vehicle, i.e. the thrust must be aligned with the z body axis, and due to the unknown disturbance $\mathbf{b}$. Applying the backstepping procedure, we define the new backstepping error

$$\mathbf{z}_3 = \hat{\mathbf{u}} - \mathbf{u}^\star \tag{3.14}$$

and the new Lyapunov function

$$V_3 = V_2 + \frac{1}{2}\mathbf{z}_3^T\mathbf{z}_3,$$

with time derivative

$$\dot{V}_3 \leq -W_3(\mathbf{z}_1,\mathbf{z}_2,\mathbf{z}_3) + \mathbf{z}_3^T(k_3\mathbf{z}_3 + \frac{\partial V_2}{\partial \mathbf{z}_2}^T + \dot{\mathbf{z}}_3) + \tilde{\mathbf{b}}_1^T(\frac{\partial V_2}{\partial \mathbf{z}_2}^T - \frac{1}{k_{b1}}\dot{\hat{\mathbf{b}}}_1), \tag{3.15}$$

where $W_3(\mathbf{z}_1,\mathbf{z}_2,\mathbf{z}_3) = W_2 + k_3\mathbf{z}_3^T\mathbf{z}_3$ is a positive definite function.

The time derivative of the error state $\mathbf{z}_3$ is

$$\dot{\mathbf{z}}_3 = -\frac{\dot{T}}{m}R\mathbf{e}_3 - \frac{T}{m}RS(\boldsymbol{\omega})\mathbf{e}_3 + \dot{\hat{\mathbf{b}}}_1 - \mathbf{p}_d^{(3)} - \hat{\dot{\mathbf{u}}}^\star - \frac{\partial \mathbf{u}^\star}{\partial \mathbf{z}_2}\tilde{\mathbf{b}}_1, \tag{3.16}$$

where $\hat{\dot{\mathbf{u}}}^\star$ denotes the estimate of the time derivative of $\mathbf{u}^\star$ obtained using $\hat{\mathbf{b}}_1$ instead of the unknown $\mathbf{b}$. The time derivative of the virtual actuation can be expressed as

$$\frac{d\mathbf{u}^\star}{dt} = \frac{\partial \mathbf{u}^\star}{\partial \mathbf{z}_1}\frac{d\mathbf{z}_1}{dt} + \frac{\partial \mathbf{u}^\star}{\partial \mathbf{z}_2}\frac{d\mathbf{z}_2}{dt},$$

where the external disturbance appearing only linearly in the term $\frac{d\mathbf{z}_2}{dt}$. We have thus that the error when performing the estimation using $\hat{\mathbf{b}}_1$ is given by

$$\dot{\mathbf{u}}^\star - \hat{\dot{\mathbf{u}}}^\star = \frac{\partial \mathbf{u}^\star}{\partial \mathbf{z}_2}\tilde{\mathbf{b}}_1.$$

Substituting $\dot{\mathbf{z}}_3$ in (3.15) and defining the input vector

$$\boldsymbol{\mu} = \begin{bmatrix} \dot{T} & \omega_1 & \omega_2 \end{bmatrix}^T$$

and the matrix

$$M(T) = \begin{bmatrix} 0 & 0 & -T \\ 0 & T & 0 \\ -1 & 0 & 0 \end{bmatrix},$$

we get an expression for the Lyapunov function time derivative,

$$\dot{V}_3 \leq -W_3(\mathbf{z}_1,\mathbf{z}_2,\mathbf{z}_3) + \mathbf{z}_3^T\left(\frac{1}{m}RM(T)\boldsymbol{\mu} + k_3\mathbf{z}_3 + \frac{\partial V_2}{\partial \mathbf{z}_2}^T + \dot{\hat{\mathbf{b}}}_1 - \mathbf{p}_d^{(3)} - \hat{\dot{\mathbf{u}}}^\star\right) + \tilde{\mathbf{b}}_1^T\left(\frac{\partial V_2}{\partial \mathbf{z}_2}^T - \frac{\partial \mathbf{u}^\star}{\partial \mathbf{z}_2}^T\mathbf{z}_3 - \frac{1}{k_{b1}}\dot{\hat{\mathbf{b}}}_1\right).$$

that can be rendered negative semi-definite to achieve convergence of the trajectory tracking error to zero, with the appropriate control inputs, $\dot{T}$ and $\boldsymbol{\omega}$, and estimator law for $\dot{\hat{\mathbf{b}}}_1$.

We tackle the estimation of the disturbance using a projection operator that keeps the estimate $\hat{\mathbf{b}}_1$ within some *a priori* defined set and verifies the smoothness properties required for the iterative application of the backstepping procedure. Consider the estimate control law,

$$\dot{\hat{\mathbf{b}}}_1 = k_{b1}\,\mathrm{Proj}(\xi,\hat{\mathbf{b}}_1) = k_{b1}\left(\xi - \frac{\eta_1\eta_2}{2(\epsilon^2-2\epsilon B)^{n+1}B^2}\hat{\mathbf{b}}_1\right) \tag{3.17}$$

with

$$\begin{aligned}
\xi &= \frac{\partial V_2}{\partial \mathbf{z}_2}^T - \frac{\partial \mathbf{u}^\star}{\partial \mathbf{z}_2}^T \mathbf{z}_3,\\
\eta_1 &= \begin{cases} (\hat{\mathbf{b}}_1^T\hat{\mathbf{b}}_1 - B^2)^{n+1}, & \text{if } (\hat{\mathbf{b}}_1^T\hat{\mathbf{b}}_1 - B^2) > 0 \\ 0, & \text{otherwise}\end{cases},\\
\eta_2 &= \hat{\mathbf{b}}_1^T\xi - \sqrt{(\hat{\mathbf{b}}_1^T\xi)^2 + \delta^2},
\end{aligned}$$

where $\epsilon > 0$ and $\delta > 0$ are arbitrary parameters and B is the bound on the norm of the unknown parameter. The smooth projection operator is taken from [CdQD06] and has the following properties,

P1 – $\|\hat{\mathbf{b}}(t)\| \le B + \epsilon, \forall t \ge 0$;

P2 – $\tilde{\mathbf{b}}^T\,\mathrm{Proj}(\xi,\hat{\mathbf{b}}) \ge \tilde{\mathbf{b}}^T\xi$;

P3 – $\|\mathrm{Proj}(\xi,\hat{\mathbf{b}})\| \le \|\xi\|\left(1+\frac{B+\epsilon}{B}\right)^2 + \frac{B+\epsilon}{2B^2}\delta$;

P4 – $\mathrm{Proj}(\xi,\hat{\mathbf{b}})$ is at least of class C^n.

From the estimator control law (3.17) and property P2 we derive the upper bound for the Lyapunov function derivative

$$\dot{V}_3 \le -W_3(\mathbf{z}_1,\mathbf{z}_2,\mathbf{z}_3) + \mathbf{z}_3^T\left(\frac{1}{m}RM(T)\boldsymbol{\mu} + k_3\mathbf{z}_3 + \frac{\partial V_2}{\partial \mathbf{z}_2}^T + \dot{\hat{\mathbf{b}}}_1 - \mathbf{p}_d^{(3)} - \dot{\hat{\mathbf{u}}}^\star\right). \tag{3.18}$$

Moreover, property P4 ensures that the derivatives of the estimate are continuous up to $\hat{\mathbf{b}}_1^{(n+1)}$. At this point, for vehicles actuated in angular velocity, we can actuate on the control inputs $\boldsymbol{\mu}$ and render (3.18) negative semi-definite to achieve convergence of the trajectory tracking error to zero.

We are now able to state Theorem 15, regarding the design of a stabilizing control law. The Theorem requires the following assumption, which is met under the appropriate conditions, to be detailed in the sequel.

Assumption 14. *The thrust actuation verifies $T(t) \ge \epsilon > 0$ for all time $t > 0$.*

Theorem 15. *Let the quadrotor kinematics and dynamics be described by* (3.1)-(3.3), *let $\mathbf{p}_d(t) \in C^3$ be the desired trajectory, and consider the transformation to error coordinates $\mathbf{z}_1$,*

$\mathbf{z}_2$, $\mathbf{z}_3$ given by (3.9a), (3.9b), (3.14), *respectively. For any $\omega_3(t)$, the closed-loop system that results from applying the control law*

$$\boldsymbol{\mu} = -mM^{-1}(T)R^T\left(k_3\mathbf{z}_3 + \frac{\partial V_2}{\partial \mathbf{z}_2} + \dot{\hat{\mathbf{b}}}_1 - \mathbf{p}_d^{(3)} - \hat{\mathbf{u}}^\star\right) \tag{3.19}$$

and the estimator law (3.17) *achieves trajectory tracking by guaranteeing that the errors $\mathbf{z}_1$, $\mathbf{z}_2$, and $\mathbf{z}_3$ converge to zero for any initial condition. Moreover, the disturbance estimate $\hat{\mathbf{b}}_1$ converges asymptotically to the unknown constant disturbance $\mathbf{b}$.*

Proof. The proposed control law (3.19) is well defined, in the conditions of Assumption 14. Starting with the positive definite Lyapunov function

$$V = \phi(\mathbf{z}_1)^T\mathbf{1} + \frac{1}{2}\Big(\Omega(\mathbf{z}_2 - \sigma(\mathbf{z}_1)) + \Omega(\sigma(\mathbf{z}_1))\Big)^T\Big(\Omega(\mathbf{z}_2 - \sigma(\mathbf{z}_1)) + \Omega(\sigma(\mathbf{z}_1))\Big) + \tfrac{1}{2}\mathbf{z}_3^T\mathbf{z}_3 + \tfrac{1}{2k_{b1}}\tilde{\mathbf{b}}_1^T\tilde{\mathbf{b}}_1,$$

and computing its time derivative, in closed-loop, we have that

$$\dot{V} \leq -\sigma(\mathbf{z}_1)^T\sigma(\mathbf{z}_1) - k_2\mathbf{z}_2^T\rho(\mathbf{z}_2) - k_3\mathbf{z}_3^T\mathbf{z}_3,$$

which is a negative semidefinite function. Since the quadrotor error dynamics are non-autonomous, we resort to Barbalat's Lemma to prove convergence of $\dot{V}$ to zero. From the unboundedness of V with respect to $\mathbf{z}_1$, $\mathbf{z}_2$,$\mathbf{z}_3$ and $\tilde{\mathbf{b}}_1$, and observing that $\dot{V}$ is negative semi-definite, we conclude that the states $\mathbf{z}_1$, $\mathbf{z}_2$,$\mathbf{z}_3$ and $\tilde{\mathbf{b}}_1$ are bounded. The external input $\mathbf{p}_d^{(3)}$ is bounded by assumption and $\dot{\hat{\mathbf{b}}}_1$ is bounded from property P4 of the projection operator and boundedness of the error states and estimation. We have thus that $\ddot{V}$ is bounded and, consequently, $\dot{V}$ is uniformly continuous. We can therefore apply Barbalat's Lemma to prove convergence of $\dot{V}$ to zero and, consequently, of the states $\mathbf{z}_1$, $\mathbf{z}_2$ and $\mathbf{z}_3$ to the origin. □

For quadrotors actuated in torque, we need to continue applying the backstepping procedure. Let us look at the Lyapunov derivative upper bound (3.18) and define the final backstepping error,

$$\mathbf{z}_4 = \frac{1}{m}RM(T)\boldsymbol{\mu} + k_3\mathbf{z}_3 + \frac{\partial V_2}{\partial \mathbf{z}_2}^T + \dot{\hat{\mathbf{b}}}_1 - \mathbf{p}_d^{(3)} - \hat{\mathbf{u}}^\star. \tag{3.20}$$

The error time derivative, finally featuring the torque controls, is

$$\dot{\mathbf{z}}_4 = \frac{1}{m}RS(\boldsymbol{\omega})M(T)\boldsymbol{\mu} + \frac{1}{m}R\dot{M}(T)\boldsymbol{\mu} + \frac{1}{m}RM(T)\boldsymbol{\nu} + \hat{\mathbf{h}} + \frac{\partial}{\partial \mathbf{z}_2}\left(k_3\mathbf{z}_3 + \frac{\partial V_2}{\partial \mathbf{z}_2}^T + \dot{\hat{\mathbf{b}}}_1 - \mathbf{p}_d^{(3)} - \hat{\mathbf{u}}^\star\right)\tilde{\mathbf{b}}_2. \tag{3.21}$$

where we performed the input transformation

$$\boldsymbol{\nu} = \begin{bmatrix}\ddot{T} & \tau_1 & \tau_2\end{bmatrix}^T \tag{3.22}$$

and $\hat{\mathbf{h}}$ is the estimate of

$$\mathbf{h} = \frac{d}{dt}\left(k_3\mathbf{z}_3 + \frac{\partial V_2}{\partial \mathbf{z}_2}^T + \dot{\hat{\mathbf{b}}}_1 - \mathbf{p}_d^{(3)} - \hat{\mathbf{u}}^\star\right)$$

obtained using the estimate $\hat{\mathbf{b}}_2$ instead of the unknown disturbance $\mathbf{b}$. The estimation error is given by

$$\mathbf{h} - \hat{\mathbf{h}} = \frac{\partial}{\partial \mathbf{z}_2}\left(k_3\mathbf{z}_3 + \frac{\partial V_2}{\partial \mathbf{z}_2}^T + \dot{\hat{\mathbf{b}}}_1 - \mathbf{p}_d^{(3)} - \hat{\mathbf{u}}^\star\right)\tilde{\mathbf{b}}_2.$$

Let us consider the final Lyapunov function,

$$V_4 = V_3 + \frac{1}{2}\mathbf{z}_4^T\mathbf{z}_4 + \frac{1}{2k_{b2}}\tilde{\mathbf{b}}_2^T\tilde{\mathbf{b}}_2$$

with $k_{b2} > 0$ and verify that its time derivative is

$$\begin{aligned}\dot{V}_4 \le -W_4(\mathbf{z}_1,\mathbf{z}_2,\mathbf{z}_3,\mathbf{z}_4) + \mathbf{z}_4^T\Big(\mathbf{z}_3 + k_4\mathbf{z}_4 + \frac{1}{m}RS(\boldsymbol{\omega})M(T)\boldsymbol{\mu} + \frac{1}{m}R\dot{M}(T)\boldsymbol{\mu} + \frac{1}{m}RM(T)\boldsymbol{\nu} + \hat{\mathbf{h}}\Big)\\ + \tilde{\mathbf{b}}_2^T\left(\frac{\partial}{\partial \mathbf{z}_2}\left(k_3\mathbf{z}_3 + \frac{\partial V_2}{\partial \mathbf{z}_2}^T + \dot{\hat{\mathbf{b}}}_1 - \mathbf{p}_d^{(3)} - \hat{\mathbf{u}}^\star\right)^T \mathbf{z}_4 - \frac{1}{k_{b2}}\dot{\hat{\mathbf{b}}}_2\right).\end{aligned}$$

At this point, we can establish a control law for $\boldsymbol{\nu}$ and an estimation law for $\mathbf{b}_2$ that, in conjunction with the previously proposed estimation law (3.17), renders the Lyapunov function negative semi-definite and achieves trajectory tracking. This result is established in the following Theorem.

Theorem 16. *Let the quadrotor kinematics and dynamics be described by* (3.1)-(3.4)*, let* $\mathbf{p}_d(t) \in C^4$ *be the reference trajectory, and consider the transformation to error coordinates* $\mathbf{z}_1$, $\mathbf{z}_2$, $\mathbf{z}_3$, $\mathbf{z}_4$, *given by* (3.9a), (3.9b), (3.14), (3.20)*, respectively. For any bounded* $\tau_3(t)$*, the closed-loop system that results from applying the input transformation* (3.22)*, the control law*

$$\boldsymbol{\nu} = -mM^{-1}(T)R^T\Big(\mathbf{z}_3 + k_4\mathbf{z}_4 + \frac{1}{m}RS(\boldsymbol{\omega})M(T)\boldsymbol{\mu} + \frac{1}{m}R\dot{M}(T)\boldsymbol{\mu} + \hat{\mathbf{h}}\Big), \tag{3.23}$$

and the estimator laws (3.17) *and*

$$\dot{\hat{\mathbf{b}}}_2 = k_b \operatorname{Proj}\left(\frac{\partial}{\partial \mathbf{z}_2}\left(k_3\mathbf{z}_3 + \frac{\partial V_2}{\partial \mathbf{z}_2}^T + \dot{\hat{\mathbf{b}}}_1 - \mathbf{p}_d^{(3)} - \hat{\mathbf{u}}^\star\right)^T \mathbf{z}_4, \hat{\mathbf{b}}_2\right),$$

achieves trajectory tracking by guaranteeing that the errors $\mathbf{z}_1$, $\mathbf{z}_2$, $\mathbf{z}_3$, *and* $\mathbf{z}_4$ *converge to zero for any initial condition verifying*

$$\sqrt{2V(0)} < g - (B + \epsilon) - \|\ddot{\mathbf{p}}_d(t)\|_\infty - \mathbf{u}^\star_{max},$$

where B *is the bound on the external disturbance,* $\|\cdot\|_\infty$ *denotes the supremum norm (also called infinity norm) of a function and* $\mathbf{u}^\star_{max}$ *is the upper bound on the virtual control law* $\mathbf{u}^\star(\mathbf{z}_1,\mathbf{z}_2)$*. Moreover, the disturbance estimate* $\hat{\mathbf{b}}_1$ *converges asymptotically to the unknown constant disturbance* $\mathbf{b}$.

Proof. The proposed control law (3.23) is well defined, in the conditions of Assumption 14. Starting with the positive definite Lyapunov function

$$V = \phi(\mathbf{z}_1)^T \mathbf{1} + \frac{1}{2}\Big(\Omega(\mathbf{z}_2 - \sigma(\mathbf{z}_1)) + \Omega(\sigma(\mathbf{z}_1))\Big)^T \Big(\Omega(\mathbf{z}_2 - \sigma(\mathbf{z}_1)) + \Omega(\sigma(\mathbf{z}_1))\Big) + \tfrac{1}{2}\mathbf{z}_3^T\mathbf{z}_3 + \tfrac{1}{2}\mathbf{z}_4^T\mathbf{z}_4 + \tfrac{1}{2k_b 1}\tilde{\mathbf{b}}_1^T\tilde{\mathbf{b}}_1 + \tfrac{1}{2k_b 2}\tilde{\mathbf{b}}_2^T\tilde{\mathbf{b}}_2,$$

and computing its time derivative, in closed-loop, we have that

$$\dot{V} \leq -\sigma(\mathbf{z}_1)^T\sigma(\mathbf{z}_1) - k_2\mathbf{z}_2^T\rho(\mathbf{z}_2) - k_3\mathbf{z}_3^T\mathbf{z}_3 - k_4\mathbf{z}_4^T\mathbf{z}_4,$$

which is a negative semi-definite function of the error states and the estimation errors, and is strictly negative definite with regard to the error states. Since the quadrotor error dynamics are non-autonomous, we resort to Barbalat's Lemma to prove convergence of $\dot{V}$ to zero. From the unboundedness of V with respect to the states $\mathbf{z}_1$, $\mathbf{z}_2$,$\mathbf{z}_3$, and $\mathbf{z}_4$ and the estimation errors $\tilde{\mathbf{b}}_1$ and $\tilde{\mathbf{b}}_2$, and observing that $\dot{V}$ is negative semi-definite, we conclude that the states, the estimates and estimation errors are bounded. Since $\dot{V}$ is semi-definite negative then the Lyapunov function is upper bounded by $V(0)$ for all time. From that fact and the definition of the error $\mathbf{z}_3$ it follows that $|\mathbf{z}_3| \leq \sqrt{2V(0)}$. Observing the bound on error $\mathbf{z}_3$, its definition (3.14) with (3.13), and property P1 of the smooth projection operator, we can establish the following conservative lower bound for the thrust input

$$|T| \geq m\Big(g - (B+\epsilon) - \|\ddot{\mathbf{p}}_d(t)\|_\infty - \mathbf{u}^\star_{\max} - \sqrt{2V(0)}\Big). \tag{3.24}$$

The external reference $\mathbf{p}_d$ and its derivatives are bounded by assumption and $\dot{\hat{\mathbf{b}}}_1$ and $\dot{\hat{\mathbf{b}}}_2$ are bounded from property P4 of the projection operator and boundedness of the error states and disturbance estimations. From the boundedness of the state $\mathbf{z}_3$, the definitions (3.13) and (3.14), and boundedness of the virtual control law (3.11), $\ddot{\mathbf{p}}$ and estimate $\hat{\mathbf{b}}_1$ we conclude that the thrust force T is bounded. From the definition (3.20) and boundedness of $\mathbf{z}_4$ we conclude that $\boldsymbol{\mu}$ is bounded if the initial error is within the conditions of the Theorem. Finally, boundedness of the time derivative $\dot{\mathbf{z}}_4$ follows from the boundedness of the states, estimates, and the terms in the control law (3.22). The estimate $\hat{\mathbf{h}}$ and the partial derivatives in (3.21) are bounded since they are smooth functions of the states and bounded external variables and have no singularities.

We have shown that in the conditions of the Theorem the control law (3.23) is well defined and $\ddot{V}$ is bounded, from which follows that the time derivative $\dot{V}$ is uniformly continuous. We can therefore apply Barbalat's Lemma to prove convergence of $\dot{V}$ to zero and, consequently, of the error states $\mathbf{z}_1$, $\mathbf{z}_2$, $\mathbf{z}_3$ and $\mathbf{z}_4$ to the origin.

Convergence of the estimate $\hat{\mathbf{b}}_1$ to $\mathbf{b}$ is a consequence of the convergence of the error states to the origin, the definition (3.14) and the dynamics equation (3.10). At the error system origin, we have $\mathbf{u}^\star = \mathbf{0}$. From (3.14) it follows that $\hat{\mathbf{u}} = \mathbf{0}$ and from (3.10) we get $\mathbf{u} = \mathbf{0}$, leading to the conclusion that the estimate $\hat{\mathbf{b}}_1$ converges to the real external disturbance $\mathbf{b}$. □

The rotational degree of freedom allowed for $\omega_3(t)$ in the control law (3.19), and subsequently for $\tau_3(t)$ in (3.23), by the term $S(\boldsymbol{\omega})\mathbf{e}_3$ in (3.16) is due to the axial symmetry exhibited by the quadrotor and can be exploited to control the heading of the vehicle independently of the trajectory tracking laws (3.19) or (3.23). An additional feature of the proposed actuation laws is that they depend only on bounded functions of the position error. This is a desirable property since the initial position error can be arbitrarily large and, without the saturation, would lead to physically infeasible control actuations.

The main drawback of both proposed trajectory tracking controllers is that they can only be applied if Assumption 14 holds. A conservative estimate of the initial states for which $T(t) \geq \epsilon$ is guaranteed for all $t > 0$ can be obtained using the definition of the backstepping error (3.14) together with the bounds for the errors and estimation derived from the Lyapunov function and its derivative. Using $\|\cdot\|_\infty$ to denote the maximum norm (also called infinity norm) of a function, we obtain the following lower bound for the thrust, for all $t > 0$,

$$|T(t)| \geq mg - (B + \epsilon) - \|\ddot{\mathbf{p}}_d(t)\|_\infty - \|\mathbf{u}^\star\|_\infty - \sqrt{2V(0)}.$$

If the initial conditions and desired trajectories are such that the lower bound for $|T(t)|$ is positive, then the thrust $T(t)$ that results from applying the proposed control law is guaranteed to take only positive or only negative values.

3.5 Experimental setup

In order to experimentally validate the proposed control algorithms a rapid prototyping and testing architecture was developed using a Matlab/Simulink environment to seamlessly integrate the sensors, the control algorithm and the communication with the vehicles. The vehicle used for the experiments is a radio controlled Blade mQX quadrotor [bla], depicted in Figure 3.1(a). This aerial vehicle is very agile and maneuverable, readily available and inexpensive, making it the ideal platform for implementing the controllers proposed in the present work. The quadrotor weighs 80 g with battery included and the arm length from the center of mass to each motor is 11 cm. The available commands are thrust force and angular velocity.

Due to the lack of support for onboard sensors, the state of the vehicle must be estimated through external sensors. In our setup we use a VICON T-Series optical motion capture system (OMCS) [VIC], comprising 12 cameras, together with markers attached to the quadrotor. The OMCS is able to accurately locate and estimate the positions of the markers, from which it obtains position and orientation measurements for the aircraft. The particular OMCS used for obtaining the experimental results is a high performance system, able to operate with sub-millimeter and sub-degree precision at up to 250 Hz. The performance is such that the linear velocity can be well estimated from the position measurements by a simple backwards Euler difference, with relatively low noise level. For the experimental setup, the state measurements from the motion capture system are obtained at 50 Hz, allowing for improved accuracy.

The vehicles use a 2.4 GHz wideband direct sequence spread spectrum (DSSS) signal to generate a robust radio link with on-channel interference resistance. This radio technology also allows for the simultaneous use of several vehicles in a confined space, enabling formation flight. The commercial off-the-shelf quadrotor vehicles are designed to be human piloted with remote controls but not directly from a computer. In order to be able to send commands to a quadrotor from a computer we identified the radio chip inside the remote control and connected the serial interface of the radio frequency (RF) module to a computer serial port. Figure 3.2 shows four disassembled RF modules which allow for an extension of the experimental setup to up to four vehicles flying simultaneously. To maintain the radio link, the radio transmitters must receive the control signals via serial port and send them to the vehicle once every 22.5 ms.

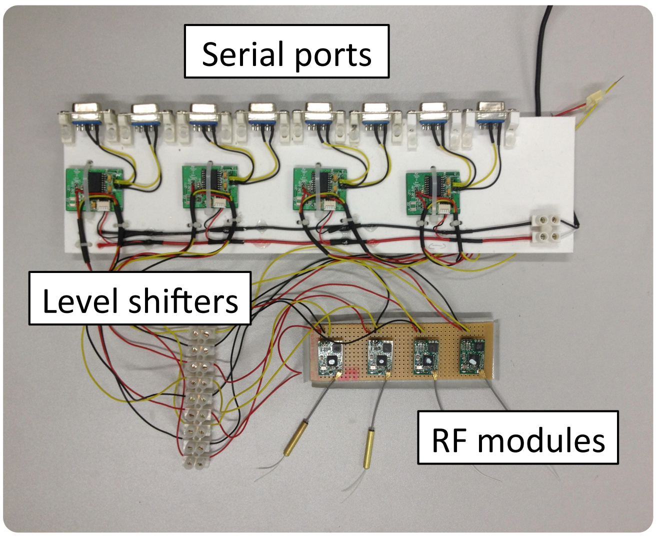

Figure 3.2: Serial port to RF interface used to generated the quadrotor radio control signals from a computer.

A graphical representation of the overall architecture is presented in Figure 3.3. We use two computer systems, one running the VICON motion tracking software and the Simulink model which generates the command signals sent to the other computer through an Ethernet connection; and a second one that receives the command signals and sends them through the serial port to the RF module at intervals of 22.5 ms. The decision to separate control and communications was made to avoid jitter in the transmission of the serial port signals to the RF module, which occurred when running all the systems in the same computer, and lead to erratic communication with the vehicle.

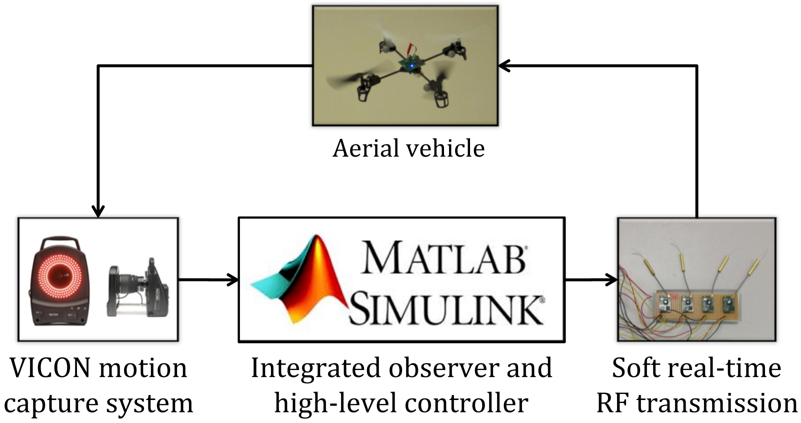

Figure 3.3: Quadrotor control architecture.

The Matlab/Simulink interface (see Figure 3.4) enables a fast iteration between simulation and experimental testing of control algorithms. A VICON block handles the reception of estimates from the motion capture system and outputs the quadrotor state; computation of the control signals is performed based on measured or simulated vehicle state; and the actuation signals are ultimately relayed to the second computer for radio transmission to the quadrotor or to a simulator block.

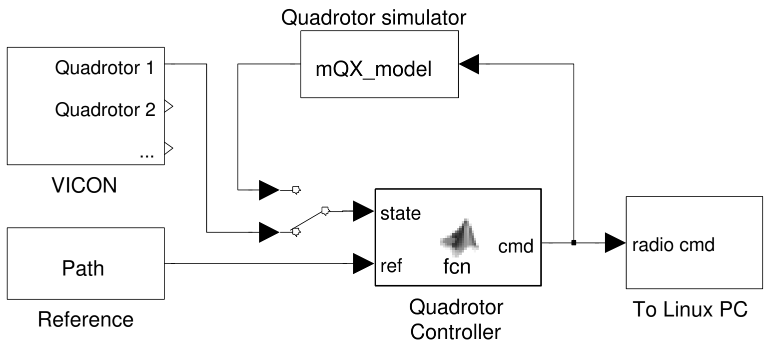

Figure 3.4: Simulink block diagram of the quadrotor controller featuring the alternative VICON sensor or quadrotor simulator, reference input, and output to the RF module.

Identification

Identification of the platform was performed by applying different constant commands over several experiments and measuring the thrust force and angular velocity response of the vehicle. The thrust force was measured by attaching weights to the quadrotor and finding the thrust command that balanced it. For the angular velocity a command was applied and the angular velocity measured directly with the motion capture system. The radio control system accepts commands in the range $[0,1]$ for the thrust and $[-1,1]$ for the angular velocities.

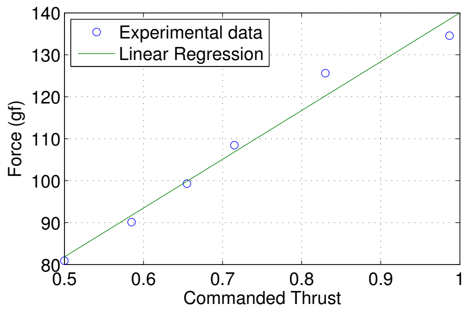

(a) Linear regression of thrust commands.

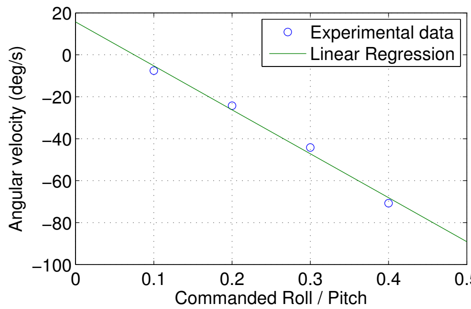

(b) Linear regression of roll commands.

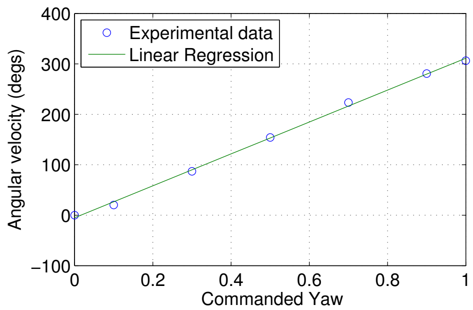

(c) Linear regression of yaw commands.

Figure 3.5: Quadrotor commands identification.

The identification results are presented in Figure 3.5. The radio control (RC) commands were found to relate linearly with the vehicle outputs. The maximum thrust generated by the propellers is then approximately 1.37 N (equivalent to 140 g) and varies slightly with the battery charge. Keeping in mind that the commands for angular velocity range between $[-1,1]$, the maximum angular velocity that can be commanded is 200 deg/s for the x and y axes and 300 deg/s for the z axis. However, the commands issued to the quadrotor are not instantaneously followed. This delay nonlinearity can be well approximated by considering the motors as first order dynamic systems with a pole at 1.5 Hz.

3.6 Experimental results

For the first experimental evaluation of the proposed controller we selected for the desired trajectory a lemniscate (figure eight) parameterized as

$$\mathbf{p}_d(t) = \frac{3}{2} R_x(-\pi/4) R_z(-\pi/6) \begin{bmatrix} \frac{\sin(\phi(t))\cos(\phi(t))}{\sin(\phi(t))^2+1} \\ \frac{\cos(\phi(t))}{\sin(\phi(t))^2+1} \\ 0 \end{bmatrix} + \begin{bmatrix} 0 \\ 0 \\ -1 \end{bmatrix},$$

where $\phi(t)$ obeys

$$\dot{\phi}(t) = V\sqrt{1+\sin^2 t}.$$

This parametrization results in a trajectory with unitary norm time derivative and constant desired speed for the quadrotor of V m/s.

The control law coefficients are $k_3 = 4$, $k_b = 1$, and the initial estimate $\hat{\mathbf{b}}(0)$ is set to zero. For the sigmoid function we use

$$\sigma(s) = \frac{M\,r\,s}{\sqrt{1+r^2 s^2}},$$

which has the bound $|\sigma(s)| \leq M$ and derivative at the origin $\sigma'(s) = r$, with $M = 1.5$ and $r = 3$. As yaw input action we use $\omega_3(t) = 0$.

A comparison between the reference trajectory, a lemniscate in an inclined plane described at a speed of $V = 1$ m/s, and the actual quadrotor trajectory is presented in Figure 3.6. The quadrotor is initially in a landed state, located approximately at the origin, and the initial reference position is approximately $(1, 1, -1.5)$. Both of these locations are identified by purple markers. The figure shows that the quadrotor trajectory converges to the reference trajectory in a straight fashion, without unnecessary trajectory deviations or changes of direction. After the initial transient, corresponding to the first haft of the figure eight, the position error is small, as evinced by the nearly identical reference and actual lemniscate trajectories.

The time evolution of the actual quadrotor position and of the reference is shown in Figure 3.7. The quadrotor follows closely the desired path with neglectible error in steady state. The trajectory tracking root mean square (RMS) error in steady state is 8.5 cm and the maximum error is 16.8 cm. The position error in steady state can be attributed to unmodeled dynamics of the plant and to the fact that the issued commands are not perfectly followed by the aircraft. The main contributions to the unmodeled dynamics are threefold: *i)* there exist unmodeled cross-couplings between the angular velocity commands and lateral forces acting on the quadrotor, due to an uneven and not perfectly symmetric mass distribution of the vehicle; *ii)* the issued thrust and angular velocity commands are not perfectly followed due to motor inertia and incorrect identification of

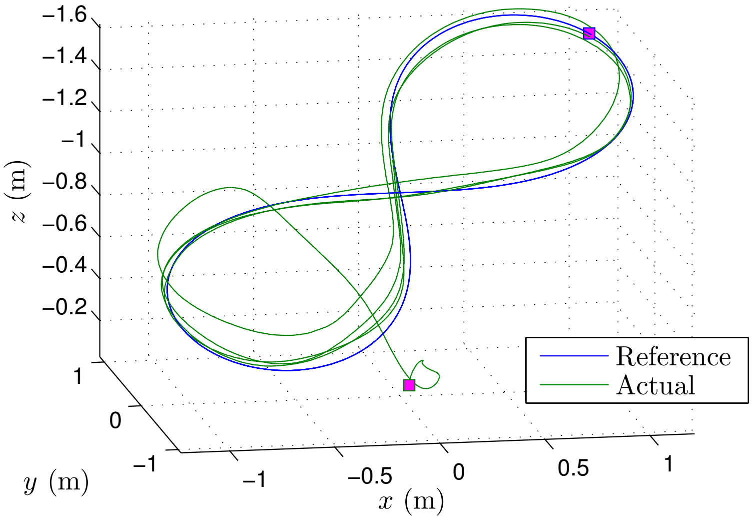

Figure 3.6: Comparison of the reference and vehicle trajectories.

the relationship between the thrust command and the generated thrust force; *iii)* there exist non-constant disturbances affecting the vehicle. Notice that the vehicle has a large initial position error, leading to the saturation function having a preponderant role in the control signal. Despite this unfavorable initial configuration, the actuation commands are kept within their performance limits (see Figure 3.9) and convergence to the reference trajectory occurs in just 5 seconds time, after which only small corrections are performed to the quadrotor trajectory.

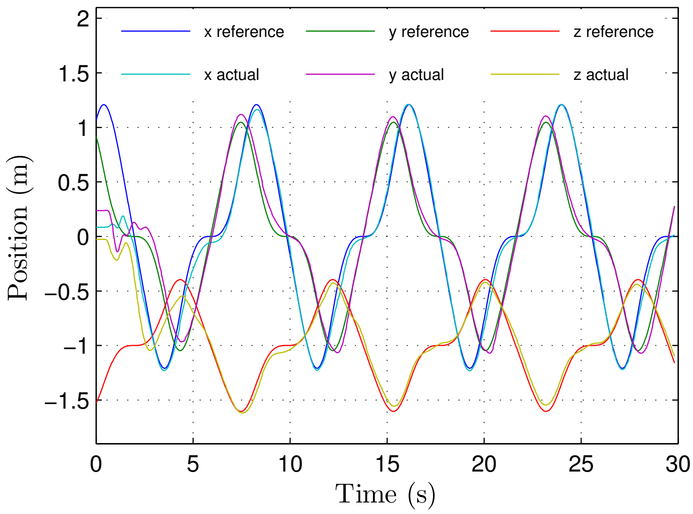

Figure 3.7: Time evolution of the position and reference signals.

Although the trajectory tracking experiment is performed on a closed division, with wind disturbances arising only from an air conditioning system, the effect of the integral action is evidenced on the vertical axis. After the initial transient, where the vertical error decreases rapidly, there is a slower approximation of the altitude to the desired one, until they match in steady state. This slower convergence is the result of the imposed integral action, through the disturbance estimator, which enables perfect theoretical tracking, even though the thrust command to thrust force relation is not perfectly known. The time evolution of the disturbance estimate is presented in Figure 3.8. Also visible is the convergence of the estimations of the lateral force errors, in average, to a constant value. These can arise either from uneven mass distribution of the quadrotor or from the fact that the motor and transmission gears have imperfections that result in different rotation velocities, for the same command signal. The estimation does not converge to a constant value but presents some periodic ripples. The ripples can be explained by the existence of unmodeled dynamics, which disturb the system. The period of the ripples is the same as the period of the trajectory, which is consistent with the unmodeled dynamics hypothesis.

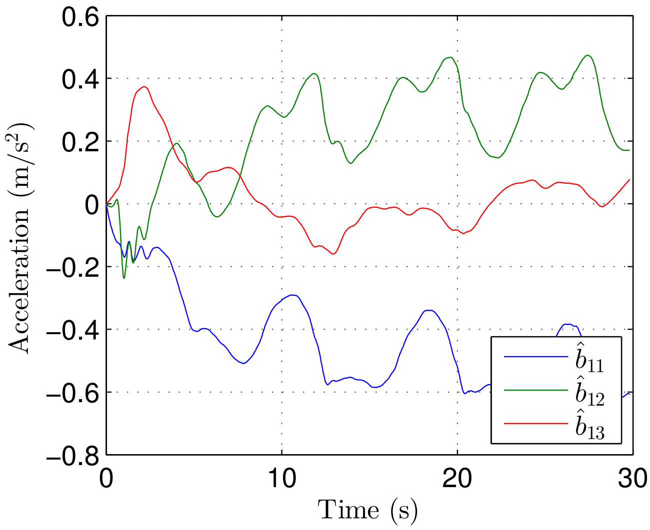

Figure 3.8: Force disturbance estimate.

The quadrotor actuation signals are depicted in Figure 3.9. The initial transient starts with a high thrust, to take the quadrotor to the desired height, and large angular velocity commands, to turn the quadrotor to the desired direction to minimize the errors. Once in steady state, the actuation signals are primarily the ones necessary to drive the controller through the reference trajectory, with only small corrections being performed according to the control law, without large variations. The effect of the integral action can also be seen in the thrust actuation, as it slowly increases with time, compensating for imprecisions in the conversion between commanded and actual thrust due to its variation with battery charge. Moreover, the thrust actuation is always well above zero and Assumption 14 holds for all the trajectory.

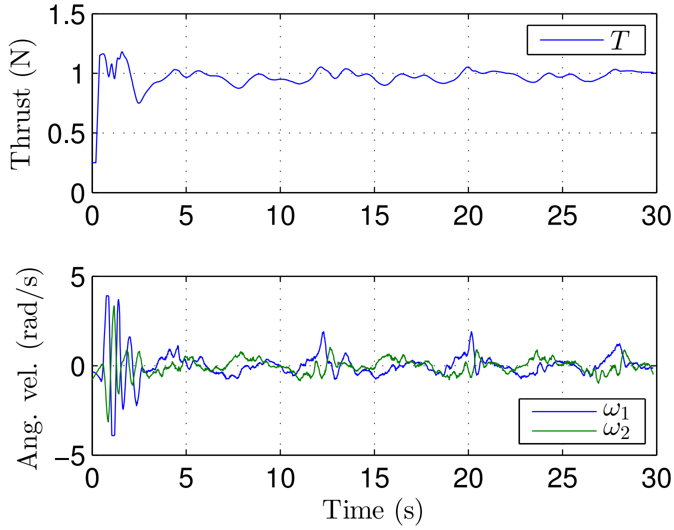

Figure 3.9: Time evolution of the actuation signals.

Finally, the time evolution of the backstepping errors is shown in Figure 3.10.

3.6.1 Torque actuation simulation

We also performed simulation runs of our proposed controller on a quadrotor actuated in torque and thrust. The quadrotor was modeled to be identical to the physical quadrotors. We consider a mass of $m = 0.080\,\text{kg}$, an inertia tensor $\mathbb{J} = \text{diag}(4.5, 4.5, 9) \cdot 10^{-4}\,\text{Nm}$, and motors with a pole at 1.5 Hz, which is not taken into account when developing the controller. The control law coefficients are $k_3 = 4$, $k_4 = 5$, $k_{b1} = k_{b2} = 1$, and the initial estimates $\hat{\mathbf{b}}_1(0)$ and $\hat{\mathbf{b}}_2(0)$ are set to zero. A disturbance $\mathbf{b} = \begin{bmatrix} 0.3 & 0.2 & 0.1 \end{bmatrix}^T$ was included in the simulation. For the sigmoid functions we use $\sigma(s) = \frac{M\,r\,s}{\sqrt{1+r^2s^2}}$, with $M = 1$ and $r = 1$ and $\rho(s) = \frac{M\,r\,s}{\sqrt{1+r^2s^2}}$, with $M = 1$ and $r = 2$. As yaw input action we use $\tau_3(t) = 0$.

Figures 3.11 and 3.12 show comparisons of the reference and actual trajectories, along space and time. The figures are similar to the ones obtained experimentally, with convergence to the trajectory being attained in around the 7 seconds mark, or equivalently, after one lap around the figure eight. Due to the unmodeled vehicle dynamics, resulting from characterizing the motors as first-order dynamic systems, the trajectory convergence is not perfect. Small residual errors can be observed even in steady state, and are evidenced more clearly in Figure 3.13, showing the time evolution of the backstepping errors. Despite the unmodeled dynamics the RMS position error is only 3.4 cm and the maximum error is 7.0 cm.

Observing Figure 3.14, one can perceive that the estimate $\hat{\mathbf{b}}_1$ converges to the real value $\mathbf{b}$ and there is not much influence due to the unmodeled dynamics. The second estimate on the other hand, is highly affected by motor dynamics, due to its dynamic proximity. The estimate $\hat{\mathbf{b}}_1$ would have converged to the actual disturbance, $\hat{\mathbf{b}}_1 = \mathbf{b}$, in the absence of motor dynamics, as shown in Theorem 16.

The time evolution of the quadrotor actuation is depicted in Figure 3.15. Again, a transient is clearly visible in the first seconds of simulation, where the thrust and torque vary rapidly, until the vehicle is settled close to the desired trajectory. The actuation values for the transient are within the normal values for the steady state and the singularity $T = 0$ is not approached, even during the transient.

3.7 Concluding remarks

This chapter presented a state feedback solution to the problem of stabilizing an underactuated quadrotor vehicle along a predefined trajectory in the presence of constant force disturbances. A Lyapunov function for the system was derived using adaptive backstepping techniques and made possible by dynamic extension of the actuation. A pair of sufficiently smooth estimators were introduced so as to compensate for the force disturbance and add integral action to the system. Control solutions for different levels of actuation control, angular velocity and torque, depending on the aircraft, were proposed and tested.

Experimental data for trajectory tracking applied to a small-scale quadrotor vehicle was presented which evidenced the effects of the adaptive action and demonstrated the robustness and performance of the proposed control law. Realistic simulation data using a non-ideal torque and thrust actuated quadrotor model is also presented, where the robustness and performance of the proposed controllers with sufficiently smooth estimators were assessed.

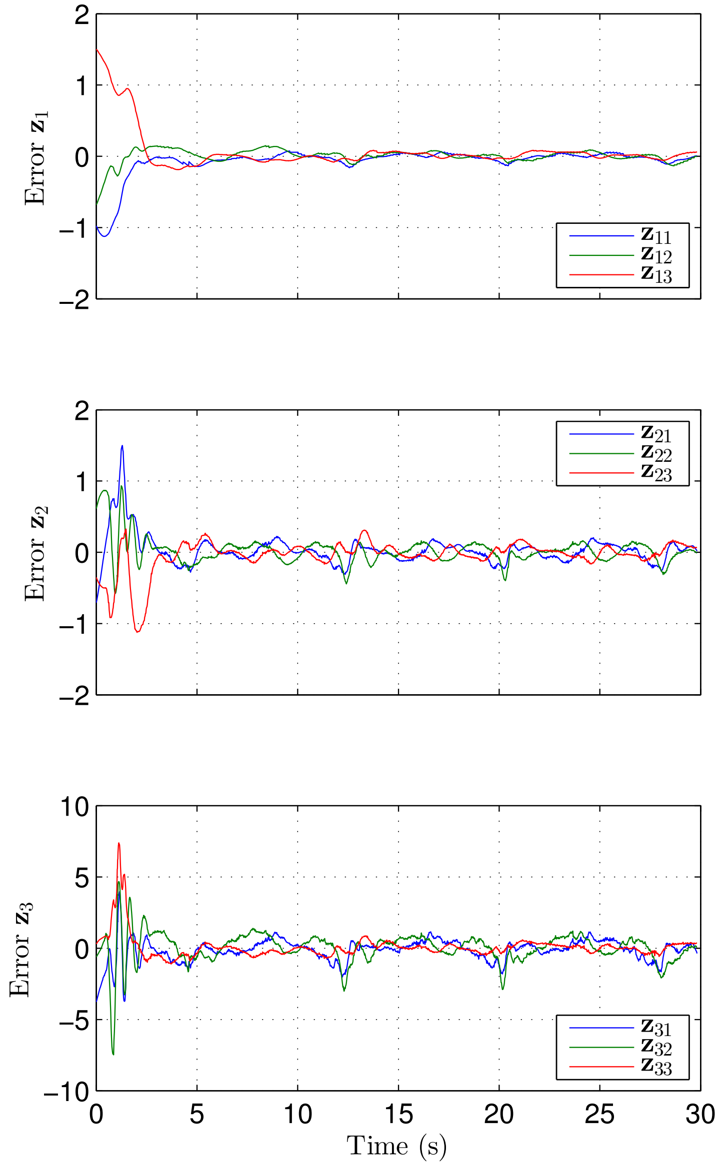

Figure 3.10: Time evolution of the error signals.

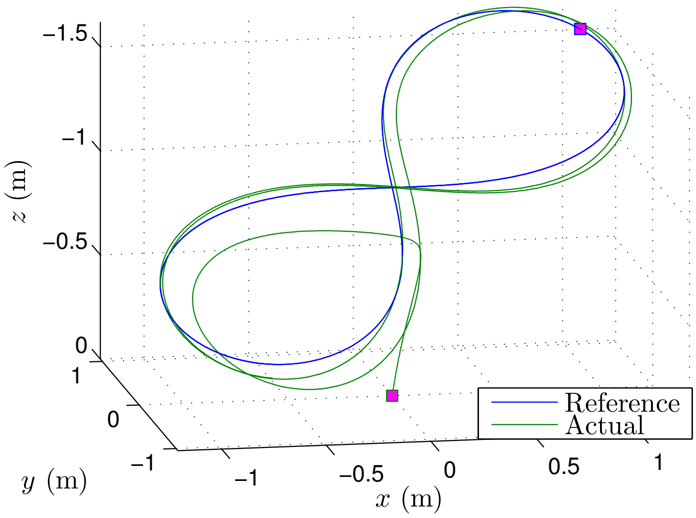

Figure 3.11: Comparison of the reference and vehicle trajectories.

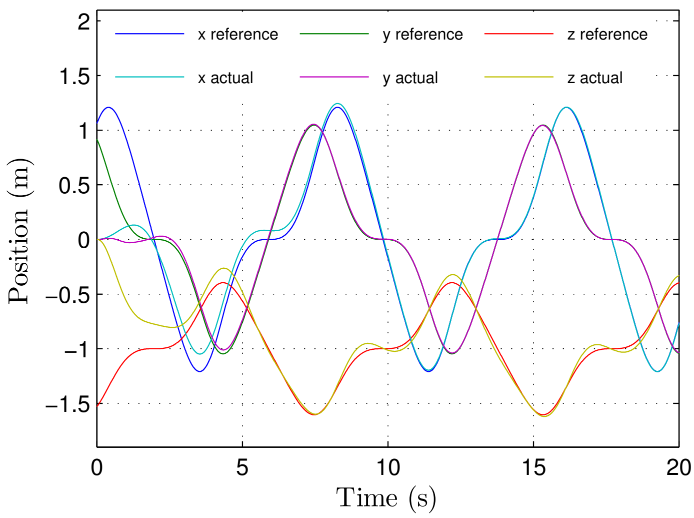

Figure 3.12: Time evolution of the position and reference signals.

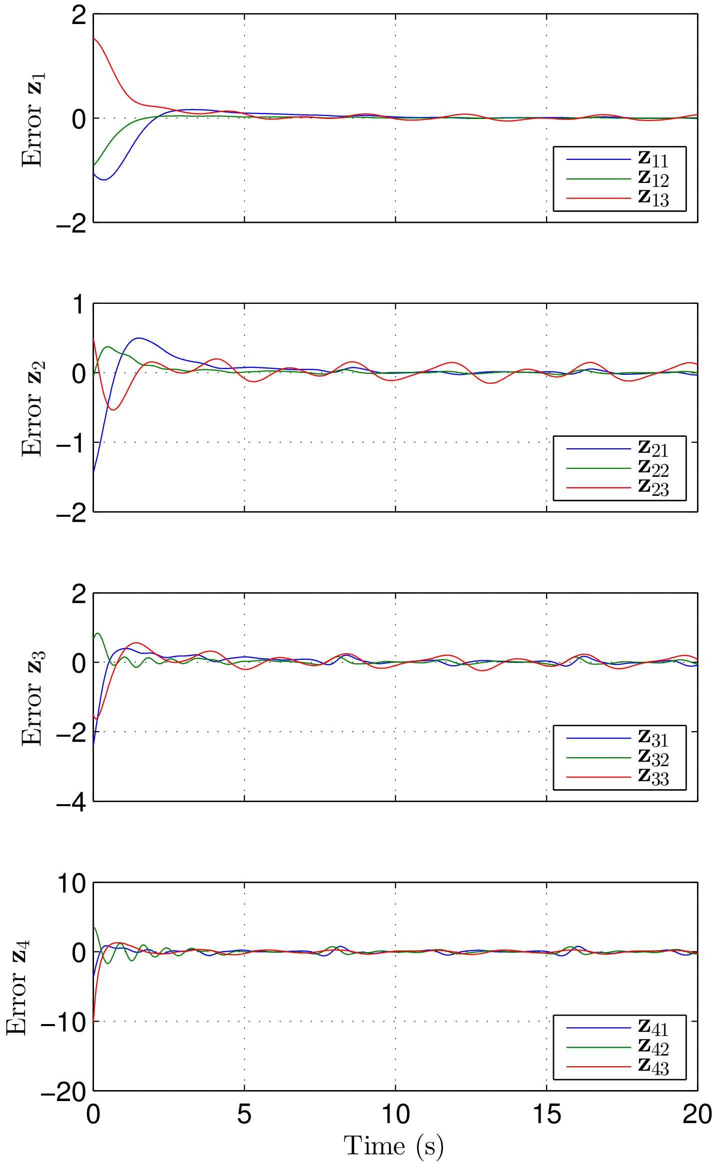

Figure 3.13: Time evolution of the error signals.

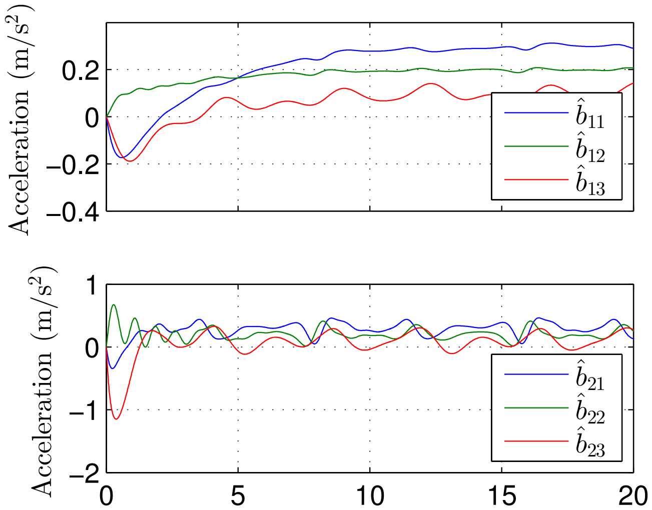

Figure 3.14: Force disturbance estimate.

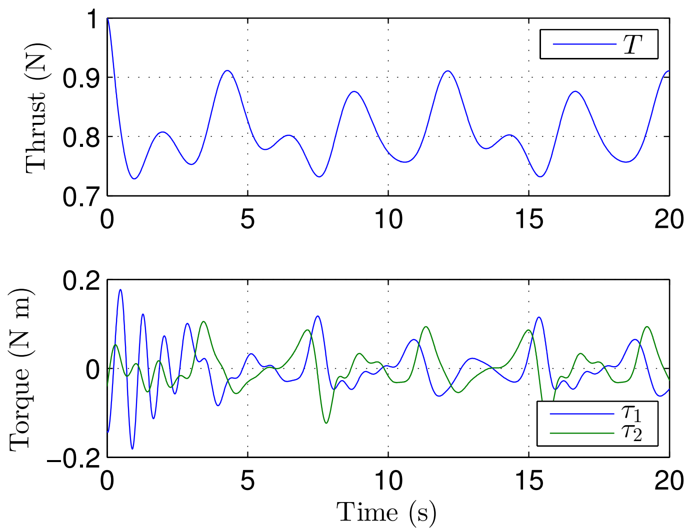

Figure 3.15: Time evolution of the actuation signals.

4

Rotorcraft path following control for extended flight envelope coverage

This chapter addresses the design and experimental evaluation of a global controller to steer a quadrotor vehicle along a predefined path. The global quadrotor controller can be seen as an adaptation or extension of the controller proposed in the previous chapter, for which only local stability properties could be proven. The problem is formulated so as to enforce bounds on the actuation while guaranteeing robustness against constant wind disturbances. The proposed solution consists of a nonlinear adaptive state feedback controller for thrust and torque actuation that *i)* guarantees global convergence of the closed-loop path following error to zero in the presence of constant wind disturbances and *ii)* ensures that the actuation does not grow unbounded as a function of the position error. Simulation results and experimental results, which include a hovering flight in the slipstream of a mechanical fan, are presented to assess the performance and robustness of the proposed controller.

4.1 Introduction

The trajectory tracking controllers proposed in [FDF00, MH04] and in Chapter 3 build on the dynamic augmentation principle of appending two integrators to the thrust input. The control laws are valid as long as non-zero thrust is applied at all times, meaning that zero thrust situations must not arise when the vehicle is perfectly tracking the desired trajectory neither when moving towards it. Since in the aforementioned controllers the thrust is commanded by its second time derivative, it becomes difficult to determine the set of initial conditions that do not lead to zero thrust commands while the vehicle is converging to the path. An upper bound on the Lyapunov function initial value can be computed that guarantees non-zero thrust for the whole trajectory. However, that bound is extremely conservative and can impose restrictions on the initial conditions that are too strict. Global trajectory tracking controllers have been proposed in [HHMS09] and [RT11] but conservative conditions on the allowable control action are required to keep the thrust force positive that lead to a significant reduction in thrust force available specifically for vehicle control. The addition of adaptive control to reject external perturbations further reduces the effective component of the control action.

The thrust singularity is inherent to the quadrotor dynamics and prevents the design of (almost) global asymptotically stabilizing controllers. It arises whether the thrust is directly controlled or whether the second derivative of the thrust is used as control input. To lift the non-zero thrust restriction and thereby obtain a globally defined controller, we consider the problem of path following [MS08]. As an alternative to trajectory tracking, path following solutions typically result in smoother convergence to the path and less demand on the control effort. A common approach to the path following problem is to parameterize the desired path using a scalar variable, such as the arc-length, and then select a timing law for that parameter [SK07, AHK08].

Robustness to external disturbances is crucial for aerial vehicles as, in typical operating conditions, they are subject to wind and possibly unknown payload distributions, which make the vehicles deviate from their nominal model. Several approaches have been proposed for aerial vehicles to deal with disturbances. The control approach proposed in [ANT11] is based on linearization and piecewise affine approximations and the controlled output is attitude and not position. In the experimental setting, the wind disturbance is generated by a set of electrical fans, whose airflow is passed through a pipe-system, rendering the flow affecting the quadrotor laminar and less turbulent. The works [JJT12] and [NMRS11] propose controllers for attitude robust to external disturbances. In both cases experimental results are presented but the considered disturbances include only unknown parameters or payloads. Trajectory tracking controllers that render aerial vehicles robust to external disturbances are considered in [HHMS09], [KMAO12], and [ROR10], but these works present only simulation results.

We explore the extra degree of freedom provided by the path following law (as opposed to a trajectory tracking law) to obtain global convergence to the path without any singularities. The desired path is specified by a sufficiently smooth parameterized 3-D curve. The attitude of the vehicle is naturally prescribed (up to a rotation about the body z axis) by solving the path following problem. During the controller design, the attitude is handled in its natural space, the Special Orthogonal group SO(3), as a rotation matrix. This avoids the introduction of artifacts related only to the parameterization of SO(3), as is the case of singularities with Euler angles and multiple coverings with the quaternion representation [BB00].

The main contribution of this chapter is the design of a robust global path following control law and the development of an experimental setup for rapid testing and tuning in a real vehicle. The control law is not subject to restrictions on the thrust magnitude or the desired thrust direction, is bounded in the position error, and rejects constant force disturbances, as is the case of constant wind or model uncertainties such as imperfect knowledge of the mass of the vehicle. To ensure that the actuation does not grow unbounded as a function of the distance to the path, which initially can be arbitrarily large, a saturation function is applied to the position errors used for feedback. We show that, for a large class of sufficiently smooth reference path curves, the resulting control law guarantees global convergence of the path following error to zero. Although the complementary control techniques are not new, their joint application to obtain a globally stabilizing path following controller for a quadrotor is a novel contribution to this topic. The experimental evaluation of the control law is performed in a setup integrating the quadrotor vehicle, sensors, and radio communication with a quadrotor simulator, allowing for fast iterations between simulation and testing that expedite the process of tuning the controller gains.

This chapter is structured as follows: The proposed problem and control objective are stated in Section 4.2. Controller design is described in Section 4.3. Experimental and simulation results illustrating the performance and robustness of the proposed control laws are presented in Section 4.4 and Section 4.5 summarizes the contents of the chapter.

4.2 Problem statement

Let the desired path $\mathbf{p}_d(\gamma) \in \mathbb{R}^3$ be a curve of class at least C^4, parametrized by $\gamma \in \mathbb{R}$. The control objective consists of designing a control law for the quadrotor actuations $T(t)$ and $\boldsymbol{\tau}(t)$ and a timing law for the path parameter $\gamma(t)$ that ensures convergence of the vehicle's position $\mathbf{p}(t)$ to the path $\mathbf{p}_d(\gamma)$ with the largest possible basin of attraction. Throughout the remainder of the chapter, the time dependence of variables is often omitted to lighten notation.

Although for the path following problem the vehicle's velocity is not required to converge to a given signal, its progression along the path can be controlled through an adequate choice of the timing law $\gamma(t)$. As a secondary control objective, $\dot{\gamma}$ is required to follow a given reference velocity profile $\dot{\gamma}_r(t)$.

We consider the full state of the vehicle to be available for feedback. For the experimental results the full state is provided by a high speed OMCS, based on a set of external cameras tracking reflective markers on the vehicle, as described in section 3.6.

4.3 Controller design

In order to accomplish the path following objective, we now perform the following change of variables, where the new variables correspond to the inertial position and velocity errors

$$\mathbf{z}_1 = \mathbf{p} - \mathbf{p}_d(\gamma), \tag{4.1a}$$

$$\mathbf{z}_2 = R\mathbf{v} - \dot{\mathbf{p}}_d, \tag{4.1b}$$

with derivatives given by

$$\dot{\mathbf{z}}_1 = \mathbf{z}_2, \tag{4.2a}$$

$$\dot{\mathbf{z}}_2 = -\tfrac{T}{m}R\mathbf{e}_3 + g\mathbf{e}_3 - \ddot{\mathbf{p}}_d + \mathbf{b}. \tag{4.2b}$$

This subsystem can be regarded as three independent double integrators, each one driven by one of the entries of the input vector $-\frac{T}{m}R\mathbf{e}_3 + g\mathbf{e}_3 - \ddot{\mathbf{p}}_d + \mathbf{b}$.

To devise a control law that steers the aerial vehicle along the path $\mathbf{p}_d(\gamma)$ we consider a two stage process. First, a *virtual controller*, with certain properties, is designed for the translational subsystem without taking into account the dynamic specificities of the quadrotor. Starting with this double integrator controller as an initial solution, the input error resulting from the vehicle underactuation is backstepped through the rotational subsystem until a control law for the angular velocity or torque actuation is reached.

Let $\mathbf{u}^\star$ be a state feedback controller for a three dimensional double integrator system with states $\mathbf{x}_1$ and $\mathbf{x}_2$ that, for a Lyapunov function $V_{DI}(\mathbf{x}_1,\mathbf{x}_2)$, renders its closed-loop time derivative a strictly negative definite function $\dot{V}_{DI}(\mathbf{x}_1,\mathbf{x}_2) = -W_{DI}(\mathbf{x}_1,\mathbf{x}_2) < 0$. An example of such a controller was presented in chapter 3. In addition, an example of a more general controller for a double integrator can be found in appendix A and is easily extended for the multidimensional case by noting that all three double integrators are independent. We now apply the double integrator Lyapunov function to the error system (4.2) and add an additional term to mitigate the effect of the unknown disturbance on a first level. This results in the tentative Lyapunov function for the entire quadrotor system

$$V_1 = V_{DI}(\mathbf{z}_1,\mathbf{z}_2) + \int_0^{\|\mathbf{z}_0\|} \sigma(\tau)\,\mathrm{d}\tau + \int_0^{\|\mathbf{b}\|} \sigma^{-1}(\tau) - \mathbf{b}^T\mathbf{z}_0 \tag{4.3}$$

with time derivative

$$\dot{V}_1 = -W_{DI}(\mathbf{z}_1,\mathbf{z}_2) + \frac{\partial V_{DI}}{\partial \mathbf{z}_2}\Big(-\tfrac{T}{m}R\mathbf{e}_3 - \mathbf{u}^\star + g\mathbf{e}_3 - \ddot{\mathbf{p}}_d + \sigma(\mathbf{z}_0)\Big), \tag{4.4}$$

where $\mathbf{z}_0$ is an integral state given by

$$\mathbf{z}_0 = \int_0^t \frac{\partial V_{DI}}{\partial \mathbf{z}_2}^T.$$

The addition of the integral terms to the Lyapunov function draws inspiration from [HHMS09] and is used to cancel out the external disturbance in the Lyapunov derivative and add a bounded integral term to the desired thrust direction. Positive definiteness of the Lyapunov function with respect to $\mathbf{z}_0$ comes from a particular application of Young's inequality

$$\mathbf{b}^T\mathbf{z}_0 \leq \|\mathbf{b}\|\|\mathbf{z}_0\| \leq \int_0^{\|\mathbf{z}_0\|} \sigma(\tau)\mathrm{d}\tau + \int_0^{\|\mathbf{b}\|} \sigma^{-1}(\tau)\mathrm{d}\tau,$$

where σ is a saturation function and σ^{-1} is its inverse.

Partitioning the rotation matrix in column vectors as $R = [\mathbf{r}_1\ \mathbf{r}_2\ \mathbf{r}_3]$, the thrust control law is designed as

$$T = T_d\mathbf{r}_{3d}^T\mathbf{r}_3, \tag{4.5}$$

where the desired thrust T_d and desired thrust direction $\mathbf{r}_{3d}$ depend on the double integrator stabilizing virtual force

$$F_d = m(-\mathbf{u}^\star + g\mathbf{e}_3 - \ddot{\mathbf{p}}_d + \sigma(\mathbf{z}_0)) \tag{4.6}$$

and are defined as

$$T_d = \|F_d\|, \quad \mathbf{r}_{3d} = \frac{F_d}{\|F_d\|}. \tag{4.7}$$

The closed-loop derivative (4.4) can be rewritten as

$$\dot{V}_1 = -W_{DI}(\mathbf{z}_1, \mathbf{z}_2) - \frac{T_d}{m}\frac{\partial V_{DI}}{\partial \mathbf{z}_2}S(\mathbf{r}_3)^2\mathbf{r}_{3d},$$

where the vector $S(\mathbf{r}_3)^2\mathbf{r}_{3d}$ belongs to the plane perpendicular to the thrust direction and can be regarded as an input error due to the under-actuation of the translational subsystem. An illustration of the vectors involved is provided in Figure 4.1.

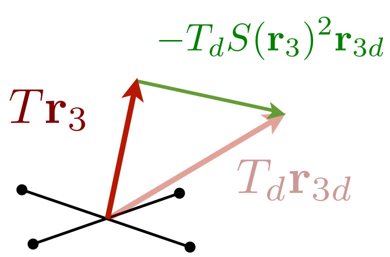

Figure 4.1: The thrust actuation, desired thrust vector, and the corresponding vector error.

When the thrust is aligned with the desired direction, i.e. $\mathbf{r}_3 = \mathbf{r}_{3d}$, the input error is zero and regulation to zero of the path following error is achieved. The error between the desired and the actual thrust direction can be written in vector form as

$$\mathbf{z}_3 = \mathbf{r}_3 - \mathbf{r}_{3d},$$

or as an angular error z_θ given by the relation

$$\cos z_\theta = \mathbf{r}_3^T\mathbf{r}_{3d}. \tag{4.8}$$

We now extend the tentative Lyapunov function to include the angular error as follows

$$V_2 = V_1 + \tfrac{1}{2k_a}\mathbf{z}_3^T\mathbf{z}_3 + \tfrac{1}{2k_{b1}}\tilde{\mathbf{b}}_1^T\tilde{\mathbf{b}}_1 = V_1 + \tfrac{1}{k_a}(1-\mathbf{r}_3^T\mathbf{r}_{3d})) + \tfrac{1}{2k_{b1}}\tilde{\mathbf{b}}_1^T\tilde{\mathbf{b}}_1,$$

and compute its closed-loop derivative as

$$\begin{aligned}\dot{V}_2 = -W_2(\mathbf{z}_1, \mathbf{z}_2, z_\theta) + \mathbf{r}_{3d}^T RS(\mathbf{e}_3)\left(\tfrac{1}{k_a}(\boldsymbol{\omega} - R^T S(\mathbf{r}_{3d})\widehat{\dot{\mathbf{r}}_{3d}}) - S(\mathbf{e}_3)R^T\left(\frac{T_d}{m}\frac{\partial V_{DI}}{\partial \mathbf{z}_2}^T + k_3\mathbf{r}_{3d}\right)\right) \\ - \tilde{\mathbf{b}}_1^T\left(\tfrac{1}{k_a}\frac{\partial \mathbf{r}_{3d}}{\partial \mathbf{z}_2}S(\mathbf{e}_3)R^T\mathbf{r}_{3d} + \tfrac{1}{k_{b1}}\dot{\hat{\mathbf{b}}}_1\right), \quad (4.9)\end{aligned}$$

where k_a, k_3 are positive control gains and W_2 is a positive definite function, given by

$$W_2(\mathbf{z}_1, \mathbf{z}_2, z_\theta) = W_{DI}(\mathbf{z}_1, \mathbf{z}_2) + k_3 \sin^2 z_\theta.$$

For W_2 we used the relation $-\mathbf{r}_{3d}^T S(\mathbf{r}_3)^2\mathbf{r}_{3d} = \sin^2 z_\theta$.

The symbol $\widehat{\dot{\mathbf{r}}_{3d}}$ represents the estimate of the time derivative of $\mathbf{r}_{3d}$ obtained by using the estimate $\hat{\mathbf{b}}_1$ of the external disturbance instead of $\mathbf{b}$, when performing the necessary calculations. The estimation error is given by

$$\dot{\mathbf{r}}_{3d} - \widehat{\dot{\mathbf{r}}_{3d}} = \left(\frac{\partial \mathbf{r}_{3d}}{\partial \mathbf{z}_2}\right)^T \tilde{\mathbf{b}}_1.$$

For quadrotors controlled in angular velocity we can, at this stage, set the actuation $\boldsymbol{\omega}$ such that (4.9) is negative semi-definite, as detailed subsequently in Lemma 18. For vehicles with actuation in torque we introduce the last backstepping error

$$\mathbf{z}_4 = -S(\mathbf{e}_3)^2\left(\tfrac{1}{k_a}(\boldsymbol{\omega} - R^T S(\mathbf{r}_{3d})\widehat{\dot{\mathbf{r}}_{3d}}) - S(\mathbf{e}_3)R^T\left(\frac{T_d}{m}\frac{\partial V_{DI}}{\partial \mathbf{z}_2}^T + k_3\mathbf{r}_{3d}\right)\right) \quad (4.10)$$

and the new Lyapunov function and its time derivative,

$$\begin{aligned}V &= V_2 + \tfrac{1}{2}\mathbf{z}_4^T\mathbf{z}_4 + \tfrac{1}{k_{b2}}\tilde{\mathbf{b}}_2^T\tilde{\mathbf{b}}_2, \\ \dot{V} &= -W_3(\mathbf{z}_1, \mathbf{z}_2, \sin z_\theta, \mathbf{z}_4) - \mathbf{z}_4^T S(\mathbf{e}_3)^2(\tfrac{1}{k_a}\boldsymbol{\tau} + \hat{\mathbf{h}} + k_4\mathbf{z}_4 + S(\mathbf{e}_3)R^T\mathbf{r}_{3d}) \\ &\quad - \tilde{\mathbf{b}}_1^T\left(\tfrac{1}{k_a}\frac{\partial \mathbf{r}_{3d}}{\partial \mathbf{z}_2}S(\mathbf{e}_3)R^T\mathbf{r}_{3d} + \tfrac{1}{k_{b1}}\dot{\hat{\mathbf{b}}}_1\right) + \tilde{\mathbf{b}}_2^T\left(\frac{\partial \mathbf{z}_4}{\partial \mathbf{z}_2}\mathbf{z}_4 - \tfrac{1}{k_{b2}}\dot{\hat{\mathbf{b}}}_2\right)\end{aligned}$$

where $W_3(\mathbf{z}_1, \mathbf{z}_2, \sin z_\theta, \mathbf{z}_4) = W_2(\mathbf{z}_1, \mathbf{z}_2, \sin z_\theta) + k_4\mathbf{z}_4^T\mathbf{z}_4$ is a positive definite function and $\hat{h}$ is an estimate of

$$\mathbf{h} = -S(\mathbf{e}_3)^2\frac{d}{dt}\left(-\tfrac{1}{k_a}R^T S(\mathbf{r}_{3d})^2\widehat{\dot{\mathbf{r}}_{3d}} - S(\mathbf{e}_3)R^T\left(\tfrac{T_d}{m}\frac{\partial V_{DI}}{\partial \mathbf{z}_2}^T + k_3\mathbf{r}_{3d}\right)\right). \quad (4.11)$$

As previously with $\dot{\mathbf{r}}_{3d}$, the quantity $\mathbf{h}$ depends on the unknown disturbance $\mathbf{b}$. Applying the same procedure, we denote as $\hat{\mathbf{h}}$ the estimate obtained by using the estimate $\hat{\mathbf{b}}_2$ instead of the unknown disturbance. The resulting estimation error is

$$\tilde{\mathbf{h}} = \mathbf{h} - \hat{\mathbf{h}} = \left(\frac{\partial \mathbf{z}_4}{\partial \mathbf{z}_2}\right)^T \tilde{\mathbf{b}}_2.$$

We can now use the remaining actuation $\boldsymbol{\tau}$ and the estimation laws $\dot{\hat{\mathbf{b}}}_1$ and $\dot{\hat{\mathbf{b}}}_2$ to render $\dot{V}$ negative semidefinite and achieve convergence of the path following error to zero. We state this formally in Lemma 17, assuming that the control law is well-defined. In the next section we show how the timing law can be chosen so that the control law is always well-defined, meaning that the expression for F_d given in (4.6) never reaches zero.

Lemma 17. *Let the quadrotor kinematics and dynamics be described by* (3.1)-(3.4), *let* $\mathbf{p}_d(\gamma(t)) \in C^4$ *be the desired trajectory, and consider the transformation to error coordinates* $\mathbf{z}_1$, $\mathbf{z}_2$, z_θ, $\mathbf{z}_4$ *given by* (4.1a), (4.1b), (4.8), (4.10), *respectively. For any bounded* $\tau_3(t) \in C^1$, *the closed-loop system that results from applying the input transformation* (3.6), *the control laws* (4.5), *the torque*

$$\boldsymbol{\tau} = k_a S(\mathbf{e}_3)^2 \left(\hat{\mathbf{h}} - S(\mathbf{e}_3) R^T \mathbf{r}_{3d} + k_4 \mathbf{z}_4\right) + \tau_3(t)\mathbf{e}_3, \tag{4.12}$$

and the estimator laws

$$\dot{\hat{\mathbf{b}}}_1 = -\tfrac{k_{b1}}{k_a} \frac{\partial \mathbf{r}_{3d}}{\partial \mathbf{z}_2} S(\mathbf{e}_3) R^T \mathbf{r}_{3d}, \quad \dot{\hat{\mathbf{b}}}_2 = k_{b2} \frac{\partial \mathbf{z}_4}{\partial \mathbf{z}_2} \mathbf{z}_4,$$

achieves global trajectory tracking, by guaranteeing that the errors $\mathbf{z}_1$ *and* $\mathbf{z}_2$ *converge to zero for any initial condition. In addition, the error vector* $(\mathbf{z}_1, \mathbf{z}_2, z_\theta, \mathbf{z}_4)$ *converges to one of the equilibrium points in the set* $\{(\mathbf{0}, \mathbf{0}, 0, \mathbf{0}), (\mathbf{0}, \mathbf{0}, \pi, \mathbf{0})\}$ *and the desired equilibrium point* $(\mathbf{z}_1, \mathbf{z}_2, z_\theta, \mathbf{z}_4) = (\mathbf{0}, \mathbf{0}, 0, \mathbf{0})$ *is uniformly asymptotically stable.*

Proof. We assume that the control law is well defined, i.e. $T_d \neq 0$. Starting with the positive definite Lyapunov function

$$V = V_{DI} + \int_0^{\|\mathbf{z}_0\|} \sigma(\tau)\,\mathrm{d}\tau + \int_0^{\|\mathbf{b}\|} \sigma^{-1}(\tau)\mathrm{d}\tau - \mathbf{b}^T \mathbf{z}_0 + \tfrac{1}{k_a}(1 - \cos z_\theta) + \tfrac{1}{2}\mathbf{z}_4^T \mathbf{z}_4 + \tfrac{1}{2k_{b1}} \tilde{\mathbf{b}}_1^T \tilde{\mathbf{b}}_1 + \tfrac{1}{2k_{b2}} \tilde{\mathbf{b}}_2^T \tilde{\mathbf{b}}_2,$$

and computing its time derivative we have that

$$\dot{V} = -W_{DI}(\mathbf{z}_1, \mathbf{z}_2) - k_3 \sin^2 z_\theta - k_4 \mathbf{z}_4^T \mathbf{z}_4$$

is a negative semidefinite function. Since the quadrotor error dynamics are non-autonomous, we resort to Barbalat's Lemma to prove convergence of $\dot{V}$ to zero. From the unboundedness of V with respect to $\mathbf{z}_1$, $\mathbf{z}_2$, $\mathbf{z}_4$, $\tilde{\mathbf{b}}_1$ and $\tilde{\mathbf{b}}_2$, and observing that $\dot{V}$ is negative semi-definite, we conclude that the states $\mathbf{z}_1$, $\mathbf{z}_2$, $\mathbf{z}_4$, $\tilde{\mathbf{b}}_1$ and $\tilde{\mathbf{b}}_2$ are bounded. The state z_θ evolves in a compact set. The external inputs $\tau_3(t)$ and $\mathbf{p}_d^{(4)}$ are bounded by assumption and boundedness of the auxiliary function (4.11) comes from boundedness of the errors and estimates. We have thus that $\ddot{V}$ is bounded and, consequently, $\dot{V}$ is uniformly continuous. We can therefore apply Barbalat's Lemma to prove convergence of $\dot{V}$ to zero and, consequently, of the states $\mathbf{z}_1$, $\mathbf{z}_2$, and $\mathbf{z}_4$ to the origin and of z_θ to the set $\{0, \pi\}$. The closed-loop trajectories

$(\mathbf{z}_1(t), \mathbf{z}_2(t), z_\theta(t), \mathbf{z}_4(t))$ converge to the invariant set $\{(\mathbf{0},\mathbf{0},0,\mathbf{0}),(\mathbf{0},\mathbf{0},\pi,\mathbf{0})\}$ or, equivalently, the closed-loop trajectories $(\mathbf{z}_1,\mathbf{z}_2,\mathbf{z}_3,\mathbf{z}_4)$ converge to the set $\{(\mathbf{0},\mathbf{0},\mathbf{0},\mathbf{0}),(\mathbf{0},\mathbf{0},-2\mathbf{e}_3,\mathbf{0})\}$. For initial conditions such that $V(0) < 2k_a$, the time derivative of V is negative definite, meaning that the origin is uniformly asymptotically stable. □

For the sake of completeness, we rewrite now Lemma 18 for quadrotors actuated in angular velocity. The proof is omitted as its arguments follow closely those of the Proof for Lemma 17.

Lemma 18. *Let the quadrotor kinematics and dynamics be described by* (3.1)-(3.3), *let* $\mathbf{p}_d(\gamma(t)) \in C^3$ *be the desired trajectory, and consider the transformation to error coordinates* $\mathbf{z}_1$, $\mathbf{z}_2$, z_θ *given by* (4.1a), (4.1b), (4.8), *respectively. For any bounded* $\omega_3(t) \in C^1$, *the closed-loop system that results from applying the control laws* (4.5),

$$\boldsymbol{\omega} = -S(\mathbf{e}_3)^2\left(R^T S(\mathbf{r}_{3d})\widehat{\dot{\mathbf{r}}_{3d}} + k_a S(\mathbf{e}_3)R^T\left(\frac{T_d}{m}\frac{\partial V_{DI}}{\partial \mathbf{z}_2}^T + k_3\mathbf{r}_{3d}\right)\right) + \omega_3(t)\mathbf{e}_3, \tag{4.13}$$

and the estimator law

$$\dot{\hat{\mathbf{b}}}_1 = -\tfrac{k_{b1}}{k_a}\frac{\partial \mathbf{r}_{3d}}{\partial \mathbf{z}_2}S(\mathbf{e}_3)R^T\mathbf{r}_{3d},$$

achieves global trajectory tracking, by guaranteeing that the errors $\mathbf{z}_1$ *and* $\mathbf{z}_2$ *converge to zero for any initial condition. In addition, the error vector* $(\mathbf{z}_1,\mathbf{z}_2,z_\theta)$ *converges to the set* $\{(\mathbf{0},\mathbf{0},0),(\mathbf{0},\mathbf{0},\pi)\}$ *and the desired equilibrium point* $(\mathbf{z}_1,\mathbf{z}_2,z_\theta) = (\mathbf{0},\mathbf{0},\mathbf{0})$ *is uniformly asymptotically stable.*

The rotational degree of freedom allowed by $\tau_3(t)$ and $\omega_3(t)$ in (4.12) and (4.13), respectively, is due to the axial symmetry exhibited by the quadrotor and is used in the sequel to control the heading of the vehicle independently of the path following law. Notice that both actuations T and $\boldsymbol{\tau}$ or $\boldsymbol{\omega}$ depend only on bounded functions of the position error. This is a desired property since the position error can be arbitrarily large, depending on the initial conditions for the quadrotor.

4.3.1 Path following timing law

The proposed controller achieves the path following objective as long as the control laws (4.13) and (4.12) are well-defined, which depend on (4.7) being different from zero. In this section we explore the use of the degree of freedom provided by the path parameter $\gamma(t)$ to guarantee that the path following controllers are well-defined. More specifically, the timing law for $\gamma(t)$ ensures that $F_d \neq \mathbf{0}$, which using the definition (4.6) expands to

$$-\mathbf{u}^\star + g\mathbf{e}_3 - \ddot{\mathbf{p}}_d + \sigma(\mathbf{z}_0) \neq \mathbf{0}, \tag{4.14}$$

is satisfied at all times. Recall that $\mathbf{u}^\star$ is a state feedback control law for the three dimensional double integrator system comprising the states $\mathbf{z}_1$ and $\mathbf{z}_2$. As a secondary control objective we drive the path speed $\dot{\gamma}$ to a reference speed profile $\dot{\gamma}_r(t)$.

The second order time derivative of the desired path vector is

$$\ddot{\mathbf{p}}_d = \dot{\gamma}^2 \mathbf{p}_d''(\gamma) + \ddot{\gamma}\mathbf{p}_d'(\gamma).$$

Substituting $\ddot{\mathbf{p}}_d$ in (4.14) we obtain

$$-\mathbf{u}^\star + g\mathbf{e}_3 - \dot{\gamma}^2\mathbf{p}_d''(\gamma) - \ddot{\gamma}\mathbf{p}_d'(\gamma) + \sigma(\mathbf{z}_0) \neq \mathbf{0} \tag{4.15}$$

with $\ddot{\gamma}$ as the control input. Without loss of generality we consider that the desired path has a parameter derivative of unitary norm, $\|\mathbf{p}_d'(\gamma)\| = 1$. We now devise a control law for $\ddot{\gamma}$ appropriate for paths featuring

$$\|\mathbf{e}_3^T\mathbf{p}_d'(\gamma)\| < \alpha \tag{4.16}$$

for some design parameter verifying $0 < \alpha \leq \frac{\sqrt{3}}{3}$. For paths verifying only $\|\mathbf{e}_1^T\mathbf{p}_d'(\gamma)\| > \alpha$ or $\|\mathbf{e}_2^T\mathbf{p}_d'(\gamma)\| > \alpha$, the same principles can be used to derive similar timing laws and, as such, these cases will not be presented here. If the desired path violates these three conditions on $\mathbf{p}_d'(\gamma)$ then it can be separated in smaller path segments, each verifying at least one of the previous conditions.

Let $R(\gamma) = R(\theta(\gamma), \mathbf{n})$ be a rotation matrix defined by its angle-axis representation with

$$\begin{aligned} \theta &= \arctan(\mathbf{e}_1^T\mathbf{p}_d'(\gamma), \mathbf{e}_2^T\mathbf{p}_d'(\gamma)), \\ \mathbf{n} &= \mathbf{e}_3 \end{aligned} \tag{4.17}$$

and left multiply (4.15) to obtain the following system of equations that cannot be simultaneously verified

$$v_1 - \ddot{\gamma}\sqrt{1 - (\mathbf{e}_3^T\mathbf{p}_d'(\gamma))^2} = 0, \tag{4.18}$$

$$v_2 = 0, \tag{4.19}$$

$$v_3 - \ddot{\gamma}\mathbf{e}_3^T\mathbf{p}_d'(\gamma) = 0, \tag{4.20}$$

where

$$v_i = \mathbf{e}_i^T R(\gamma)(-\mathbf{u}^\star + g\mathbf{e}_3 - \dot{\gamma}^2\mathbf{p}_d''(\gamma) + \sigma(\mathbf{z}_0)). \tag{4.21}$$

Notice that $R(\gamma)$ is carefully crafted so as to eliminate $\ddot{\gamma}$ from the vector component v_2. At this point, we design a control law for $\ddot{\gamma}$ that drives $\dot{\gamma}$ to $\dot{\gamma}_r$ but perturb it when necessary so that (4.18)-(4.19) are never simultaneously verified.

Local perturbation of $\ddot{\gamma}$ is achieved through two bump functions (see [Lee03] for a detailed definition) of class C^∞ that are used in the design of the timing law,

$$\Psi_{A,B}(s) = \begin{cases} 1 & , 0 \le s < A \\ \tanh\left(-\dfrac{\lambda(s)}{1-\lambda(s)^2} + \dfrac{1}{2}\right) & , A < s < B \\ 0 & , B < s \\ \Psi_{A,B}(-s) & , s < 0 \end{cases}$$

$$\Phi_{A,B}(s) = 1 - \Psi(s),$$

where

$$\lambda(s) = \frac{2s - A + B)}{(B-A)}$$

and A and B are positive parameters with $B > A$. This function is identically one for $|s| < A$ and zero for $|s| > B$. A graphical representation of the bump functions is presented in Figure (4.2) for $A = 0.5$ and $B = 1$.

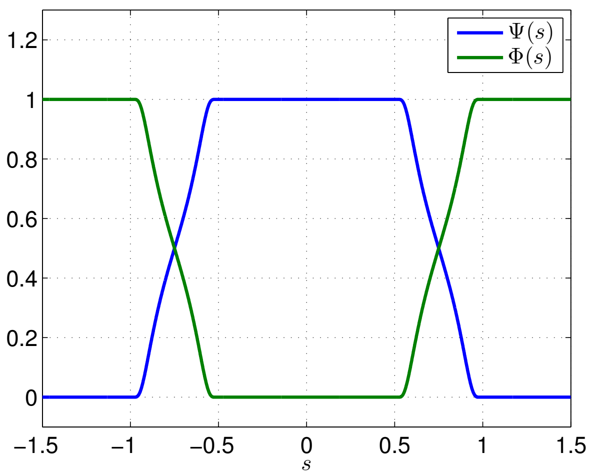

Figure 4.2: Bump-like functions of class C^∞.

We can now state the following result.

Lemma 19. *Let $\mathbf{p}_d(\gamma) \in \mathbb{R}^3$ be a function of at least class C^4 such that $\|\mathbf{p}_d'(\gamma)\| = 1$ and (4.16) are verified for all γ and $\mathbf{e}_1^T R(\gamma)\mathbf{p}_d''(\gamma) = 0$ or*

$$\frac{\mathbf{e}_1^T R(\gamma)\mathbf{p}_d''(\gamma)}{\mathbf{e}_2^T R(\gamma)\mathbf{p}_d''(\gamma)} \tag{4.22}$$

is bounded for all γ (or its limit is bounded, when undefined). Controlling the path progression parameter γ through

$$\ddot{\gamma} = -(1 - \Psi_{A,B}(v_2))\left(k_1(\dot{\gamma} - \dot{\gamma}_r) + k_3(\dot{\gamma} - \dot{\gamma}_r)^3 - \ddot{\gamma}_r\right) + \Psi_{A,B}(v_2)\frac{v_1 - M}{\sqrt{1 - (\mathbf{e}_3^T \mathbf{p}_d'(t))^2}} \tag{4.23}$$

with $M \neq 0$ guarantees that the path following control laws (4.5) *and* (4.12) *are always well-defined and that $\dot{\gamma}$ converges to $\dot{\gamma}_r$.*

Proof. Define the velocity tracking error between the actual velocity and the reference velocity profile as

$$z_\gamma = \dot{\gamma} - \dot{\gamma}_r(t)$$

and consider the quadratic Lyapunov function

$$V_\gamma = \tfrac{1}{2} z_\gamma^2.$$

Its time derivative is

$$\dot{V}_\gamma = -(1-\Psi_{A,B}(v_2))(k_1 z_\gamma^2 + k_3 z_\gamma^4) + z_\gamma \Psi_{A,B}(v_2)\left(\frac{v_1 - M}{\sqrt{1-(\mathbf{e}_3^T \mathbf{p}_d'(\gamma))^2}} - \ddot{\gamma}_r\right). \tag{4.24}$$

Sufficiently far from the singularity, when $|v_2| > B$, the time derivative (4.24) is reduced to

$$\dot{V}_\gamma = -k_1 z_\gamma^2 - k_3 z_\gamma^4.$$

The velocity error is driven to zero, bounded, and the control law (4.23) is well defined. Let us now examine the opposite case, where $|v_2| \leq B$. Starting with the definition of v_2 in (4.21) and solving for the path velocity we get

$$\dot{\gamma}^2 = \frac{\mathbf{e}_2^T R(-\mathbf{u}^\star + g\mathbf{e}_3 + \sigma(\mathbf{z}_0)) - v_2}{\mathbf{e}_2^T R(\gamma)\mathbf{p}_d''(\gamma)}.$$

Substituting the previous equation in (4.23) we get

$$\begin{aligned}\ddot{\gamma} = -(1-\Psi_{A,B}(v_2))(k_1 z_\gamma + k_3 z_\gamma^3 - \ddot{\gamma}_r) + \Psi_{A,B}(v_2)\tfrac{1}{\sqrt{1-(\mathbf{e}_3^T \mathbf{p}_d'(\gamma))^2}}\Big[\mathbf{e}_1^T R(\gamma)\Big(-\mathbf{u}^\star + g\mathbf{e}_3 + \sigma(\mathbf{z}_0)\Big) \\ -\frac{\mathbf{e}_1^T R(\gamma)\mathbf{p}_d''(\gamma)}{\mathbf{e}_2^T R(\gamma)\mathbf{p}_d''(\gamma)}\Big(\mathbf{e}_2^T R(\gamma)(\mathbf{u}^\star + g\mathbf{e}_3 + \sigma(\mathbf{z}_0)) - v_2\Big) - M\Big].\end{aligned} \tag{4.25}$$

Since the terms in γ and γ^3 are stabilizing and all the variables are bounded, in the condition of the theorem we have that $\ddot{\gamma}$ is bounded and neither the path parameter γ nor its derivatives grow unbounded in finite time. □

The fact that the only singularity in (4.25) comes from the denominator allows us to use the conditions (4.22) to verify *a priori* the stability of the timing law, even near its singularity, as they are uniquely defined by the desired path. The discussion in the proof of Lemma 19 is applicable to reference paths which have been normalized on their path progression to have unit norm parameter derivative. This is a desirable situation since we want to aggregate all the velocity behavior in the path derivative $\dot{\gamma}$, independently of the path itself $\mathbf{p}_d(\gamma)$. In such situation, the tracking of a path with constant velocity corresponds to a constant $\dot{\gamma}$. However, the relation (4.22) can also be written for a non-normalized path enabling to check if it is a feasible path without having to normalize. Let $\mathbf{p}_r(\gamma)$ be a path definition and $\mathbf{p}_d(\gamma)$ the corresponding path normalized so as to have unitary norm derivative. Expanding the normalization of $\mathbf{p}_r$ and the definition of $\mathrm{R}(\gamma)$ in (4.17) leads to a simple formula to verify if the timing law is well defined. Then, the following relationship can be determined

$$\frac{\mathbf{e}_1^T R(\gamma)\mathbf{p}_d''}{\mathbf{e}_2^T R(\gamma)\mathbf{p}_d''} = \frac{\|\mathbf{p}_r'\|^2 \mathbf{p}_{r3}' \mathbf{p}_{r3}'' - \mathbf{p}_r'^T \mathbf{p}_r'' (\mathbf{p}_{r3}')^2}{\|\mathbf{p}_r'\|^2 (\mathbf{p}_{r2}' \mathbf{p}_{r1}'' - \mathbf{p}_{r1}' \mathbf{p}_{r2}'')},$$

from which follows directly that paths lying on a horizontal plane ($\mathbf{p}_{r3}' = 0$) are all feasible.

4.3.2 Yaw degree of freedom

In a path following situation, the attitude of the vehicle is automatically prescribed up to a rotation around the body z axis. This is specified in (3.7) and is corroborated by the control laws (4.12) and (4.13) obtained in the previous section, where the actuation torque $\tau_3(t)$ or angular velocity $\omega_3(t)$ are arbitrary functions. We can thus explore this extra degree of freedom to achieve an additional control objective, which should be carefully chosen so that it does not conflict with the original path following objective.

A simple possibility is to guarantee convergence of ω_3 to zero, by application of the control law $\tau_3 = -k\omega_3$, or the trivial control $\omega_3 = 0$ for vehicles controlled in angular velocity. In this situation the yaw angle does not vary significantly, or remains constant, for all the trajectory. A more interesting and useful goal is to control the yaw angle so that internal sensors that equip the vehicle (such as cameras or laser scanners) are correctly aligned to better accomplish their tasks. In this chapter, since the quadrotor in consideration does not possess internal sensors, we align the yaw angle to ensure that the vehicle has zero side-slip angle, i.e., the vehicle follows the desired path with zero velocity component along the body y axis.

Combining (3.7), which describes the path following equilibrium, with the additional constraint

$$[0\ 1\ 0]^T \mathbf{v}_d = v_{2d} = 0$$

we can arrive at the following expression for the desired rotation matrix

$$R_d = \begin{bmatrix} -\frac{S(\mathbf{r}_{3d})^2 \mathbf{p}_d'}{\|S(\mathbf{r}_{3d})^2 \mathbf{p}_d'\|} & \frac{S(\mathbf{r}_{3d})\mathbf{p}_d'}{\|S(\mathbf{r}_{3d})\mathbf{p}_d'\|} & \mathbf{r}_{3d} \end{bmatrix} \tag{4.26}$$

where the third column of R_d is given by (4.7). Clearly, (4.26) can only be used if $S(\mathbf{r}_{3d})\dot{\mathbf{p}}_d \neq 0$. When this is not the case, any pair $(\mathbf{r}_{1d}, \mathbf{r}_{2d})$ such that $R_d = [\mathbf{r}_{1d}\ \mathbf{r}_{2d}\ \mathbf{r}_{3d}] \in \mathrm{SO}(3)$ yields $v_{2d} = 0$. Since the control law for path following already ensures that $\mathbf{r}_3$ converges to $\mathbf{r}_{3d}$, to guarantee that v_{2d} approaches zero, we need only have convergence of $\mathbf{r}_2$ to $\mathbf{r}_{2d}$

or equivalently of $\mathbf{r}_{2d}^T\mathbf{r}_2$ to one. Once again, we stress that working directly with the rotation matrix as opposed to adopting a parameterization has the advantage of avoiding singularities and unwinding behavior of the system's trajectories [BB00].

Consider first the case of torque controlled quadrotor vehicles. Having defined R_d completely, straightforward but rather lengthy computations provide expressions for both ω_{3d} and its time derivative $\dot{\omega}_{3d}$. Gathering all these elements, we define the following PD-like control law for τ_3

$$\tau_3 = -l_2(\omega_3 - \omega_{3d} + l_1\mathbf{r}_{2d}^T\mathbf{r}_1) + \dot{\omega}_{3d} - l_1\frac{d}{dt}(\mathbf{r}_{2d}^T\mathbf{r}_1) \tag{4.27}$$

with $l_1 > 0$ and $l_2 > 0$. Computing the time derivative of the Lyapunov function $W = (\omega_3 - \omega_{3d} + l_1\mathbf{r}_{2d}^T\mathbf{r}_1)^2$ we can verify that it is negative definitive, which implies that ω_3 converges to $\omega_{3d} - l_1\mathbf{r}_{2d}^T\mathbf{r}_1$. For vehicles controlled in angular velocity this translates trivially to setting

$$\omega_3 = \omega_{3d} - l_1\mathbf{r}_{2d}^T\mathbf{r}_1. \tag{4.28}$$

Clearly this is not enough to guarantee that $\mathbf{r}_2$ approaches $\mathbf{r}_{2d}$, however some insight that this convergence is happening can be gained by noting that the term $-l_1\mathbf{r}_{2d}^T\mathbf{r}_1$ opposes growth in the angular distance between $\mathbf{r}_2$ and $\mathbf{r}_{2d}$. More formally, we can define the states

$$\begin{aligned}\xi &= \omega_3 - \omega_{3d} + l_1\mathbf{r}_{2d}^T\mathbf{r}_1 \in \mathbb{R}\\ \eta &= 1 - \mathbf{r}_{2d}^T\mathbf{r}_2 \in [0,\ 2]\end{aligned}$$

and verify that, at the path following equilibrium given by $\mathbf{z}_1 = \mathbf{z}_2 = \mathbf{z}_\theta = \mathbf{z}_4 = 0$, and $\xi = 0$, the dynamic system for η is described by

$$\dot{\eta} = -l_1(2-\eta)\eta \tag{4.29}$$

and the origin of this system is asymptotically stable.

If we consider the closed-loop quadrotor system that results from applying the control laws (4.5) and (4.12) with (4.27), the system (4.29) can be thought of as the quadrotor zero dynamics. We can therefore conclude that the overall closed-loop system has an asymptotically stable equilibrium point at the origin, which follows from the asymptotic stability of $\mathbf{z}_1 = \mathbf{z}_2 = \mathbf{z}_\theta = \mathbf{z}_4 = \mathbf{0}$ and $\xi = 0$.

4.4 Experimental results

In order to experimentally validate the proposed control algorithms we use the rapid prototyping and testing architecture described in Section 3.6. The vehicle used for the experiments is a radio controlled Blade mQX quadrotor [bla], depicted in Figure 3.1(a).

4.4.1 Path following

For the first experimental evaluation of the proposed controller we selected for the desired path a lemniscate (figure eight) parameterized by γ according to

$$\mathbf{p}_d(\gamma) = \begin{bmatrix} \cos(\pi/4) & \sin(\pi/4) & 0 \\ -\sin(\pi/4) & \cos(\pi/4) & 0 \\ 0 & 0 & 1 \end{bmatrix} \begin{bmatrix} \frac{\sin(\phi(\gamma))\cos(\phi(\gamma))}{\sin(\phi(\gamma))^2+1} \\ \frac{\cos(\phi(\gamma))}{\sin(\phi(\gamma))^2+1} \\ 1 \end{bmatrix},$$

where $\phi(\gamma)$ is defined as

$$\phi(\gamma) = \int_0^\gamma \sqrt{1+\sin^2(\tau)}\mathrm{d}\tau \, .$$

This parametrization results in a path derivative with unitary norm. The desired progression along the path is governed by $\dot{\gamma}_r = V\,\Psi_{0.5,1}(\|\mathbf{z}_1\|)$. For large position errors, $\dot{\gamma}_r$ is zero to ensure that the desired position waits for the vehicle to reach it. When the vehicle is close to the path the desired parameter derivative $\dot{\gamma}_r$ takes a constant value to enforce a vehicle velocity of constant norm V.

As the double integrator control law we use a vector application of

$$u^\star(x_1,x_2) = -k_2(x_2+\sigma(x_1)) - \sigma(x_1) - \sigma'(x_1)x_2.$$

The control law coefficients are $k_2 = 3$, $k_3 = 1$, $k_4 = 3$, $k_a = 20$, $k_{b1} = 1$, $k_{b2} = k_{b1}/k_a$. The unknown disturbance is set at $\mathbf{b} = [0.3, -0.2, 0.1]^T$ (m s^{-2}) for the simulation and the initial estimates $\hat{\mathbf{b}}_1(0)$ and $\hat{\mathbf{b}}_2(0)$ are set to zero. The heading is driven by the control laws (4.27) and (4.28) with $l_1 = l_2 = 1$. For the sigmoid function we use

$$\sigma(s) = 2\frac{s}{\sqrt{1+s^2}},$$

and as timing law parameters and initial conditions we use $k_\gamma = 1$, $V = 1$, $\gamma(0) = 0$ and $\dot{\gamma}(0) = 1$. For the simulation with torque actuation we consider $\mathbb{J} = I_3/100$ where I_3 is the 3×3 identity matrix.

A comparison of a segment of the reference path, the actual quadrotor path and a simulation path starting with the same initial condition as the actual path is presented in Figure 4.3. Small position errors can be seen for the simulation due to the initial conditions for the quadrotor state and disturbance estimation and due to imposed force disturbance $\mathbf{b}$. These errors eventually converge to zero as the estimation errors go to zero and path following is achieved. The time evolution of the actual quadrotor position and the reference for the lemniscate trajectory is shown in Figure 4.4. The quadrotor follows closely the desired path, with a maximum error of 8 cm and mean error of 4 cm for the path shown in Figure 4.3. This small position error can be attributed to unmodeled dynamics of the plant and to the fact that the issued commands are not perfectly followed

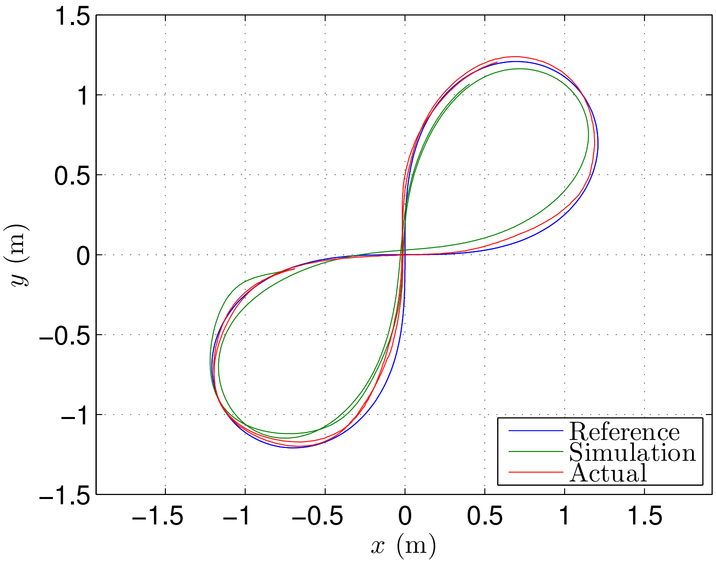

Figure 4.3: Reference and quadrotor paths.

by the aircraft. The main contributions to the unmodeled dynamics are threefold: *i*) there exist unmodeled cross-couplings between the angular velocity commands and lateral forces acting on the quadrotor, due to an uneven and not perfectly symmetric mass distribution of the vehicle; *ii*) the issued thrust and angular velocity commands are not followed instantly due to motor inertia; *iii)* there exists a non-constant wind disturbance affecting the vehicle.

Although the path following experiment is performed on a closed division, without much wind disturbance, the effect of the integral action is evidenced on the vertical axis. The vertical steady state error is neglectable (see Figure 4.4, owing to the existence of both the integral term $\sigma(\mathbf{z}_0)$ in (4.6) and the disturbance estimator $\hat{\mathbf{b}}$, even though the thrust command to thrust force relation is not perfectly known.

The command signals and the quadrotor angular velocity derived from attitude measurements are depicted in Figure 4.5. Even though the commands are not followed perfectly the controller is robust enough so that this mismatch results in small position errors.

4.4.2 Robustness to external disturbances

The previous experiment shows that the proposed quadrotor controller accomplishes its goals in a windless setup, despite the fact that the thrust command to thrust force ratio is known only approximately and is subject to change with the battery charge. However, the first trial does not fully evidence the controller behavior in the presence of wind disturbances. In order to attest the controller's robustness we devised a second

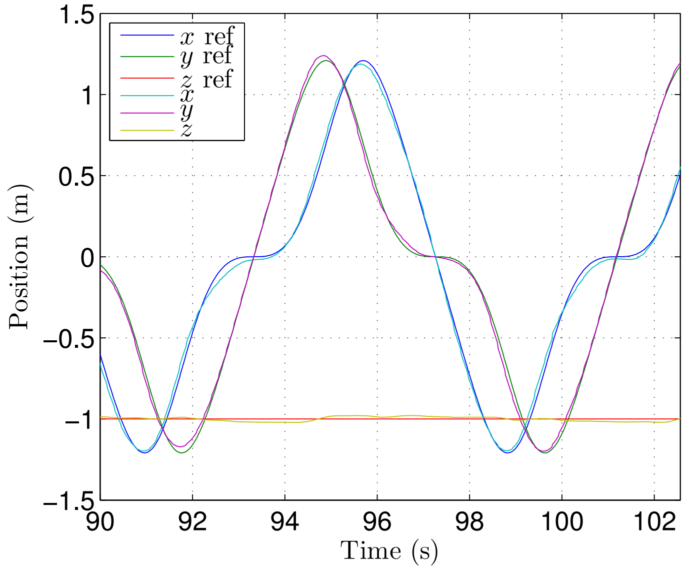

Figure 4.4: Time evolution of the position and reference signal.

experiment where the quadrotor is forced to hover in the slipstream of a mechanical fan, as pictured in Figure 4.6.

With the fan turned off, we initially hover the vehicle and then turn the fan on, creating an airflow that the quadrotor controller is designed to reject. The results of the experiment are shown in Figures 4.7 and 4.8, where only the data along the airflow axis is plotted for better visualization.

The effect of the airflow disturbance can be seen around the 10 s time instant, when the fan is turned on and the integral term $\sigma(\mathbf{z}_0)$ in (4.6) and the estimator $\hat{\mathbf{b}}_1$ start adapting to the new environmental conditions. The position error grows from effectively zero to 15 cm, when the fan is turned on, but quickly returns back to zero due the action of the integral terms.

As a consequence of the integral terms and the new conditions, the quadrotor tilts against the airflow so that it can hover at a designated location and not be dragged by the fan's slipstream. This is evidenced by Figure 4.8, where the pitch angle goes from an average of −1.5 degrees, in a windless situation, to 7 degrees, when the mechanical fan is working. Also visible in the figure is the increase in noise in the pitch angle that occurs while the disturbance is active, due to the turbulent and narrow airflow generated by the mechanical fan.

4.4.3 Saturation and negatived thrust

In this section we present the results from a simulation run of the controller that is illustrative of the saturation function effect and of the control method stability and

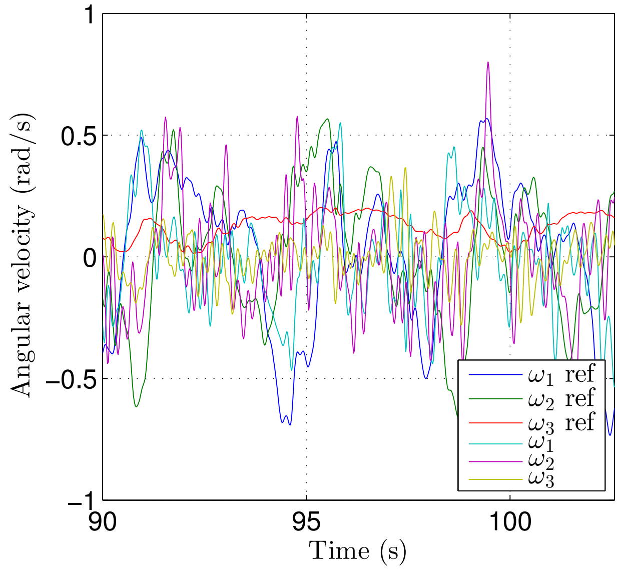

Figure 4.5: Time evolution of the actuation signals.

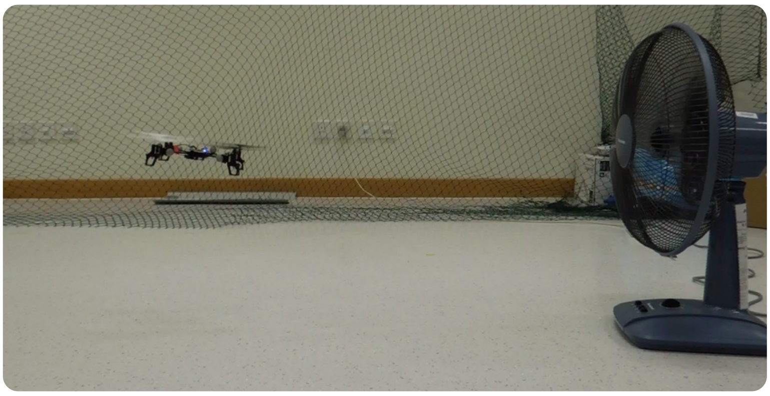

Figure 4.6: Setup of the quadrotor vehicle and the disturbance generator.

robustness properties for aerial vehicles actuated in torque. We used the same desired path and controller parameters as described in Section 4.4.1.

At the initial time instant the vehicle state is at rest at $\mathbf{p}(0) = [10, -5, -3]^T$ (m) and turned upside down, presenting $\mathbf{r}_3(0) = [0, 0, -1]^T$. This extremely unfavorable orientation is chosen to illustrate a zero thrust actuation condition during the initial transient. The initial position, corresponding to a large position error, enables the observation of the transient behavior induced by the saturations in the control law.

Figure 4.9 depicts the time evolution of all the components of the path following and backstepping errors. The convergence rates of the different errors vary but it can be seen that a situation close to path following is attained in about 15 seconds time. The fastest error to converge is $\mathbf{z}_4$, which is almost zero in less than 5 seconds time. The effect of the

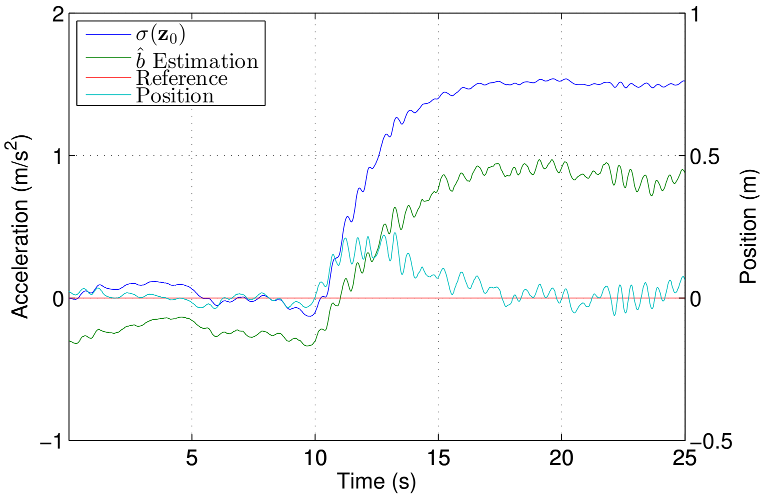

Figure 4.7: Time evolution of the disturbance estimation and related signals, restricted to the slipstream axis, when subject to a wind disturbance.

σ saturation is clearly visible on the position and velocity error. The initial convergence of the vehicle to the path is performed almost at constant velocity for x and y (see from 0 to 5 seconds). Once the main effect of the saturation ceases, all errors start to converge simultaneously and are negligible after the 15 seconds mark. The remaining error is due to the influence of the estimators and is gradually reduced to zero as time passes. Notice that the due to the integral action of the controller we are able to reject the unknown constant force disturbance.

It is worth to notice that due the initial unfavorable orientation, the direction of $\mathbf{r}_3$ suffers an inversion, as indicated by the evolution of the error component from $\mathbf{z}_{33} = -2$ ($\mathbf{r}_3 = -\mathbf{r}_{d3}$) to $\mathbf{z}_{33} = 0$ ($\mathbf{r}_3 = \mathbf{r}_{d3}$).

The quadrotor actuation does not vary significantly from its nominal values, apart from the initial transient, as shown in Figure 4.10. The effect of the initial unfavorable orientation is also visible in the thrust actuation. Its initial value is negative and becomes positive when the vehicle returns to a more standard orientation.

The time evolution of the path parameter derivative is depicted in Figure 4.11. The evolution of $\dot{\gamma}$ is ruled by the timing law (4.23) and converges to $V = 1$ for sufficiently small path following error. The large initial position error dictates a slow progression along the path, with $\dot{\gamma}$ approaching zero. Only when the path following error is small does the parameter's derivative reach an inflection point, to finally converge to the steady state value of 1.

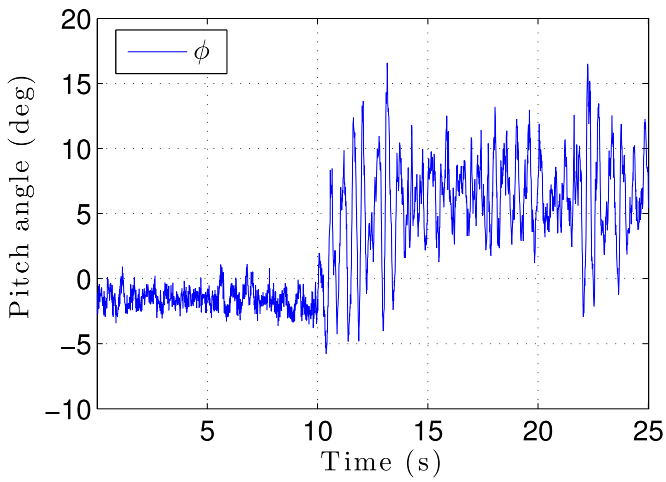

Figure 4.8: Time evolution of the quadrotor pitch angle when subject to a wind disturbance.

4.5 Concluding remarks

This chapter presented a state feedback solution to the problem of steering a quadrotor vehicle along a predefined path. The proposed solution guarantees global convergence of the path following error to zero, for a large class of three-dimensional paths. The nonlinear controller, which was designed using Lyapunov-based backstepping techniques, ensures that the actuation does not grow unbounded as function of the position error and allows for zero thrust actuation to be applied when the vehicle is converging to the path. The proposed controller was designed to be robust to unknown constant force disturbances that arise from the presence of wind or imperfect knowledge of vehicle parameters. Additionally, the vehicle's progression along the path is controlled to follow a predefined speed profile and simultaneously maintain the path following control law well-defined. A final degree of freedom in the control laws is explored so that the vehicle flies with zero side-slip angle. Experimental and simulation results were presented for vehicles controlled in both angular velocity and torque to assess the performance of the proposed controllers. The robustness of the controller to non-ideal wind disturbances was experimentally demonstrated using a mechanical fan as a disturbance generator. Future work remains to be carried on input saturation as the proposed controller generates inputs which are bounded with respect to the position error but can grow unbounded on the remaining errors.

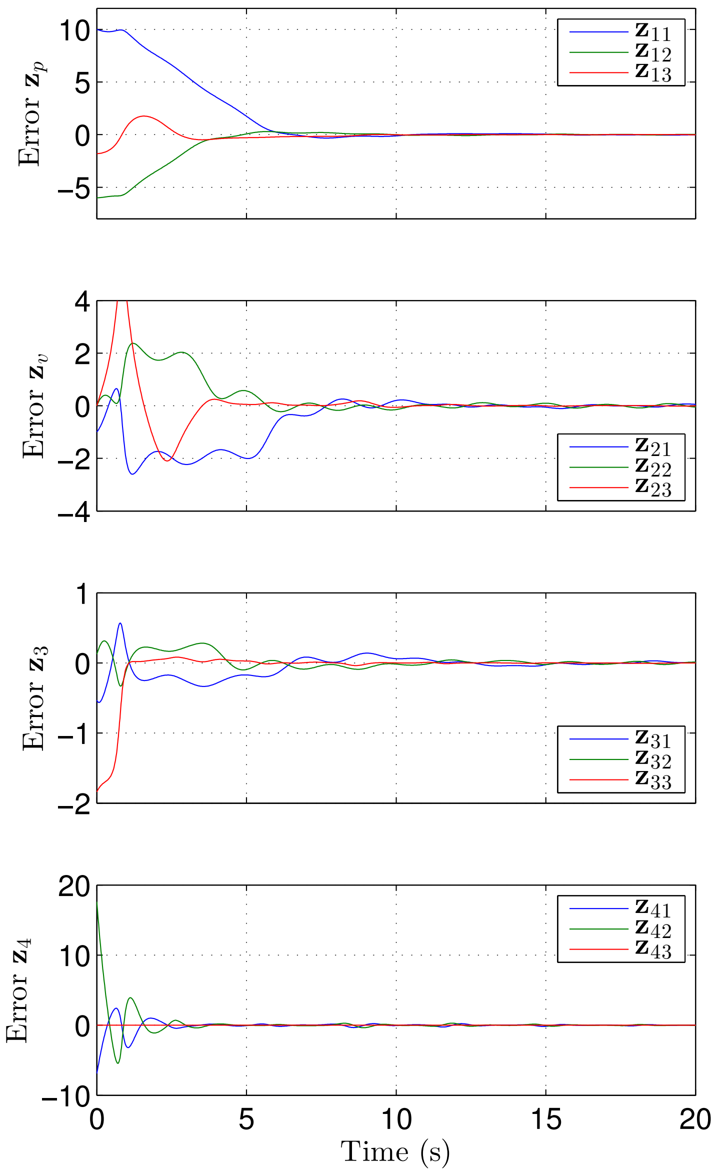

Figure 4.9: Path following errors

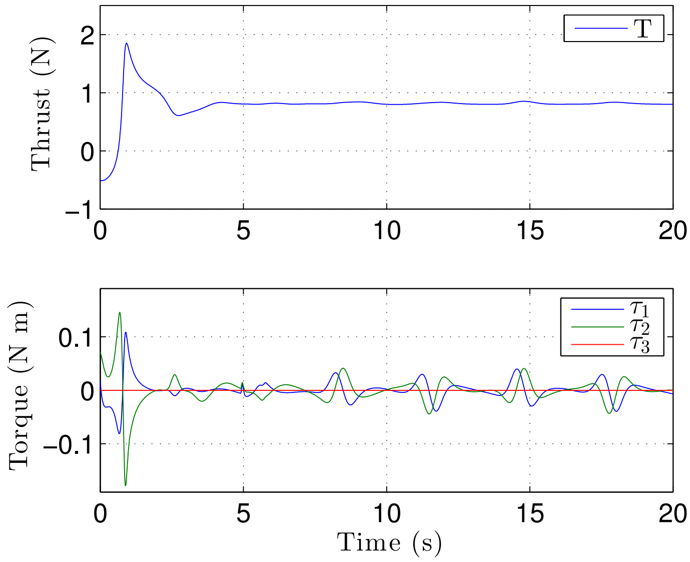

Figure 4.10: Actuations

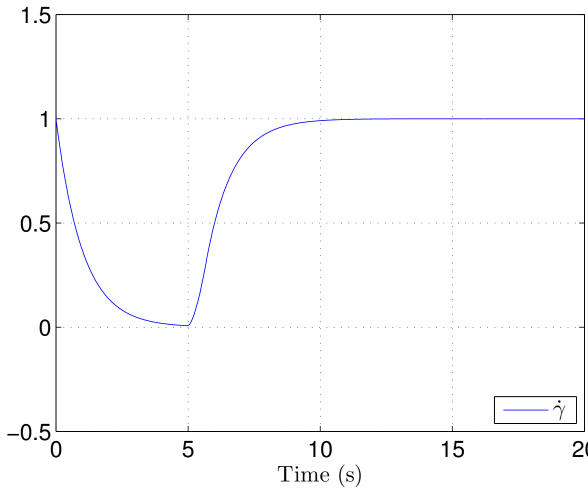

Figure 4.11: Parameter time derivative

5

Robust take-off and landing for a quadrotor vehicle

This chapter addresses the problem of robust take-off and landing of a quadrotor UAV in critical scenarios, such as in presence of sloped terrains and surrounding obstacles. Throughout the maneuver the vehicle is modeled as a hybrid automaton whose states reflect the different dynamic behavior exhibited by the UAV. The original take-off or landing problems are then addressed as the problem of tracking suitable reference signals in order to achieve the desired transitions between different hybrid states of the automaton. Reference trajectories and feedback control laws are derived to explicitly account for uncertainties in both the environment and the vehicle dynamics. Simulation and experimental results demonstrate the effectiveness of the proposed solution and highlight the advantages with respect to more standard open-loop strategies, especially for the cases in which the slope of the terrain renders the take-off and landing maneuvers more critical to be achieved.

5.1 Introduction

To be truly autonomous, an UAV must perform maneuvers that encompass not only the normal flight conditions, like hover or forward flight, but also the take-off and landing maneuvers, where interaction with the ground occurs. In the critical take-off phase the autopilot controller must provide robustness to uncertainties in both the environment and the dynamical vehicle model. In most of the available literature, automated take-off maneuvers for aerial rotorcraft are performed in a semi open-loop fashion.

In this chapter of the thesis, we target both the problem of automatic take-off and landing in critical scenarios where heuristic "open-loop" approaches can not be used to guarantee successful maneuvers and control solutions able to finely steer the vehicle along appropriate trajectories are needed. The prototypical scenario motivating our attempts is sketched in Figure 5.1, for the takeoff situation. The presence of a left-sided obstacle along

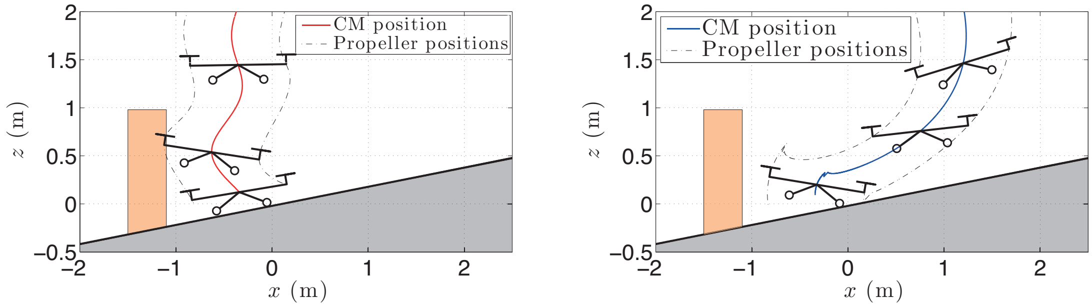

Figure 5.1: Left: the quadrotor hits an obstacle if uncontrolled vertical thrusts are applied. Right: a safe take-off maneuver.

with a sloped terrain makes the application of heuristic take-off strategies, for instance based on the application of uncontrolled large vertical thrusts aiming to rapidly detach the vehicle from the ground, inappropriate as leading to hit the obstacle (see the sketch on left of Figure 5.5). Indeed, as shown on the right of the figure, successful take-off maneuvers necessarily require a first phase in which the vehicle is tilted clockwise by pivoting about the landing gear, followed by a getaway maneuver in which the vehicle slides to the right while keeping the contact with the ground, before definitely taking-off at a safe distance from the obstacle. The accomplishment of this kind of maneuver, in turn, is challenging due to the changes of the dynamics governing the vehicle in the different phases and to the possible uncertainties characterizing the environment and the vehicle.

Regarding the landing maneuver, early research work with demonstrated experimental results considered horizontal flat and stable landing surfaces. To land, the aircraft was simply commanded through position or velocity tracking maneuvers until contact with the ground was made, see e.g. [BS07] and [RSZF07]. The more challenging problem of landing an autonomous helicopter on an oscillating platform, such as the deck of a ship at sea, was considered in [MIS02]. In this work the authors devise an inner-model based control solution, based on the assumption that the vertical oscillation is the result of the superposition of sinusoids of unknown amplitude, phase and frequency. More recently, a landing controller able to cope with a landing platform that is moving vertically with unknown dynamics was developed in [HHMR12], where landing is achieved based on optical flow measurements. The proposed landing controller is designed based on a time-scale separation principle between the attitude and position subsystems but the final stability analysis is performed for the full nonlinear model of the quadrotor. The related problem of landing on a horizontally moving platform was studied in [VBA10], where the authors tackle the problem of landing the vehicle on a platform moving in the horizontal plane. In order to land successfully, the vehicle tracks a desired velocity component in the z-direction while a 2D-tracking controller leads the vehicle to hover above the moving platform. The quadrotor control system is decomposed in an outer-loop for translational velocity control and an inner-loop for attitude control, where the inner-loop is designed to be considerably faster than the outer-loop so as to decouple both dynamics. In that situation the attitude is considered as a control input for the outer-loop. The landing controller is finalized with a 2D tracking controller to drive the quadrotor to hover on the moving platform. The controller however assumes perfect state measurement and tracking, with no emphasis given to robustness.

Non-traditional approaches to landing have been developed in [MSK10] and [LDC10], where solutions for landing aerial vehicles by perching on vertical walls are studied. In the first work the authors design a claw and grippers that allow for a quadrotor vehicle to robustly perch in a vertical wall by following an appropriate trajectory until it comes to a halt at the desired goal or an error is detected. The procedure is robust in the sense that if an error, or a too large trajectory deviation, is detected then the quadrotor is commanded to hover at the original location and the perching maneuver is reattempted. Similarly, the latter work proposes a solution for the control of miniature airplanes with the objective of landing on vertical surfaces where perching is made possible by fitting the aircraft with arrays of microspines.

Recently, particular emphasis has been payed to other flight conditions where interaction with the environment occurs, whether it is contact with vertical walls, with the ground or even using an arm-like extension to interact with objects [FNM+12, MN12]. These flight regimes are considerably more challenging for the aircraft operation than free flight as even small errors can result in catastrophic consequences, due to the proximity of the rotor's fast rotating blades to the environment. Additionally, special attention has to be payed to the dynamics of the vehicle, as these change according to the type of contact being established. As such, for a successful operation in a wide range of mission scenarios, robust controllers must be designed for each flight regime that ensure the vehicle completes the maneuver without incidents, despite possible parameter or modeling uncertainties. The use of a VTOL vehicle to apply forces to the environment while maintaining flight stability was proposed in [ATH+10]. In that work a classical quadrotor platform is augmented with an additional actuator, a propeller aligned with the horizontal plane, so that the vehicle can generate lateral forces when in physical contact with the wall while maintaining a leveled attitude. Similarly, in [FNM+12] a quadrotor vehicle is fitted with an arm, which is used to interact with the environment. An impedance controller is proposed to allow the UAV to dock to a vertical surface while applying a force by means of the manipulator's end-effector and maintaining stability. Further exploration of flight modes were physical contact with the environment occurs culminated in [MN12], which focuses on the interaction of a ducted-fan aerial vehicle with a vertical surface, where sliding is allowed. The ducted-fan is a VTOL rotorcraft vehicle able to hover like a helicopter or quadrotor but whose fuselage is more appropriate for general contact with the environment, as the sole rotating propeller is protected from accidental contacts by the duct. Control of the vehicle position and of the exerted force is achieved by means of state feedback control laws and their stability properties, in particular the system's zero dynamics, are thoroughly analyzed. An additional operative mode considered in this work is the ducted fan vehicle as a mobile robot. Due to the mechanics of the vehicle, the force generated by the rotor is not restricted to the thrust direction but can be oriented laterally. In this way, by fitting the ducted fan landing gear with wheels, it is possible to have the vehicle always in contact with the ground but moving laterally, for thrust forces below the lift-off threshold.

Grasping of objects is yet another kind of interaction with the environment that was studied in [PBD11] and [MFK11]. In the former work a helicopter is fitted with a compliant grasper and the dynamic load disturbances are rejected resorting to a PID controller. Bounds under which the helicopter system carrying a load is stable are presented, together with stability conditions for partial contact with objects resting on a surface. The latter manuscript considers the cooperation of multiple robots to transport a payload attached with cables and details the kinematic constraints and the mechanics underlying stable equilibria of the underactuated system.

The essence of the different dynamic behaviors of an aerial vehicle when interacting with the environment and the conditions for commutation between each operating mode can be easily captured by a hybrid automaton. Hybrid automata constitute a subset of the larger class of hybrid dynamical systems [GST09] and allow to model a complex system in a modular way by collecting simpler dynamical models, each one focusing only on a precise operating mode of the system. Hybrid controllers have been successfully applied for the trajectory tracking of aerial vehicles in different setups, from which we highlight two. In [KHM+98], a hybrid controller is designed to fulfill multiple hierarchical objectives and includes a tactical planner, responsible for the higher level behavior of the aircraft, and a trajectory planner, which generates the desired trajectory for each mode. The performance of each of the individual nonlinear controllers is demonstrated by the authors, although an analysis of the overall switched system is not presented. A different hierarchical control architecture for aggressive maneuvering applicable to autonomous helicopters is proposed in [FDF99]. In this latter work, the hybrid controller is based on an automaton whose states represent feasible trajectory primitives. The selection of maneuvers, and hence the generation of the complete trajectory, is cast as an optimal control problem. The proposed control methodology, however, assumes perfect tracking of the nominal trajectory. In both papers, different states of the automata correspond to different trajectories and not to different dynamics of the vehicle. Additionally, in the former work, the overall switched system stability analysis is not presented and, in the latter, perfect tracking of the nominal trajectories is assumed.

The methodology we adopt to address the takeoff and landing problems borrows from the control framework proposed in [MNG09] and builds upon previous work on ground interactions [NMG09] and interactions with structures in the environment [NGM11]. In this approach, the vehicle is modeled as a *hybrid automaton* where each state corresponds to a different operating condition, where the vehicle is subject to different dynamics, according to the nature of the ground contact. The control methodology presented in the following requires that the current operative mode of the UAV is known. For the specific take-off and landing operations that are considered in this chapter, the operative mode can be retrieved by merging the information deriving from contact or force sensors, to be placed at each extremity of the vehicle's landing gear, with the knowledge of the velocity and the attitude of the system obtained through a standard inertial navigation unit.

Once the hybrid automaton is defined, the take-off control problem is addressed as trajectory generation and tracking control problems. In particular, both the reference signals and the feedback laws for each operating mode are derived considering explicitly the presence of uncertainties. The references are designed such that their practical, and not perfect, tracking ensures that the desired transitions happen, despite the possible presence of parametric or modeling uncertainties. Other approaches to maneuver based motion-planning include [FDF05] and [SF08], where supervisor hybrid controllers are also used to ensure that a sequence of maneuvers is followed robustly.

The main contribution of this chapter consists in the explicit design of the hybrid automaton, robust reference maneuvers, and low-level controllers for a quadrotor vehicle. We derive the dynamics for a quadrotor pivoting and/or sliding along a slope and construct a robust hybrid controller, along with the definition of appropriate reference trajectories, that allows for fully autonomous robust take-off and landing of the vehicle. Robust reference maneuvers are obtained as solutions of constrained optimal control problems.

The remainder of this chapter is organized as follows. Section 5.2 presents the hybrid automaton model for the vehicle. The robust control architecture is discussed in Section 5.3, comprising with the generation of the robust reference maneuvers, low-level controllers and the supervisor. Section 5.4 describes the simulation results for the takeoff maneuver and Section 5.5 discusses the experimental results obtained for the landing maneuver. Concluding remarks and final considerations are presented in Section 5.6.

5.2 Quadrotor hybrid model

The UAV considered in this chapter is a quadrotor aircraft actuated in force, generated by the four propellers. For sake of simplicity, we consider only the "planar dynamics" on the configuration manifold $\mathbb{S}^1 \times \mathbb{R}^2$. The general "spatial dynamics", defined on the configuration manifold $SO(3) \times \mathbb{R}^3$, can be dealt with by properly adapting the presented arguments.

Figure 5.2(a) presents a graphical description of the quadrotor geometry and the landing environment. The ground is modeled as a flat surface at an angle β with the horizontal. A body-fixed frame $\{\mathcal{B}\} = \{CM, \vec{j}_B, \vec{k}_B\}$ is attached to the quadrotor's center of mass (CM), with the vector $\vec{k}_B$ pointing upward, along the thrust direction. The inertial frame $\{\mathcal{I}\} = \{O, \vec{j}, \vec{k}\}$ is defined by the vectors $\vec{j}$ and $\vec{k}$ that point North and up, respectively. An additional frame $\{\mathcal{L}\} = \{O, \vec{j}_L, \vec{k}_L\}$ is attached to the origin of $\{\mathcal{I}\}$ and rotated with respect to $\{\mathcal{I}\}$ by an angle β. The angle θ denotes the rotation angle from the inertial frame to the body frame.

The planar model of the quadrotor, illustrated in Figure 5.2(b), has two counter-rotating motors for propulsion, generating forces F_1 and F_2, and a landing gear with two points of contact with the ground, denoted by A and B. The distance from the center of mass to each motor and to each contact point are denoted by r and ℓ, respectively. The angle with vertex in CM and subtended by the motor and contact point is denoted by γ. The shorthand $\ell_g = \ell\cos(\gamma)$ is introduced to simplify mathematical expressions. The aerodynamic forces generated by the motors at each of the propellers are represented by F_1 and F_2.

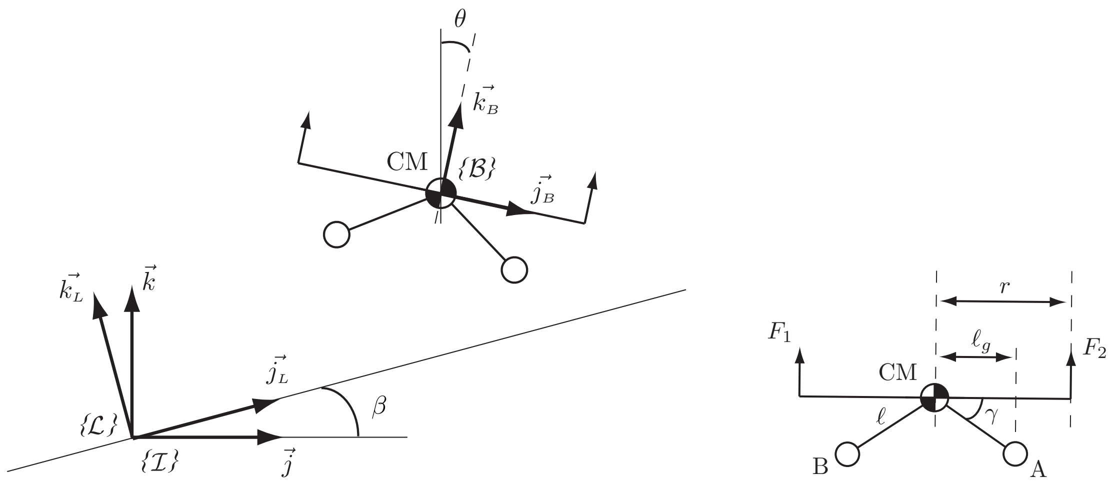

(a) Reference Frames (b) Quadrotor geometry

Figure 5.2: Take-off slope and quadrotor

The coordinates of CM in the $\{\mathcal{I}\}$ and $\{\mathcal{L}\}$ reference frames are denoted by (x, z) and (x_L, z_L), respectively, and are related by

$$x_L = x\cos\beta + z\sin\beta,$$
$$z_L = -x\sin\beta + z\cos\beta.$$

The coordinates of the contact point A (α, ζ), expressed in the $\{\mathcal{L}\}$ frame can be written as

$$\alpha = x\cos\beta + z\sin\beta + \ell\cos(\theta+\gamma+\beta),$$
$$\zeta = -x\sin\beta + z\cos\beta - \ell\sin(\theta+\gamma+\beta).$$

Due to the symmetry of the quadrotor, we only consider maneuvers where rotation occurs around the contact point A, resulting in $\theta(t)+\beta \geq 0$, for the operating modes where contact with the ground exists. The symmetric situation is dealt with similarly and will not be discussed in this work.

To simplify computations, the state of the quadrotor is expressed in different coordinate systems, according to its operative mode. When in free flight, the quadrotor state is described by the center of mass coordinates (x, z), the angle θ angle, and their respective derivatives. In situations where contact with the ground occurs, the quadrotor state is completely described by the states α, $\dot{\alpha}$, θ, and $\dot{\theta}$, decoupling the translational motion of the contact point from the rotational motion around the contact point.

In what follows, we adopt the standard *Coulomb friction model* [HFC08] to describe the interaction between the UAV and the terrain. The friction force F_f is bounded in norm by the product of the normal contact force F_N and the friction coefficient μ, as expressed by the constraint $|F_f| \leq \mu F_N$. In case of sliding between the quadrotor and the ground, the magnitude of the friction force is maximum and opposes the movement, resulting in $F_f = -\mu\mathrm{sign}(\dot{\alpha})F_N$, where

$$F_N = (mg\cos\beta - (F_1+F_2)\cos(\theta+\beta)), \tag{5.1}$$

and $\dot{\alpha}$ is the contact point velocity along the slope. In a non-sliding situation, the vehicle will remain at rest until the tangent component of the external forces acting on the vehicle overcomes the friction force limit, $|F_f| \leq \mu F_N$. To allow the quadrotor to start at rest when taking off, and to come to a rest when landing, we require that $\tan\beta < \mu$. Additionally, for simplicity, we consider just one friction coefficient, corresponding to a situation where the kinetic and static coefficients are the same. This nonlinear behavior of the friction force can be modeled in a hybrid automata framework by considering different states for the rest and the sliding situations.

For the development of our quadrotor automaton, we consider five operating modes. These depend on the number of contact points with the ground, and on the relative motion between the vehicle and the ground, which determine different vehicle dynamics. The operating modes are described as follows.

- *Free Flight (FF)* - In this operating mode the quadrotor is in *free flight* and no contact with the landing slope occurs.

- *Take-off-and-Landing (TL and TLs)* - In a *take-off-and-landing* situation, there exists a single contact point between the quadrotor and the ground, depicted as A in Figure 5.3(a). The shorthand notation TL denotes the non-sliding situation and TLs the take-off-and-landing mode where sliding exists between the quadrotor and the ground.
- *Landed (LL and LLs)* - In the *landed* operating mode, the landing gear is in full contact with the ground, with both points A and B touching the landing slope, see Figure 5.3(b). The shorthand notation LL denotes the non-sliding situation and LLs the landing operative mode were the quadrotor slides on the ground.

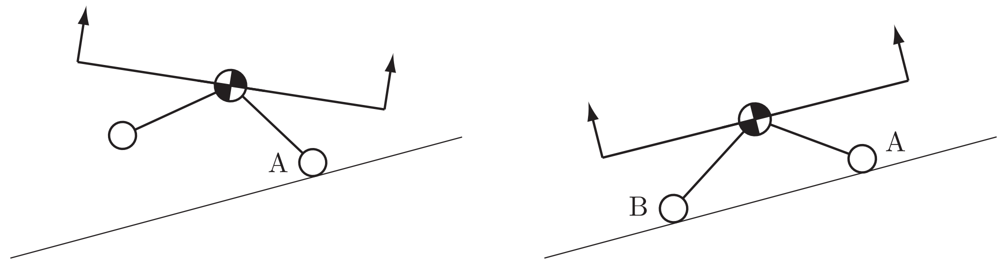

(a) Take-off-and-Landing and Take-off-and-Landing sliding (TL/TLs)

(b) Landed and Landed sliding (LL/LLs)

Figure 5.3: Quadrotor operating modes

Before dwelling into the dynamics and hybrid model description we introduce the following mathematical notation, used throughout this chapter. The expression $g : X \to Y$ indicates that g is a *map* with domain X and codomain Y. Similarly, $h : X \rightrightarrows Y$ denotes a *set-valued map* h with domain X and codomain Y. The *sign* function $\text{sign}(x) : \mathbb{R} \to \mathbb{R}$ extracts the sign of a real number. It is defined as $\text{sign}(x) = -1$, if x is negative, $\text{sign}(x) = 1$, if x is positive, and $\text{sign}(0) = 0$. The symbol $\wedge$ denotes the logical AND operator.

5.2.1 Dynamics of the operating modes

Free flight

In this operating mode the aircraft is airborne. The free flight planar quadrotor is modeled as a rigid body evolving on $\text{SE}(2) = \mathbb{S}^1 \times \mathbb{R}^2$, namely

$$\begin{aligned} m\ddot{x} &= (F_1 + F_2)\sin\theta + \delta_x, \\ m\ddot{z} &= (F_1 + F_2)\cos\theta - mg + \delta_z, \\ J\ddot{\theta} &= (F_1 - F_2)r, \end{aligned} \tag{5.2}$$

where m and J denote respectively the mass and moment of inertia of the vehicle, g the gravity acceleration, and δ_x and δ_z are exogenous disturbance acting along the lateral and vertical direction. Aerodynamic drag forces are not considered as they are negligible at velocities near the hover condition. To support the employment of the simplified dynamical model proposed above, the Free Flight controller is designed to be robust to external disturbances, which can encompass wind disturbances and modeling uncertainties and errors, up to a given limit.

Partial interaction with the ground

In the TL and TLs modes of operation, there is only one contact point of the quadrotor with the ground, as evidenced in Figure 5.3(a). The vehicle's motion is restricted to rotation around the contact point A and translation of the contact point along the slope. Recalling that $\alpha \in \mathbb{R}$ is the $\vec{j}_L$ coordinate of the contact point A in the $\{\mathcal{L}\}$ reference frame and that $\theta \in (-\pi, \pi]$ is the rotation angle from the $\{\mathcal{I}\}$ to the $\{\mathcal{B}\}$ reference frame, the generalized forces acting on the vehicle in these operating modes are

$$
\begin{aligned}
\mathcal{F}_1(F_1, F_2, \dot{\alpha}, \theta) &= (F_1 + F_2)\sin(\theta + \beta) - \mu \operatorname{sign}(\dot{\alpha})(mg\cos\beta - (F_1 + F_2)\cos(\theta + \beta)), \\
\mathcal{F}_2(F_1, F_2) &= F_1(r + \ell_g) - F_2(r - \ell_g).
\end{aligned}
$$

The Lagrangian function of the system in the TL and TLs modes, considering the kinetic and potential energies, is

$$
\begin{aligned}
\mathcal{L} &= \tfrac{1}{2}m(\dot{x}^2 + \dot{z}^2) + \tfrac{1}{2}J\dot{\theta}^2 - mgz \\
&= \tfrac{1}{2}m(\dot{\alpha}^2 + \dot{\theta}^2\ell^2 + 2\dot{\alpha}\dot{\theta}\ell\sin(\theta + \beta + \gamma)) + \tfrac{1}{2}J\dot{\theta}^2 - mg(\alpha\sin\beta + \ell\sin(\theta + \gamma)).
\end{aligned}
$$

In order to simplify the design of controller for the dynamic system we define two virtual controls, F_α and F_θ, related to the real actuations by

$$
\begin{pmatrix} F_\alpha \\ F_\theta \end{pmatrix} = L(\theta)^{-1} G(\theta) M \begin{pmatrix} F_1 \\ F_2 \end{pmatrix} \tag{5.3}
$$

where M, $G(\theta)$, and $L(\theta)$ are given by

$$
\begin{aligned}
M &= \begin{pmatrix} 1 & 1 \\ r + \ell_g & \ell_g - r \end{pmatrix}, \\
G(\theta) &= \begin{pmatrix} \sin(\theta + \beta) + \mu\operatorname{sign}(\dot{\alpha})\cos(\theta + \beta) & 0 \\ 0 & 1 \end{pmatrix}, \\
L(\theta) &= m\begin{pmatrix} 1 & \ell\sin(\theta + \gamma + \beta) \\ \ell\sin(\theta + \gamma + \beta) & \ell^2 + J/m \end{pmatrix},
\end{aligned} \tag{5.4}
$$

respectively. This input transformation is always defined, since $L(\theta)$ is invertible for all θ, and results on the following dynamics, after solving the Lagrangian equations defining the system,

$$
\ddot{\alpha} = F_\alpha + h_\alpha(\theta, \dot{\theta}, \dot{\alpha}, \mu), \quad \ddot{\theta} = F_\theta + h_\theta(\theta, \dot{\theta}, \dot{\alpha}, \mu), \tag{5.5}
$$

where

$$h_\alpha(\theta,\dot\theta,\dot\alpha,\mu) = \frac{1}{J+m\ell^2\cos^2(\beta+\gamma+\theta)}\Big(-g(J+m\ell^2)(\mu\cos\beta\,\mathrm{sign}(\dot\alpha)+\sin\beta)$$
$$+gm\ell^2\cos(\gamma+\theta)\sin(\gamma+\theta+\beta)-\ell(J+m\ell^2)\cos(\gamma+\theta+\beta)\dot\theta^2\Big), \quad (5.6)$$

$$h_\theta(\theta,\dot\theta,\dot\alpha,\mu) = \frac{m\ell}{J+m\ell^2\cos^2(\beta+\gamma+\theta)}\Big(\cos(\gamma+\theta+\beta)(-g\cos\beta+\ell\sin(\gamma+\theta+\beta)\dot\theta^2)$$
$$+g\mu\cos\beta\sin(\gamma+\theta+\beta)\mathrm{sign}(\dot\alpha)\Big). \quad (5.7)$$

The input transformation (5.3) is invertible if and only if the matrix $G(\theta)$ is non-singular, as matrix M is full rank. That is, the original forces F_1 and F_2 are recoverable from F_α and F_θ if

$$\sin(\theta+\beta)+\mu\,\mathrm{sign}(\dot\alpha)\cos(\theta+\beta)\neq 0.$$

Note that the inverse transformation depends on a number of physical parameters, and in particular on μ which is typically uncertain.

The dynamics (5.5) apply only to a quadrotor *sliding* along the slope. In the *take-off and landing* operating mode, the vehicle is in a non-sliding situation. The α position is constant and the dynamic system is reduced to the angular component of (5.5) with $\dot\alpha = 0$, resulting in

$$\ddot\theta = F_\theta + h_\theta(\theta,\dot\theta,0,\mu). \quad (5.8)$$

Equations (5.5) and (5.8) describe a 4-state dynamical model for the vehicle. The coordinates of the center of mass and its derivatives are uniquely defined by the states α, $\dot\alpha$, θ, and $\dot\theta$.

Complete interaction with the ground

In the LL and LLs operating modes, the vehicle is completely landed and only the ground contact friction affects the motion of the vehicle. As in these configurations it is impossible to generate forces along the $\vec{j_L}$ axis of the $\{\mathcal{L}\}$ frame, the only effect of the controls F_1, F_2 is to reduce the normal force F_N, consequently reducing the friction force F_f. The dynamic model for the LLs operating mode is completely described by the dynamical system

$$m\ddot\alpha = -mg\sin\beta - \mu\,\mathrm{sign}(\dot\alpha)F_N, \quad \dot\theta = 0, \quad (5.9)$$

with F_N given by (5.1). When in the LL operating mode, this reduces to

$$\dot\alpha = 0, \quad \dot\theta = 0, \quad (5.10)$$

and the vehicle's state remains constant. In these operative modes, and in order to prevent physically impossible transitions from LL to FF by employing discontinuous forces, we extend the system input with two integrators, where (v_1, v_2) are the residual control inputs

$$\dot{F}_1(t) = v_1(t), \qquad \dot{F}_2(t) = v_2(t). \tag{5.11}$$

5.2.2 Hybrid model of the overall dynamics

A description of the overall dynamics is obtained by means of a *hybrid automaton* whose states correspond to the operating modes described in the preceding section. A hybrid automaton is identified by the following objects, instanced here for the specific case of the planar quadrotor.

Operating modes

The quadrotor automaton comprises the set $\mathcal{Q}$ of *operating modes*, denoted by $\mathcal{Q} = \{LL, LLs, TL, TLs, FF\}$.

Domain map

The state of the system $\xi \in \mathbb{R}^6$ is described by either $(x, \dot{x}, z, \dot{z}, \theta, \dot{\theta})$ or $(\alpha, \dot{\alpha}, z_L, \dot{z}_L, \theta, \dot{\theta})$. When the UAV is in contact with the ground (LL, LLs, TL, and TLs operating modes), the preferred reference frame and the state $\xi = (x, \dot{x}, z, \dot{z}, \theta, \dot{\theta})$ are the $\{\mathcal{L}\}$ frame, yielding $\xi = (\alpha, \dot{\alpha}, z_L, \dot{z}_L, \theta, \dot{\theta})$, while the $\{\mathcal{I}\}$ frame is preferred for the free flight mode. The inputs F_1 and F_2, which correspond to the forces generated by the propellers, are bounded by a minimum and maximum value, leading to the definition of the input domain $U \subset \mathbb{R}^2$ as the compact interval $U = [F_{\min}, F_{\max}] \times [F_{\min}, F_{\max}]$. The domain mapping $\mathcal{D} : \mathcal{Q} \rightrightarrows \mathbb{R}^6 \times \mathbb{R}^2$ defines, for each operating mode, the set of values that the state ξ and the control input u may take.

Flow map

The flow map $f : \mathcal{Q} \times \mathbb{R}^6 \times \mathbb{R}^2 \to \mathbb{R}^6$ describes for each operating mode $q \in \{LL, LLs, TL, TLs, FF\}$ the evolution of the state variables. In each operating mode q we have the dynamic system $\dot{\xi} = f(q, \xi, u)$, where each function $f(q, \xi, u)$ is derived from the differential equations (5.2), (5.5), (5.8), (5.9), and (5.10).

Edges

The set of edges $\mathcal{E} \subset \mathcal{Q} \times \mathcal{Q}$ includes all the pairs (q_1, q_2) such that a transition between the modes q_1 and q_2 is possible, for some combination of state and actuation. For the take-off and landing procedure, we consider the transitions depicted in Figure 5.4. We do not consider direct edges linking LL to FF or FF to LL as these transitions are not considered in the following design of the take-off and landing maneuvers due to possible robustness issues. Observe also that they can be equivalently obtained by passing instantaneously trough the intermediate operative modes TL and TLs.

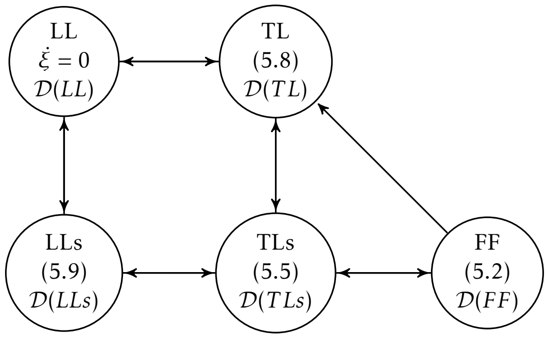

Figure 5.4: Planar quadrotor hybrid automaton

Guard mapping

The set-valued guard mapping $\mathcal{G} : \mathcal{E} \rightrightarrows \mathbb{R}^6 \times \mathbb{R}^2$ determines, for each edge $(q_1, q_2) \in \mathcal{E}$, the set $\mathcal{G}(\{q_1, q_2\})$ to which the quadrotor state ξ and inputs F_1, F_2, must belong so that a transition from q_1 to q_2 can occur. There are three main groups of transitions to consider for the take-off and landing procedures. The transition from two contact points (LL and LLs operating modes) to one contact point (TL, TLs) is governed by the sign of the torque F_τ at point A,

$$F_\tau(\theta, F_1, F_2) = (F_1 + F_2) l_g + (F_1 - F_2) r - mg\ell \cos(\theta + \gamma),$$

and the inverse transition depends on the angle of the vehicle with the slope, $\theta + \beta$, and also on sign of F_τ. The operating mode transitions between free flight and the TLs mode depend on the force perpendicular to the slope $F_\perp$,

$$F_\perp(\theta, F_1, F_2) = (F_1 + F_2)\cos(\theta + \beta) - mg\cos\beta,$$

and the height of the quadrotor relative to the ground. Lastly, the transitions between the *at rest* and the *sliding* modes are governed by the relation between the force along the slope at the contact point ($F_\alpha + h_\alpha$), the perpendicular force $F_\perp$, and the vehicle's velocity along the slope $\dot{\alpha}$, according to the Coulomb friction model. The function

$$\begin{aligned} F_{\text{slide}}(\theta, \dot{\theta}, F_1, F_2, \mu) = {} & |F_\alpha(\theta, \dot{\theta}, \mu, F_1, F_2) + h_\alpha(\theta, \dot{\theta}, 0, \mu)| \\ & - \mu \frac{mg\cos\beta}{m\cos^2(\theta + \beta + \gamma)} + \mu \frac{(F_1 + F_2)\cos(\theta + \beta)}{m\cos^2(\theta + \beta + \gamma)} \end{aligned}$$

encapsulates these relations. A transition from a non-sliding mode to a *sliding* mode occurs for $F_{\text{slide}} > 0$, whereas a reverse transition happens when the velocity along the slope reaches zero and $F_{\text{slide}} < 0$. In the landed operating mode, this function is reduced to

$$F_{\text{slide}}(-\beta, 0, F_1, F_2, \mu) = mg\sin\beta - \mu(mg\cos\beta - (F_1 + F_2)).$$

Reset maps

For each $(q_1, q_2) \in \mathcal{E}$ and $(\xi, u) \in \mathcal{G}(\{q_1, q_2\})$, the reset map $\mathcal{R} : \mathcal{E} \times \mathbb{R}^6 \times \mathbb{R}^2 \to \mathbb{R}^6$ identifies the jump of the state variable ξ during the operating mode transition from q_1 to q_2. The jumps in the state reflect instantaneous changes which are caused by the collisions of the contact points with the landing slope and also the use of either frame $\{\mathcal{L}\}$ or $\{\mathcal{I}\}$ to describe the state, according to the operating mode.

In the take-off maneuver the nominal transitions do not involve impact with the ground and thus all the reset maps are trivially the identity maps. The only reset maps that result from physical interaction are the ones governing the transitions from FF to TLs and TL to LL. In particular, for reference trajectory generation, we model the map $\mathcal{R}(\{TL, LL\}, (\xi, u))$ under the assumption of an inelastic collision and the map $\mathcal{R}(\{FF, TLs\}, (\xi, u))$ is modeled under the assumption of inelastic impact along the perpendicular of the landing slope and by considering energy conservation – see among others [Bro96]. This results in a trivial transition from TL to LL where the angular velocity of the vehicle is simply set to zero when the second landing gear makes contact with the landing slope. The transition from Free Flight to the TLs operating mode is more complex and is analyzed in the sequel. The kinetic energy of the vehicle, ignoring the constant lateral velocity along the slope, before and after the impact is given respectively by

$$E^- = \frac{1}{2}m(\dot{\zeta}_{CM}^-)^2 + \frac{1}{2}m(\dot{\alpha}_{CM}^-)^2 + \frac{1}{2}\mathbb{J}(\dot{\theta}^-)^2$$

and

$$E^+ = \frac{1}{2}m(\dot{\alpha}_{CM}^+)^2 + \frac{1}{2}m\ell_g^2\cos^2\gamma(\dot{\theta}^+)^2,$$

where $(\alpha_{CM}, \zeta_{CM})$ are the coordinates of the center of mass in frame $\{\mathcal{L}\}$. With $c_E \in (0, 1]$ an energy loss coefficient, it turns out that $(E^+)^2 = c_E(E^-)^2$ and then

$$\dot{\theta}^+ = c_E\sqrt{\dot{\zeta}_{CM}^-/(\ell_g^2\cos^2\gamma) + \mathbb{J}\dot{\theta}^-/(m\ell_g^2\cos^2\gamma)}.$$

and

$$(\dot{\alpha}_{CM}^+)^2 = \sqrt{c_E}(\dot{\alpha}_{CM}^-)^2.$$

Then by considering the constraint on ζ_{CM} characterizing $\mathcal{D}_{TLs}$ and $\mathcal{D}_{TLs}$ we obtain $\dot{\zeta}_{CM}^+ = \dot{\theta}^+\ell\cos(\theta^+ + \gamma + \beta)$.

5.3 The control problem

5.3.1 Robust control strategy and architecture

With the hybrid automaton in hand, the problem of performing a take-off maneuver can be reformulated as a problem of changing the operative mode q from the initial landed configuration LL to the final free-flight mode FF, by passing through intermediate states like TL and TLs. The problem requires control policies achieving a transition to a desired operative mode robustly with respect to uncertainties in the model and environment parameters. At the same time, all transitions leading to an undesired final configuration must be avoided. Motivated by the scenario in Figure 5.5, the targeted take-off maneuver involves the transition between the following sequence of hybrid states $LL \rightarrow TL \rightarrow TLs \rightarrow FF$. In all the above sequence the state LLs is regarded as a non-ideal state to be avoided in the course of the maneuver. Indeed, the system in the LLs mode lacks of control authority in the lateral direction, rendering LLs an undesired state when targeting robust maneuvers.

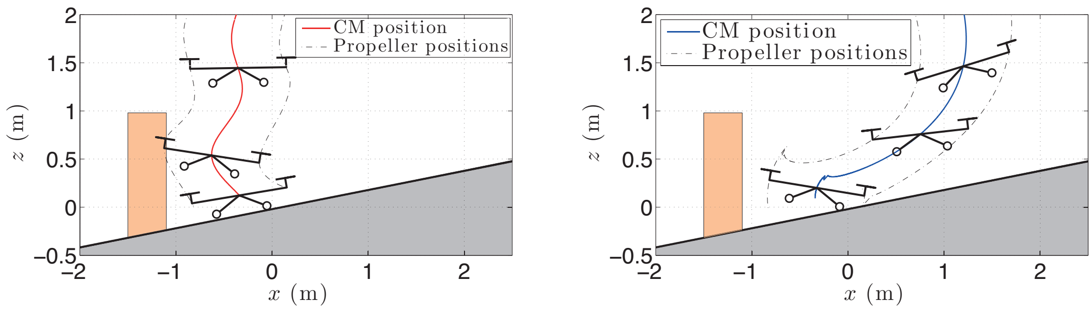

Figure 5.5: Left: the quadrotor hits an obstacle if uncontrolled vertical thrusts are applied. Right: a safe take-off maneuver.

Inspired by the general framework proposed in [MNG09], the control problem is divided into two different steps. The first step amounts to computing, for each of the three desired transitions ($LL \rightarrow TL$, $TL \rightarrow TLs$ and $TLs \rightarrow FF$) and for the final free flight mode, reference trajectories for both the states ξ and the inputs u of the system, jointly denoted as *reference maneuvers*, whose tracking guarantees that the desired transition takes place. A key issue is to generate *robust reference maneuvers* whose practical, and not perfect, tracking guarantees the desired transition while preventing the system to entering undesired modes. In the proposed framework robustness is quantified in terms of a design parameter $\epsilon > 0$ that roughly expresses how far the actual motion of the system's state and input can be with respect to the reference maneuver in order to have the desired transition effectively imposed.

The second step consists of designing feedback control laws guaranteeing that, for the given reference maneuvers, the tracking error (both in the state and in the input) is upper bounded by ϵ so that the planned transition is enforced. To this purpose the proposed control architecture (sketched in Figure 5.6) is constituted by a set of low level controllers, associated to the specific operative modes in which the vehicle operates, and a supervisor. The role of the latter is to enable the appropriate low level controller, and to feed it with the appropriate robust reference maneuver. The key requirement behind the design of the low level controllers is to guarantee that, under appropriate restrictions on the initial conditions and bound on the parametric/exogenous disturbances, the tracking error is upper bounded by ϵ.

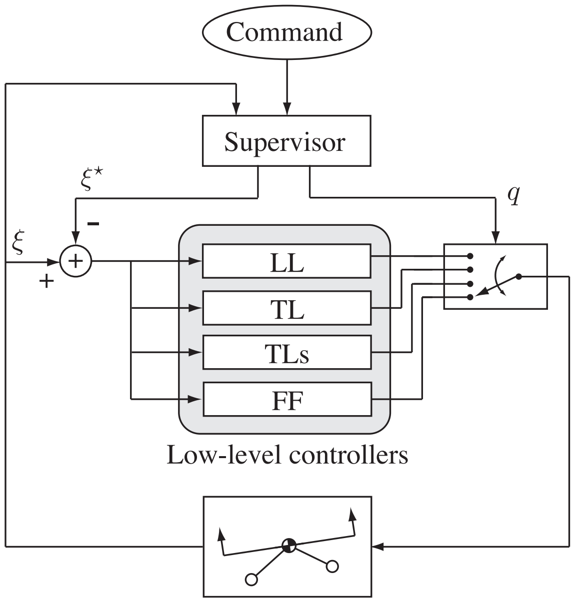

Figure 5.6: Proposed control architecture, featuring the supervisor and low-level controllers.

5.3.2 Design of robust reference maneuvers

The computation of robust reference maneuvers regarding a desired transition between the generic hybrid states $q_1^\star$ and $q_2^\star$ involves a problem of nominal inversion of the system dynamics in the operative mode $q_1^\star$ that can be approached in different ways. In this chapter, the problem is formulated as an optimal problem and a numerical tool is used for the practical computation of the reference maneuvers (see Section 5.4 for details on the adopted numerical tool). With $\dot{\xi} = f(q_1^\star, \xi, u, \rho)$ the model of the system in the operative mode $q_1^\star$ with parametric uncertainty ρ, the optimal problem is formulated, in general terms, as follow:

$$
\begin{aligned}
&\min_{u^\star(t),\xi^\star(t),t_f} \; t_f + \int_{t_0}^{t_f} \|u^\star(\tau)\|^2 d\tau \\
&\text{subject to} \\
&(a)\ \dot{\xi}^\star = f(q_1^\star, \xi^\star(t), u^\star(t), \rho_0), \quad \xi^\star(t_0) = \xi_0^\star,\ t \in [t_0, t_f] \\
&(b)\ u^\star(t) \in \mathcal{U}, \quad t \in [t_0, t_f] \\
&(c)\ \chi_\epsilon(q_1^\star, q_2^\star, \xi^\star(t), u^\star(t)) \le 0, \quad t \in [t_0, t_f] \\
&(d)\ \Psi_\epsilon(q_1^\star, q_2^\star, \xi^\star(t_f), u^\star(t_f)) \le 0.
\end{aligned}
$$

In the previous formulation the index cost is clearly shaped in order to trade-off the time needed to accomplish the desired maneuver (note that the final time t_f is a degree-of-freedom) and the required control energy, which depends on the magnitude of the forces generated by the quadrotor propellers. The constraints (a) and (b) force the solution to be functionally controllable for the nominal system in the operative mode $q_1^\star$ and to fulfill actuator limitations characterizing the real system. In this respect it is worth noting that nominal value ρ_0 of the uncertainty ρ is used in (a), namely that an inversion of the *nominal* system is necessarily targeted. A special role in (a) is played by the initial condition $\xi_0^\star$ that is a degree-of-freedom to be played in order to properly concatenate consecutive reference maneuvers in the sequence of transitions. Finally, the functions $\chi_\epsilon(\cdot)$ and $\Psi_\epsilon(\cdot)$ in (c) and (d) must be properly specified in order to have the maneuver $(\xi^\star(t), u^\star(t))$ solution of the optimal problem accomplishing the desired transition task. In this respect, by bearing Section 5.3.1 and the meaning of the parameter ϵ in the definition of robust transition maneuver, the function $\chi_\epsilon(\cdot)$ must be specified in a way that maneuvers $(\xi^\star(t), u^\star(t))$ fulfilling (c) are necessarily ϵ-far from any undesired guard set (i.e. guard set different from $\mathcal{G}(q_1^\star, q_2^\star)$), so that switches to undesired hybrid modes are avoided. In a more precise way $\chi_\epsilon(\cdot)$ must be such that any $(\xi^\star(t), u^\star(t))$ fulfilling (c) necessarily satisfies

$$
(x^\star(t), u^\star(t)) \bigcap \left(\bigcup_{(q_1^\star, q_2) \in \mathcal{E},\, q_2 \neq q_2^\star} \mathcal{G}(q_1^\star, q_2) + \mathcal{B}_\epsilon \right) = \emptyset
$$

for all $t \in [t_0, t_f]$. Furthermore, possible other path constraints, such as the avoidance of obstacles nearby the take-off area, can be taken into account in the definition of $\chi_\epsilon(\cdot)$ by defining forbidden regions in the x-z plane.

As far as the constraint (d) is concerned, the function $\Psi_\epsilon(\cdot)$ must be properly shaped in a way that any maneuver $(\xi^\star(t), u^\star(t))$ fulfilling (d) at time t_f is necessarily ϵ-inside the guard set $\mathcal{G}(q_1^\star, q_2^\star)$, namely

$$
(\xi^\star(t_f), u^\star(t_f)) + \mathcal{B}_\epsilon \subset \mathcal{G}(q_1^\star, q_2^\star).
$$

In this way any actual maneuver $(\xi(t), u(t))$ that is ϵ-close to $(\xi^\star(t), u^\star(t))$ necessarily enters, at a time upper bounded by t_f, the set $\mathcal{G}(q_1^\star, q_2^\star)$ so that the desired transition is enforced.

It is worth noting that possible uncertainties characterizing the environment (such as the slope of the terrain, the friction coefficient, the position of nearby obstacles, etc.) affect, in general, the definition of the guard sets and thus the design of $\chi_\epsilon(\cdot)$ and $\Psi_\epsilon(\cdot)$. In this respect a crucial issue in the specification of $\chi_\epsilon(\cdot)$ and $\Psi_\epsilon(\cdot)$ is to adopt the *a priori* knowledge about the uncertainties (such as compact sets where they range) so that the fulfillment of (c) and (d) leads to the desired transition robustly.

The above optimization problem is solved for each of the transition maneuvers $LL \to TL$, $TL \to TLs$, and $TLs \to FF$, with the constraints derived keeping in mind the description of the hybrid automaton presented in Section 5.2. In order keep the analysis at a tractable level, we only consider uncertainties in the ground friction coefficient μ, which affects the modes where contact with the ground exists, and no uncertainties in the slope β of the landing surface. About the value of μ we assume to know only upper and lower bounds denoted by μ^U and μ^L, respectively, and we let $\mu_0 \in [\mu^L, \mu^U]$ be the nominal value of μ.

5.3.3 Design of low-level controllers

In this part we address the design of the local controllers in each operating mode involved in the take-off maneuver. The goal of the controller is guarantee that, under appropriate restrictions on the initial conditions and of the exogenous disturbances, the specific reference maneuver is tracked with an error that is upper bounded by ϵ so that the desired transition takes place.

Low level controller in the LL mode

With $u^\star(t) = (v_1^\star(t), v_2^\star(t)) : [t_0, t_f] \to \mathbb{R}^2$ and $\xi^\star(t) = (F_1^\star(t), F_2^\star(t)) : [t_0, t_f] \to \mathbb{R}^2$ a robust reference maneuver solution of the optimal problem in Section 5.3, for some $\epsilon > 0$ and dynamics (5.10) and (5.11), the control law is simply chosen as

$$v_1 = -k(F_1 - F_1^\star) + v_1^\star, \quad v_2 = -k(F_2 - F_2^\star) + v_2^\star \tag{5.12}$$

where k is a positive design parameter.

Low level controller in the TL mode

With $u^\star(t) = (F_1^\star(t), F_2^\star(t)) : [t_0, t_f] \to \mathbb{R}^2$ and $\xi^\star(t) = (\theta^\star(t), \dot{\theta}^\star(t)) : [t_0, t_f] \to \mathbb{R}^2$ a robust reference maneuver solution of the optimal problem in Section 5.3.2, applied to the TL mode dynamics (5.8), for some $\epsilon > 0$, we define (see (5.3))

$$F_\theta^\star(t) = \begin{pmatrix} 0 & 1 \end{pmatrix} L(\theta^\star(t))^{-1} G(\theta^\star(t)) M \begin{pmatrix} F_1^\star(t) \\ F_2^\star(t) \end{pmatrix}$$

for all $t \in [t_0, t_f]$.

The control law for the TL dynamics (5.8) is then chosen as

$$F_\theta = -K_P(\theta - \theta^\star + K_D(\dot\theta - \dot\theta^\star)) + F_\theta^\star \tag{5.13}$$

with K_D, K_P positive design parameters. It turns out that K_D and K_P can be tuned so that the closed-loop trajectory tracks, with an error bounded by ϵ, the reference maneuver provided that initial error and the uncertainty on μ are sufficiently small. This is detailed in the next proposition (whose proof is deferred in Appendix B.1) in which we let $u = (F_1, F_2)$ and $\xi = (\theta, \dot\theta)$.

Proposition 20. *Consider the closed-loop system resulting from* (5.8) *and* (5.13)*. Let* $K_D > 0$*. There exists a* $K_P^\star > 0$ *such that for all* $K_P \geq K_P^\star$ *there exist* $\Delta_{TL,0} > 0$ *and* $\Delta_{TL,\mu} > 0$ *such that if* $\|\xi(t_0) - \xi^\star(t_0)\| < \Delta_{TL,0}$ *and* $\|\mu - \mu_0\| \leq \Delta_{TL,\mu}$ *the following holds*

$$\|(\xi(t) - \xi^\star(t), u(t) - u^\star(t))\| < \epsilon \qquad \forall\ t \in [t_0, t_f].$$

Low level controller in the TLs mode

With $u^\star(t) = (F_1^\star(t), F_2^\star(t)) : [t_0, t_f] \to \mathbb{R}^2$ and $\xi^\star(t) = (\alpha^\star(t), \dot\alpha^\star(t), \theta^\star(t), \dot\theta^\star(t)) : [t_0, t_f] \to \mathbb{R}^4$ a robust reference maneuver solution of the optimal problem in Section 5.3.2, for some $\epsilon > 0$ and using the dynamics (5.5), we define (see (5.3))

$$\begin{pmatrix} F_\alpha^\star(t) \\ F_\theta^\star(t) \end{pmatrix} = L(\theta^\star(t))^{-1} G(\theta^\star(t)) M \begin{pmatrix} F_1^\star(t) \\ F_2^\star(t) \end{pmatrix}$$

for all $t \in [t_0, t_f]$.

The control law for the TLs dynamics (5.5) is then chosen as

$$\begin{aligned} F_\alpha &= -K_P(\alpha - \alpha^\star + K_D(\dot\alpha - \dot\alpha^\star)) + F_\alpha^\star \\ F_\theta &= -K_P(\theta - \theta^\star + K_D(\dot\theta - \dot\theta^\star)) + F_\theta^\star \end{aligned} \tag{5.14}$$

with K_D, K_P positive design parameters. The main properties of the closed-loop system are detailed in the next proposition in which it is show how, for an appropriate tuning of K_D and K_P, the actual closed-loop trajectory remains ϵ-close to the robust reference maneuver provided that the initial condition is sufficiently close to the reference and the uncertainty on μ is sufficiently small. In the statement of the proposition we let $u = (F_1, F_2)$ and $\xi = (\alpha, \dot\alpha, \theta, \dot\theta)$.

Proposition 21. *Consider the closed-loop system* (5.5) *and* (5.14). *There exist a* $K_D^\star > 0$ *and, for all positive* $K_D \le K_D^\star$*, a* $K_P^\star > 0$ *such that for all* $K_D \le K_D^\star$ *and* $K_P \ge K_P^\star$ *there exist* $\Delta_{TLs,0} > 0$ *and* $\Delta_{TLs,\mu} > 0$ *such that if* $\|\xi(t_0) - \xi^\star(t_0)\| < \Delta_{TLs,0}$ *and* $\|\mu - \mu_0\| \le \Delta_{TLs,\mu}$ *the following holds*

$$\|(\xi(t) - \xi^\star(t), u(t) - u^\star(t))\| < \epsilon \qquad \forall\, t \in [t_0, t_f].$$

The proof of the proposition is deferred in Appendix B.2.

Control in free flight

Let $u^\star(t) = (F_1^\star(t), F_2^\star(t)) : [t_0, t_f] \to \mathbb{R}^2$ and $\xi^\star(t) = (z^\star(t), \dot z^\star(t), x^\star(t), \dot x^\star(t), \theta^\star(t), \dot\theta^\star(t)) : [t_0, t_f] \to \mathbb{R}^6$ a robust reference maneuver solution of the optimal problem in Section 5.3.2 for some $\epsilon > 0$ and using the free flight operative mode dynamics (5.2). The control law governing the quadrotor is free-flight is chosen as follow

$$\begin{pmatrix} F_1 \\ F_2 \end{pmatrix} = \frac{1}{2}\begin{pmatrix} \dfrac{1}{\cos\theta} & 1 \\ \dfrac{1}{\cos\theta} & -1 \end{pmatrix}\begin{pmatrix} u_1 + (F_1^\star + F_2^\star)\cos\theta^\star \\ u_2 + F_1^\star - F_2^\star \end{pmatrix} \tag{5.15}$$

where

$$\begin{aligned} u_1 &= -k_1(z - z^\star) - k_2(\dot z - \dot z^\star) \\ u_2 &= -K_P(K_D(\dot\theta - \dot\theta^\star) + \tan\theta - \tan\theta^\star + \theta_{\text{out}}) \end{aligned} \tag{5.16}$$

and

$$\theta_{\text{out}} = \lambda_2 \sigma\left(\frac{K_2}{\lambda_2}\zeta\right), \quad \zeta = \dot x - \dot x^\star + \lambda_1 \sigma\left(\frac{K_1}{\lambda_1}(x - x^\star)\right) \tag{5.17}$$

where K_D, K_P, k_i, λ_i, K_i, with $i = \{1, 2\}$, are positive design parameters and $\sigma(\cdot)$ is a saturation function. The proposed control structure rests upon the design idea proposed in [IMS03] and can be interpreted as a cascade control structure constituted by an inner loop, controlling the angular $(\theta, \dot\theta)$ dynamics, and an outer loop governing the lateral $(x, \dot x)$ and vertical $(z, \dot z)$ dynamics. The next proposition details the tuning of the previous controller in order to achieve the desired asymptotic properties. In the statement of the proposition we let $u = (F_1, F_2)$, $\xi = (z, \dot z, x, \dot x, \theta, \dot\theta)$. Furthermore, the tuning of the controller is given in terms of two parameters u^L and u^U defined as

$$u^L := \min_{t \in [t_0, t_f]} (F_1^\star(t) + F_2^\star(t))\cos\theta^\star(t), \qquad u^U := 2F_{\max}.$$

For a proof, we refer the reader to [IMS03] (see also [MN07]).

Proposition 22. *Consider the closed-loop system given by* (5.2) *and* (5.15)-(5.17) *where* δ_x *and* δ_z *are exogenous bounded disturbances. Let* k_1, k_2 *be positive parameters and let* λ_i, K_i *be chosen as* $\lambda_i = \varepsilon^{i-1}\lambda_i^\star$, $K_i = \varepsilon K_i^\star$, $i = 1, 2$, *where* ε *is a design parameter and* $(\lambda_i^\star, K_i^\star)$ *satisfy*

$$\frac{\lambda_2^\star}{K_2^\star} < \frac{\lambda_1^\star}{4}, \quad 8K_1^\star\lambda_1^\star < u_L\lambda_2^\star, \quad 24\frac{K_1^\star}{K_2^\star} < \frac{1}{6}\frac{u_L}{u_U}.$$

There exist $K_D^\star > 0$, $K_P^\star(K_D) > 0$ *and* $\varepsilon^\star(K_P) > 0$ *such that for any positive* $K_D < K_D^\star$, $K_P \geq K_P^\star(K_D)$ *and* $\varepsilon \leq \varepsilon^\star(K_P)$ *there exist* $\Delta_{FF,0} > 0$ *and* $\Delta_{FF,d} > 0$ *such that if* $\|\xi(t_0) - \xi^\star(t_0)\| \leq \Delta_{FF,0}$ *and* $\|(\delta_x, \delta_z)\|_\infty \leq \Delta_{FF,d}$ *the following holds*

$$\|(\xi(t) - \xi^\star(t), u(t) - u^\star(t)\| < \epsilon \qquad \forall\, t \in [t_0, t_f].$$

5.3.4 Supervisor design

With the definition of robust reference maneuvers and the properties of the low-level controllers highlighted above, the design of the supervisor reduces to orchestrate the switch of the low-level controllers and drive them with the appropriate reference maneuver according to the actual state of the vehicle. Specifically, we assume that four robust reference maneuvers $(\xi_{LL}^\star, u_{LL}^\star) : [t_{01}, t_{f1}] \to \mathcal{D}(LL)$, $(\xi_{TL}^\star, u_{TL}^\star) : [t_{02}, t_{f2}] \to \mathcal{D}(TL)$, $(\xi_{TLs}^\star, u_{TLs}^\star) : [t_{03}, t_{f3}] \to \mathcal{D}(TLs)$, $(\xi_{FF}^\star, u_{FF}^\star) : [t_{04}, t_{f4}] \to \mathcal{D}(FF)$ are given as solutions of the optimal problem developed in Section 5.3.2 for some fixed ϵ and respective operative mode. Furthermore, with the reference maneuvers and ϵ fixed, we fix the four low-level controllers according to the structures and the design principles specified in Section 5.3.3. Specifically, we let u_{LL}, u_{TL}, u_{TLs}, u_{FF} be the control laws designed respectively in (5.12), (5.13), (5.14) and (5.15)-(5.17)

The supervisor logic switches the low-level controller according to the actual state $q(t)$ of the vehicle. The latter takes value in the set $\{LL, TL, TLs, FF\}$ and it is supposed to be known by the reading of sensors appropriately placed in the quadrotor airframe. The supervisor logic is thus simply $u(t) = u_{q(t)}(t)$. In the next items we detail the main properties achieved by the resulting closed-loop system that show how the desired take-off maneuver takes place. The claims in the items come immediately by joining the notion of robust reference maneuver and the properties of the low-level controllers highlighted in the Propositions in Section 5.3.3.

- Let $F_1(t_{01})$, $F_2(t_{02})$ be fulfilling the initial state restriction in the landed operative mode. Then there exists a time $t_{s1} \leq t_{f1}$ such that $q(t) = LL$ for all $t \in [t_{01}, t_{s1})$ and $q(t_{s1}) = TL$. At time t_{s1} the low-level controller is thus switched to u_{TL}.

- Let the uncertainties on the friction value be fulfilling $|\mu - \mu_0| \leq \Delta_{TL,\mu}$ with $\Delta_{TL,\mu}$ coming from Proposition 20. Then there exists a time $t_{s2} \leq t_{s1} + t_{f2} - t_{02}$ such that $q(t) = TL$ for all $t \in [t_{s1}, t_{s2})$ and $q(t_{s2}) = TLs$. At time t_{s2} the low-level controller is thus switched to u_{TLs}.

- Let the uncertainties on the friction value be fulfilling $|\mu - \mu_0| \leq \Delta_{TLs,\mu}$ and let $\xi^\star(t_{03})$ and $\xi(t_{s2})$ be such that $\|\xi(t_{s2}) - \xi^\star(t_{03})\| \leq \Delta_{TLs,0}$ with $\Delta_{TLs,\mu}$ and $\Delta_{TLs,0}$ introduced in Proposition 21. Then there exists a time $t_{s3} \leq t_{s2} + t_{f3} - t_{03}$ such that $q(t) = TLs$ for all $t \in [t_{s2}, t_{s3})$ and $q(t_{s3}) = FF$. At time t_{s3} the low-level controller is thus switched to u_{FF}.

- Let the exogenous disturbances (δ_x, δ_z) be fulfilling $\|(\delta_x, \delta_z)\|_\infty \leq \Delta_{FF,d}$ and let $\xi^\star(t_{04})$ and $\xi(t_{s3})$ be such that $\|\xi(t_{s3}) - \xi^\star(t_{04})\| \leq \Delta_{FF,0}$ with $\Delta_{FF,d}$ and $\Delta_{FF,0}$ introduced in Proposition 22. Then for all $t \in [t_{s3}, t_{s3} + t_{f4} - t_{04}]$ the vehicle evolves robustly in free-flight by tracking the reference maneuver with an error upper bounded by ϵ.

5.4 Simulation results

In this section we present the results from a simulation run of the proposed controller conducted using a software simulator for hybrid systems [GST09]. To compute the reference maneuvers as solutions to the constrained optimal control problems formulated in Section 5.3.2, a numerical tool, named DIDO, has been adopted. DIDO implements a *direct collocation method* (see for example [Bet01] for an overview of numerical optimization techniques) based upon Legendre pseudo-spectral (PS) approximation. A detailed description of the tool can be found in [Ros04]. The numerical optimization process of DIDO can be controlled by setting the number of node points. Limiting to 20 the maximum number of nodes employed to generate the maneuvers used in the simulations, obtaining in few seconds feasible suboptimal solutions to be used directly as references.

The vehicle and terrain parameters are $m = 1$ kg, $J = 0.5$ kg m^2, $l_g = 0.3$ m, $\gamma = 30°$, $r = 0.5$ m, $\beta = 0.2$ rad, $\mu = 0.45$, and $\mu_0 = 0.5$. The controller design parameters are $K_P = 3$, $K_D = 3$ for the TL and TLs modes local controllers and $K_D = 0.3$, $K_P = 70$ for the FF controller. To attest the robustness of the proposed controller to sensor noise, the measurements of the states have been corrupted with additive gaussian white noise of zero mean and standard deviation of 0.02 m, 0.02 m/s, 1.14° and 1.14°/s. The vertical bars overimposed on the figures denote the time instants when a transition of hybrid state occurs.

For the take-off procedure, the reference trajectory consists of a sequence of robust approach maneuvers LL→TL, TL→TLs, and TLs→FF, resulting in the vehicle sliding up the slope. This maneuver is chosen in contrast with the situation presented in Figure 5.5, where the application of a heuristic take-off procedure results in the quadrotor sliding down the slope and hitting an obstacle.

The time evolution of the system's states and actuations are presented in Figure 5.7. The discontinuities that arise in the forces and the reference trajectories are due to the fact that the initial conditions for the new transition maneuver do not necessarily correspond to the end conditions of the approach maneuver leading into it. The final discrepancy between the desired and the actual trajectory is due to an imperfect knowledge of the friction coefficient μ. As a consequence, practical tracking of the trajectories is achieved, with an error smaller than ϵ, and the maneuver culminates with a successful robust transition to the free flight operative mode.

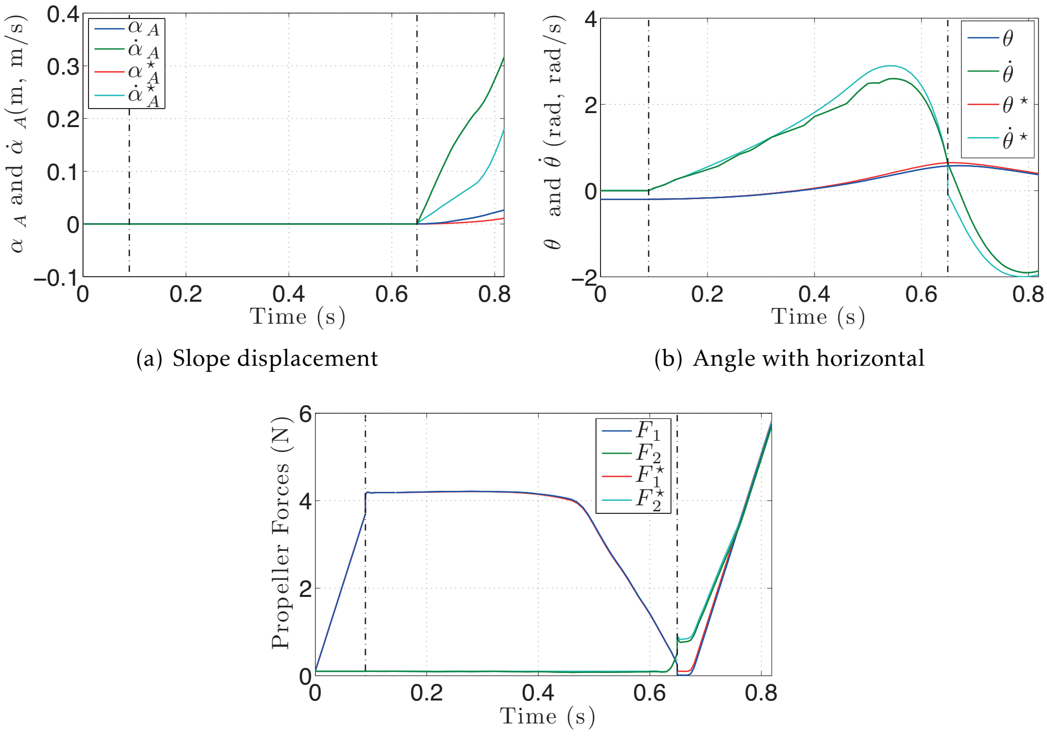

(a) Slope displacement

(b) Angle with horizontal

(c) Actuations

Figure 5.7: Comparison of the simulation maneuver and the desired maneuver for the quadrotor take-off.

5.5 Experimental Results

In this section we present the results for an experimental run of the proposed hybrid controller. The inputs for the quadrotor used in this experiment do not include each motor force individually, thereby preventing the straight forward experimental testing of the theoretical framework. To overcome this issue, the $\ddot{\theta}$ dynamics are integrated in simulation using the appropriate dynamics (5.2), (5.5) or (5.8), together with the inputs F_1 and F_2 coming from the low level controllers. The resulting angular velocity $\dot{\theta}$ and the total thrust are then used as inputs for the physical quadrotor. This setup is depicted in Fig. 5.8, where VICON denotes the OMCS that measures the vehicle's position and velocity.

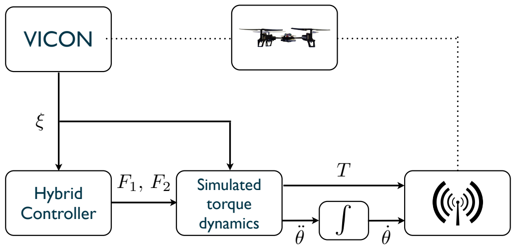

Figure 5.8: Experimental setup with simulated quadrotor state.

5.5.1 Transition maneuvers

The proposed complete landing maneuver is depicted in Fig. 5.9. The landing procedure starts in free flight, where a horizontal landing path is tracked. This eventually leads to a collision with the sloped ground, at which instant the supervisor selects the TLs controller and starts tracking a reference maneuver that leads the quadrotor to the TL state. The quadrotor then slides up the slope, tracking a TLs to TL trajectory, until it comes to a halt at a desired location. Upon coming to a halt, the quadrotor transitions to the TL operating mode and the supervisor uses the TL low-level controller to track a TL to LL trajectory that finally levels the quadrotor with the ground, without starting to slide again. Once all the landing gear contact points touch the ground and the final transition to the Landed mode is complete, the motors are turned off and the quadrotor remains at rest.

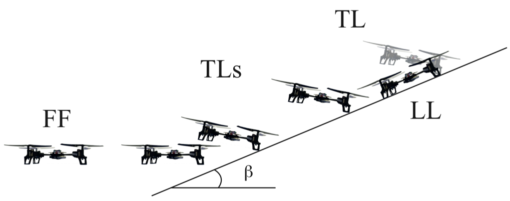

Figure 5.9: Sketch of a complete quadrotor landing maneuver

FF → TLs robust transition maneuver

For taking the aircraft from free flight to the takeoff-and-landing sliding operating mode we propose a maneuver that leads to the quadrotor sliding up. In that situation we have $\dot{\alpha} > 0$, which results in a G matrix that is well-conditioned (see (5.4)), thereby avoiding problems when inverting (5.3) to obtain the inputs F_1 and F_2. In addition, the maneuver was chosen to have a minimal impact on the quadrotor upon touchdown on the landing slope. The quadrotor is chosen to track a horizontal line at a constant velocity until the contact point A of the landing gear touches the landing slope. For the quadrotor model in

(5.2), the reference maneuver is defined as

$$
\begin{aligned}
x^\star(t) &= x_0,\\
y^\star(t) &= y_0 + v_y(t - t_0),\\
\theta^\star(t) &= 0,\\
F_1^\star(t) = F_2^\star(t) &= mg/2,
\end{aligned}
$$

for positive lateral velocity v_y, initial conditions $x_0, y_0 \in \mathbb{R}$ and initial time $t_0 \in \mathbb{R}$. The positive velocity corresponds to a landing maneuver where the quadrotor lands from the lower side of the slope. If tracked with an error smaller than ϵ, this maneuver ensures that only one of the quadrotor's landing gears hits the slope and that the quadrotor starts to slide on the ground, forcing a transition to the TLs mode. The time instant at which the transition occurs depends on the location of the slope, the quadrotor initial position (x_0, y_0) and the lateral approach velocity v_y.

TLs $\rightarrow$ TL robust transition maneuver

Following Fig. 5.9, in the TLs operating mode the quadrotor tracks a straight line along the slope and decreases its velocity, until it comes to a halt. We define a reference maneuver with constant acceleration for the contact point and a fixed tilt angle as follows

$$
\begin{aligned}
\alpha^\star(t) &= \alpha_0 + v_\alpha(t - t_0) - a_\alpha(t - t_0)^2,\\
\theta^\star(t) &= \theta_0,
\end{aligned}
$$

for initial conditions $\alpha_0 \in \mathbb{R}$ and positive parameters v_α, a_α and θ_0. The corresponding reference inputs $F_1^\star(t)$ and $F_2^\star(t)$ are obtained by dynamic inversion of vehicle model. A set of maneuvers with different initial condition parameters at the initial time instant t_0 is considered so as to cover the whole region of possible initial conditions that arises when the tracking of the preceding maneuver is not perfect. The tilt angle θ_0 that the quadrotor follows while sliding should be slightly positive so that the quadrotor is able to slide along the slope robustly, without returning to the free flight operating mode. The transition to TL occurs when $\dot{\alpha} = 0$. That final time instant, denoted as t_f, depends on the initial velocity v_α and the desired acceleration a_α. The final landing location along the slope also depends on these two parameters and the initial location of the quadrotor. It can be made constant for all trajectories by varying the acceleration parameter a_α

$$
a_\alpha = \frac{v_\alpha^2}{\alpha^\star(t_f) - \alpha^\star(t_0)}.
$$

Figure 5.10: Quadrotor performing a TLs to TL robust transition maneuver

TL $\rightarrow$ LL robust transition maneuver

Once the quadrotor comes to a halt, the objective is to bring it to the slope level, without inducing a sliding movement again. In this operating mode we are only interested in controlling the tilt angle, for which we define the reference trajectory

$$\theta^\star(t) = \theta_0 - v_\theta t. \tag{5.18}$$

for a positive parameter v_θ. The quadrotor is finally leveled with the landing slope when $\theta^\star(t) = -\beta$. The reference input is determined by (5.18) and the reference *total thrust*, $T^\star = F_1^\star + F_2^\star$, which is chosen to converge from its initial value down to zero. In order for the maneuver to be robust, the balance between $T^\star(t)$ and $\theta^\star(t)$ must be such that the vehicle is always ϵ-far from restarting to slide during the whole transition maneuver. For the duration of this transition maneuver, the displacement of the landing gear contact point is constant, i.e. $\alpha(t) = \alpha_0$.

5.5.2 Experimental setup

To adapt the physical setup to a 2D control setting, the quadrotor is restricted to a vertical plane along the slope and its yaw is kept such that two of its landing gear contact points are aligned with the slope direction, as shown in Fig. 5.11. For the proposed maneuver, the quadrotor lands from the left to the right, relative to the figure, keeping the yaw angle such that both the right side contact points touch the slope at the same time. Landing with a correct yaw angle allows the quadrotor to tilt and continue in the same plane, therefore, satisfying the 2D approximation.

The quadrotor's 2D physical parameters are $l_g = r = 0.09\,\text{m}$, $h_{CM} = 0.025\,\text{m}$, $\ell = \sqrt{l_g^2 + h_{CM}^2}$, $\gamma = 15.5°$. The landing slope has a $\beta = 20°$ incline. The friction coefficient is taken as $\mu_0 = 1$. The controller design parameters are $K_{P\theta} = 3$, $K_{D\theta} = 0.2$, $K_{P\alpha} = 0.2$, $K_{D\alpha} = 0.15$, for the TL and TLs modes local controllers.

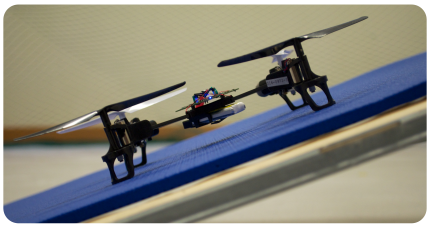

Figure 5.11: Quadrotor aligned with the landing slope.

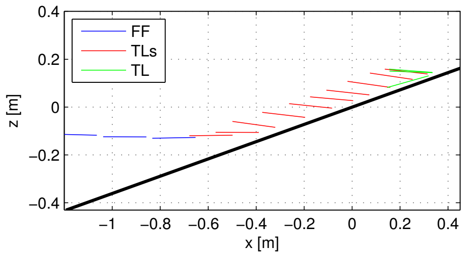

Figure 5.12: Profile view of the complete quadrotor landing maneuver

5.5.3 Landing results

For the landing procedure, the reference trajectory consists of a sequence of robust approach maneuvers FF→TLs, TLs→TL, and TL→LL, resulting in the vehicle sliding up the slope and coming to a halt at the desired landing point. The tracking of the quadrotor displacement and tilt angle is presented in Figs. 5.13 and 5.14. The figures are divided in four sections, corresponding to the four operation states transversed, with each one being labeled FF, TLs, TL or LL according to the respective operating mode. The transition to TLs occurs around 8 s and at 11.5 s the quadrotor stops sliding and enters the TL state. Finally, around 12 s the quadrotor has two points of contact with the ground and enters the LL state, completing the landing procedure.

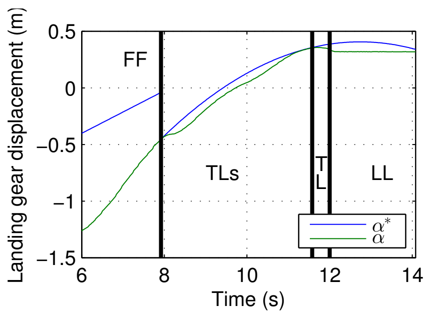

Figure 5.13: Horizontal displacement along the slope.

Observing Figure 5.13 we can see the effects of the initial impact with the slope at the 8 s. The quadrotor starts an initial slide along the slope but looses velocity. This

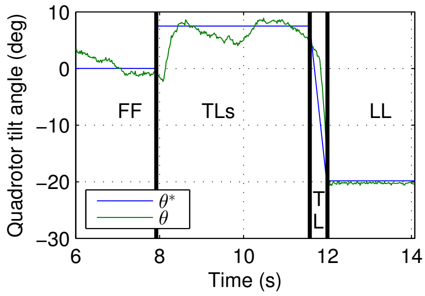

Figure 5.14: Quadrotor tilt angle.

velocity is quickly recovered as the quadrotor tries to track the desired maneuver. Finally, the quadrotor comes to a halt and a transition to TL occurs, with the landed state being attained shortly after. Despite all the uncertainties existing in the model, the controller proves to be robust and maintains the tracking error small.

Looking at Fig. 5.14, we see the time evolution of the quadrotor's tilt angle. In free flight this angle is approximately zero, as asserted in the reference maneuver discussion in Section 5.5.1. Once in TLs, the quadrotor tracks a reference maneuver where $\theta_0 = 7.5°$. This tilt angle is close enough to the initial angle and confers increased controllability to the quadrotor. Additionally, it helps to avoid a return to free flight situation, as could happen easily if the reference maneuver was defined with $\theta_0 = 0$. Once the TL state is entered, the quadrotor tries to follow a constant angular velocity trajectory that leads to the complete contract of the landing gear with the landing slope.

The evolution of the motor forces F_1 and F_2 throughout the maneuver is presented in Fig. 5.15. During the FF and TLs landing phases, the forces are similar in magnitude, reflecting a control of constant tilt angle. In TL however, F_2 drops drastically, when forcing the rotation of the quadrotor and consequent landing. Nonetheless, F_1 and F_2 are always positive and within the limits of the quadrotor actuation.

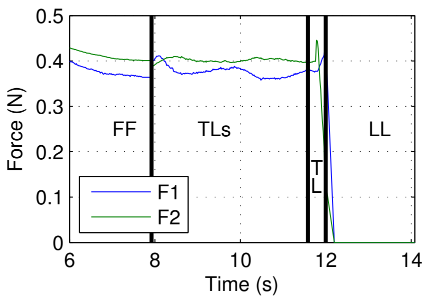

Figure 5.15: Quadrotor forces generated by the propellers.

The evolution of the distance of both landing gear extremities to the slope is shown in Fig 5.16. In FF, both distances decrease at the same rate until contact with the ground happens at 8 s and the quadrotor enters the TLs state. After the transition, the contact point A (see Fig. 5.2(b)) remains on the slope for the duration of the maneuver. The contact point B on the landing gear gains a slight distance and then remains approximately constant, as the quadrotor tilts to track θ_0 and goes up the slope. Once in the TL operating mode, the distance of point B diminishes, as the quadrotor rotates, until both points are in contact with the landing slope. The distance is computed from the quadrotor position and attitude, knowing the slope's location and incline. The small resulting errors are due to imperfections in the landing slope surface.

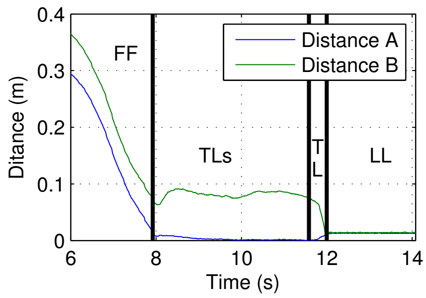

Figure 5.16: Distance of the landing gear to the slope.

5.6 Concluding remarks

This chapter addressed the problem of robust take-off and landing control of a quadrotor UAV, considering explicitly the interaction with the ground, that guarantees successful maneuvers even in sloped terrains and in the presence of external disturbances and uncertain parameters. The vehicle was modeled as a hybrid automaton, whose states reflect the different dynamic behaviors exhibited by the UAV. The take-off and landing procedures were then cast as the problem of changing the operating mode from the initial to the final desired state, through the edges allowed for the hybrid automaton. The transitions between intermediate operating modes were achieved through the application of low-level feedback controllers, associated with each mode, to track robust reference signals. The supervisor and the combined properties of the low-level controllers and reference trajectories ensures that the desired intermediate transitions are attained, robustly to with respect to uncertainties in the model and environment parameters, and that the final desired state is reached.

Experimental results using a small scale radio controlled quadrotor vehicle were presented to assess the feasibility of the proposed hybrid controller, demonstrating the effectiveness of the proposed solution, especially for the cases in which the slope of the terrain renders the landing maneuver more critical to be achieved. Simulation results were also presented for the takeoff maneuver, where a standard takeoff procedure would results in a collision, due to the slope of the terrain and the presence of a nearby obstacle.

Future works will be primarily focused on improvements to the hybrid dynamical model and the hybrid controller, towards having a vehicle that can operated resorting only to internal sensors. In particular, a complex integration of the sensors (contact, force) and avionics equipments will be required, extending the standard sensing capabilities of the vehicle in order to robustly detect the current operative mode. This latter issue suggests also to investigate methodological solutions aiming at improving robustness to the possible uncertainties that may affect the measure of the current hybrid state. Another interesting research topic is the appropriate extension of the proposed framework to a third dimension, by adapting the presented arguments, allowing the controller to handle more complex scenarios in terms of the characteristics of the possible environment of operation.

6 Integrated Solution to Quadrotor Stabilization and Attitude Estimation Using a Pan and Tilt Camera

This chapter presents an integrated solution to the problem of stabilizing a quadrotor and estimating its attitude. The solution comprises a nonlinear attitude observer and a nonlinear controller for position and attitude stabilization of a quadrotor, which are combined in a cascaded architecture. The attitude estimates are obtained from rate gyro measurements, corrupted by bias, and the image coordinates of a set of landmarks on the terrain which are acquired by a controllable pan and tilt camera. Lateral-longitudinal stabilization is achieved with a nested saturation control law by feedback of the image measurements, estimated body attitude, and corrected angular velocity measurements. The vehicle is stabilized vertically using an additional vertical position sensor. Resorting to the input-to-state stability property of the controller, the quadrotor position and attitude are shown to converge to the desired equilibrium point and the convergence is robust to estimation errors. Additionally, the pan and tilt camera is actively actuated to keep the landmarks visible in the image sensor for most operating conditions. The robustness and performance of the proposed control and estimation architecture is illustrated through both simulation and experimental results.

The operation of autonomous vehicles indoors and in obstructed or occluded locations (e.g. in the vicinity of tall and cluttered structures), where GPS signals are unreliable or simply unavailable, calls for alternative solutions based on local sensor measurements such as captured images [CH06, CH07]. Computer vision has long been recognized as an extremely flexible technique for sensing the environment and acquiring valuable information for pose estimation and control. Awareness of this potential has brought about a widespread interest in the field of vision-based control and localization.

The literature on vision-based rigid-body stabilization and estimation highlights important questions and indicates possible solutions to i) keep feature visibility along the system's trajectories for a large region of attraction [CWK02], [CSHA07], ii) minimize the required knowledge about the 3-D model of the observed object [MC02], iii) guarantee convergence in the presence of camera parametric uncertainty and image measurement noise [MC02], iv) establish observability conditions for attitude estimation [AH06]. A variety of algebraic and iterative estimation methods based on point and line correspondences have been proposed (see for example [YSKS04]). In [MTR+09], an inertial navigation system aided by computer vision is used to estimate the relative position, attitude and velocity. Algorithms for attitude estimation greatly benefit from the integration with inertial sensors, namely rate gyros and accelerometers as well as from the use of dynamic filtering and observer techniques [MTR+09, RG03, LD03].

Apart from rigid-body stabilization, vision-based control has been used to accomplish other tasks relying on different image features, such as straight line and curve representations [MH05, MKS99], and image centroids or higher order image moments [TC05]. For example, in [MH05], the authors propose an image-based controller to track parallel linear features for an underactuated vehicle. A controller for point stabilization based on backstepping and optical flow is presented in [MCH08]. A follow-the-leader problem for mobile robots equipped with panoramic cameras is addressed in [VSS04]. In [MKS99], the authors consider the problem of steering a mobile robot to track a ground curve by controlling the shape of the curve in the image plane. In both [MKS99] and [VSS04], the two-dimensional nature of the problem removes depth ambiguity from the image measurements, which indicates that an extension to 3-D space may not be straightforward.

The main contribution of this chapter is an integrated solution to motion stabilization and attitude estimation based on rate gyro measurements and visual information about a set of landmarks placed on the terrain, which are retrieved by a pan and tilt camera. The proposed nonlinear observer estimates the quadrotor attitude and the rate gyros bias, driving the estimation error exponentially fast to the origin. The pan and tilt camera controller differs from other solutions present in the literature (see e.g. [CH07]) as it does not require explicit estimation of the camera's position and velocity. The controller for quadrotor stabilization follows the approach proposed in [IMS03] and [MN07] and imposes a two-time scale dynamics, decoupling the vertical from the lateral-longitudinal subsystem. The vertical controller can be viewed as a time-varying proportional-derivative (PD) controller. A nested saturations control scheme is used to stabilize the lateral-longitudinal subsystem, which has a feedforward structure. In the proposed controller, only measurements from the available sensors and estimates from the attitude observer are used, instead of classical full-state feedback. Notwithstanding, due to the robustness and input-to-state stability (ISS) properties of each individual controller and the convergence rates guaranteed by the proposed observer, the overall stability of the interconnected system is established.

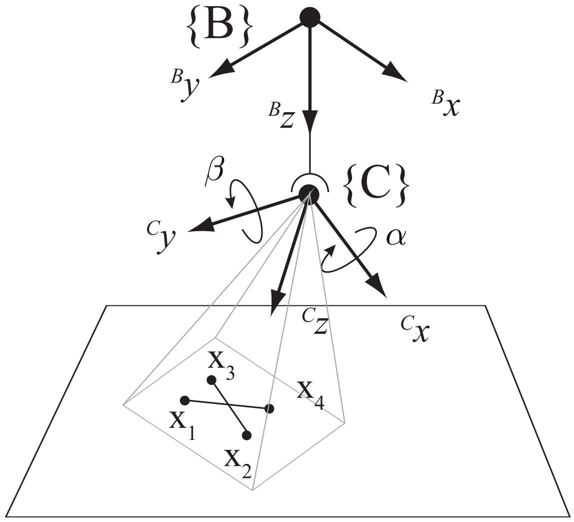

Figure 6.1: Diagram of the camera and landmarks setup.

The remainder of this chapter is organized as follows. The problem formulation is presented in Section 6.1, together with the pan and tilt camera model. The attitude observer is discussed in Section 6.2 and the nonlinear controller for the pan and tilt camera is described in Section 6.3. The quadrotor vehicle controller based on image measurements is proposed in Section 6.4, where the stability properties of the proposed feedback control architecture that includes the quadrotor and the camera controllers are shown. Simulation and experimental results are presented in Sections 6.5 and 6.6 attesting the robustness and feasibility of the proposed estimation and control architecture. Finally, concluding remarks are given in Section 6.7.

6.1 Problem formulation

In this chapter, we design a control law for the quadrotor, a control law for the pan and tilt camera and an estimator for the vehicle attitude, whose interconnection stabilizes the quadrotor in hover above certain terrain landmarks.

The problem setup is illustrated in Fig. 6.1, where the reference frames used to derive the quadrotor and camera models are depicted. We consider a fixed inertial frame $\{\mathcal{I}\}$ and a body frame $\{\mathcal{B}\}$ attached to the vehicle's center of mass. The configuration of $\{\mathcal{B}\}$ with respect to $\{\mathcal{I}\}$ is given by the pair $(R, \mathbf{p}) = ({}^I_BR, {}^I\mathbf{p}_B)$. Connected to the aerial vehicle is a pan and tilt camera with reference frame denoted by $\{\mathcal{C}\}$. Its origin coincides with the camera's center of projection, and the z-axis is aligned with the camera optical axis. The observed scene consists of four points, whose coordinates in $\{\mathcal{I}\}$ are denoted by ${}^I\mathbf{x}_i \in \mathbb{R}^3$, $i \in 1, \ldots, 4$. Without loss of generality, the origin of $\{\mathcal{I}\}$ is assumed to coincide with the centroid of the feature points so that $\sum_{i=1}^4 {}^I\mathbf{x}_i = 0$. Moreover, the landmarks are assumed to belong to the x–y plane.

We develop our control architecture taking into account that an external state measurement solution, such as a motion capture system, is not available to the vehicle, modeling realistic conditions in GPS-denied environments. As such, the control laws are required to make use solely of the camera images and onboard sensor measurements. We consider that a triad of rate gyros is installed onboard the platform and that it is aligned with $\{\mathcal{B}\}$, providing measurements of the body angular velocity $\boldsymbol{\omega}_B$ corrupted by a constant unknown bias term $\mathbf{b}$, such that

$$\boldsymbol{\omega}_r = \boldsymbol{\omega}_B + \mathbf{b}, \qquad \dot{\mathbf{b}} = \mathbf{0}.$$

In summary, the available measurements are the camera images, the pan and tilt camera angles, the angular rate measurements corrupted by bias and absolute altitude, provided by e.g. a pressure sensor, independent of the distance to the ground.

For controller design, we use the quadrotor dynamic model described in section 3.2, and summarized by (3.1)-(3.4), while the remaining system components are modeled in the sequel.

6.1.1 Camera model

As shown in Fig. 6.1, the camera can perform pan and tilt motions corresponding to the angles α and β, respectively. As such, the rotation matrix from $\{\mathcal{C}\}$ to $\{\mathcal{B}\}$ is given by

$$\begin{gathered} {}^{B}_{C}R = R_{\text{pan}} R_{\text{tilt}}, \\ R_{\text{pan}} = R_x(\alpha), \quad R_{\text{tilt}} = R_y(\beta) \end{gathered} \tag{6.1}$$

where $R_x(\cdot)$ and $R_y(\cdot)$ denote rotation matrices about the camera x-axis and y-axis, respectively. We denote the configuration of $\{\mathcal{C}\}$ with respect to $\{\mathcal{I}\}$ by $({}^{I}_{C}R, {}^{I}\mathbf{p}_C) \in SE(3)$, where ${}^{I}_{C}R$ is the rotation matrix from $\{\mathcal{C}\}$ to $\{\mathcal{I}\}$ and ${}^{I}\mathbf{p}_C$ the position of the origin of $\{\mathcal{C}\}$ with respect to $\{\mathcal{I}\}$. Then, the 3-D coordinates of the feature points expressed in $\{\mathcal{C}\}$ can be written as

$$\mathbf{r}_i = {}^{I}_{C}R^{T\,I}\mathbf{x}_i + {}^{C}\mathbf{p}_I,$$

for $i \in 1, \ldots, 4$ and where ${}^{C}\mathbf{p}_I = -{}^{C}_{I}R\,{}^{I}\mathbf{p}_C$. Using the perspective camera model [RG03], the 2-D image coordinates $\mathbf{y}_i \in \mathbb{R}^2$ of the landmark points are expressed as

$$\begin{bmatrix} \mathbf{y}_i \\ 1 \end{bmatrix} = \delta_i A \mathbf{r}_i, \tag{6.2}$$

where $A \in \mathbb{R}^{3\times 3}$ is the camera calibration matrix, assumed to be known, and δ_i is an unknown scalar encoding depth information and given by $\delta_i = (\mathbf{u}_3^T \mathbf{r}_i)^{-1}$, where $\mathbf{u}_3 = [0\ 0\ 1]^T$.

6.2 Attitude observer

In this section, we present a nonlinear observer for the vehicle attitude and angular velocity based on the image coordinates of the landmarks angular velocity measurements corrupted with constant bias. The nonlinear attitude observer follows [BCV+11] and is designed to match the rigid body attitude kinematics (3.3) by taking the form

$$\dot{\hat{R}} = \hat{R}S(\hat{\boldsymbol{\omega}}_B), \tag{6.3}$$

where $\hat{\boldsymbol{\omega}}_B$ is the feedback term designed to compensate for the estimation errors. The attitude and bias estimation errors are defined as $\tilde{R} = \hat{R}R^T$ and $\tilde{\mathbf{b}} = \hat{\mathbf{b}} - \mathbf{b}$, respectively. Using (3.3) and (6.3), the rotation error dynamics are given by

$$\dot{\tilde{R}} = \tilde{R}S(R(\hat{\boldsymbol{\omega}}_B - \boldsymbol{\omega}_B)). \tag{6.4}$$

Special care must be payed when defining the landmark feature's positions so as to ensure that all the rotational degrees of freedom are observable. This property is lost, for instance, when all the landmarks are collinear. The following assumption is a necessary condition to ensure that we can obtain a correct attitude estimation based on image measurements, as discussed in [BCV+11] and references therein.

Assumption 23. *There are at least four landmarks of which no three are collinear.*

The feedback law is a function of the angular rate measurements and the image coordinates of the landmarks. To derive it, we start by defining the following matrices

$$X = \begin{bmatrix} {}^I\mathbf{x}_1 & \cdots & {}^I\mathbf{x}_4 \end{bmatrix}, \quad Y = \begin{bmatrix} \mathbf{y}_1 & \cdots & \mathbf{y}_4 \\ 1 & \cdots & 1 \end{bmatrix},$$

where ${}^I\mathbf{x}_i$ are the 3-D coordinates of the feature points expressed in $\{\mathcal{I}\}$ and $\mathbf{y}_i$ the corresponding 2-D image coordinates. Recall that, as discussed in Section 6.1, without loss of generality, the origin of $\{\mathcal{I}\}$ coincides with the centroid of the feature points so that $X\mathbf{1} = 0$ and the landmarks belong to the x–y plane. The following result allows us to establish a relation between the image coordinates and the camera attitude.

Lemma 24. *Let* $\boldsymbol{\sigma} = [\sigma_1\ \sigma_2\ \sigma_3\ \sigma_4]^T \in \mathbb{R}^4 \setminus \{\mathbf{0}\}$ *and* $\boldsymbol{\rho} = [\rho_1\ \rho_2\ \rho_3\ \rho_4]^T \in \mathbb{R}^4 \setminus \{\mathbf{0}\}$ *be such that* $Y\boldsymbol{\sigma} = \mathbf{0}$, $X\boldsymbol{\rho} = \mathbf{0}$, *and* $\mathbf{1}^T\boldsymbol{\rho} = 0$, *where* $\mathbf{1} = [1\ 1\ 1\ 1]^T$. *Consider that the landmarks satisfy Assumption 23 and the camera configuration is such that the image is not degenerate (neither a point nor a line). Then, the depth variables* δ_i *can be written as*

$$\delta_i = \mu\frac{\rho_i}{\sigma_i},$$

where $\mu \in \mathbb{R}$, $\rho_i \neq 0$, *and* $\sigma_i \neq 0$ *for* $i \in \{1, \ldots, 4\}$.

Proof. See proof of [BCV+11, Lemma 1] □

Writing (6.2) in matrix form and using Lemma 24, we have

$$Y = A({}^I_C R^T X - {}^C\mathbf{p}_I \mathbf{1}^T)\mu D_\sigma^{-1} D_\rho,$$

where $D_\rho = \mathrm{diag}(\boldsymbol{\rho})$. From the feature centroid constraint $X\mathbf{1} = 0$, it follows that

$$\mu {}^I_C R^T X = A^{-1} Y D_\rho^{-1} D_\sigma (I_4 - \frac{1}{4}\mathbf{1}\mathbf{1}^T),$$

which encodes information about the attitude of the camera up to a scale factor. We can use the properties of the rotation matrix and the positive depth constraint $\delta_i > 0$ to obtain the normalized vector readings

$${}^C\bar{\mathbf{x}}_i = {}^I_C R^{T\,I}\bar{\mathbf{x}}_i = \mathrm{sign}(\mu)\frac{\mu {}^I_C R^{T\,I}\mathbf{x}_i}{\|\mu {}^I_C R^{T\,I}\mathbf{x}_i\|}, \tag{6.5}$$

where $\mathrm{sign}(\mu) = \mathrm{sign}\,(\rho_i/\sigma_i)$ and ${}^I\bar{\mathbf{x}}_i = {}^I\mathbf{x}_i/\|{}^I\mathbf{x}_i\|$, $i = 1,\ldots,4$. Note that no discontinuity is introduced by the use of the sign(.) function.

We now proceed with designing the observer where (6.5) and previous definitions are instrumental in allowing to write the observer dynamics in terms of the image location of the landmarks.

6.2.1 Observer Design

Recall that the bias in angular velocity measurements is assumed to be constant, i.e. $\dot{\mathbf{b}} = \mathbf{0}$, and consider the proposed Lyapunov function

$$V_R = \frac{\|\tilde{R} - I_3\|_F^2}{2} + \frac{1}{2k_b}\|\tilde{\mathbf{b}}\|^2 = \mathrm{tr}(I_3 - \tilde{R}) + \frac{1}{2k_b}\|\tilde{\mathbf{b}}\|^2,$$

where $k_b > 0$. From the attitude error dynamics (6.4) and noting that, by the properties of skew matrices,

$$\mathrm{tr}(NS(\mathbf{a})) = -S^{-1}(N - N^T)^T\mathbf{a},\ \text{for } N \in \mathbb{R}^{3\times 3},\ \mathbf{a} \in \mathbb{R}^3,$$

we obtain the time derivative

$$\dot{V}_R = \mathbf{s}_\omega^T(\hat{\boldsymbol{\omega}}_B - \boldsymbol{\omega}_B) + \frac{1}{k_b}\dot{\tilde{\mathbf{b}}}^T\tilde{\mathbf{b}}, \tag{6.6}$$

where

$$\mathbf{s}_\omega = R^T S^{-1}(\tilde{R} - \tilde{R}^T).$$

Consider now the attitude feedback law

$$\begin{aligned}\hat{\boldsymbol{\omega}}_B &= \boldsymbol{\omega}_r - \hat{\mathbf{b}} - k_\omega \mathbf{s}_\omega \\ &= \boldsymbol{\omega}_B - \tilde{\mathbf{b}} - k_\omega \mathbf{s}_\omega,\end{aligned} \tag{6.7}$$

where $k_\omega > 0$. Substituting the estimator (6.7) in (6.6) and defining the bias estimator update law

$$\dot{\hat{\mathbf{b}}} := k_b \mathbf{s}_\omega, \tag{6.8}$$

the Lyapunov function derivative becomes $\dot{V}_R = -k_\omega \|\mathbf{s}_\omega\|^2$. Taking into account the feedback law (6.7) and the update law (6.8), the closed loop attitude error dynamics can be written as

$$\begin{aligned} \dot{\tilde{R}} &= -k_\omega \tilde{R}(\tilde{R} - \tilde{R}^T) - \tilde{R} S(R\tilde{\mathbf{b}}), \\ \dot{\tilde{\mathbf{b}}} &= k_b R^T S^{-1}(\tilde{R} - \tilde{R}^T). \end{aligned} \tag{6.9}$$

Exploiting results derived for linear time-varying (LTV) systems in [LP02], it can be shown that the trajectories of the system (6.9) converge exponentially fast to the desired equilibrium point. Global asymptotic stability is however precluded by topological limitations associated with the points that satisfy $\|\tilde{R} - I_3\|_F^2 = 8$ (for further information see e.g. [BB00]). The stabilization result for the proposed controller is formally stated in the sequel.

Theorem 25. *Assume that $\boldsymbol{\omega}_B$ is bounded and $\dot{\mathbf{b}} = \mathbf{0}$. Then, for any initial condition satisfying*

$$\frac{\|\tilde{\mathbf{b}}(t_0)\|^2}{8 - \|\tilde{R}(t_0) - I_3\|_F^2} < k_b, \tag{6.10}$$

the estimation error $\tilde{\mathbf{x}} = (\tilde{R}, \tilde{\mathbf{b}})$ is bounded and $\|\tilde{R}(t) - I_3\|_F^2 < 8$ for all $t \geq t_0$. Moreover, the attitude and bias estimation errors converge exponentially fast to the equilibrium point $(\tilde{R}, \tilde{\mathbf{b}}) = (I_3, 0)$ for any initial condition satisfying (6.10).

The proof of this theorem follows a similar reasoning to the one used in the proof of [BCV+11, Theorem 1] and is therefore not presented.

Remark 26. *Note that the conditions of Theorem 25 are not restrictive, since $\boldsymbol{\omega}_B$ is intrinsically bounded due to the practical limitation on the energy of the system and the condition* (6.10) *can always be satisfied inside the almost global domain of attraction by tuning the gains.*

We now detail how to express the estimation laws (6.9) solely as a function of the image measurements and the biased gyro measurements. Consider the identity

$$Q S^{-1}(N - N^T) = S^{-1}(Q N Q^T - Q N^T Q^T),$$

where $N \in \mathbb{R}^{3\times3}$, $Q \in \mathrm{SO}(3)$, and the relation

$${}^I_C R = R^B_C R = {}^I \bar{X} {}^C \bar{X}^\dagger,$$

where ${}^B_C R$ is given by (6.1), ${}^C\bar{X} = [{}^C\bar{\mathbf{x}}_1, \ldots, {}^C\bar{\mathbf{x}}_4, {}^C\bar{\mathbf{x}}_i \times {}^C\bar{\mathbf{x}}_j]$, ${}^I\bar{X} = [{}^I\bar{\mathbf{x}}_1, \ldots, {}^I\bar{\mathbf{x}}_4, {}^I\bar{\mathbf{x}}_i \times {}^I\bar{\mathbf{x}}_j]$, for any linearly independent ${}^I\bar{\mathbf{x}}_i$ and ${}^I\bar{\mathbf{x}}_j$, and ${}^C\bar{X}^\dagger = {}^C\bar{X}^T({}^C\bar{X}{}^C\bar{X}^T)^{-1}$ is the Moore-Penrose inverse of

${}^{C}\bar{X}$. Using the following derivation, the feedback term $\mathbf{s}_\omega$ can be expressed as an explicit function of the sensor readings and known quantities

$$\begin{aligned}\mathbf{s}_\omega &= R^T S^{-1}(\tilde{R} - \tilde{R}^T)\\ &= S^{-1}(R^T \tilde{R} R - R\tilde{R}^T R^T)\\ &= S^{-1}(R^T \hat{R} - \hat{R}^T R)\\ &= S^{-1}({}^{B}_{C}R({}^{C}\bar{X}^{\dagger})^{T\,I}\bar{X}^T \hat{R} - \hat{R}^{T\,I}\bar{X}^{C}\bar{X}^{\dagger\,B}_{\ C}R^T).\end{aligned}$$

6.3 Pan and tilt controller

The camera frame attitude kinematics can be described by

$${}^{I}_{C}\dot{R} = {}^{I}_{C}RS(\boldsymbol{\omega}_C),$$

where $\boldsymbol{\omega}_C \in \mathbb{R}^3$ denotes the camera angular velocity. Taking the time derivative of (6.1), and noting that ${}^{I}_{C}R = {}^{I}_{B}R^{B}_{C}R$, straightforward computations show that $\boldsymbol{\omega}_C$ can be written as

$$\boldsymbol{\omega}_C = {}^{C}_{B}R\boldsymbol{\omega}_B + R_{\text{tilt}}^T[\dot{\alpha}\ \dot{\beta}\ 0]^T, \tag{6.11}$$

where $\dot{\alpha}$ and $\dot{\beta}$ are the time derivatives of the camera pan and tilt angles, respectively.

In summary, to develop an active vision system using the camera pan and tilt degrees of freedom, we let $\bar{\mathbf{y}}$ be the image of the landmarks' centroid given by $[\bar{\mathbf{y}}^T\ 1]^T = \bar{\delta}A\bar{\mathbf{r}}$, where $\bar{\mathbf{r}} = -{}^{I}_{C}R^{T\,I}\mathbf{p}_C$ denotes the position of $\{\mathcal{I}\}$ expressed in $\{\mathcal{C}\}$ and $\bar{\delta} = (\mathbf{u}_3^T\bar{\mathbf{r}})^{-1}$. The control objective is to design a control law for $\dot{\alpha}$ and $\dot{\beta}$ based on the measurements of $\boldsymbol{\omega}_B$ and $\mathbf{y}_i$, $i \in \{1,\ldots,4\}$, such that $\bar{\mathbf{y}}$ approaches the center of the image plane.

6.3.1 Camera Pan and Tilt Controller

We resort to Lyapunov theory and consider the following candidate Lyapunov function

$$W = \frac{1}{2}\bar{\mathbf{r}}^T\Pi_{\mathbf{u}_3}\bar{\mathbf{r}} = \frac{1}{2}(r_x^2 + r_y^2), \tag{6.12}$$

where $\bar{\mathbf{r}} = [r_x\ r_y\ r_z]^T$ and $\Pi_{\mathbf{u}_3} = I - \mathbf{u}_3\mathbf{u}_3^T$ denotes the projection onto the plane orthogonal to $\mathbf{u}_3$. Using the expression for $\boldsymbol{\omega}_C$ given in (6.11), the camera position kinematics can be written as

$$\begin{aligned}\dot{\bar{\mathbf{r}}} &= S(\bar{\mathbf{r}})\boldsymbol{\omega}_C - \mathbf{v}_C\\ &= S(\bar{\mathbf{r}})(R_{\text{tilt}}^T R_{\text{pan}}^T\boldsymbol{\omega}_B + R_{\text{tilt}}^T[\dot{\alpha}\ \dot{\beta}\ 0]^T) - \mathbf{v}_C,\end{aligned} \tag{6.13}$$

where $\mathbf{v}_C$ is the camera linear velocity. Recall that by definition $\bar{\mathbf{r}}$ coincides with the position of the landmarks' centroid and its image is given by $\bar{\mathbf{r}}$. Therefore, by guaranteeing that the Lyapunov function W is decreasing, or equivalently $[r_x\ r_y]$ is approaching the origin, we can ensure that $\bar{\mathbf{y}}$ is approaching the center of the image plane. To simplify the notation and without loss of generality, assume from now on that $A = I$ so that $\bar{\mathbf{y}} = \begin{bmatrix} r_x & r_y \end{bmatrix}^T / r_z$.

Lemma 27. *Let the camera position kinematics be described by* (6.13) *and assume that the rigid body and camera motions are such that* $r_z > 0$ *and* $\cos\beta \neq 0$. *Consider the control law for the camera pan and tilt angular velocities given by*

$$\begin{bmatrix} \dot{\alpha} \\ \dot{\beta} \end{bmatrix} = k_c \begin{bmatrix} 0 & -\frac{1}{\cos\beta} \\ 1 & 0 \end{bmatrix} \bar{\mathbf{y}} - \begin{bmatrix} 1 & 0 & -\tan\beta \\ 0 & 1 & 0 \end{bmatrix} R_{pan}^T \boldsymbol{\omega}_B, \tag{6.14}$$

where $k_c > 0$. *Then, the time derivative of the Lyapunov function* W *along the system trajectories satisfies*

$$\dot{W} \leq -(k_c - \epsilon) W, \quad \forall \, \|\Pi_{\mathbf{u}_3} \bar{\mathbf{r}}\| \geq \frac{1}{\epsilon} \|\Pi_{\mathbf{u}_3} \mathbf{v}_C\|, \tag{6.15}$$

and $0 < \epsilon < k_c$.

Proof. By taking the time derivative of (6.12) and using the expressions for $\dot{\bar{\mathbf{r}}}$ given in (6.13), we obtain

$$\dot{W} = \bar{\mathbf{r}}^T \Pi_{\mathbf{u}_3} (r_z S(\mathbf{u}_3) \boldsymbol{\omega}_C - \mathbf{v}_C) \tag{6.16}$$

Choosing $\boldsymbol{\omega}_C$ such that

$$S(\mathbf{u}_3) \boldsymbol{\omega}_C = -k_c \Pi_{\mathbf{u}_3} \bar{\mathbf{y}} \tag{6.17}$$

yields $\dot{W} = -k_c W - \bar{\mathbf{r}}^T \Pi_{\mathbf{u}_3} \mathbf{v}_C$ and consequently (6.15) holds. Substituting (6.11) in (6.17) and solving for $\dot{\alpha}$ and $\dot{\beta}$ we obtain the control law (6.14). □

Remark 28. *If we apply the control law* (6.14) *to the system with state* $\Pi_{\mathbf{u}_3} \bar{\mathbf{r}} = [r_x \; r_y]^T$ *and interpret* $\mathbf{v}_C$ *as input, it follows from* (6.15) *that the system is exponentially input-to-state stable (ISS). As such, the distance between the image of the centroid* $\bar{\mathbf{y}}$ *and the origin is ultimately bounded by* $\|\Pi_{\mathbf{u}_3} \mathbf{v}_C / r_z\|$ *and converges exponentially fast to that bound. Moreover, if* $\Pi_{\mathbf{u}_3} \mathbf{v}_C / r_z$ *converges to zero so does* $\bar{\mathbf{y}}$.

The proposed control law (6.14) has a significant advantage over classical eye-in-hand system controllers, which are based on the inversion of the error Jacobian matrix to achieve an exponential decrease of the error. The inverse of the error Jacobian matrix for the present pan and tilt camera system is

$$J_{\mathbf{e}}^{-1} = \begin{bmatrix} 0 & \frac{1}{r_z \cos\beta - r_x \sin\beta} \\ -\frac{1}{r_z} & \frac{r_y \sin\beta}{r_z^2 \cos\beta - r_x r_z \sin\beta} \end{bmatrix},$$

where the Jacobian is computed from the equality

$$\dot{\mathbf{e}} = \dot{\bar{\mathbf{r}}} = J_{\mathbf{e}} \begin{bmatrix} \dot{\alpha} \\ \dot{\beta} \end{bmatrix} + \frac{\partial \bar{\mathbf{r}}}{\partial t},$$

with the error given by $\mathbf{e} = \bar{\mathbf{r}} - \mathbf{0}$ and $\bar{\mathbf{r}} = \begin{bmatrix} r_x & r_y \end{bmatrix}^T$. Clearly, the error Jacobian matrix has singularities not present in the proposed control law. By exploiting the structure of $\dot{W}$ in (6.16), we obtain a controller that still achieves exponential decay of the error for the zero-disturbance case $\mathbf{v}_C = \mathbf{0}$, and whose only singularity does not depend on the vehicle's position but is intrinsic to the camera's geometry. Moreover, the control law given in (6.14) is effectively image-based in the sense that it uses solely the image coordinates $\bar{\mathbf{y}}$, whereas using the inverse of the Jacobian matrix would require reconstruction of the depth coordinate r_z.

6.4 Quadrotor controller

The quadrotor control objective consists of designing a control law for the quadrotor actuations $\mathbf{f}$ and $\mathbf{n}$, which ensures the convergence of the horizontal position in frame $\{\mathcal{I}\}$ to zero with the largest possible basin of attraction, while maintaining the landmarks visible in the image sensor and the vehicle's vertical coordinate stable.

As sensor measurements, the image coordinates of the landmarks are available for feedback in addition to the vehicle's attitude and angular velocity estimations from the proposed observer and the camera pan and tilt angles. Moreover, we consider the vehicle equipped with an absolute vertical position sensor. The vertical position sensor here considered can be a simple barometric sensor, providing the vehicle altitude, which differs from the distance to the ground.

In order to achieve the stabilization goal, the proposed controller makes use of partial information on the position and body linear velocity which are not directly measured. The 2-D image coordinates of the landmarks' $\mathbf{y}_i$ together with the rotation matrices ${}^B_I R$ and ${}^C_B R$ provide us with means of obtaining, up to a scale factor, the position $\mathbf{p}$ and the body linear velocity ${}^I\mathbf{v} = [{}^I v_x \, {}^I v_y \, {}^I v_z]^T$, both expressed in the inertial frame. For that purpose, we first determine the direction of the landmarks, or more precisely their position up to a scale factor with respect to the body, expressed in the inertial frame. To simplify the necessary notation, let us introduce a new reference frame $\{\mathcal{L}\}$, with the same origin as $\{\mathcal{B}\}$ but with the orientation of $\{\mathcal{I}\}$. Let $\begin{bmatrix} x_i & y_i & z \end{bmatrix}^T = {}^L_C R\,\mathbf{r}_i$ be the coordinates of the landmarks expressed in $\{\mathcal{L}\}$. Choosing $1/z$ as the scale factor, the direction of the landmarks in frame $\{\mathcal{L}\}$ can be obtained from

$$\begin{bmatrix} x_i/z \\ y_i/z \\ 1 \end{bmatrix} = \frac{{}^L_C R \begin{bmatrix} \mathbf{y}_i^T & 1 \end{bmatrix}^T}{\mathbf{u}_3^T \, {}^L_C R \begin{bmatrix} \mathbf{y}_i^T & 1 \end{bmatrix}^T} \triangleq \mathbf{s}_i. \tag{6.18}$$

where $[x_i \; y_i \; z]^T = {}^I_C R\,\mathbf{r}_i$ are the coordinates of the landmarks expressed in $\{\mathcal{L}\}$. The $\mathbf{s}_i$ points can be thought of as the images of the landmarks in a *virtual* camera, attached to the vehicle but with a fixed orientation relative to the inertial frame. Moreover, the position of the vehicle can be estimated up to a scaling factor by computing (6.18) with the centroid $\bar{\mathbf{y}}$ in the place of $\mathbf{y}_i$. Taking the time derivative of (6.18), the following relation is obtained for the vehicle velocities, expressed either in $\{\mathcal{L}\}$ or $\{\mathcal{I}\}$,

$$\begin{bmatrix} \frac{{}^I v_x}{z} - \frac{x_i\,{}^I v_z}{z^2} \\ \frac{{}^I v_y}{z} - \frac{y_i\,{}^I v_z}{z^2} \\ 0 \end{bmatrix} = \dot{\mathbf{s}}_i, \tag{6.19}$$

where the right-hand-side time derivative is a function of variables for which measurements or estimators exist ${}^L_C R = {}^I_C R$, $\boldsymbol{\omega}_C$, $\mathbf{y}_i$, and $\dot{\mathbf{y}}_i$.

Since (6.19) is valid for every landmark, the vehicle velocity can be partially recovered from the $\dot{\mathbf{s}}_i$ measurements by solving an overdetermined equation system in order to obtain a least squares solution for ${}^I\mathbf{v}/z$. This solution is akin to the computation performed in [MCH08] to obtain ${}^I\mathbf{v}/z$ based on the derivative of the average of spherical images of features. Notice, however, that unlike [MCH08], in this work we use estimates of the attitude, whose estimation error is reflected in the position and velocity estimates.

The proposed controller makes use of the *unit quaternions* to represent the attitude, in contrast with the rotation matrix parametrization used previously. Unit quaternions $\mathbf{q} \in \mathbb{S}^4$, are written in the form $\mathbf{q} = \begin{bmatrix} q_0 & q^T \end{bmatrix}^T$, where the *scalar* part $q_0 \in \mathbb{R}$ is related to the rotation angle $\theta \in [0, \Pi_{\mathbf{u}_3})$ and the *vector* part $q = [q_1\ q_2\ q_3]^T \in \mathbb{R}^3$ to the axis of rotation $\mathbf{n} \in \mathbb{S}^3$ through

$$\mathbf{q}(\theta, \mathbf{n}) = \begin{bmatrix} q_0 \\ q \end{bmatrix} = \begin{bmatrix} \cos(\theta/2) \\ \mathbf{n}\sin(\theta/2) \end{bmatrix}.$$

In general, there is an ambiguity in the unit quaternion parametrization as $\mathbf{q}$ and $-\mathbf{q}$ represent the same attitude. However, in the present case, as the attitude controller guarantees $q_0(t) > \epsilon$ for all time. Then, for all system trajectories, there is a bijective correspondence of the quaternion representation and the rotation matrix representation

The methodology adopted to address the quadrotor vehicle control problem is in line with the state feedback controller proposed in [IMS03]. However, as the full system state is not directly available for feedback, the controller is modified to exploit the image measurements and attitude estimates to stabilize the quadrotor position at the desired location. The controller comprises a vertical stabilization law together with a lateral-longitudinal-attitude stabilization law. The latter law enforces two-time scale dynamics and decouples the lateral-longitudinal dynamics from the attitude dynamics.

6.4.1 Stabilization of the vertical error dynamics

The control objective of the vertical stabilization law is to drive the vehicle to a given reference altitude $h^\star$. Let h_0 be the altitude of frame $\{\mathcal{I}\}$. Then, the altitude of the vehicle and its height in the inertial frame are related by $h(t) = h_0 + z(t)$, where $z(t)$ is the

z-coordinate of the vehicle in frame $\{\mathcal{I}\}$. In order to simplify the notation we pose the vertical stability problem in terms of driving $z(t)$ to $z^\star = h^\star - h_0$ while avoiding collisions with the ground by enforcing $z(t) > 0$ for all time. The dynamic equation for the altitude,

$$m\ddot{z} = (1 - 2q_1^2 - 2q_2^2)T - mg, \tag{6.20}$$

is derived from the altitude definition and the linear dynamics of the vehicle system represented in (3.1) and (3.2). We propose a control law for the thrust T that drives the vehicle to a fixed altitude $z^\star$ through

$$T = \frac{mg - k_1(z - z^\star) - k_2\frac{\dot{z}}{z}}{1 - (2q_1^2 + 2q_2^2)} \tag{6.21}$$

where k_1 and k_2 are positive parameters. The resulting closed-loop altitude dynamics are

$$m\ddot{z} = -k_1(z - z^\star) - \frac{k_2}{z}\dot{z}, \tag{6.22}$$

which amount to a double integrator driven by a PD controller with a time-varying derivative gain due to the nature of $z(t)$. The closed-loop is asymptotically stable for initial conditions $z(t_0) > 0$ since both proportional and derivative gains are always negative and, as proved in the sequel, ensures the quadrotor altitude is always positive and prevents crashes against the ground. A subsequent choice of the attitude control law guarantees that the quadrotor never overturns, and thus $2q_1^2 + 2q_2^2 < 1$ for all time, precluding the loss of altitude control through thrust actuation. For now, we take that fact as assumption and state the following lemma, regarding the altitude control.

Lemma 29. *Consider the quadrotor altitude dynamic system described by the closed-loop system comprising* (6.20) *and* (6.21) *with* $k_1, k_2 > 0$. *If the initial conditions fulfill* $z(0) > 0$, *then the control law is well defined and* $z(t) > 0$ *for all time, even in the presence of attitude observer errors. Additionally, the cascade of the attitude observer and the altitude controller is exponentially stable.*

Proof. Let us define the auxiliar state

$$\xi = z \exp\left(\frac{1}{k_2}\left(m\dot{z} + \int_0^t k_1(z(\tau) - z^\star)\mathrm{d}\tau\right)\right)$$

and notice that, with the imposed closed-loop dynamics (6.22), it has a constant value as $\dot{\xi} = 0$. Since $\xi(t) = \xi(0)$ is positive and the exponential of a number is always positive, it results that $z(t) > 0$ for all time and thus collisions with the ground are always avoided.

Asymptotic stability of $(z, \dot{z}) = (z^\star, 0)$ is established from LaSalle's invariance principle and the Lyapunov function

$$V_z = \frac{1}{2}k_1(z - z^\star)^2 + \frac{1}{2}m\dot{z}^2,$$

which has negative semi-definite time derivative

$$\dot{V}_z = -k_2 \frac{\dot{z}^2}{z} \leq 0.$$

An additional consequence of the convergence of $(z, \dot{z})$ to $(z^\star, 0)$ and the constancy of the auxiliar state ξ is that the altitude is lower and upper bounded for all time and $z(t) > \epsilon$ for some $\epsilon > 0$.

Furthermore, LTV system theory asserts that the convergence is indeed exponential. Let the state $\mathbf{x} = \begin{bmatrix} \dot{z} & z - z^\star \end{bmatrix}^T$ and compute

$$\dot{\mathbf{x}} = \begin{bmatrix} A(t) & B \\ -C & 0 \end{bmatrix} \mathbf{x} = \begin{bmatrix} -\frac{k_2}{z(t)} & -k_1 \\ 1 & 0 \end{bmatrix} \mathbf{x}. \tag{6.23}$$

to obtain an LTV system equivalent to the altitude dynamics (6.22) Let $P = \frac{1}{k_1}$ and notice that

$$A^T(t)P + PA(t) = -2\frac{k_2}{k_1 z(t)} = -Q(t)$$

with $Q(t)$ bounded as $0 < q_m < Q(t) < q_M$. Under these conditions, the LTV system (6.23) is uniformly exponentially stable [LP02].

The interconnection of the attitude observer and the altitude subsystem can be regarded as a cascade of two exponentially stable systems with $A(t) = -\frac{k_2}{z(t)}$ bounded for all trajectories. In these circumstances, the cascade is also exponentially stable [SI89, Proposition 2.1]. Finally, impact with the ground is also avoided when the altitude subsystem is perturbed by the orientation errors. This can be established by letting $\Delta_1(t)$ be the perturbations due to the estimation errors and considering that the state

$$\xi = z \exp\left(\frac{1}{k_2}\left(m\dot{z} + \int_0^t k_1(z(\tau) - z^\star) - \Delta_1(\tau)\mathrm{d}\tau\right)\right) \tag{6.24}$$

is constant for the perturbed vertical dynamics

$$m\ddot{z} = -k_1(z - z^\star) - \frac{k_2}{z}\dot{z} + \Delta_1(t).$$

To complete the proof it must be determined that the pathological cases of the finite time escape and convergence to zero or divergence to infinity are impossible for the altitude. This is proven by taking into account that the state ξ in (6.24) is constant and $z^\star$ is strictly positive. The case of finite time escape is impossible since it implies that $z(t)$, $\dot{z}(t)$ and consequently ξ all diverge to infinity, which is in contradiction to the previously established result that the state ξ is constant. Likewise, were $z(t)$ to converge to zero, it would result on ξ converging to zero. In that situation, the argument of the exponential would be dominated by the integral term, whose argument is a strictly negative number. Divergence of the altitude to infinity with time is also impossible since, if we take it as a premiss, it results in a ξ state that diverges to infinity. Since ξ is proven to be constant all the aforementioned situations are impossible for the dynamic system at hand and thus, even in the presence of attitude disturbances, $z(t)$ has a lower and upper bound and converges to the desired $z^\star$. □

6.4.2 Stabilization of the lateral and longitudinal dynamics

To stabilize the quadrotor in hover, the proposed vertical stabilizer (6.21) needs to be combined with a controller for the torque actuation $\mathbf{n}$ that stabilizes both the attitude and the lateral-longitudinal dynamics. In order to achieve these goals, we interpret the attitude as a *virtual control input* for the lateral-longitudinal dynamics. In this setting, the attitude follows the virtual control law with fast dynamics and a slower outer control loop generates the virtual control for the attitude so as to stabilize the lateral-longitudinal dynamics. The proposed attitude-lateral-longitudinal closed-loop simultaneously stabilizes the lateral and longitudinal dynamics and ensures the quadrotor does not overturn, that is, $q_0(t) > \epsilon$ for all time.

The lateral-longitudinal-attitude sybsystem dynamics for a quadrotor vehicle, with equations of motion (3.1)-(3.4) and the thrust defined as (6.21), are described by the following system of equations, where quaternions are used to represent the vehicle attitude,

$$
\begin{aligned}
\dot{y} &= v_y, \\
m\dot{v}_y &= d(\mathbf{q})q_1 + m(\mathbf{q})q_2q_3 + \delta_y, \\
\dot{x} &= v_x, \\
m\dot{v}_x &= -d(\mathbf{q})q_2 + m(\mathbf{q})q_1q_3 + \delta_x, \\
\dot{q}_0 &= -\frac{1}{2}q^T\boldsymbol{\omega}_B, \\
\dot{q} &= \frac{1}{2}(q_0I_4 + S(q))\boldsymbol{\omega}_B, \\
\mathbb{J}\dot{\boldsymbol{\omega}}_B &= -S(\boldsymbol{\omega}_B)\mathbb{J}\boldsymbol{\omega}_B + \mathbf{n}.
\end{aligned} \tag{6.25}
$$

The components x, y, v_x and v_y are written in frame $\{\mathcal{I}\}$, the attitude functions $d(\mathbf{q})$ and $m(\mathbf{q})$ are given by

$$
\begin{aligned}
d(\mathbf{q}) &= \frac{2mgq_0}{1-(2q_1^2+2q_2^2)}, \\
m(\mathbf{q}) &= -\frac{2mg}{1-(2q_1^2+2q_2^2)},
\end{aligned} \tag{6.26}
$$

and δ_x, δ_y are asymptotically vanishing signals (see Lemma 29) defined as

$$\delta_x = \frac{2q_1q_3 + 2q_0q_2}{1-(2q_1^2+2q_2^2)}(-k_1(z-z^\star) - k_2\frac{\dot{h}}{z}),$$
$$\delta_y = \frac{2q_2q_3 - 2q_0q_1}{1-(2q_1^2+2q_2^2)}(-k_1(z-z^\star) - k_2\frac{\dot{h}}{z})).$$

The control law for the attitude subsystem is chosen as the proportional-derivative law

$$\mathbf{n} = K_P(\eta - K_D\hat{\boldsymbol{\omega}}_B) \tag{6.27}$$

where $K_P > 0$ and $K_D > 0$ are design parameters and

$$\eta = q^\star - \hat{q}$$

is the attitude error with $q^\star$ defined as the *virtual control* input for the $x-y$ system and $\hat{q}$ the vectorial part of the quaternion estimate obtained with proposed observer system (6.9). The quadrotor attitude estimation subsystem in closed-loop with the control feedback (6.27) results in the following dynamics, written in quaternion representation

$$\dot{q}_0 = -\frac{1}{2}q^T\boldsymbol{\omega}_B \tag{6.28}$$
$$\dot{q} = \frac{1}{2}(q_0I_4 + S(q))\boldsymbol{\omega}_B \tag{6.29}$$
$$\mathbb{J}\dot{\boldsymbol{\omega}}_B = -S(\boldsymbol{\omega}_B)\mathbb{J}\boldsymbol{\omega}_B + k_P((q^\star - q) - k_D\boldsymbol{\omega}_B) + \Delta_2(t), \tag{6.30}$$

where the external input

$$\Delta_2(t) = k_P\tilde{q} + k_D\tilde{\boldsymbol{\omega}}_B$$

includes the errors resulting from the observer measurements and vanishes exponentially fast. According to Proposition 5.7.1 in [IMS03], which we restate for the sake of completeness, proper tuning of the torque control law (6.27) ensures boundedness of the attitude subsystem trajectories and consequent stabilization of the vertical error dynamics, even in the presence of attitude and bias estimation errors.

Proposition 30. *For some* $0 < \epsilon < 1$, *fix compact sets of initial conditions* $\mathcal{Q}$, Ω *for the observer estimates* $\hat{q}(t)$ *and* $\hat{\boldsymbol{\omega}}_B(t)$, *respectively, such that*

$$\mathcal{Q} \subset \{\hat{q} \in \mathbb{R}^3 : \|\hat{q}\| < \sqrt{1-\epsilon^2}\}.$$

Then there exist $K_D^\star(\|\Delta(t)\|_\infty) > 0$ *and positive numbers* $K_P^\star(K_D^\star)$, $\lambda^\star(K_D^\star)$ *such that, for any initial conditions* $(\hat{q}(0), \hat{\boldsymbol{\omega}}_B(0)) \in \mathcal{Q}\times\Omega$ *and* $\|q^\star(t)\| < \lambda^\star$, *the trajectories of the attitude subsystem* (6.28)-(6.30) *are bounded and satisfy* $\hat{q}_0(t) > \epsilon$ *for all time.*

Remark 31. *A corollary of this Proposition is that the quadrotor does not overturn for initial attitude and bias estimation errors satisfying* $\sqrt{\frac{1}{2}\tilde{q}_0(0)^2 + \frac{1}{2}\tilde{\mathbf{b}}(0)^T\tilde{\mathbf{b}}(0)} < \epsilon$.

To achieve convergence of the overall system, the virtual control input $q^\star$ is generated from the quadrotor position and velocities by a *nested saturation* control law. Consider the new state variables

$$\zeta_1 = \frac{1}{z}\begin{bmatrix} y \\ x \end{bmatrix},$$
$$\zeta_2 = \frac{1}{z}\begin{bmatrix} v_y \\ v_x \end{bmatrix} + \lambda_1 \sigma\left(\frac{K_1}{\lambda_1}\zeta_1\right) - \frac{v_z}{z}\zeta_1,$$

where $\sigma(\mathbf{x}) = (\sigma(x_1), \ldots, \sigma(x_n))$ is a saturation function and $v_z = \dot{z}$. Notice that the states ζ_1 and ζ_2 are readily obtained from x/z, y/z and ${}^I\mathbf{v}/z$, whose estimates can be derived from the camera sensor and attitude estimate.

Fix for $q^\star$ the nested saturation structure

$$q^\star = -P_2\lambda_2\sigma\left(\frac{K_2}{\lambda_2}\hat{\zeta}_2\right), \tag{6.31}$$

where

$$P_2 = \begin{bmatrix} 1 & 0 \\ 0 & -1 \\ 0 & 0 \end{bmatrix}$$

and $\hat{\zeta}_2$ is the estimate for ζ_2 obtained applying (6.18) with the image centroid $\bar{\mathbf{y}}$ and the attitude estimate $\hat{R}$. The time derivatives of the states are then

$$\dot{\zeta}_1 = \zeta_2 - \lambda_1\sigma(\frac{K_1}{\lambda_1}\zeta_1),$$
$$m\dot{\zeta}_2 = \frac{D}{z}\left(-P_2\lambda_2\sigma(\frac{K_2}{\lambda_2}\zeta_2) + \eta\right) + mK_1\sigma'(\frac{K_1}{\lambda_1}\zeta_1)\dot{\zeta}_1$$
$$+ \delta_1 + \delta_2 + \Delta_3,$$

where

$$D = \begin{bmatrix} d(\mathbf{q}) & m(\mathbf{q})q_3 & 0 \\ m(\mathbf{q})q_3 & -d(\mathbf{q}) & 0 \end{bmatrix},$$

the exogenous inputs δ_1 and δ_2 are given by

$$\delta_1 = \begin{bmatrix} \delta_x \\ \delta_y \end{bmatrix}/z,$$
$$\delta_2 = \frac{k_1(z - z^\star) + k_2\frac{\dot{h}}{z})}{z}\zeta_1 + m\frac{v_z^2}{z^2}\zeta_1 - m\frac{v_z}{z}\dot{\zeta}_1,$$

and the errors due to the attitude estimator are encapsulated in

$$\Delta_3 = \frac{D}{z}\left(-P_2\lambda_2\left(\sigma(\tfrac{K_2}{\lambda_2}\zeta_2) - \sigma(\tfrac{K_2}{\lambda_2}\hat{\zeta}_2)\right) + \tilde{q}\right).$$

From the exponential convergence of the altitude $(z - z^\star)$ and the attitude estimation error $\tilde{q}$ to the origin and by noting that the growth of $\|\zeta_1\|$, $\|\zeta_2\|$ is, at most, quadratic, we can establish that the exogenous inputs and estimation induced errors are asymptotically vanishing and converge exponentially fast to zero. From definition (6.26) and the attitude and vertical controllers, we have the bounds $0 < d^L \leq d(\mathbf{q}, t) \leq d^U$ and $0 < z^L < z(t) < z^U$. The following result is an adaptation of Proposition 5.7.2 and Theorem 5.7.5 in [IMS03] and gives guarantees for the proposed quadrotor stabilization law.

Theorem 32. *Let K_D be fixed according to Proposition 5.7.1 in [IMS03] and let $K_i^\star$ and $\lambda_i^\star$, $i = 1, 2$, be such that the following inequalities are satisfied*

$$\frac{\lambda_2^\star}{K_2^\star} < \frac{\lambda_1^\star}{4}, \quad 4\lambda_1^\star K_1^\star < \frac{1}{m}\frac{d^L}{z^U}\frac{\lambda_2^\star}{8}, \quad 24\frac{K_1^\star}{K_2^\star} < \frac{1}{6}\frac{d^L}{d^U}\frac{z^L}{z^U}. \tag{6.32}$$

Then, there exist positive numbers $K_P^\star$ and $\epsilon^\star$ such that, taking

$$\lambda_i = \epsilon^i \lambda_i^\star \text{ and } K_i = \epsilon K_i^\star, \; i = 1, 2, \tag{6.33}$$

for all $K_P > K_P^\star$ and $0 < \epsilon \leq \epsilon^\star$, the state trajectories of the system (6.25) *in closed-loop with the controller defined by* (6.21), (6.27) *and* (6.31) *converge asymptotically to the origin for any initial condition such that $z(0) > 0$, $(x(t), v_x(t), y(t), v_y(t)) \in \mathbb{R}^4$, $(\hat{q}(0), \hat{\omega}_B(0)) \in \mathcal{Q} \times \Omega$ and $|\tilde{q}_0(0)| < q_0(0)$.*

Proof. The proof follows from the arguments in [IMS03] where the statement is proven for constant $z(t) = Z$ and exogenous disturbances $\delta_2(t) = 0$, $\Delta(t) = [\Delta_1(t)\, \Delta_2(t)\, \Delta_3(t)]^T = 0$. The statement of Theorem 32 is shown by noting that the additional disturbances $\delta_2(t)$ and $\Delta(t)$ are asymptotically vanishing. The lateral-longitudinal subsystem does not have finite escape time and the trajectory $(\zeta_1(t), \zeta_2(t))$ exists and is bounded for any $t > 0$. Since the disturbance $\delta_2(t)$ is asymptotically vanishing, there exists a finite time $T^\star$ such that for $t > T^\star$ the disturbances are within the bounds for which the convergence of (ζ_1, ζ_2) to the origin is ensured by using the gains in (6.33), satisfying (6.32). The remainder of the claims in the theorem statement follows identically from [IMS03]. □

Remark 33. *At this point, it is important to notice that the vehicle controller can be obtained by feedback of the image coordinates and their derivatives, vertical coordinate, and vehicle attitude estimate for the thrust, and by feedback of the image coordinates and their derivatives, attitude estimates and angular velocities of the camera and vehicle for the torque.*

Gathering the previous results regarding the pan and tilt camera, stabilization of the vertical position, attitude and lateral-longitudinal subsystems, we can now state the following theorem which summarizes the main results of the chapter and corresponds to the control architecture represented in Fig. 6.2. The camera controller K_{camera} is given by (6.14) and the vertical position controller K_{vertical} by (6.21), respectively. The lateral-longitudinal controller $K_{\text{lat-long}}$ and the attitude controller are described by (6.31) and

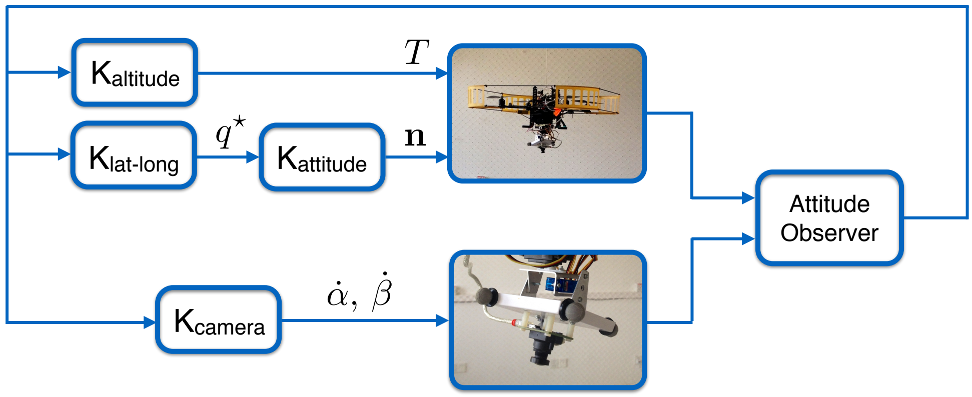

Figure 6.2: Block diagram of the cascaded control architecture.

(6.27), respectively. Lastly, the attitude observer estimates ${}^I_B R$ and $\boldsymbol{\omega}_B$ through (6.3), (6.7) and (6.8).

Theorem 34. *Consider a quadrotor described by the dynamic system* (3.3)-(3.2) *equipped with a pan and tilt camera modeled by* (6.1) *with dynamics* (6.14), *and apply the set of camera and quadrotor controllers* (6.14), (6.21), (6.27) *and* (6.31), *using the quadrotor attitude and rate gyro bias estimator* (6.7)-(6.8). *Then, for any initial condition* $z(0) > 0$, $(x(t), v_x(t), y(t), v_y(t)) \in \mathbb{R}^4$, $(\hat{q}(0), \hat{\boldsymbol{\omega}}_B(0)) \in \mathcal{Q} \times \Omega$ *and* $|\tilde{q}_0(0)| < q_0(0)$ *such that the landmarks are visible in the image plane of the camera, the vehicle's position, attitude, velocities converge asymptotically to* ${}^I\mathbf{p}_B = [0\ 0\ z^\star]^T$, ${}^I_B R = I_3$, $\mathbf{v}_B = \mathbf{0}$, *and* $\boldsymbol{\omega}_B = \mathbf{0}$, *respectively, whereas the camera's velocity and image coordinates converge to* $\boldsymbol{\omega}_C = 0$ *and* $\bar{\mathbf{y}} = 0$, *respectively.*

Proof. The stated result follows from Theorems 32 and 25. Theorem 32 states that convergence of the vehicle position and velocity to zero is achieved, even in the presence of attitude estimation errors. Convergence of the landmarks' centroid image coordinates to zero is achieved if the vehicle velocity and bias error converge to zero, which is guaranteed by Theorem 25. □

6.5 Simulation results

In this section, we present the results from a simulation run of the proposed control architecture. At the beginning, the quadrotor is assumed at rest. The camera points towards a set of landmarks that are visible, and the centroid of the landmarks is not coincident with origin of the image plane. The objective of the simulation is to hover the quadrotor over the centroid of the landmarks at a reference vertical position. The vehicle parameters, control and estimation gains are $m = 1$ kg, $\mathbb{J} = 0.5I_3$ kg m^2, $\lambda_1 = 10$, $\lambda_2 = 0.3$, $K_1 = 0.3$, $K_2 = 0.3$, $K_P = 10$, $K_D = .5$, $k_1 = 0.1$, $k_2 = 6$, $k_b = 0.001$ and $k_\omega = 0.01$.

Figure 6.3 presents the time evolution of the quadrotor position error expressed in inertial coordinates. We can verify that the error converges from the initial $\mathbf{e} = [8\ {-6}\ {-3}]^T$ m to zero and is negligible after about 20 seconds.

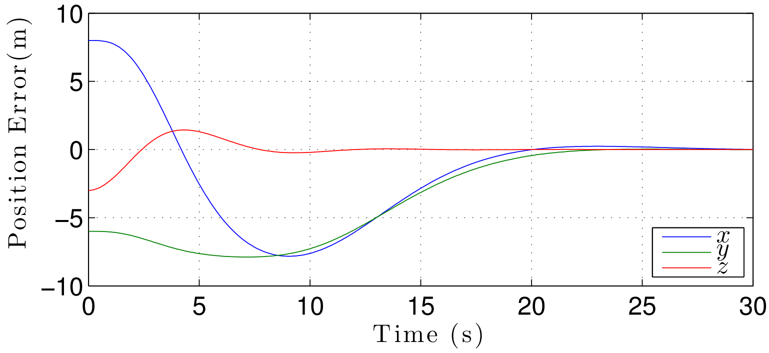

Figure 6.3: Inertial position error of the quadrotor.

The position of the landmarks' centroid in the image plane is displayed in Fig. 6.4. The centroid $\bar{\mathbf{y}}$ converges asymptotically to the origin as the velocity of the quadrotor converges asymptotically to zero. The initial transient vanishes rapidly, lasting only a couple of seconds, and then convergence slows down as the vehicle comes to a halt. The disturbance effect of the quadrotor linear velocity and estimation errors on the time evolution of $\bar{\mathbf{y}}$ can be observed in the figure by noting that the convergence to the origin is not monotonic.

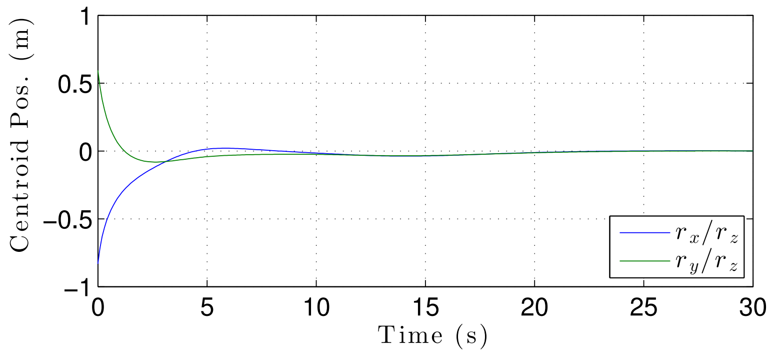

Figure 6.4: Landmarks' centroid position in image coordinates.

The quadrotor actuations are shown in Fig. 6.5. The initial thrust is smaller than gravity force, thereby making the quadrotor move down, closer to the desired altitude. When the altitude finally stabilizes, the thrust also stabilizes to a steady-state value where it compensates gravity. The high initial actuation for the torque drives the thrust vector to point in the direction of the landmarks. Once this is accomplished, the torque actuation necessary to counteract the vehicle's movement is gradually smaller until the quadrotor comes to a full stop over the landmarks.

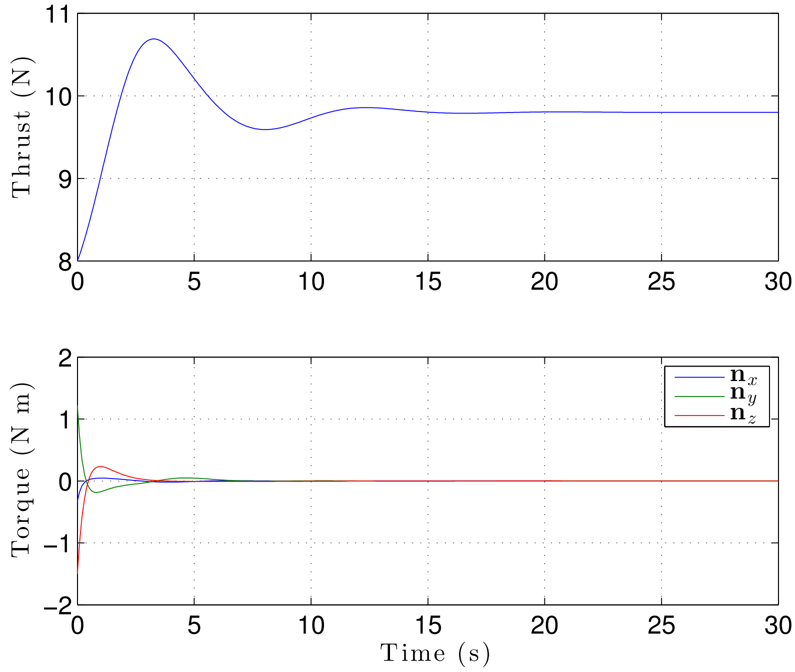

Figure 6.5: Thrust and torque quadrotor actuations.

6.6 Experimental results

We evaluated the performance and robustness of the proposed controllers and estimators at the SCORE lab flying arena at the University of Macau. The facilities are equipped with a motion capture system that provides ground-truth data for the vehicle and camera positions, allowing to assess the real-world performance of the proposed estimator, as well as of the controllers.

The setup is depicted in Fig. 6.6, in which the motion capture cameras, the quadrotor and the landmark markers are visible. We use an Asctec Pelican quadrotor with an onboard Atom computer as our flying platform. The onboard computer communicates with the low-level Asctec autopilot to obtain gyro measurements at 100Hz and acquires and processes camera frames at 30 Hz to identify the four markers. The raw gyro data and image coordinates of the markers are then transmitted to a ground station where the nonlinear observer and controller loops are implemented. The final computed commands for the quadrotor are then transmitter back to the onboard computer that issues them to the low-level Asctec autopilot. Due to restrictions in the experimental setup, it was not possible to use the attitude controller (6.27) to drive the vehicle. Instead of commanding directly the quadrotor motors, we relied on an inner control-loop for the attitude, which

Figure 6.6: Experimental setup at the University of Macau. The motion capture cameras, the quadrotor equipped with the pan and tilt camera, and the landmark markers are visible.

is implemented onboard the vehicle and receives attitude commands, such as the ones given by the proposed lateral-longitudinal controller (6.31).

The steerable platform connects the camera to the quadrotor through two servo motors (see Fig. 6.7, controlling each the pan and tilt angles of the platform. The platform is adorned with reflective markers, so that ground-truth data can be obtained using the motion capture system. The input to the servos was restricted to the interval $[-0.3, 0.3]$ rad/s to avoid jerk in the movements.

The camera lens is an M12 mount lens with focal length of 2.1 mm and its calibration matrix was determined *a priori*. The relevant parameters are the focal length $f = 344.1$ pixels and the calibrated camera optical center $(c_x, c_y) = (368.6, 220.0)$ pixels. The imaging sensor area is 752 by 480 pixels.

We now proceed with the analysis of a representative run of the proposed controller and estimator, focusing first on the pan and tilt camera control. The camera coordinates of the markers and intersection point are depicted in Fig. 6.8 and are clearly far from the

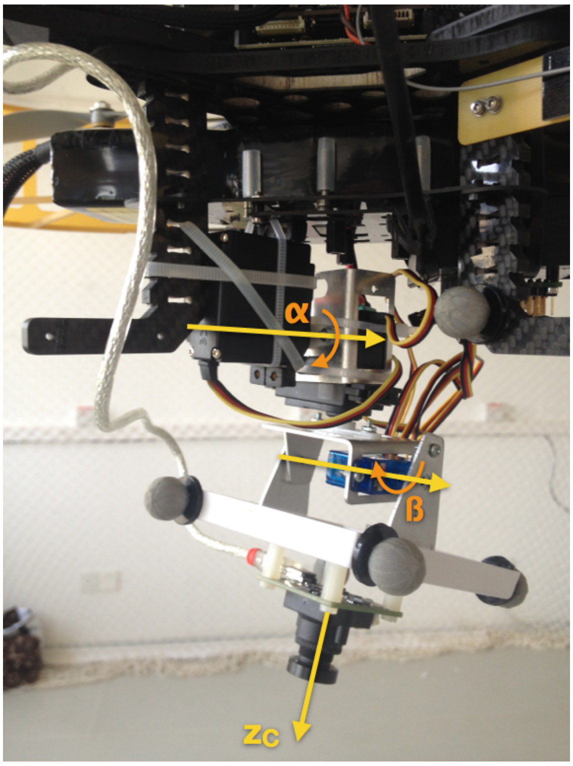

Figure 6.7: The camera setup with pan and tilt rotation axes signaled.

image plane limits throughout the whole maneuver. The time evolution of the coordinates of the makers in the camera reference frame is shown in Fig. 6.9. The initial transient is due to the quadrotor tilting and moving towards the desired location once the controller is enabled. The pan and tilt servos are not able to respond fast enough so as to totally mitigate the initial motion of the vehicle. However, the initial transient error converges to values around zero. The corresponding camera pan and tilt angles are presented in Fig. 6.10. There we can see the influence of the saturation on the input angular velocities, particularly during the interval $[1,3]$s, where the descending slope for pan and tilt is constant ($-0.3\,\mathrm{rad/s}$) due to the input saturation. The pan and tilt angles are obtained directly from the actuation servos. The error in Euler angles between the measurements and the motion capture system ground-truth is shown in Fig. 6.11. We can see that throughout most of the maneuver the error for each particular euler angle is less than 0.05 rad (2.9 deg).

To have a better picture of the global control, we plot the camera coordinates of the intersection point in the *virtual camera* frame, that is, a camera that is always oriented towards the ground, in Fig. 6.12. The coordinates converge to the optical center of the calibrated camera, $(c_x, c_y) = (368.6, 220.0)$ pixels, corresponding to the quadrotor hovering above the centroid of the landmarks.

The time evolution of the attitude estimation error is shown in Fig. 6.13. After the

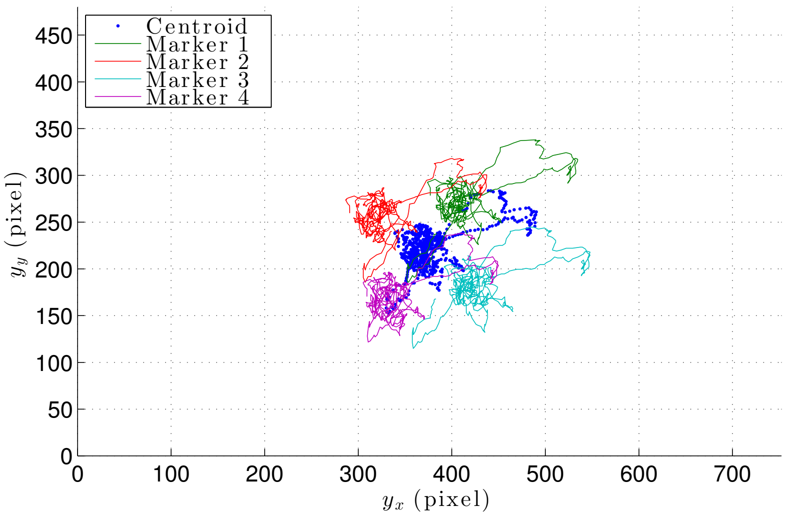

Figure 6.8: Marker's location in camera sensor during the stabilization maneuver.

initial transient the errors are small, with a maximum error of about 0.05 rad, the same order of magnitude of the camera installation errors. The initial error is larger than in steady state due to the larger initial mismatch between the camera pan and tilt angles measurements used for the attitude estimation and the real pan and tilt angles obtained from ground-truth. The error between the measured and real angles is patent in Fig. 6.11 and a correlation between higher pan and tilt error and corresponding higher estimation error can be perceived, particular in the initial instants following $t = 0\,\mathrm{s}$ and again at $t = 11\,\mathrm{s}$.

The attitude commands to the quadrotor are depicted in Fig. 6.14 and the position error relative to the centroid of the landmarks is shown in Fig. 6.15. We can see that there is an initial transient where the position of the quadrotor converges rapidly to the landmarks. Once hovering the markers, the position error is always below 20 cm, which attests to the performance of the proposed controller, despite the non-idealities present in the overall system.

6.7 Concluding remarks

This chapter proposed a cascaded architecture comprising a nonlinear attitude observer and a nonlinear controller for the stabilization of a quadrotor vehicle based on image measurements of a set of landmarks obtained from a pan and tilt camera and biased rate gyros. The vehicle was stabilized vertically to a given altitude by resorting to a

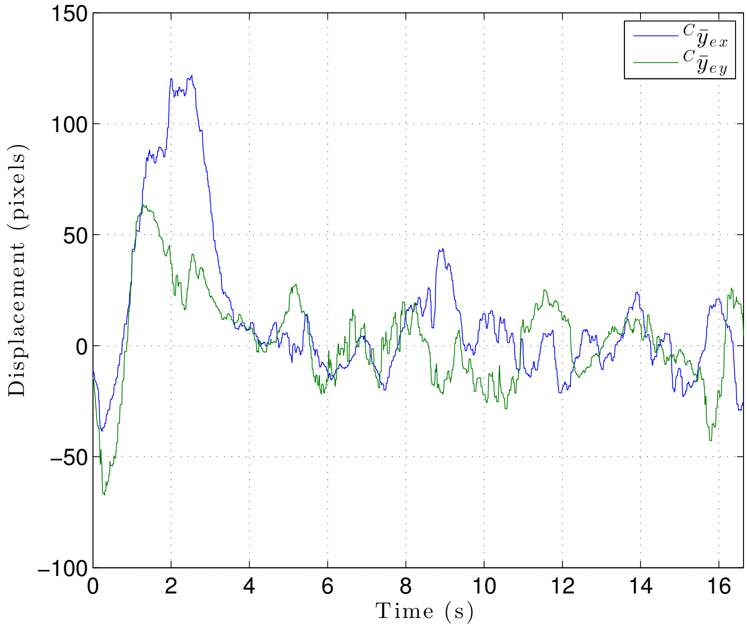

Figure 6.9: Marker's location in camera sensor.

proportional-derivative control law based on image measurements and a vertical position sensor. The lateral-longitudinal stabilization was achieved with a nested saturation control law using feedback of the image measurements, estimated body attitude and angular rate. Both controllers were shown to be input-to-state-stable with respect to the attitude and rate gyros bias estimation errors, which guarantees the closed-loop stability of the overall cascaded architecture. During the whole stabilization procedure the pan and tilt camera was actuated so as to keep the image of the landmarks' centroid at the center of the image plane. Experimental and simulation results exhibited good performance and attested the applicability of the proposed technique, even in non-ideal conditions. Future work will focus on the extension of the proposed control and estimation architecture to allow for richer quadrotor control objectives, such as trajectory tracking or path following, always with a focus on using explicitly the image sensor measurements without recovering the quadrotor state.

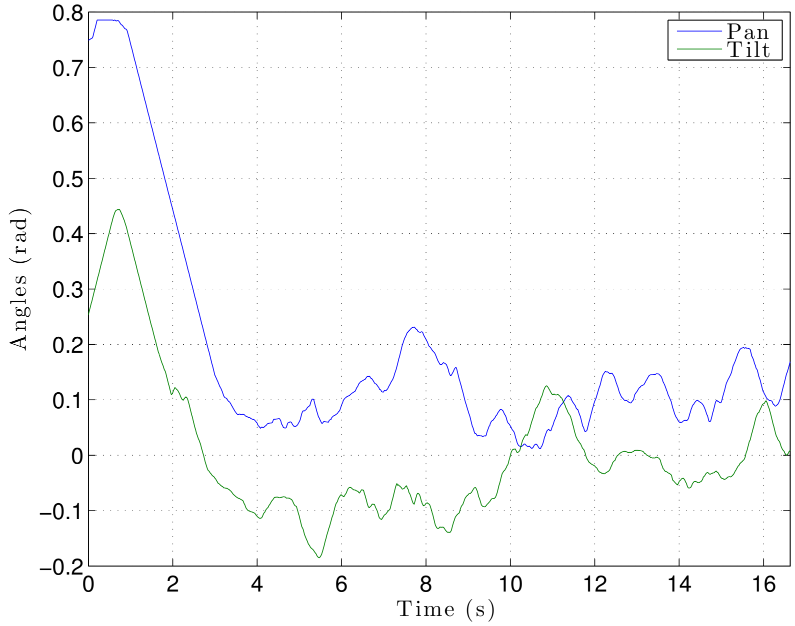

Figure 6.10: Pan and tilt camera measured angles.

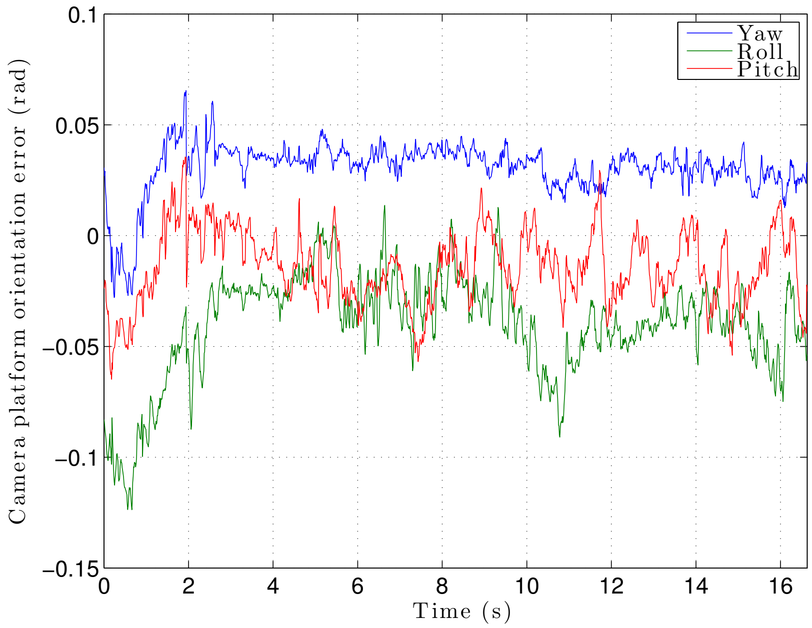

Figure 6.11: Orientation error of the camera pan and tilt platform.

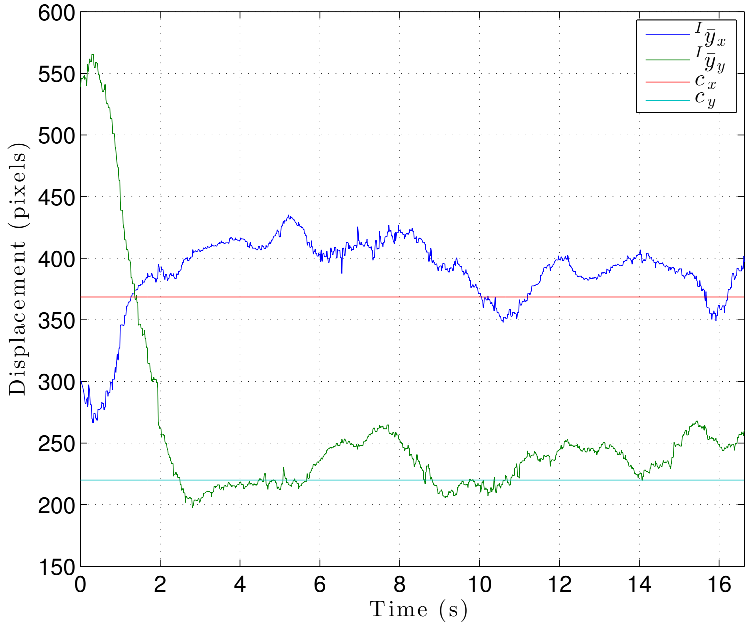

Figure 6.12: Virtual camera coordinates of the intersection point.

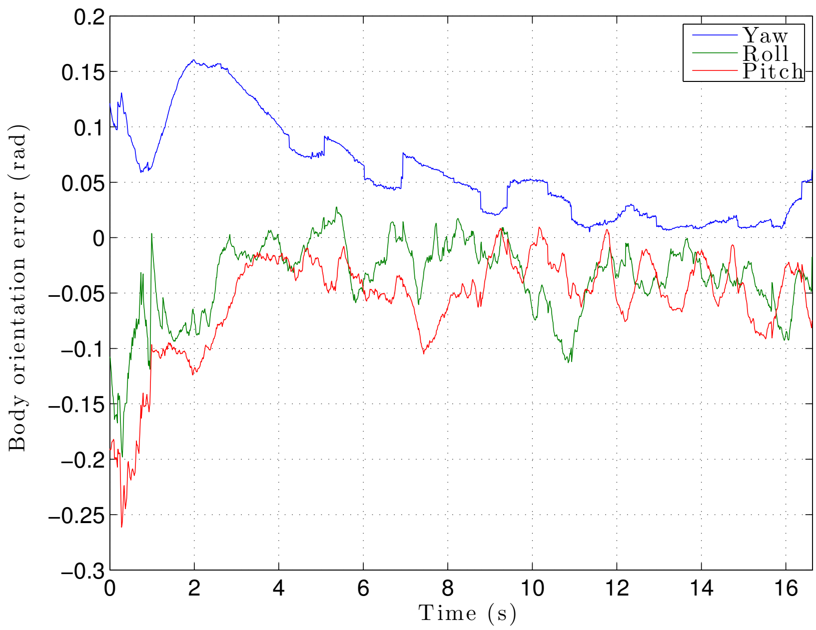

Figure 6.13: Difference of observer estimates and ground-truth.

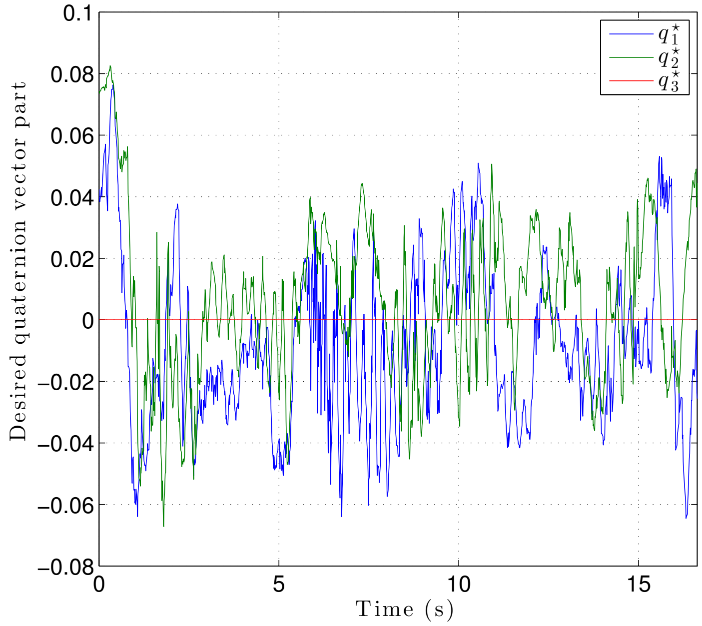

Figure 6.14: Vectorial part of desired orientation quaternion.

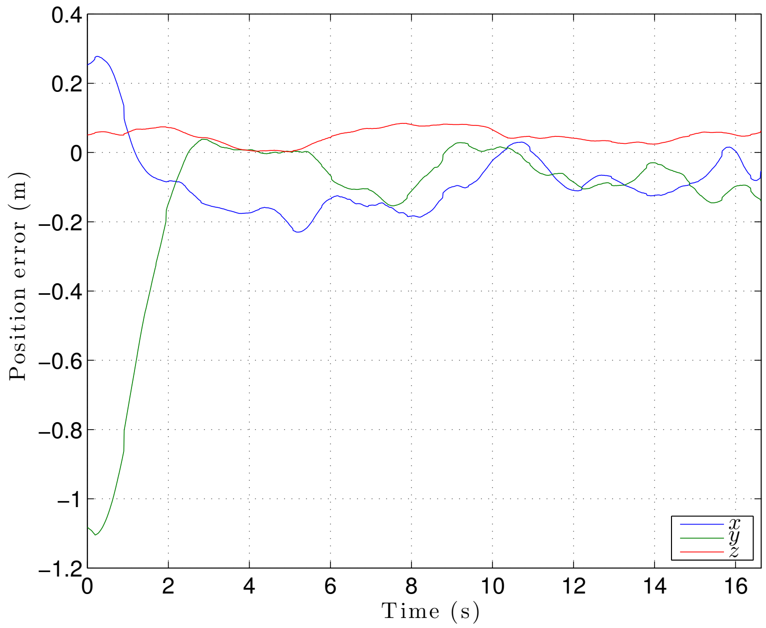

Figure 6.15: Position error.

7 Conclusions

This thesis addressed a number of modeling and motion control problems posed by the development of autonomous air vehicles. Its main contributions can be summarized as follows:

- A landmark-based controller for force and torque actuation that guarantees almost global asymptotic stability of the desired equilibrium point for a fully-actuated rigid body.

- A trajectory tracking controller for steering a quadrotor vehicle along a time-dependent trajectory that asymptotically stabilizes the closed-loop system, even in the presence of constant force disturbances, and ensures that the actuation does not grow unbounded as a function of the position error.

- A global controller to steer a quadrotor vehicle along a predefined path, with a secondary control objective related to the velocity and robust to constant wind disturbances.

- An approach to the robust take-off and landing of a quadrotor UAV in critical scenarios, such as the presence of sloped terrains and surrounding obstacles.

- A cascaded control architecture comprising a nonlinear attitude observer and a nonlinear controller for vision-based position and attitude stabilization of a quadrotor.

Chapter 2 presented a landmark-based solution to the problem of stabilizing a fully-actuated rigid body while keeping the force and torque actuation within predefined bounds. A landmark-based error function was introduced for potential energy shaping and combined with a dissipative force map to obtain a dissipative closed-loop system that has an AGAS equilibrium point at the minimum of the error function. The prescribed bounds on the actuation were enforced by appropriately scaling a modified version of the error function and defining a bounded dissipative force map.

In Chapter 3 we proposed a state feedback solution to the problem of stabilizing an underactuated quadrotor vehicle along a predefined trajectory in the presence of constant force disturbances. A Lyapunov function for the system was derived using adaptive backstepping techniques and made possible by dynamic extension of the actuation. A pair of sufficiently smooth estimators was introduced so as to compensate for the force disturbance and add integral action to the system. Control solutions for different levels of actuation control, which depend on the aircraft, were proposed and tested. A rapid prototyping and testing architecture was developed to expedite the development process by creating an abstraction layer that integrates the sensors, controller, and communication with the vehicle. Experimental data for trajectory tracking applied to a small-scale quadrotor vehicle was presented which evidenced the effects of the adaptive action and demonstrated the robustness and performance of the proposed control law. Realistic simulation data using a non-ideal torque and thrust actuated quadrotor model is also presented, where the robustness and performance of the proposed controller with a smooth double estimator is assessed.

Chapter 4 presented a state feedback solution to the problem of steering a quadrotor vehicle along a predefined path. The proposed solution guarantees global convergence of the path following error to zero, for a large class of three-dimensional paths. The nonlinear controller, which was designed using Lyapunov-based backstepping techniques, ensures that the actuation does not grow unbounded as function of the position error and allows for zero thrust actuation to be applied when the vehicle is converging to the path. The proposed controller was designed to be robust to unknown constant force disturbances that arise from the presence of wind or imperfect knowledge of vehicle parameters. Additionally, the vehicle's progression along the path is controlled to follow a predefined speed profile and simultaneously maintain the path following control law well-defined. A final degree of freedom in the control laws is explored so that the vehicle flies with zero side-slip angle. Experimental and simulation results were presented for vehicles controlled in both angular velocity and torque to assess the performance of the proposed controllers. The robustness of the controller to non-ideal wind disturbances was experimentally demonstrated using a mechanical fan as a disturbance generator.

In Chapter 5 we addressed the problem of robust take-off control of a quadrotor UAV, considering explicitly the interaction with the ground, so as to guarantee successful maneuvers even in sloped terrains and in the presence of external disturbances and uncertain parameters. The vehicle was modeled as a hybrid automaton, whose states reflect the different dynamic behaviors exhibited by the UAV. The take-off procedure was then cast as the problem of changing the operating mode from the initial to the final desired state, through the edges allowed for the hybrid automaton. The transitions between intermediate operating modes were achieved through the application of low-level feedback controllers, associated with each mode, to track robust reference signals. The supervisor and the combined properties of the low-level controllers and reference trajectories ensures that the desired intermediate transitions are attained, robustly to with respect to uncertainties in the model and environment parameters, and that the final desired state is reached. Experimental and simulation results were presented to assess the performance of the proposed hybrid controller, demonstrating the effectiveness of the proposed solution, especially for the cases in which the slope of the terrain renders the landing and take-off maneuvers more critical to be achieved.

Chapter 6 proposed a cascaded architecture comprising a nonlinear attitude observer and a nonlinear controller for the stabilization of a quadrotor vehicle based on image measurements of a set of landmarks obtained from a pan and tilt camera and biased rate gyros. The vehicle was stabilized vertically to a given altitude with a proportional-derivative (PD) control law based on image measurements and a vertical position sensor. The lateral-longitudinal stabilization was achieved with a nested saturation control law using feedback of the image measurements, estimated body attitude and angular rate. Both controllers were shown to be ISS with respect to the attitude and rate gyros bias estimation error, which allows for the closed-loop stability of the cascaded architecture. During the whole stabilization procedure the pan and tilt camera was actuated so as to keep the image of the landmarks' centroid at the center of the image plane. Simulation results exhibited good performance and attested the applicability of the proposed technique.

7.1 Directions for future work

The results presented in this thesis leave several avenues open for future research. The most obvious continuation to the work presented in Chapter 2 is its extension to a trajectory tracking problem and its application to under-actuated vehicles such as quadrotors, helicopter or fixed-wind aircraft. Steps in this direction have already been taken in the remaining Chapters of this Thesis.

Regarding Chapter 3, direction of future work opened by this Thesis are the generalization of the proposed control law to one that can be guaranteed to be almost-global. Also of interest is the consideration of saturated control actuation and the derivation of a law that ensures bounds on the thrust and torque inputs.

Future extensions to the work presented in Chapter 4 remain to be carried on input saturation as the proposed controller generates inputs which are bounded with respect to the position and velocity errors but can grow unbounded on the other backstepping errors.

Following Chapter 5, opportunities for future research are opened on the experimental validation of the proposed solution for the take-off problem, as well as improvements to the hybrid dynamical model and the hybrid controller. In particular, for the experimental activity, a complex integration of the sensors (contact, force) and all the avionics equipments will be required, extending the standard sensing capabilities of the vehicle in order to robustly detect the current operative mode based solely on onboard sensors. This latter issue suggests also to investigate methodological solutions aiming at improving robustness to the possible uncertainties that may affect the measure of the current hybrid state. Another interesting research topic is the appropriate extension of the proposed framework to a third dimension, by adapting the presented arguments, allowing the controller to handle more complex scenarios in terms of the characteristics of the possible environment of operation.

Finally, the most immediate line of work on Chapter 6 is the extension of the proposed control architecture from the stabilization problem to solving the trajectory tracking control problem for a quadrotor. Additionally, other onboard sensors can be used to enhance the attitude estimations, typically through accelerometer measurements. The role of accelerometers for attitude estimation has been subject of scientific debate where [MS10] first pointed out problems with typical model simplifications and observer implementations. The more recent work [LMBM14] provides insightful details on the true role of accelerometer measurements that can be adapted to further enhance the proposed observer law.

As the motion control of aerial vehicles in free flight is reaching its maturity, new and interesting challenges lie ahead. The recent trend of having the aerial vehicles interacting with the environment opens an array of possibilities that include landing and sliding on inclined slopes (as presented in Chapter 5), wall perching, grasping and manipulation, and load transportation. In all these cases, special attention has to be payed to the dynamics of the system, as these change significantly with respect to the free flight dynamics. The maturity of single vehicle control also opens the avenue of multiple vehicle cooperation. Cooperative control of multi-vehicle systems is advantageous in carrying out tasks such as surveillance and search, where it results in a faster and more efficient process, and mapping of large areas like the sea floor, providing results in a faster and more efficient manner. Multiple sensing robots moving in a coordinated manner can also be perceived as a distributed network of sensors, altogether accomplishing a larger sensing task or alternatively providing robustness to sensor loss in critical environments.

Challenges in maintaining a multi-vehicle formation while moving in space are posed by the inter-vehicle communication topology and necessity to implement collision avoidance (inter-vehicle and with the environment).

An interesting intersection of the two proposed future work avenues is the problem of load transportation using multiple vehicles, as the operation of multiple vehicles to assist the load transportation can extend significantly the range of the missions and increase payload capacity. Closed-loop solutions for the slung-load transport problem can be envisaged adopting two alternative approaches: From a robustness perspective, with the load considered as a disturbance on the nominal multi-vehicle system, and from a position control perspective, wherein the multibody dynamics are explicitly modeled and feedback of the load position is used in order to steer it along a path.

A

Double integrator

A.1 Arbitrarily bounded controller for a double integrator system with strict Lyapunov function

Consider the double integrator system

$$\dot{x}_1 = x_2,$$
$$\dot{x}_2 = u,$$

driven by the saturated input

$$u = \sigma(k_1 x_1 + k_2 x_2) \tag{A.1}$$

bounded by $\sigma_{\max}$ as $|u| \leq \sigma_{\max}$. Define the positive definite matrix P as

$$P = \begin{bmatrix} a & -a\frac{k_1}{k_2} \\ -a\frac{k_1}{k_2} & k_1 \end{bmatrix}$$

with $a > \frac{k_2^2}{k_1}$ and positive k_1, k_2. To establish the global asymptotic stability of the origin we consider the Lyapunov function

$$V(x_1, x_2) = \frac{1}{2}\begin{bmatrix} \sigma(k_1 x_1 + k_2 x_2) \\ x_2 \end{bmatrix} P \begin{bmatrix} \sigma(k_1 x_1 + k_2 x_2) & x_2 \end{bmatrix} + \int_0^{k1x1+k2x2} \sigma(\tau)\mathrm{d}\tau$$

and compute it's derivative as

$$\dot{V}(x_1, x_2) = \begin{bmatrix} \sigma(k_1 x_1 + k_2 x_2) \\ x_2 \end{bmatrix} Q \begin{bmatrix} \sigma(k_1 x_1 + k_2 x_2) & x_2 \end{bmatrix}$$

where Q is the definite negative matrix defined as

$$Q = \begin{bmatrix} a\frac{k_1}{k_2} - k_2 - ak_2\sigma'(k_1 x_1 + k_2 x_2) & ak_1\sigma'(k_1 x_1 + k_2 x_2) \\ ak_1\sigma'(k_1 x_1 + k_2 x_2) & -a\frac{k_1^2}{k_2}\sigma'(k_1 x_1 + k_2 x_2) \end{bmatrix}.$$

The proposed controller (A.1) renders the closed-loop time derivative of the double integrator dynamic system a strictly negative definite function as $\dot{V}(x_1, x_2) = -W(x_1, x_2) \leq 0$, where the positive definite function W is

$$W(x_1, x_2) = -\begin{bmatrix} \sigma(k_1 x_1 + k_2 x_2) \\ x_2 \end{bmatrix} Q \begin{bmatrix} \sigma(k_1 x_1 + k_2 x_2) & x_2 \end{bmatrix}.$$

B

Proofs for Chapter 5

B.1 Proof of Proposition 20

With $\tilde{\theta}(t) = \theta(t) - \theta^\star(t)$ the closed-loop error dynamics can be written as

$$\ddot{\tilde{\theta}} = -K_P(\tilde{\theta} + K_D\dot{\tilde{\theta}}) + \Psi_\theta(\tilde{\theta}, \dot{\tilde{\theta}}),$$

where

$$\Psi_\theta(\tilde{\theta}, \dot{\tilde{\theta}}) = h_\theta(\theta^\star + \tilde{\theta}, \dot{\theta}^\star + \dot{\tilde{\theta}}, 0, \mu) - h_\theta(\theta^\star, \dot{\theta}^\star, 0, \mu),$$

with $h_\theta(\cdot)$ defined in (5.7). Form this the result immediately follows by using the fact that $\Psi_\theta(\cdot,\cdot)$ is locally Lipschitz and the definition of u.

B.2 Proof of Proposition 21

Let $\tilde{\theta} := \theta - \theta^\star$ and $\tilde{\alpha} := \alpha - \alpha^\star$, and note that (5.5) in the new coordinates transform as

$$\ddot{\tilde{\theta}} = \tilde{F}_\theta + \Psi_\theta(\tilde{\theta}, \dot{\tilde{\theta}}, \dot{\tilde{\alpha}}, t) + \delta_\theta(t), \quad \ddot{\tilde{\alpha}} = \tilde{F}_\alpha + \Psi_\alpha(\tilde{\theta}, \dot{\tilde{\theta}}, \dot{\tilde{\alpha}}, t) + \delta_\alpha(t),$$

where (see (5.6) and (5.7))

$$\begin{aligned}
\Psi_\theta(\tilde{\theta}, \dot{\tilde{\theta}}, \dot{\tilde{\alpha}}, t) &= h_\theta(\theta^\star + \tilde{\theta}, \dot{\theta}^\star + \dot{\tilde{\theta}}, \dot{\alpha}^\star + \dot{\tilde{\alpha}}, \mu) - h_\theta(\theta^\star, \dot{\theta}^\star, \dot{\alpha}^\star, \mu) \\
\Psi_\alpha(\tilde{\theta}, \dot{\tilde{\theta}}, \dot{\tilde{\alpha}}, t) &= h_\alpha(\theta^\star + \tilde{\theta}, \dot{\theta}^\star + \dot{\tilde{\theta}}, \dot{\alpha}^\star + \dot{\tilde{\alpha}}, \mu) - h_\alpha(\theta^\star, \dot{\theta}^\star, \dot{\alpha}^\star, \mu) \\
\delta_\theta(t) &= (\mu - \mu_0)\frac{g\cos\beta\sin(\theta^\star + \gamma + \beta)}{\ell\cos(\theta^\star(t) + \gamma + \beta)^2}\mathrm{sign}(\dot{\alpha}^\star(t)) \\
\delta_\alpha(t) &= -(\mu - \mu_0)\frac{g\cos\beta}{\cos(\theta^\star(t) + \gamma + \beta)^2}\mathrm{sign}(\dot{\alpha}^\star(t))
\end{aligned}$$

and $\tilde{F}_\theta := F_\theta - F_\theta^\star$, $\tilde{F}_\alpha := F_\alpha - F_\alpha^\star$ with F_θ and F_α defined in (5.14). We observe that, by definition of $\theta^\star$, the functions $\delta_\alpha(t)$ and $\delta_\theta(t)$ satisfies $|\delta_\delta(t)| \le L_\delta|\mu - \mu_0|$ and $|\delta_\alpha(t)| \le L_\alpha|\mu - \mu_0|$ for all $t \ge 0$, for some positive constants L_δ and L_α.

Define the change of variables $\theta_1 := \tilde{\theta}$, $\theta_2 := \dot{\tilde{\theta}} + \frac{1}{K_D}\tilde{\theta}$, $\alpha_1 := \tilde{\alpha}$, $\alpha_2 := \dot{\tilde{\alpha}} + \frac{1}{K_D}\tilde{\alpha}$ which transforms the closed-loop error system into

$$\begin{aligned}\dot{\theta}_1 &= -\tfrac{1}{K_D}\theta_1 + \theta_2,\\ \dot{\theta}_2 &= -K_P K_D\theta_2 + \Psi_\theta(\theta_1, \theta_2 - \tfrac{1}{K_D}\theta_1, \alpha_2 - \tfrac{1}{K_D}\alpha_1, t) - \tfrac{1}{K_D^2}\theta_1 + \tfrac{1}{K_D}\theta_2 + \delta_\theta,\end{aligned} \tag{B.1}$$

and

$$\begin{aligned}\dot{\alpha}_1 &= -\tfrac{1}{K_D}\alpha_1 + \alpha_2,\\ \dot{\alpha}_2 &= -K_P K_D\alpha_2 + \Psi_\alpha(\theta_1, \theta_2 - \tfrac{1}{K_D}\theta_1, \alpha_2 - \tfrac{1}{K_D}\alpha_1, t) - \tfrac{1}{K_D^2}\alpha_1 + \tfrac{1}{K_D}\alpha_2 + \delta_\alpha.\end{aligned} \tag{B.2}$$

Let $\rho := \min_{t\in[t_0,t_f]}\theta^\star(t) + \beta$ and note that $\rho > \epsilon > 0$. Define the Lyapunov function $V(\theta_1, \theta_2, \alpha_1, \alpha_2) = V_\theta(\theta_1, \theta_2) + V_\alpha(\alpha_1, \alpha_2)$ where

$$V_\theta(\theta_1, \theta_2) := \frac{\theta_1^2}{\rho - |\theta_1|} + \frac{1}{2}\theta_2^2, \quad V_\alpha(\alpha_1, \alpha_2) := \frac{1}{2}\left(\alpha_1^2 + \alpha_2^2\right),$$

and note that $V(\theta_1, \theta_2, \alpha_1, \alpha_2)$ is defined and radially unbounded on the domain $(-\rho, \rho) \times \mathbb{R} \times \mathbb{R} \times \mathbb{R}$. Furthermore, let $\Omega(\ell) := \{(\theta_1, \theta_2, \alpha_1, \alpha_2) \ : \ V \le \ell^2\}$, a level set of V.

By using the fact that $\Psi_\theta(\cdot)$ and $\Psi_\alpha(\cdot)$ are locally Lipschitz and vanishing in $\theta_1 = 0$, $\theta_2 - \frac{1}{K_D}\theta_1 = 0$, $\alpha_2 - \frac{1}{K_D}\alpha_1 = 0$, for any ℓ there exist positive L_1 and L_2 such that for all $(\theta_1, \theta_2, \alpha_1, \alpha_2) \in \Omega_\theta(\ell)$ the following hold

$$\begin{aligned}|\Psi_\theta(\theta_1,\, \theta_2 - \tfrac{1}{K_D}\theta_1,\, \alpha_2 - \tfrac{1}{K_D}\alpha_1,\, t)| &\le L_1(K_D)|\theta_1| + L_1(K_D)|\alpha_1| + L_2|\theta_2| + L_2|\alpha_2|\\ |\Psi_\alpha(\theta_1,\, \theta_2 - \tfrac{1}{K_D}\theta_1,\, \alpha_2 - \tfrac{1}{K_D}\alpha_1,\, t)| &\le L_1(K_D)|\theta_1| + L_1(K_D)|\alpha_1| + L_2|\theta_2| + L_2|\alpha_2|,\end{aligned}$$

for all $t \ge 0$.

The time derivative of V_θ and V_α along the solutions of (B.1)-(B.2), can be upper bounded as

$$\begin{aligned}\dot{V}_\theta \ &\le \ T(\theta)\Big(-\tfrac{1}{K_D}\theta_1^2 + |\theta_1||\theta_2|\Big) + (-K_P K_D + L_2 + \tfrac{1}{K_D})\theta_2^2\\ &\quad +(L_1(K_D) + \tfrac{1}{K_D^2})|\theta_1||\theta_2| + L_1(K_D)|\theta_2||\alpha_1| + L_2|\theta_2||\alpha_2| + |\theta_2||\delta_\theta|\end{aligned}$$

$$\begin{aligned}\dot{V}_\alpha \ &\le \ \Big(-\tfrac{1}{K_D}\alpha_1 + \alpha_2\Big) + (-K_P K_D + L_2 + \tfrac{1}{K_D})\alpha_2^2\\ &\quad +(L_1(K_D) + \tfrac{1}{K_D^2})|\alpha_1||\alpha_2| + L_2|\theta_2||\alpha_1| + L_1(K_D)|\theta_1||\alpha_2| + |\alpha_2||\delta_\alpha|\end{aligned}$$

where $T(\theta_1) = \left(2 + \theta_1^2/|\theta_1|\right)/(\rho - |\theta_1|)^2$. Note that $T(\theta_1) \ge 2/\rho^2$ for all $\theta_1 \in \mathbb{R}$. By completing the squares, it follows that for any ℓ and for any c there exists a $K_D^\star > 0$ and a $K_P^\star(K_D) > 0$ such that for any positive $K_D \le K_D^\star$ and $K_P \ge K_P^\star$ the following bound on $\dot{V}$ can be established

$$\dot{V} \le -\gamma\|(\theta_1, \theta_2, \alpha_1, \alpha_2)\| + c\|(\delta_\theta, \delta_\alpha)\|$$

for all $(\theta_1, \theta_2, \alpha_1, \alpha_2) \in \Omega_\ell$, where γ is a positive constant. From this the result follows by standard Lyapunov arguments by using the definition of u, of $(\delta_\theta, \delta_\alpha)$ and by noting that for any ℓ and K_D there exist a $\Delta_{TLs,0}$ such that

$$\begin{aligned}\{(\theta_1, \theta_2, \alpha_1, \alpha_2) \in \mathbb{R}\times\mathbb{R}\times\mathbb{R}\times\mathbb{R} \, : \\ |\theta_1| \le \Delta_{TLs,0}, \ |\theta_2 - \tfrac{1}{K_D}\theta_1| \le \Delta_{TLs,0} \\ |\alpha_1| \le \Delta_{TLs,0}, \ |\alpha_2 - \tfrac{1}{K_D}\alpha_1| \le \Delta_{TLs,0}\} \subset \Omega(\ell).\end{aligned}$$

B.3 Proof of Proposition 22

Define the error coordinates $\tilde{z} = z - z^\star$, $\tilde{x} = x - x^\star$ and $\tilde{\theta} = \theta - \theta^\star$. In these coordinates the closed-loop system (5.2) and (5.15)-(5.17) reads as

$$m\ddot{\tilde{z}} = -k_1\tilde{z} - k_2\dot{\tilde{z}} + \delta_z \tag{B.3}$$

$$\begin{aligned} m\ddot{\tilde{x}} &= (\tan(\tilde{\theta} + \theta^\star) - \tan\theta^\star)u^\star + \tan\theta\, u_1(\tilde{z}, \dot{\tilde{z}}) + \delta_x \\ J\ddot{\tilde{\theta}} &= -rK_P(K_D\dot{\tilde{\theta}} + \tan(\tilde{\theta} + \theta^\star) - \tan\theta^\star + \theta_{\text{out}}(\tilde{x}, \dot{\tilde{x}}))\end{aligned} \tag{B.4}$$

with θ_{out} defined in (5.17). This system can be interpreted as the cascade of the vertical error system with state $(\tilde{z}, \dot{\tilde{z}})$ driving the lateral and angular dynamics with state $(\tilde{x}, \dot{\tilde{x}})$ and $(\tilde{\theta}, \dot{\tilde{\theta}})$. Since k_1 and k_2 are positive the vertical subsystem is clearly input-to-state stable with respect to the exogenous disturbance δ_z without restrictions on the initial state and on the input. The lateral and angular subsystem has been studied in [IMS03] (see also [MN07]). In particular, by Proposition 5.7.2 of [IMS03], the system in question, with the tuning of the parameters K_P, K_D, K_i and λ_i, $i = 1, 2$, specified in the statement of Proposition 22, can be proved to be input-to-state stable with respect to the inputs u_1 and δ_x without restrictions on the initial state and nonzero restrictions (dependent on ε) on the inputs. Thus, by standard cascade arguments, it follows that the whole system (B.3)-(B.4), with exogenous inputs (δ_x, δ_z) is input-to-state-stable without restrictions on the initial state and nonzero restrictions (dependent on ε) on the inputs. From this, the claim of the proposition follows by using the expression of u in (5.16).

Bibliography

[Aer] Aeronautics Ltd. Pipeline monitoring & oil and gas security. Available online at http://www.aeronautics-sys.com/?CategoryID=259&ArticleID=188.

[AH06] A.P. Aguiar and J.P. Hespanha. Minimum-energy state estimation for systems with perspective outputs. *IEEE Transactions on Automatic Control*, 51(2):226–241, February 2006.

[AHK08] A. Pedro Aguiar, J Hespanha, and P Kokotović. Performance limitations in reference tracking and path following for nonlinear systems. *Automatica*, 44(3):598–610, January 2008.

[Ang01] David Angeli. Almost global stabilization of the inverted pendulum via continuous state feedback. *Automatica*, 37(7):1103–1108, July 2001.

[Ang04] David Angeli. An almost global notion of input-to-state stability. *IEEE Transactions on Automatic Control*, 49(6):866–874, June 2004.

[ANT11] Kostas Alexis, George Nikolakopoulos, and Anthony Tzes. Switching model predictive attitude control for a quadrotor helicopter subject to atmospheric disturbances. *Control Engineering Practice*, 19(10):1195 – 1207, 2011.

[ATH+10] A. Albers, S. Trautmann, T. Howard, Trong Anh Nguyen, M. Frietsch, and C. Sauter. Semi-autonomous flying robot for physical interaction with environment. In *Proceedings of the*, pages 441–446, 2010.

[BB00] Sanjay P. Bhata and Dennis S. Bernstein. A topological obstruction to continuous global stabilization of rotational motion and the unwinding phenomenon. *Systems & Control Letters*, 39(1):63–70, January 2000.

[BCV+11] S. Brás, R. Cunha, J.F. Vasconcelos, C. Silvestre, and P. Oliveira. A nonlinear attitude observer based on active vision and inertial measurements. *IEEE Transactions on Robotics*, 27(4):664–677, August 2011.

[Bet01] J.T. Betts. *Practical Methods for Optimal Control Using Nonlinear Programming*. SIAM, 2001.

[BL04] Francesco Bullo and Andrew D. Lewis. *Geometric control of mechanical systems*, volume 49 of *Texts in Applied Mathematics*. Springer, New York, 2004.

[bla] Horizon hobby inc. Available online at http://www.bladehelis.com.

[BM99] F. Bullo and R. M. Murray. Tracking for fully actuated mechanical systems: A geometric framework. *Automatica*, 35(1):17–34, 1999.

[Bri] British Antarctic Survey. Unmanned aerial vehicles (uav) - scientific technique. Available online at http://www.antarctica.ac.uk/bas_research/techniques/uav/index.php.

[Bro96] B. Brogliato. *Nonsmooth Mechanics Model, Dynamics and Control*. Springer, 1996.

[BS07] S. Bouabdallah and R. Siegwart. Full control of a quadrotor. In *Intelligent Robots and Systems, 2007. IROS 2007. IEEE/RSJ International Conference on*, pages 153 –158, 29 2007-nov. 2 2007.

[BSO09] P. Batista, C. Silvestre, and P. Oliveira. Position and Velocity Optimal Sensor-based Navigation Filters for UAVs. In *Proceedings of the American Control Conference*, pages 5404–5409, Saint Louis, USA, June 2009.

[BSO10] Pedro Batista, Carlos Silvestre, and Paulo Oliveira. Optimal position and velocity navigation filters for autonomous vehicles. *Automatica*, 46(4):767 – 774, 2010.

[CBM06] N.A. Chaturvedi, A.M. Bloch, and N.H. McClamroch. Global stabilization of a fully actuated mechanical system on a riemannian manifold including control saturation effects. In *Proceedings of the IEEE Conference on Decision and Control*, pages 6116–6121, December 2006.

[CDL04] P. Castillo, A. Dzul, and R. Lozano. Real-time stabilization and tracking of a four-rotor mini rotorcraft. *IEEE Transactions on Control Systems Technology*, 12(4):510 – 516, July 2004.

[CdQD06] Z. Cai, M.S. de Queiroz, and D.M. Dawson. A sufficiently smooth projection operator. *IEEE Transactions on Automatic Control*, 51(1):135 – 139, January 2006.

[CH06] F. Chaumette and S. Hutchinson. Visual servo control, part I: Basic approaches. *IEEE Robotics and Automation Magazine*, 13(4):82–90, December 2006.

[CH07] F. Chaumette and S. Hutchinson. Visual servo control, part II: Advanced approaches. *IEEE Robotics and Automation Magazine*, 14(1):109–118, March 2007.

[CM07] N.A. Chaturvedi and N.H. McClamroch. Attitude stabilization of the inverted 3D pendulum on TSO(3) with control saturation. In *Proceedings of the IEEE Conference on Decision and Control*, pages 1910–1915, December 2007.

[CMB07] N.A. Chaturvedi, N.H. McClamroch, and D.S. Bernstein. Stabilization of a specified equilibrium in the inverted equilibrium manifold of the 3D pendulum. In *Proceedings of the American Control Conference*, pages 2485–2490, June 2007.

[CMcTN07] J. A. Castellanos, R. Martínez-cantín, J. D. Tardós, and J. Neira. Robocentric map joining: Improving the consistency of ekf-slam. *Robotics and Autonomous Systems*, 55:21–29, 2007.

[CSH08] Rita Cunha, Carlos Silvestre, and João Pedro Hespanha. Output-feedback control for stabilization on SE(3). *Systems & Control Letters*, 57(12):1013–1022, December 2008.

[CSHA07] R. Cunha, C. Silvestre, J. Hespanha, and A.P. Aguiar. Vision-based control for rigid body stabilization. In *Proceedings of the IEEE Conference on Decision and Control*, pages 2345–2350, December 2007.

[CWK02] N.J. Cowan, J.D. Weingarten, and D.E. Koditschek. Visual servoing via navigation functions. *IEEE Transactions on Robotics and Automation*, 18(4):521–533, August 2002.

[DSL09] A. Das, K. Subbarao, and F. Lewis. Dynamic inversion with zero-dynamics stabilisation for quadrotor control. *Control Theory Applications, IET*, 3(3):303–314, March 2009.

[Emb] Embention. Applications of uavs. Available online at http://www.embention.com/applications.htm.

[FDF99] E. Frazzoli, M.A. Dahleh, and E. Feron. A hybrid control architecture for aggressive maneuvering of autonomous helicopters. In *Proceedings of the IEEE Conference on Decision and Control*, volume 3, pages 2471 –2476 vol.3, 1999.

[FDF00] E. Frazzoli, M.A. Dahleh, and E. Feron. Trajectory tracking control design for autonomous helicopters using a backstepping algorithm. In *Proceedings of the American Control Conference*, volume 6, pages 4102–4107, 2000.

[FDF05] E. Frazzoli, M.A. Dahleh, and E. Feron. Maneuver-based motion planning for nonlinear systems with symmetries. *IEEE Transactions on Robotics*, 21(6):1077 – 1091, December 2005.

[FNM+12] M. Fumagalli, R. Naldi, A. Macchelli, R. Carloni, S. Stramigioli, and L. Marconi. Modeling and control of a flying robot for contact inspection. In *Proceedings of the IEEE/RSJ International Conference on Intelligent Robots and Systems*, pages 3532–3537, October 2012.

[GHM08] N. Guenard, T. Hamel, and R. Mahony. A practical visual servo control for an unmanned aerial vehicle. *IEEE Transactions on Robotics*, 24(2):331 –340, April 2008.

[GL13] Bryan Godbolt and Alan F. Lynch. Model-based helicopter uav control: Experimental results. *Journal of Intelligent & Robotic Systems*, pages 1–13, 2013.

[GMHT08] Steven L. Waslander Gabriel M. Hoffmann and Claire J. Tomlin. Quadrotor helicopter trajectory tracking control. In *Proceedings of the AIAA Guidance, Navigation, and Control Conference*, Honolulu, HI, August 2008.

[GST09] R. Goebel, R. Sanfelice, and A. Teel. Hybrid dynamical systems. *IEEE Control Systems Magazine*, 29(2):28–93, April 2009.

[Gui12] Erico Guizzo. Robotic aerial vehicle captures dramatic footage of fukushima reactors, April 2012. Available online at http://spectrum.ieee.org/automaton/robotics/industrial-robots/robotic-aerial-vehicle-at-fukushima-reactors.

[HFC08] A. Harnoy, B. Friedland, and S. Cohn. Modeling and measuring friction effects. *IEEE Control Systems Magazine*, 28(6):82 –91, December 2008.

[HHMR12] Bruno Hérissé, Tarek Hamel, Robert E. Mahony, and François-Xavier Russotto. Landing a vtol unmanned aerial vehicle on a moving platform using optical flow. *IEEE Transactions on Robotics*, pages 77–89, 2012.

[HHMS09] Minh-Duc Hua, T. Hamel, P. Morin, and C. Samson. A control approach for thrust-propelled underactuated vehicles and its application to vtol drones. *IEEE Transactions on Automatic Control*, 54(8):1837 –1853, August 2009.

[HSDM09] Shuo Han, Andrew D. Straw, Michael H. Dickinson, and Richard M. Murray. A real-time helicopter testbed for insect-inspired visual flight control. In *Proceedings of the IEEE International Conference on Robotics and Automation*, pages 3055 –3060, May 2009.

[IMS03] Alberto Isidori, Lorenzo Marconi, and Andrea Serrani. *Robust autonomous guidance: an internal model approach*. Advances in industrial control. Springer, London, 2003.

[JJT12] S.H. Jeong, Seul Jung, and M. Tomizuka. Attitude control of a quad-rotor system using an acceleration-based disturbance observer: An empirical approach. In *Advanced Intelligent Mechatronics (AIM), 2012 IEEE/ASME International Conference on*, pages 916 –921, July 2012.

[KFL06] F. Kendoul, I. Fantoni, and R. Lozano. Modeling and control of a small autonomous aircraft having two tilting rotors. *IEEE Transactions on Robotics*, 22(6):1297–1302, November 2006.

[KHM+98] T. J. Koo, F. Hoffmann, F. Ho Mann, H. Shim, B. Sinopoli, and S. Sastry. Hybrid control of an autonomous helicopter. In *In IFAC Workshop on Motion Control*, pages 285–290, 1998.

[KKK95] M Krstic, I Kanellakopoulos, and P V. Kokotovic. *Nonlinear and Adaptive Control Design*. John Wiley & Sons, Inc. New York, NY, USA, January 1995.

[KMAO12] Mokhtar Kerma, Abdellah Mokhtari, Benallegue Abdelaziz, and Yuri Orlov. Nonlinear h_{infinity} control of a quadrotor (uav), using high order sliding mode disturbance estimator. *International Journal of Control*, 0(0), 2012.

[Kob13] Marin Kobilarov. Trajectory tracking of a class of underactuated systems with external disturbances. In *In Proc. of the American Control Conference*, pages 1044–1049, 2013.

[Kod89] Daniel E. Koditschek. The application of total energy as a lyapunov function for mechanical control systems. In J. E. Marsden, P. S. Krishnaprasad, and J. C. Simo, editors, *Dynamics and Control of Multibody Systems*, volume 97 of *Contemporary Mathematics*, pages 131–158. American Mathematical Society, 1989.

[KS98] T. John Koo and Shankar Sastry. Output tracking control design of a helicopter model based on approximate linearization. In *Proceedings of the IEEE Conference on Decision and Control*, pages 3635–3640, 1998.

[LD03] J. Lobo and J. Dias. Vision and inertial sensor cooperation using gravity as a vertical reference. *IEEE Transactions on Pattern Analysis and Machine Intelligence*, 25(12):1597 – 1608, December 2003.

[LDC10] Alexis Lussier Desbiens and Mark R. Cutkosky. Landing and perching on vertical surfaces with microspines for small unmanned air vehicles. *Journal of Intelligent and Robotic Systems*, 57(1-4):313–327, January 2010.

[Lee97] John M. Lee. *Riemannian Manifolds: An Introduction to Curvature*. Springer, 1997.

[Lee03] John M. Lee. *Introduction to Smooth Manifolds*. Springer, 2003.

[LMA12] F. Leonard, A. Martini, and G. Abba. Robust nonlinear controls of model-scale helicopters under lateral and vertical wind gusts. *IEEE Transactions on Control Systems Technology*, 20(1):154–163, 2012.

[LMBM14] R.C. Leishman, J.C. Macdonald, R.W. Beard, and T.W. McLain. Quadrotors and accelerometers: State estimation with an improved dynamic model. *Control Systems, IEEE*, 34(1):28–41, February 2014.

[LML06] Taeyoung Lee, N. Harris McClamroch, and Melvin Leok. Optimal control of a rigid body using geometrically exact computations on SE(3). In *Proceedings of the IEEE Conference on Decision and Control*, pages 2710–2715, December 2006.

[LP02] A. Loría and E. Panteley. Uniform exponential stability of linear time-varying systems: revisited. *Systems & Control Letters*, 47(1):13–24, September 2002.

[MC02] E. Malis and F. Chaumette. Theoretical improvements in the stability analysis of a new class of model-free visual servoing methods. *IEEE Transactions on Robotics and Automation*, 18(2):176–186, April 2002.

[MCH08] R. Mahony, P. Corke, and T. Hamel. Dynamic image-based visual servo control using centroid and optic flow features. *Journal of Dynamic Systems, Measurement, and Control*, 130(1):011005, January 2008.

[MFK11] Nathan Michael, Jonathan Fink, and Vijay Kumar. Cooperative manipulation and transportation with aerial robots. *Autonomous Robots*, 30(1):73–86, January 2011.

[MH04] Robert Mahony and Tarek Hamel. Robust trajectory tracking for a scale model autonomous helicopter. *International Journal of Robust and Nonlinear Control*, 14(12):1035–1059, June 2004.

[MH05] R. Mahony and T. Hamel. Image-based visual servo control of aerial robotic systems using linear image features. *IEEE Transactions on Robotics*, 21(2):227–239, April 2005.

[MHP08] R. Mahony, T. Hamel, and J.-M. Pflimlin. Nonlinear complementary filters on the special orthogonal group. *IEEE Transactions on Automatic Control*, 53(5):1203 –1218, June 2008.

[MI04] F Mazenc and A Iggidr. Backstepping with bounded feedbacks. *Systems & Control Letters*, 51(3-4):235–245, March 2004.

[MIS02] L. Marconi, A. Isidori, and A. Serrani. Autonomous vertical landing on an oscillating platform: an internal-model based approach. *Automatica*, 38(1):21 – 32, 2002.

[MKS99] Yi Ma, J. Kosecka, and S.S. Sastry. Vision guided navigation for a non-holonomic mobile robot. *IEEE Transactions on Robotics and Automation*, 15(3):521–536, June 1999.

[MKS06] Michael Malisoff, Mikhail Krichman, and Eduardo Sontag. Global stabilization for systems evolving on manifolds. *Journal of Dynamical and Control Systems*, 12(2):161–184, April 2006.

[MN07] Lorenzo Marconi and Roberto Naldi. Robust full degree-of-freedom tracking control of a helicopter. *Automatica*, 43(11):1909 – 1920, 2007.

[MN12] L. Marconi and R. Naldi. Control of aerial robots: Hybrid force and position feedback for a ducted fan. *Control Systems, IEEE*, 32(4):43 –65, aug. 2012.

[MNG09] L. Marconi, R. Naldi, and L. Gentili. A control framework for robust practical tracking of hybrid automata. In *Proceedings of the IEEE Conference on Decision and Control*, 2009.

[MRU+11] B. Michini, J. Redding, N.K. Ure, M. Cutler, and J.P. How. Design and flight testing of an autonomous variable-pitch quadrotor. In *Proceedings of the IEEE International Conference on Robotics and Automation*, pages 2978 –2979, May 2011.

[MS08] Pascal Morin and Claude Samson. Motion control of wheeled mobile robots. In Bruno Siciliano and Oussama Khatib, editors, *Springer Handbook of Robotics*, pages 799–826. Springer Berlin Heidelberg, 2008. 10.1007/978-3-540-30301-5_35.

[MS10] P. Martin and E. Salaun. The true role of accelerometer feedback in quadrotor control. In *Robotics and Automation (ICRA), 2010 IEEE International Conference on*, pages 1623–1629, May 2010.

[MSK10] Daniel Mellinger, Michael Shomin, and Vijay Kumar. Control of quadrotors for robust perching and landing. *Proceedings of the International Powered Lift Conference*, 2010.

[MTR+09] Anastasios I. Mourikis, Nikolas Trawny, Stergios I. Roumeliotis, Andrew E. Johnson, Adnan Ansar, and Larry Matthies. Vision-aided inertial navigation for spacecraft entry, descent, and landing. *IEEE Transactions on Robotics*, 25(2):264–280, 2009.

[NGM11] Roberto Naldi, Luca Gentili, and Lorenzo Marconi. Modeling and control of a flying robot interacting with the environment. *Automatica*, 47(6), 2011.

[NGMS10] Roberto Naldi, Luca Gentili, Lorenzo Marconi, and Andrea Sala. Design and experimental validation of a nonlinear control law for a ducted-fan miniature aerial vehicle. *Control Engineering Practice*, 18(7):747 – 760, 2010. Special Issue on Aerial Robotics.

[NMG09] R. Naldi, L. Marconi, and L. Gentili. Robust takeoff and landing for a class of aerial robots. In *Proceedings of the IEEE Conference on Decision and Control*, 2009.

[NMRS11] C. Nicol, C.J.B. Macnab, and A. Ramirez-Serrano. Robust adaptive control of a quadrotor helicopter. *Mechatronics*, 21(6):927 – 938, 2011.

[PBD11] Paul E. I. Pounds, Daniel R. Bersak, and Aaron M. Dollar. Grasping from the air: Hovering capture and load stability. In *Proceedings of the IEEE International Conference on Robotics and Automation*, pages 2491–2498, 2011.

[PMC10] P. Pounds, R. Mahony, and P. Corke. Modelling and control of a large quadrotor robot. *Control Engineering Practice*, 18(7):691 – 699, 2010. Special Issue on Aerial Robotics.

[PPTN08] L.M. Paz, P. Pinies, J.D. Tardos, and J. Neira. Large-scale 6-dof slam with stereo-in-hand. *IEEE Transactions on Robotics*, 24(5):946 –957, October 2008.

[PW09] D. A. Paley and D. S. Warshawsky. Reduced-order dynamic modeling and stabilizing control of a micro-helicopter. In *47th AIAA Aerospace Sciences Meeting, number AIAA-2009-1350, Orlando, Florida*, January 2009.

[RG03] Henrik Rehbinder and Bijoy K. Ghosh. Pose estimation using line-based dynamic vision and inertial sensors. *IEEE Transactions on Automatic Control*, 48(2):186–199, 2003.

[rma] Yamaha rmax website. Available online at http://rmax.yamaha-motor.com.au.

[ROR10] Guilherme V. Raffo, Manuel G. Ortega, and Francisco R. Rubio. An integral predictive/nonlinear $h_{infinity}$ control structure for a quadrotor helicopter. *Automatica*, 46(1):29–39, 2010.

[Ros04] I.M. Ross. A matlab application package for solving optimal control problems. Naval Postgraduate School, Monterey ,CA, USA, 2004.

[RSTE+10] E.J. Rodríguez-Seda, J.J. Troy, C.A. Erignac, P. Murray, D.M. Stipanovic, and M.W. Spong. Bilateral teleoperation of multiple mobile agents: Coordinated motion and collision avoidance. *IEEE Transactions on Control Systems Technology*, 18(4):984 –992, July 2010.

[RSZF07] James F. Roberts, Timothy S. Stirling, Jean-Christophe Zufferey, and Dario Floreano. Quadrotor using minimal sensing for autonomous indoor flight. In *3rd US-European Workshop and Competition about Micro-Aerial Vehicles and 7th European Micro Air Vehicle conference and flight competition*, 2007.

[RT11] Andrew Roberts and Abdelhamid Tayebi. Adaptive position tracking of vtol uavs. *IEEE Transactions on Robotics*, 27(1):129–142, 2011.

[Sas99] Shankar Sastry. *Nonlinear Systems: Analysis, Stability and Control*. Interdisciplinary Applied Mathematics. Springer, New York, 1999.

[SCPP09] C. Silvestre, R. Cunha, N. Paulino, and A. Pascoal. A bottom-following preview controller for autonomous underwater vehicles. *IEEE Transactions on Control Systems Technology*, 17(2):257–266, March 2009.

[SF04] Roger Skjetne and Thor Fossen. On integral control in backstepping: Analysis of different techniques. In *Proceedings of the American Control Conference*, volume 2, pages 1899–1904, May 2004.

[SF08] R.G. Sanfelice and E. Frazzoli. A hybrid control framework for robust maneuver-based motion planning. In *Proceedings of the American Control Conference*, pages 2254 –2259, June 2008.

[SI89] S.S. Sastry and A. Isidori. Adaptive control of linearizable systems. *IEEE Transactions on Automatic Control*, 34(11):1123 –1131, November 1989.

[SK07] Eric E Sandoz and P Kokotovic. Continuous path following control for underactuated systems with bounded actuation. In *Intelligent Vehicles Symposium*, pages 1178 – 1183, May 2007.

[TC05] O. Tahri and F. Chaumette. Point-based and region-based image moments for visual servoing of planar objects. *IEEE Transactions on Robotics*, 21(6):1116–1127, 2005.

[VBA10] H. Voos and H. Bou-Ammar. Nonlinear tracking and landing controller for quadrotor aerial robots. In *Proceedings of the IEEE International Conference on Control Applications*, pages 2136 –2141, sept. 2010.

[VCSO07] J. Vasconcelos, R. Cunha, C. Silvestre, and P. Oliveira. Landmark based nonlinear observer for rigid body attitude and position estimation. In *Proceedings of the IEEE Conference on Decision and Control*, pages 1033–1038, December 2007.

[VCSO10] J.F. Vasconcelos, R. Cunha, C. Silvestre, and P. Oliveira. A nonlinear position and attitude observer on se(3) using landmark measurements. *Systems & Control Letters*, 59(3-4):155 – 166, 2010.

[VIC] Vicon motion systems. Available online at http://www.vicon.com.

[VSS04] R. Vidal, O. Shakernia, and S. Sastry. Following the flock [formation control]. *IEEE Robotics and Automation Magazine*, 11(4):14–20, December 2004.

[YSKS04] Yi Ma, Stefano Soatto, Jana Kosecka, and Shankar Sastry. *An Invitation to 3-D Vision From Images to Geometric Models*. Springer, 2004. volume 26 of Interdisciplinary Applied Mathematics.

List of Publications

[1] D. Cabecinhas, R. Cunha, and C. Silvestre. Output-feedback control for almost global stabilization of fully-actuated rigid bodies. In *Proceedings of the IEEE Conference on Decision and Control*, pages 3583–3588. IEEE, 2008.

[2] D. Cabecinhas, R. Cunha, and C. Silvestre. Almost global stabilization of fully-actuated rigid bodies. *Systems & Control Letters*, 58(9):639–645, 2009.

[3] D. Cabecinhas, R. Cunha, and C. Silvestre. Rotorcraft path following control for extended flight envelope coverage. In *Proceedings of the 48th IEEE Conference on Decision and Control, 2009 held jointly with the 2009 28th Chinese Control Conference*, pages 3460–3465. IEEE, 2009.

[4] R. Cunha, D. Cabecinhas, and C. Silvestre. Nonlinear trajectory tracking control of a quadrotor vehicle. In *Proceedings of the European Control Conference*, 2009.

[5] D. Cabecinhas, R. Naldi, L. Marconi, C. Silvestre, and R. Cunha. Robust take-off and landing for a quadrotor vehicle. In *Proceedings of the IEEE International Conference on Robotics and Automation*, pages 1630–1635. IEEE, 2010.

[6] D. Cabecinhas, C. Silvestre, and R. Cunha. Vision-based quadrotor stabilization using a pan and tilt camera. In *Proceedings of the IEEE Conference on Decision and Control*, pages 1644–1649. IEEE, 2010.

[7] D. Cabecinhas, S. Bras, Silvestre, C., P. Oliveira, and R. Cunha. Integrated solution to quadrotor stabilization and attitude estimation using a pan and tilt camera. In *Proceedings of the IEEE Conference on Decision and Control*, pages 3151–3156, December 2012.

[8] D. Cabecinhas, R. Cunha, and C. Silvestre. Saturated output feedback control of a quadrotor aircraft. In *Proceedings of the American Control Conference*, pages 4667–4602, 2012.

[9] D. Cabecinhas, R. Naldi, L. Marconi, C. Silvestre, and R. Cunha. Robust take-off for a quadrotor vehicle. *IEEE Transactions on Robotics*, 28(3):734–742, June 2012.

[10] D. Cabecinhas, R. Cunha, and C. Silvestre. Experimental validation of a globally stabilizing feedback controller for a quadrotor aircraft with wind disturbance rejection. In *Proceedings of the American Control Conference*, pages 1024–1029, June 2013.

[11] D. Cabecinhas, R. Cunha, and C. Silvestre. Experimental validation of a nonlinear quadrotor controller with wind disturbance rejection. In *Proceedings of the European Control Conference*, pages 1811–1816, July 2013.

[12] D. Cabecinhas, C.Silvestre, and R. Cunha. A nonlinear quadrotor trajectory tracking controller with disturbance rejection. In *Proceedings of the American Control Conference*, 2014.

[13] D. Cabecinhas, R. Cunha, and C. Silvestre. A globally stabilizing path following controller for rotorcraft with wind disturbance rejection. *IEEE Transactions on Control Systems Technology (in press)*, 2014.

[14] D. Cabecinhas, R. Cunha, and C. Silvestre. A robust landing and sliding maneuver controller for a quadrotor vehicle on a sloped incline. In *Proceedings of the IEEE International Conference on Robotics and Automation*. IEEE, 2014.

[15] D. Cabecinhas, R. Naldi, L. Marconi, C. Silvestre, and R. Cunha. Robust landing and sliding maneuver hybrid controller for a quadrotor vehicle. *IEEE Transactions Control Systems Technology (submitted)*, 2014.

[16] David Cabecinhas, Sérgio Brás, Rita Cunha, Carlos Silvestre, and Paulo Oliveira. Integrated solution to quadrotor stabilization and attitude estimation using a pan and tilt camera. *IEEE Transactions on Robotics (submitted)*, 2014.

[17] David Cabecinhas, Rita Cunha, and Carlos Silvestre. A nonlinear quadrotor trajectory tracking controller with disturbance rejection. *Control Engineering Practice*, 26(0):1 – 10, 2014.